Experimental study on electron impact double ionization dynamics for atomic and small molecular targets at intermediate incident energy

Chengjun Li

UNIVERSITE PARIS-SUD

Ecole Doctorale Ondes et Matière
Institut des Sciences Moléculaires d'Orsay

DISCIPLINE
Physique

THÈSE DE DOCTORAT

soutenue le 25/04/2013

par

Chengjun LI

Experimental study on electron impact double ionization dynamics for atomic and small molecular targets at intermediate incident energy

Directeur de thèse:
Elena-Magdalena STAICU-CASAGRANDE MdC(HDR) (Université Paris Sud XI)

Composition du jury :

Président du jury :	Christophe BLONDEL	DR (Université Paris Sud XI)
Rapporteurs :	Ugo ANCARANI	MdC (HDR) (Université de Lorraine)
	Amine CASSIMI	Ingénieur (HDR) (CEA, Caen)
Examinateurs :	Arne KELLER	Professeur (Université Paris Sud XI)
	Pascal LABLANQUIE	DR (Université Pierre et Marie CURIE)
Membres invités :	Azzedine BENNANI	Professeur (Université Paris Sud XI)

Contents

Chapter 2 *Experimental Apparatus*

Chapter 3 *Coplanar asymmetric (e, 3-1e) measurements on He, Ne and Ar atoms: predominance of the second-order, two-step mechanism*

General introduction

The single or multiple ionization of atoms (or molecules) by charged particle (or by photon) impact is one of the most interesting and most important domains in atomic physics [1, 2]. The electron impact ionization is among the most fundamental cases of such processes. The detailed knowledge of the single ionization (SI) and double ionization (DI) is strongly needed in other physics branches such as plasma physics, astrophysics, where the basic interaction mechanisms – ionization, excitation, electron capture, etc. – are involved. It is also needed in other sciences such as biology science, where the prime importance is to understand the various mechanisms leading to energy deposition by radiation in living matter [3].

From the study of single or double ionization by electron impact, depending on different kinematical regimes, we can obtain fundamental information on two aspects: (a) dynamical information on SI or DI process such as projectile-target interaction, electron-electron correlation, post-collision interaction (PCI), etc.; (b) target structure information using the so-called electron momentum spectroscopy (EMS).

In this work, we mainly focus on the experimental investigation of electron impact DI dynamics at intermediate incident energy for atomic targets and small molecular targets. To this purpose, we use the so-called (e,3e) and (e,3-1e) experiments which yield very detailed information in the form of fully differential cross sections.

The (e, 3e) experiments refer to electron impact DI experiments in which the scattered projectile and the two target ejected electrons are selected and analyzed in energy and direction and are detected in triple coincidence [4]. Besides, the so-called (e, 3-1e) experiments also bear the signature of DI process as in the (e, 3e) case, but they differ from (e, 3e) experiments by analyzing in energy and direction only two of the three outgoing electrons and detecting them in double coincidence [5]. In other words, the direction of the third electron is unknown as it is distributed in 4π solid angle space, whereas its energy is fixed due to the energy conservation where the residual ion is assumed to be in its ground state after interaction.

Due to the inherent small DI cross section and detection technique limitation, it is difficult to measure the (e, 3e) fully differential cross section of DI process. Up to present, with the development of multi-detection technique [4, 11], however, only few DI experiments with E_0 below 1 keV were performed, most of them being related to He.

Generally, depending on the number of interactions between incident electron and target, the various DI mechanisms can be assorted into two categories: (a) first order mechanisms characterized by one single target – projectile interaction, such as Shake Off (SO) mechanism and Two Step 1 (TS1)

mechanism; (b) second (or higher) order mechanisms characterized by two (or more than two) successive target – projectile interactions, such as Two Step 2 (TS2) mechanism. The previous DI experimental results with high incident energy ($E_0 > 5$ keV) could be described successfully by first order mechanisms [6-10]. However, McGuire [10] argued that the TS2 mechanism plays a more and more important role relative to the SO mechanism when the incident energy is decreased to less than about 1 keV. Therefore, in order to answer this questioning, new highly differential DI experimental measurements at intermediate incident energy (<1 keV) on He as well as on other atomic and molecular targets is imminently necessary. With these new DI results, we can examine the second order mechanism (TS2) contribution at intermediate incident energy on the one hand, and extend the DI studies to other more complex targets (such as small molecules) in order to examine if the second order mechanism plays a similar role for ionization of molecules, on the other hand.

In this thesis, by using the recently developed (e, 2e)/(e,3e) spectrometer with multi-angle collection and multi-coincidence detection in Orsay [4], a series of new (e, 3-1e) measurements (yielding four-fold differential cross sections, 4DCS) performed for different targets (He, Ne, Ar, N_2 and CH_4), under various energy sharings between the two ejected electrons and at an intermediate incident energy of ~ 600 eV, are presented and discussed. Moreover, new sets of (e, 3e) measurements for N_2 (yielding five-fold differential cross sections, 5DCS) are performed for the first time for a molecular target. Different first order and second order theoretical models available up to date for present experimental targets and kinematics are used for comparison with the experimental results. Moreover, the predictions of the classical 'TS2 kinematical model' developed in our group [12] are compared with all (e, 3-1e) and (e, 3e) results.

The presentation of the thesis is organized in the following way:

In chapter 1, the electron impact single and double ionization are overviewed and a brief presentation of the electron impact double ionization theory is given. A description of the different theoretical mechanisms and models is presented for the comparison with the following experimental results.

The experimental apparatus and data analysis methods are described in details in chapter 2.

In chapter 3, the coplanar asymmetric (e, 3-1e) measurements on He, Ne and Ar atoms at various energy sharing cases between the two ejected electrons are presented and discussed. These results are compared with different first and second order theoretical models and TS2 kinematical analysis prediction to confirm the predominance of the second-order, two-step mechanism in the electron impact double ionization.

The (e, 3e) and (e, 3-1e) measurements for N_2 are presented with two different equal energy sharing cases: (E_b:E_c) = (12:12) eV and (E_b:E_c) = (37:37) eV. The results of a first order theoretical model which includes correlation between the two ejected electrons are compared with the experimental results. For this more complex target, since there is no theoretical calculation for (e, 3-1e) results, only the TS2 kinematical analysis predictions are used for comparison yielding a straightforward comprehension of TS2 contribution.

In chapter 5, preliminary (e, 3-1e) results for Ne and CH_4 are obtained at intermediate incident energy. For these isoelectronic targets, it is interesting to investigate the behavior of two targets with same final kinematical state, and to search for possible molecular effects. We give some tentative explanation for these new results. However, these are to be understood as an opening for a prospective future extension of the present work. Further analysis and discussion of the results and further consideration of complementary experiments is under way.

Bibliography

1. Schulz, M., et al., *Three-dimensional imaging of atomic four-body processes.* Nature, 2003. **422**(6927): p. 48-50.
2. Rescigno, T.N., et al., *Collisional Breakup in a Quantum System of Three Charged Particles.* Science, 1999. **286**(5449): p. 2474-2479.
3. Zheng, Y., et al., *Role of Secondary Low-Energy Electrons in the Concomitant Chemoradiation Therapy of Cancer.* Physical Review Letters, 2008. **100**(19): p. 198101.
4. Catoire, F., et al., *New developments for an electron impact (e,2e)/(e,3e) spectrometer with multiangle collection and multicoincidence detection*. Review of Scientific Instruments, 2007. **78**(1).
5. Lahmam-Bennani, A., et al., *Identification of mechanisms of electron impact double ionizing collisions by e,(3-1)e experiments*. Journal of Physics B: Atomic, Molecular and Optical Physics, 1991. **24**(16): p. 3645.
6. Lahmam-Bennani, A., Duprié, C. and Duguet, A. *Electron-impact double ionization of argon studied by double and triple coincidence techniques: The first (e,3e) experiment.* Physical Review Letters, 1989. **63**(15): p. 1582-1585.
7. El Marji, B., et al., *Dynamics of the double ionization process from (e,3e) experiments: I. Absolute cross sections for argon*. Journal of Physics B: Atomic, Molecular and Optical Physics, 1997. **30**(16): p. 3677.
8. Taouil, I., et al., *Fully Determined (e,3e) Experiments for the Double Ionization of Helium.* Physical Review Letters, 1998. **81**(21): p. 4600-4603.
9. Lahmam-Bennani, A., et al., *Complete experiments for the double ionization of He: (e,3e) cross sections at 1 keV impact energy and small momentum transfer*. Journal of Physics B: Atomic, Molecular and Optical Physics, 2001. **34**(15): p. 3073.
10. McGuire, J.H., *Double Ionization of Helium by Protons and Electrons at High Velocities.* Physical Review Letters, 1982. **49**(16): p. 1153-1157.
11. Ullrich, J., et al., *Recoil-ion momentum spectroscopy*. Journal of Physics B: Atomic, Molecular and Optical Physics, 1997. **30**(13): p. 2917.
12. Lahmam-Bennani, A., et al., *Predominance of the second-order, two-step mechanism in the electron impact double ionization of helium at intermediate impact energy*. Journal of Physics B: Atomic, Molecular and Optical Physics, 2010. **43**(10): p. 105201.

Chapter 1 *Theory of electron impact double ionization and motivation of experimental investigation*

Chapter 1 *Theory of electron impact double ionization and motivation of experimental investigation*

1.1 Introduction

In recent years the studies of multiple ionization processes by charged particle impact has known considerable interest in many branches in physics such as astrophysics and plasma physics or in other science such as biology science [1], where the prime importance is to understand the various mechanisms leading to energy deposition by radiation in matter. To this end, understanding of the mechanisms of multi ionization and the role of electron correlation is of fundamental importance [2-7]. These multiple ionization processes are studied by using various incident particles, such as electrons [3, 7-10], photons [11] or other charged-particles [12-14]. Single and double electron impact ionization of atoms and molecules are the most basic and simplest processes in particle impact multiple ionization process. In this work, we focus on the electron impact double ionization (DI) mechanism study (see Fig. 1.1).

1.1.1 Electron impact ionization process and notations

As usual, electron impact multi-ionization research can be assorted into two categories: structure study (electron momentum spectroscopy (EMS)) [15] and collision dynamics study [7, 16], depending on whether the target core participates or not to the interaction. This will be introduced in detail as follows.

The electron impact single ionization (SI) or double ionization (DI) can be schematically written as

$$e_0 + A \longrightarrow e_a + e_b + A^+ \text{ or } e_0 + A \longrightarrow e_a + e_b + e_c + A^{2+} \tag{1.1}$$

and it obeys energy conservation and momentum conservation (see Fig. 1.1):

$$E_0 = E_a + E_b + E_{ion} + IP^+, \quad \vec{\boldsymbol{k}}_{\boldsymbol{0}} = \vec{\boldsymbol{k}}_{\boldsymbol{a}} + \vec{\boldsymbol{k}}_{\boldsymbol{b}} + \vec{\boldsymbol{q}}_{\boldsymbol{ion}} \text{ (SI)} \tag{1.2}$$

$$\text{or } E_0 = E_a + E_b + E_c + E_{ion} + IP^{2+}, \ \vec{\boldsymbol{k}}_{\boldsymbol{0}} = \vec{\boldsymbol{k}}_{\boldsymbol{a}} + \vec{\boldsymbol{k}}_{\boldsymbol{b}} + \vec{\boldsymbol{k}}_{\boldsymbol{c}} + \vec{\boldsymbol{q}}_{\boldsymbol{ion}} \text{ (DI).} \tag{1.3}$$

Here the notations are related to the caption of Fig. 1.1. The notations IP^+, IP^{2+} and $\vec{\boldsymbol{q}}_{\boldsymbol{ion}}$ represent SI potential, double ionization potential and target recoil momentum, respectively. The difference between SI and DI is that in SI case, there is only one ejected electron while in DI there are two ejected electrons from target after interaction. The SI and DI are usually called (e, 2e) and (e, 3e) reaction for short.

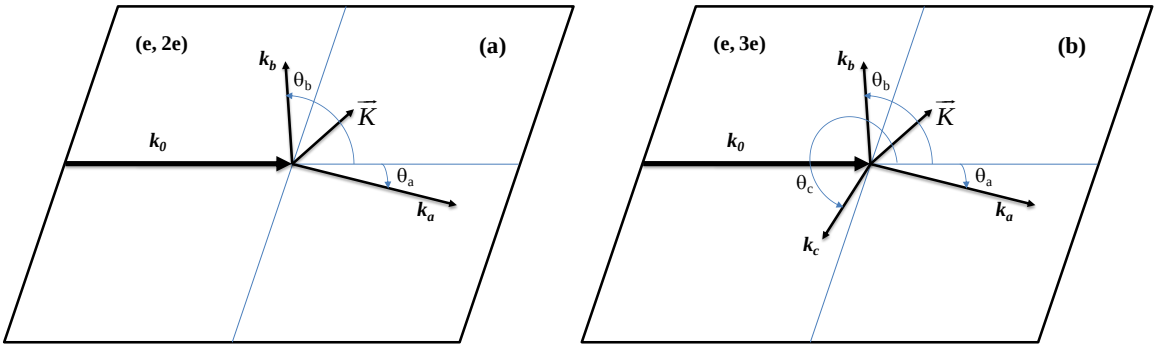

Figure 1.1 *The coplanar scattering geometry for the (e, 2e) (panel (a)) and (e, 3e) (panel (b)) experiment. The notations* $\boldsymbol{k_0}$, $\boldsymbol{k_a}$, $\boldsymbol{k_b}$, ($\boldsymbol{k_c}$), θ_a θ_b *(and* θ_c*) respresent the momentum of incident, scattered, faster ejected, slower ejected electron(s), the angles of scattered, faster ejected and slower ejected electron(s) in (e, 2e) ((e, 3e)) experiment, respectively.* $\boldsymbol{K}$ *is the momentum transfer from incident electron to the target. The (two) ejected electron(s)* e_b *(and* e_c*) is (are) detected in the plane defined by incident (*e_0*) and scattered (*e_a*) electrons with* e_a *in coincidence.*

The momentum transfer ($\vec{\boldsymbol{K}}$) is defined as the momentum difference between the incident electron (e_0) and scattered electron (e_a), as given by the following equation:

$$\vec{\boldsymbol{K}} = \vec{\boldsymbol{k}}_{\boldsymbol{0}} - \vec{\boldsymbol{k}}_{\boldsymbol{a}}. \tag{1.4}$$

A. Structure studies

The momentum transfer direction plays a key role in distinguishing between electron impact ionization structure studies (or so-called electron momentum spectroscopy (EMS)) and collision dynamics studies. As it is known, if the Bethe ridge condition is satisfied, e.g., in SI, the whole energy and all momentum are transferred to (or absorbed by) the ejected electron b. Whether in SI [15] or DI [17] case, once the Bethe ridge condition is satisfied, the residual ion plays no role but it only behaves as a spectator in the interaction process. Thus the angular distribution of single (or double) ejected electron(s) contains (or contain) the target electron momentum information (or electron-electron correlated momentum distribution) of corresponding ionized orbital(s). Under Bethe ridge condicitons Eqs. (1.2) and (1.4) become:

$$E_0 - E_a - IP^+ = E_b \text{ and } \vec{\boldsymbol{k}}_{\boldsymbol{b}} = \vec{\boldsymbol{K}} = \vec{\boldsymbol{k}}_{\boldsymbol{0}} - \vec{\boldsymbol{k}}_{\boldsymbol{a}}. \tag{1.5}$$

Similarly, for DI case, Eqs. (1.3) and (1.4) become:

$$E_0 - E_a - IP^{2+} = E_b + E_c \text{ and } \vec{\boldsymbol{k}}_{\boldsymbol{b}} + \vec{\boldsymbol{k}}_{\boldsymbol{c}} = \vec{\boldsymbol{K}} = \vec{\boldsymbol{k}}_{\boldsymbol{0}} - \vec{\boldsymbol{k}}_{\boldsymbol{a}}. \tag{1.6}$$

Traditionally, in SI (e, 2e) EMS study, symmetric coplanar or non-coplanar [18] experiments are performed at impact energies of ~1-2 keV, with two outgoing electrons sharing the energy evenly. The incident energy is significantly larger than the ionization potential and the single knock-out

collision is sufficient to eject the initially bound target electron into continuum. Multiple collisions of the projectile with the target can be safely neglected in this case. Theoretical treatment of the EMS only considers the lowest-order term (or first order term) in expansion series of transition matrix, where the magnitude of transition are treated pertubatively and the projectile and outgoing electrons are described as plane wave, such as Plane Wave Born or Impulse Approximation (PWBA or PWIA) [19].

B. Collision dynamics studies

In this thesis, we mainly focus on the experimental dynamics study of electron impact DI process. The characteristic of this category is using asymmetric kinematics where three outgoing electrons are detected at very different energies, and the momentum transfer from incident projectile to target is usually small. The incident energy is very different from one experiment to another, from threshold [20] to a few hundred eV [21] and up to 8 keV [22]. These are the conditions under which most ionizing collision occurs, and hence the main emphasis has been placed at understanding the ionization dynamics.

C. Electron impact double ionization

For DI reactions the outgoing electrons, though indistinguishable, are indexed 'a' for the fast 'scattered' one and 'b' and 'c' for the slow ejected ones (see Fig. 1.1).

The target and the residual ion are assumed to be in their ground state. The ion recoil energy E_{ion} is generally negligible because of the smallness of the electron to ion mass ratio. The recoil ion momentum $\vec{\boldsymbol{k}}_{\mathrm{ion}}$ is obtained by subtracting from the momentum transfer vector $\vec{\boldsymbol{K}}$ the momentum of the center of mass of the ejected electrons, ($\vec{\boldsymbol{k}}_{\mathrm{b}}$+$\vec{\boldsymbol{k}}_{\mathrm{c}}$). In Fig. 1.1, in a coplanar geometry case, all electrons are observed in the collision plane at in-plane angles θ_a, θ_b and θ_c with respect to incident direction, while the out-of-plane (azimuthal) angles φ_b and φ_c are set to 0 or π. The fully differential cross sections are measured in (e, 3e) experiment with completely determined kinematics (apart from spin and magnetic sublevels), where all three final electrons are simultaneously analyzed both in energy and in direction and are detected in coincidence. So measuring the double ionization rate means to resolve simultaneously the vector momentum of all particles in the continuum final state. Thus, a multi-coincidence detection technique has to be utilized. The nature of small cross sections of DI event implies very low counting rates (as compared to SI) and long data accumulating time for satisfactory statistics, etc. Hence it makes the experimental realization a challenging task.

1.1.2 Definition of different n-fold differential cross sections

Because a DI experiment involves many variables (10 variables: E_0, E_j, θ_j, φ_j with j=a, b, c) linked by energy and momentum conservations, it is necessary to unify the terminology used and a precise definition of n-fold differential cross sections. Though DI process is mainly studied in this work, a general presentation of n-fold differential cross sections definition is shown below for completeness.

The results obtained from an (e, 2e) or (e, 3e) experiment are represented in terms of cross section. This quantity gives a measurable probability of certain type of reaction. When a reaction occurs, the fragment particles resulted from the reaction are measured within a spatial window limited to a solid angle $\Delta\Omega$ and energy deviation ΔE. These cross sections observed are differential in energy and in angle for these scattered and/or ejected electrons. The integral cross section is the integral of the differential cross section on the whole sphere of observation (4π solid angle) and/or energies. Depending on different type of experiments, we can define different n-fold differential cross sections as follows.

A. Single Differential Cross Section

When only one of the emitted particles is detected in a certain direction, no matter what its energy is, we can say this corresponds to SDCS in angle, $\frac{d\sigma}{d\Omega}$. This SDCS is the integral over all energy range. This quantity has obviously more detailed information in the ionization process than the total cross section. For example, it has a great interest in molecular structure study.

If one is interested in spectroscopy aspects of the target, one can define another kind of SDCS in energy, $\frac{d\sigma}{d\mathrm{E}}$. It represents a major tool in the investigation of various fields of physics such as the study of energy loss of electrons produced in the ionosphere land. We cannot directly measure the SDCS in energy $\frac{d\sigma}{d\mathrm{E}}$, it is obtained by integrating over all angles of emission the double-differential cross sections.

B. Double Differential Cross Section

If the information on the emission angle and the energy of ejected electron are gathered at the same time, then we have a double differential cross section (DDCS) $\frac{d^2\sigma}{d\Omega dE}$. This quantity is more detailed than the SDCS since it provides the energy and angle distribution of the scattered or ejected particles after the collision.

The problem with measurements of SDCS and DDCS is the uncertainty about the process seen on one hand, and ionized states for a given energy, on the other hand. Theories used to describe the

SDCS must include all energetically possible ionization process and all states which can contribute to cross sections. To address this uncertainty, the energy and momentum transfer must be determined to specify the particular contributing ionization process. The (e, 2e) measurement technique provides such information via measurements of triple differential cross sections.

C. Triple Differential Cross Section

If the two electrons in the final state are analyzed according to their directions as well as their respective energies, it will be called triple differential cross section. In a (e2e) process this quantity is called complete differential cross section and provides details on the dynamics of interaction since it involves all kinematic parameters of the DI process, namely the energies E_0, E_a and E_b and the solid angles Ω_a and Ω_b. We note it as:

$$\sigma^{(3)} = \frac{d^3\sigma}{d\Omega_a d\Omega_b dE_a} \tag{1.7}$$

where E_b can be derived by energy conservation (see Eq. 1.2).

It represents the probability of two electrons ejected in the output channel with energies E_a and E_b and momentum $\vec{\boldsymbol{k}}_{\mathbf{a}}$ and $\vec{\boldsymbol{k}}_{\mathbf{b}}$ in the directions Ω_a and Ω_b by an incident electron energy E_0 and momentum $\vec{\boldsymbol{k}}_{\mathbf{0}}$.

In (e2e) SI experiments the scattered and ejected electrons are detected in double coincidence, which ensures that they are originated from the same ionizing event. By their sensitivity, these 'complete' experiments are of considerable importance for the understanding of the mechanisms of ionization. They can test the different theoretical models proposed to describe the projectile-target interaction and thus validate or not the approximations and/or assumptions which are underlying.

D. Five-fold Differential Cross Section and Four-fold Differential Cross Section

In DI experiments, there are three outgoing electrons in the final state, one scattered electron and two ejected electrons, namely e_a, e_b and e_c, respectively. These three electrons have nine degrees of freedom. If considering the coplanar geometry and energy conservation before and after DI interaction, these nine degrees of freedom in final state can be reduced to five, which are energies of two ejected electrons, E_a and E_b, and directions of three outgoing electrons, Ω_a, Ω_b and Ω_c. When all of these five parameters are determined in experiments, hence we call the results as five-fold differential cross section (or Fully Differential Cross Section (FDCS)), which represents a complete determination of kinematical parameters of all three outgoing electrons after DI interaction. We note this FDCS or 5DCS as:

$$\sigma^{(5)} = \frac{d^5\sigma}{dE_a dE_b\, d\Omega_a d\Omega_b d\Omega_c} \tag{1.8}$$

In (e, 3e) DI experiments the scattered and the two ejected electrons are detected in triple coincidence, which ensures that they are issued from the same ionizing event. These 'complete' 5DCS (or FDCS) experiments provide the most detailed information of DI process and can be used as a strict test to different theoretical models of describing the projectile-target DI interaction and thus validate or invalidate these theoretical models and/or approximations [7, 23, 24].

However, these experiments are technically difficult and very time consuming because of very small DI cross section (about 2-3 orders smaller than SI (e, 2e) experiments) and very low signal to noise ratio in detection. It is therefore also of interest to consider a type of experiments intermediate between (e, 2e) and (e, 3e) experiments, in which two of the three electrons present in the DI final state are detected: hence the name (e, 3-1e) experiment [25-27]. In these experiments, an arbitrary pair of electrons, (e_a, e_b) [23], (e_a, e_c) or (e_b, e_c) [28-30], is detected in coincidence, irrespective of the emission direction of the third unobserved electron. Its energy E_c is in general also unknown since the ion final state is not determined (except for He target), unless we assume that the residual ion is in its ground state. Thus, integration is performed over the solid angle of emission of one electron, say Ω_c, yielding a four-fold differential cross section, 4DCS, or

$$\sigma^{(4)} = \int \sigma^{(5)} d\Omega_c = \frac{d^4\sigma}{dE_a dE_b\, d\Omega_a d\Omega_b}. \tag{1.9}$$

1.2 Collision theory of double ionization

Ionization processes caused by charged-particle impact such as ionization with simultaneous excitation and double ionization are strongly dependent on many electron correlations [7]. However, unlike the two-electron single-photon ionization processes, which are driven entirely by correlations, charged-particle impact can cause a two electron transition in the absence of correlations simply by repeated interaction of the projectile with the target. This competition of the electron correlations in the target and a complicated dynamics of the reaction make it difficult to interpret particle-induced two-electron ionization. However, there exists a case when the correlations and dynamics can be disentangled. Indeed, if the projectile is fast, its interaction with the target can be treated perturbatively (the so-called low perturbation regime) by employing a Born series expansion. This effectively reduces the problem of four interacting charged particles to a three-body Coulomb problem which is encountered in the two-electron ionization caused by photon impact. The latter problem can be treated by employing either an asymptotically exact three-body Coulomb wave function or a close-coupling expansion to account for interaction of the two target electrons in continuum. In the following part, we will describe the pertubative theory and non-pertubative theory

briefly and focus on the formula development of the pertubative theory in §1.3, which is used for as a primary theory comparison to our experimental measurements.

1.2.1 Pertubative theory

The earliest quantum mechanical models of ionization dating from the 1920s used Born's approximations for the ionization amplitude. This model uses a scattering wave function approximated by the product of the wave function of the target atom (or molecule) and a plane wave for the incident projectile folded between the electron-electron potential and a final-state wave function that is a product of a plane wave for the fast scattered and a Coulomb wave for the slow ejected electrons.

A. Dynamical ionization theory for atomic target

In order to extend the application and enhance the precision of Born series approximation, many methods are developed for description of DI dynamical process, such as including post-collision interaction (PCI) process involving exchange of energy and angular momenta between outgoing free electrons after the collision [31-34], employing distorted wave for describing incident and scattered electrons (e.g., Distorted Wave Born Approximation (DWBA)) [35-37], employing different target wave functions [38], including second or higher order mechanisms [39] (double or multi interaction between projectile and target), etc..

Several hypotheses have been made to describe the mechanisms of the DI. In the early time, the electron impact DI problem was first discussed systematically by Tweed in 1973 [40-42] by employing Born series approximation. In these articles, Tweed used the Schrödinger equation as a starting point, the asymptotic form of the wave function is derived for the total and differential cross section. The first Born and second Born approximation are discussed in the context of DI at high incident energy and small momentum transfer. He emphasized that even at high incident electron energies the contribution from the second Born amplitude is quite important [43]. Tweed proposed the following DI mechanisms: the projectile interacts with the target to eject one of the target electrons. Another electron leaves the target because of the resulting change of the felt effective potential.

The SO process is a single interaction between the incident electron and one target electron [44, 45], leading to a first ejected electron. This first ionization is followed by a relaxation process due to the sudden change of potential that is responsible for a second ejection (see Fig. 1.2).

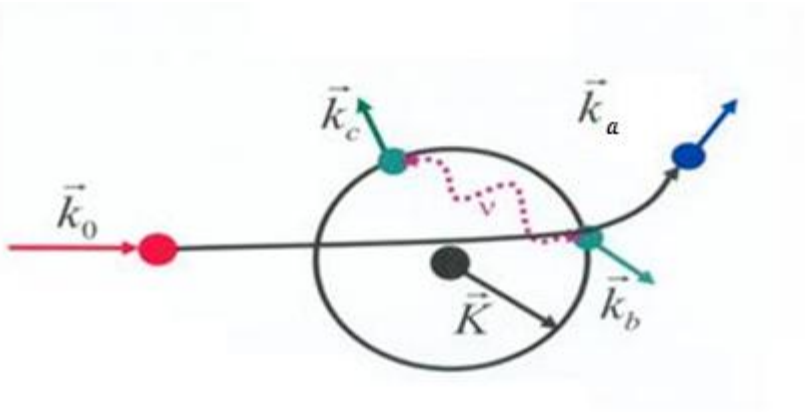

Figure 1.2 *Schematic of 'shake off' double ionization mechanism. The notations are the same as in Fig. 1.1(b).*

Carlson and Krause [45] have proposed two other mechanisms in the case of electron impact. In first case the incident projectile interacts with the target successively to eject two different target electrons, ejecting them one by one (TS2 process). In the second case, the incident projectile ejects one target electron and is scattered off from the target, then this ejected electron plays a role as an intermediate incident projectile and collide with another target electron, resulting in a pair of ejected electrons. McGuire investigated the DI of He with high energy of incident electron and estimated the contribution of two different mechanisms under investigated condition namely 'Shake Off' mechanism and 'Two-Step' mechanism. McGuire concluded that these two-step mechanisms (including the first case 'Two-Step 2' (TS2) mechanism and the second case 'Two-Step 1'(TS1) mechanism) contribute appreciably at incident energies below 1 keV [39, 46] while SO mechanism gives a constant contribution to DI, independent of incident energy.

The TS1 process [45] consists of a first interaction between the incoming electron and one target electron. It leads to a first ejected electron that interacts with another target electron. This second interaction leads to an ejection of another bound electron (see Fig. 1.3).

The TS2 process [45] takes into account two interactions between the incoming electron and the target. The first is concerned with the collision of the incoming electron with one target electron. Then the intermediate scattered electron interacts with another target electron (see Fig. 1.4).

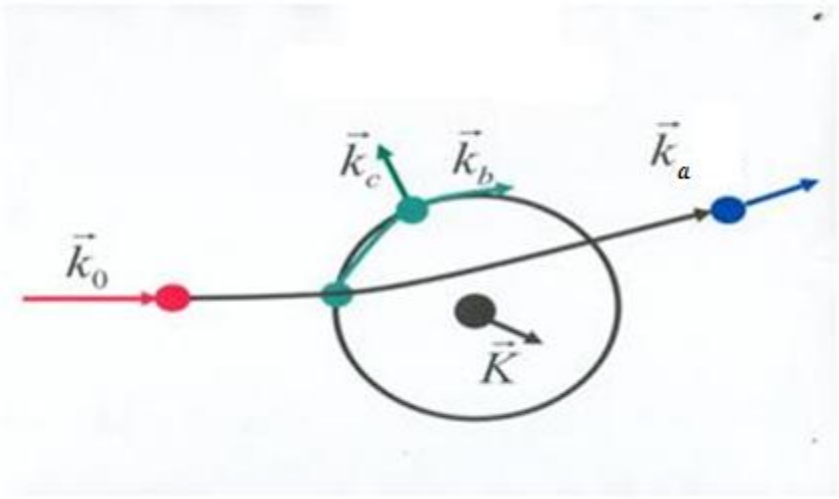

Figure 1.3 *Schematic of 'Two-Step 1' double ionization mechanism. The notations are the same as in Fig. 1.1(b).*

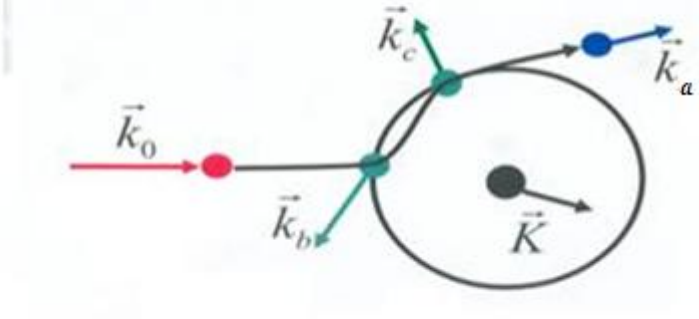

Figure 1.4 *Schematic of 'Two-Step 2' double ionization mechanism. The notations are the same as in Fig. 1.1(b).*

B. Theoretical models for molecular dynamical ionization process

There are mainly three different theoretical models for describing dynamical mechanisms in electron impact ionization of molecular targets. Of course there are other models such as modified additive rule (MAR) method model [47], two-effective-centre (TEC) [48] approximation model, but they are beyond from the present work and will not be discussed. Note that the SI or DI processes will go regarded as a pure electronic transition since the closure relation over all possible rotational and vibrational states of the residual target can be applied: the relation between the collision time and the characteristic time of the rotation and vibration justifies this. Moreover, exchange effects will be neglected since the scattered electron is faster than the ejected one in all the cases considered here.

Although presently all of the following models are used for the description of SI problem of molecular target, their frameworks are desirable to be extended for description DI process.

1) First Born Approximation Two Center Continuum model

This theoretical model uses a first Born framework in which the two-centre continuum (TCC) approximation with correct boundary conditions in the entrance and exit channels [49] is applied. The TCC accurately describes the slow ejected electron in the electrostatic field of the residual diatomic ion as it produces [50] results in very good agreement with those obtained by a partial wave treatment of the exact solution of the two-centre Schrödinger equation in prolate spheroidal coordinates [51]. Here, the relatively fast incident and scattered electrons are described by plane waves and the bound electron is given by self-consistent field (SCF) linear combination of atomic orbitals (LCAO), in which the molecular wave function is expressed as a sum of orbitals for each nucleus. In averaging over all orientations of the molecular axis, all directions are considered to be equally probable.

2) Molecular Three-body Distorted Wave approximation coupled with an Orientation-Averaged Molecular Orbital approximation model

This is molecular three-body distorted wave (M3DW) approximation coupled with an orientation-averaged molecular orbital approximation (OAMO) [52, 53]. In this approach, the OAMO is generated first and then it is used in the transition (T) matrix. As a result, the T matrix is evaluated only once with a single OAMO instead of many times for many orientations. The M3DW is a two-centre approach in which all three continuum electron wave functions are represented by distorted waves calculated on a spherically symmetric potential obtained from the Hartree-Fock charge distribution for molecular target (for instance, N_2), coupling with an averaged orientations over all molecular obtained by the OAMO method. The final state post-collision is included in the final state wave function which means that the final state post-collision interaction (PCI) between the two continuum electrons is included to all orders of perturbation theory.

3) Molecular Brauner-Briggs-Klar model

The MBBK models was first developed by C. R. Stia et al [54] to study the interference effects observed in single ionization of molecular hydrogen by electron impact [55]. In this model, the single ionization process is assumed to be produced in the proximity of one of the two molecular nuclei, while the passive electron completely screens the other molecular nucleus. Thus the molecular amplitude is reduced to a coherent sum of two three-body amplitudes (where the three bodies are the ionized electron, the scattered electron, and one or the other molecular nucleus). Moreover, the correlated motion of these three unbound particles in the final channel is considered in the same way as was done previously for the atomic case [56].

1.2.2 Non-pertubative theory

In theoretical physics, a non-perturbative theory is one does not simply describe the dynamics of perturbations around some fixed background. For this reason, non-perturbative solutions and theories yield insights into areas and subjects which perturbative methods cannot reveal.

By the late 1970s significant progress had been made in developing optical potential, coupled-channels and R-matrix methods to describe electron-atom discrete inelastic scattering. These methods relied on the development of powerful computers that enabled larger and larger calculations to be performed. Each of these methods was based on the solution of the time-independent Schrödinger equation utilizing a, in principle, convergent expansion of the scattering wave function in terms of a complete set of target states. In the following section, three of frequently used non-perturbative approach in electron impact ionization process will be introduced briefly. However,there are also other non-perturbative methods, such as R-matrix with pseudo-state (RMPS) [57-59], the integro-differential close-coupling (IDCC) method [60], etc. Nevertheless, they will not be discussed in detail.

A. Convergent close-coupling

The Convergent Close-Coupling (CCC) method is a technique for treating a projectile-target collision problem. The aim is to solve such systems at any collision energy for the major scattering and ionization processes. A full implementation of a convergent method to treat the continuum states was practically achieved by Bray and Stelbovics [61] in 1992. Initially, the method was implemented for the simplest well-studied Coulomb three-body problem of the electron scattering on atomic hydrogen for excitation and total ionization. A few years later, it was shown to work for fully differential ionization [62] as well. Furthermore, this technique has been generalized to other projectiles, including photons, positrons, and more recently to heavy projectiles such as antiprotons [63].

The strength of the CCC method is that convergence is assured in principle by using a complete set of expansion functions to construct the discretized target wave functions for the continuum. In numerical calculations the convergence is established by increasing the number of expansion functions. However, the convergence with increasing number of basis functions is slow (of the order $N^{-\alpha}$ with $\alpha<1$) and very large systems of coupled equations are required to be solved for each particle wave. With ever increasing computer power the method is being extended to more complex targets. To date the method has been restricted to ionization from the valence shell of atoms and ions.

B. Exterior complex scaling

As well known, specifying the asymtotic form of the scattering wave function for electron-impact ionization is a major challenge due to the long-range Coulomb force [64]. In order to carry out numerical calculations for ionization, one needs alternative methods to satisfy the ionization boundary condition. The Exterior Complex Scaling (ECS) is one method that seeks to eliminate the complexity of dealing with the true ionization boundary condition. This method was developed in the late 1990s [5, 65, 66] and seeks to solve the time-independent coordinate-space Schrödinger equation by rotating the configuration space coordinates into the complex plane at sufficiently large distances $r \geq R_0$, where the asymptotic form of the boundary condition can be employed without approximation and hence provide a complete *ab initio* solution.

Since the method is so computationally intensive, relatively little work has been carried out beyond the three-body problem and was limited to a narrow range of projectile energies. In order to realize the potential of the method for other targets it was vital that development of more efficient algorithms take place. The propagating exterior complex scaling method (PECS) is one of such computational enhancement and could be applied to energies near the ionization threshold and at moderately high energies, where other state-of-art methods had difficulty reaching.

C. Time-dependent close-coupling

Similarly to the ECS method the time-dependent close-coupling (TDCC) is a direct approach to the solution of the three-body Schrödinger equation, which allows one to avoid the difficulties associated with formulating the correct asymptotic boundary conditions. However, the TDCC approach differs fundamentally from these previous non-perturbative approaches in that it solves the time-dependent, rather than time-independent, Schrödinger equation. It avoids the need of a final-state boundary condition in order to extract scattering information. The TDCC approach takes advantage of the rapid advances made in high-performance computing resources to efficiently solve the discretized Schrödinger equation for two (or more) electrons moving in the field of a charged nucleus (or nuclei) [67-70].

The TDCC approach has also been extended to treat three active electrons, which is required to calculate electron impact double ionization of two-electron systems, as well as electron-impact ionization-excitation cross sections. Extension to three active electrons results in a significantly more complicated calculation compared to a two active electron case, as well as a much more computationally intensive problem. The complications are due to the large number of coupled channels which arise due to the coupling of three active electrons, which is also further complicated since the spatial and spin components of the three-electron wave function do not separate. This latter

point also complicates the projection techniques used to extract probabilities for the many excitation and ionization processes.

1.3 Three Double ionization mechanisms

In the DI experiment the cross section (1.8) is measured. This quantity, which is defined in a nine-dimensional momentum space spanned by $\vec{k}_{b/c}$ and $\vec{k}_a$, is calculated as the coherent sum of all the transition amplitudes which may lead to interference phenomena. However, in some regions of the momentum space (that can be selectively probed by the experiment by tuning $\vec{k}_{b/c}$ and $\vec{k}_a$ appropriately) the matrix elements of some terms may become particularly dominant.

As described above there are three significant double ionization pathways, namely 'shake off' (SO), 'Two-Step 1' (TS1) and 'Two-Step 2' (TS2) respectively.

Here we consider that the incoming and the scattered electrons are fast so that they can be described by plane waves. We take He as an example. The fivefold differential cross section (FDCS) in the Born approximation [44] is written as

$$\sigma^{(5)} = \frac{d^5\sigma}{dE_a\, dE_b\, d\Omega_a\, d\Omega_b\, d\Omega_c} = \frac{k_a k_b k_c}{k_0} |M_{SO} + M_{TS1} + M_{TS2}|^2 \tag{1.10}$$

The amplitudes M_{SO}, M_{TS1} and M_{TS2} correspond, respectively, to the SO, TS1 and TS2 process. The following formulae of different mechanism amplitude have been given by Dal Cappello et al [72].

A. Shake Off (SO)

This one-step mechanism (because there is only one interaction between the incoming electron and the target) can be described by the first Born approximation [71] (see §1.2.1, Sec. A and Fig. 1.2). The SO process leads to

$$M_{SO} = -\frac{1}{2\pi}\left\langle \psi_f^{(-)}(\vec{k}_b, \vec{k}_c; \vec{r}_b, \vec{r}_c) e^{i\vec{k}_a\cdot\vec{r}_0} \middle| -\frac{2}{\vec{r}_0} + \frac{1}{|\vec{r}_{0b}|} + \frac{1}{|\vec{r}_{0c}|} \middle| \psi_i(\vec{r}_b, \vec{r}_c) e^{i\vec{k}_0\cdot\vec{r}_0} \right\rangle \tag{1.11}$$

where ψ_i and $\psi_f^{(-)}$ represent the initial-state and final state wavefunctions of the system.

B. Two-Step 1 (TS1) mechanism

This TS1 mechanism is described by the first Born approximation because only one single projectile-target interaction is involved (see §1.2.1, Sec. A and Fig. 1.3).

The TS1 process leads to

$$M_{TS1} = -\left(\frac{1}{\pi}\right)\sum_n \int \frac{d\overrightarrow{k_{a'}}}{(2\pi)^3\left[k_0^2 - k_{a'}^2 - k_a^2 - 2I_n\right]} \left\langle \psi_f^{(-)}(\vec{k}_b, \vec{k}_c; \vec{r}_b, \vec{r}_c) \right| \frac{1}{|\vec{r}_{bc}|} \left| \psi_n^{(+)}(\vec{k}_{a'}; \vec{r}_b, \vec{r}_c) \right\rangle$$

$$\left\langle \psi_n^{(-)}(\vec{k}_{a'}; \vec{r}_b, \vec{r}_c) e^{i\vec{k}_a \cdot \vec{r}_0} \right| -\frac{2}{\vec{r}_0} + \frac{1}{|\vec{r}_{0b}|} + \frac{1}{|\vec{r}_{0c}|} \left| \psi_i(\vec{r}_b, \vec{r}_c) e^{i\vec{k}_0 \cdot \vec{r}_0} \right\rangle \qquad (1.12)$$

where I_n represents the energy necessary to eject one target electron leaving the residual ion He^+ in its ground state and $\psi_n^{(+)}$ (or $\psi_n^{(-)}$) is an incoming (or outgoing) Coulomb wave function; $\vec{k}_{a'}$ stands for the momentum vector of ejected electron in a first SI step which plays a role as incident electron in a second SI step.

C. Two-Step 2 (TS2) mechanism

These two step interactions between the incident electron and the target can be incorporated in the second Born approximation because two successive projectile-target interactions occur in TS2. (see §1.2.1, Sec. A and Fig. 1.4).

The TS2 process leads to [72]

$$\begin{aligned} M_{TS2} = & -\left(\frac{1}{\pi}\right)\sum_n \int \frac{d\vec{k}_{a'}}{(2\pi)^3\left[k_0^2 - k_{a'}^2 - k_b^2 - 2I_n\right]} \left\langle \psi_f^{(-)}(\vec{k}_c, \vec{r}_c) e^{i\vec{k}_a \cdot \vec{r}_0} \right| \frac{1}{|\overrightarrow{r_{0c}}|} \left| e^{i\vec{k}_{a'} \cdot \vec{r}_0} \psi_n(\vec{r}_c) \right\rangle \\ & \times \varphi\left(|\vec{k}_b - \vec{k}_c|\right) \left\langle \psi_n^{(-)}(\vec{k}_b; \vec{r}_b, \vec{r}_c) e^{i\vec{k}_{a'} \cdot \vec{r}_0} \right| -\frac{2}{\vec{r}_0} + \frac{1}{|\vec{r}_{0b}|} + \frac{1}{|\vec{r}_{0c}|} \left| \psi_i(\vec{r}_b, \vec{r}_c) e^{i\vec{k}_0 \cdot \vec{r}_0} \right\rangle \\ & - \left(\frac{1}{\pi}\right)\sum_n \int \frac{d\vec{k}_{a'}}{(2\pi)^3\left[k_0^2 - k_{a'}^2 - k_c^2 - 2I_n\right]} \left\langle \psi_f^{(-)}(\vec{k}_b, \vec{r}_b) e^{i\vec{k}_a \cdot \vec{r}_0} \right| \frac{1}{|\vec{r}_{0b}|} \left| e^{i\vec{k}_{a'} \cdot \vec{r}_0} \psi_n(\vec{r}_b) \right\rangle \\ & \times \varphi\left(|\vec{k}_b - \vec{k}_c|\right) \left\langle \psi_n^{(-)}(\vec{k}_c; \vec{r}_b, \vec{r}_c) e^{i\vec{k}_{a'} \cdot \vec{r}_0} \right| -\frac{2}{\vec{r}_0} + \frac{1}{|\vec{r}_{0b}|} + \frac{1}{|\vec{r}_{0c}|} \left| \psi_i(\vec{r}_b, \vec{r}_c) e^{i\vec{k}_0 \cdot \vec{r}_0} \right\rangle \end{aligned} \qquad (1.13)$$

with $\varphi\left(|\vec{k}_b - \vec{k}_c|\right) = e^{\pi\xi_{bc}}\,\Gamma(1 - i\xi_{bc})$ and $\xi_{bc} = \frac{1}{|\vec{k}_b - \vec{k}_c|}$.

The intermediate scattered electron, described here by a plane wave $e^{i\vec{k}_{a'} \cdot \vec{r}_0}$, collides with the second bound electron after a first ionization without or with simultaneous excitation. Because of these two successive interactions in the TS2 mechanism, the symmetry with respect to the momentum transfer direction $\vec{K} = \vec{k}_0 - \vec{k}_a$ is broken.

As mentioned above the analysis done for the matrix elements of the various transition operators is rather qualitative. A more precise estimate of the transition amplitude entails one complicated multi-dimensional integrals. E.g., McGuire [39] has estimated the importance as the incident energy is varied of the process SO, TS1, and TS2 in the case of a helium target considering the (integrated) total double ionization cross sections. The cross sections for the TS1 and TS2, are expected to behave

essentially as the product of two single ionization cross sections. Thus, these cross sections decrease rapidly with an increasing incident energy (roughly as E_0^{-1}). Hence the cross section shows a slower decrease with energy (roughly as $E_0^{-1/2}$). According to McGuire's results [39], the SO contribution should be dominant at electron impact energies larger than ≈ 1 keV.

1.4 Motivation of experimental studies of double ionization

There are two different kind of experimental setups for electron impact DI study: 'conventional' (e, 3e) multi-detection spectrometers and the (e, 2e+ion) spectrometer. Both methods use angle-multi-detection technique. Main difference is that the solid angle collected in the so-called cold target recoil ion momentum spectroscopy (COLTRIMS) (where the recoil ion is detected in coincidence with two emitted electrons) is close to 4π (with some dead zones), whereas it is a factor of 10 or so lower in the conventional (e, 3e) case and being limited to a coplanar geometry [73, 74], or to a series of discrete out-of-plane measurements [75]. The statistics are essentially limited by the accidental coincidence rate in conventional (e, 3e) experiments. On the other hand in COLTRIMS, nine momentum components are determined, one more than necessary to completely fix the kinematics, and the redundant information obtained is used to discriminate against and hence reduce the accidental coincidence. The detailed comparison between two different philosophical designed setup can be found in [7]. Therefore they have differences in many aspect, they are not mutually exclusive but mutually complementary. COLTRIMS is analog to a high-tech camera embarked on a satellite at high altitude, for instance geostationary, taking a picture of the earth. One sees all of the Earth, that is one has in principle all the information but with a modest resolution. Whereas (e, 3e) corresponds to the same high-tech camera (the same imaging techniques and the same position sensitive detectors are used), embarked for instance in a plane at lower altitude: a picture of a smaller region is taken looking at much smaller details.

In our lab, the 'conventional' (e, 3e) multi-detection spectrometer is applied for dynamical study of electron impact double ionization measurement. Historically, Orsay's group has performed (e, 3e) and (e, 3-1e) at various kinematical conditions for different targets. All parameters are listed in the following two tables (see Tabs. 1.1 and 1.2).

Table 1.1 All parameters of (e, 3e) measurements at Orsay's Group

Target	E_0 (eV)	E_a (eV)	E_b (eV)	E_c (eV)	Publication
Ar	5553	5480	20	10	Phys. Rev. Lett., 63(1989)1582 Lahmam-Bennani, A. et al
Kr	5500	5371.6	$E_b + E_c$ =90 eV		J. Phys. B, 25(1992)2873-2884, Lahmam-Bennani, A. et al
Ar	5563	5500	10	10	J. Phys. B, 30(1997)3677-3696, El Marji, B., et al
Ne	5583	5500	10	10	J. Phys. B, 31(1998)131-143, Schröter, C. et al
He	5599	5500	10	10	Phys. Rev. Lett., 81(1998)4600, Taouil, I. et al
He	1099	1000	10	10	J. Phys. B, 34(2001)3073-3087, Lahmam-Bennani, A. et al
Ar	561.4	500	9	9	J. Phys. B, 35(2002)1103-1113, Jia C. C. et al
He	601	500	11	11	Phys. Rev. A, 67(2003)010707(R), Lahmam-Bennani, A., et al
Ar	561.4	500	9	9	J. Phys. B, 36(2003)L17-L24, Jia C. C. et al
Ar	953	500	205	205	J. Phys. B, 40(2007)2871-2884, Naja, A. et al.

Table 1.2 All parameters of (e, 3-1e) measurements at Orsay's Group

Target	E_0 (eV)	E_a (eV)	E_b (eV)	E_c (eV) (undetected)	Publication
Ar	5623	5500	75	5	Phys. Rev. Lett., 63(1989)1582 Lahmam-Bennani, A. et al
Ar	5623	5500	$E_b + E_c$ =80 eV		J. Phys. B, 24(1991)675-682, Duguet, A., et al
Ar	5730	5500	$E_b + E_c$ =230 eV		J. Phys. B, 24(1991)3645-3653, Lahmam-Bennani, A., et al
Ar	5623	5500	$E_b + E_c$ =80 eV		
Ar	5500	undetected	96	17.5	J. Phys. B, 29(1996) L157-L161, El Marji, B. et al
He	5560	undetected	$E_b + E_c$ =35 eV		J. Phys. B, 28(1995) L733-L737, El Marji, B. et al
He	640	500	51	10	J. Phys. B., 35(2002), L59-L63, Lahmam-Bennani, A., et al
H_2	612	500	51	10	
He	601 621 658 613	500	(E_b:E_c)=(17:5), (37:5), (74:5) and (17:17)		J. Phys. B, 43(2010)105201, Lahmam-Bennani, A., et al.
He	663, 735	500	(E_b:E_c)=(72:12) and (144:12)		J. Phys. B, 44(2011)055201, Staicu Casagrande, E. M., et al

In this thesis, I continue the work of (e, 3e) and (e, 3-1e) experimental studies by extending the target from atomic targets (most of them are noble gases) to molecular targets (such as N_2 and CH_4) under intermediate incident energy of ~600 eV to investigate how the different mechanisms work in DI by comparing with different theoretical models. All experimental parameters studied in this thesis are listed in Tabs. 1.3 and 1.4. The experimental results are also compared with the simple TS2 kinematical model developed by Lahmam-Bennani, et al [76]. The experimental results are given and discussed in chapter 3, 4 and 5.

Table 1.3 All parameters of (e, 3e) measurements in this work

Target	E_0 (eV)	E_a (eV)	E_b (eV)	E_c (eV)	Publication
N_2	567	500	12	12	J. Phys. B, 45(2012)135201, Li, C., et al
N_2	617	500	37	37	

Table 1.4 All parameters of (e, 3-1e) measurements in this work

Target	E_0 (eV)	E_a (eV)	E_b (eV)	E_c (eV) (undetected)	Publication
He	663	500	72	12	J. Phys. B, 44(2011)055201, Staicu Casagrande, E. M., et al
He	735	500	144	12	
Ne	586.6	500	12	12	J. Phys. B, 44(2011)115201, Li, C., et al
Ne	646.6	500	72	12	
Ne	718.6	500	144	12	
Ar	567.2	500	12	12	
Ar	627.2	500	72	12	
Ar	699.2	500	144	12	
N_2	567	500	12	12	
N_2	627	500	72	12	
N_2	699	500	144	12	
N_2	617	500	37	37	J. Phys. B, 45(2012)135201, Li, C., et al
Ne	611.6	500	37	12	unpublished
Ne	636.6	500	37	37	
CH_4	612	500	37	12	
CH_4	587	500	37	37	

1.5 Bibliography

1. Zheng, Y., et al., *Role of Secondary Low-Energy Electrons in the Concomitant Chemoradiation Therapy of Cancer*. Physical Review Letters, 2008. **100**(19): p. 198101.
2. Bray, I., et al., *Electron- and photon-impact atomic ionisation*. Physics Reports, 2012. **520**(3): p. 135-174.
3. Lahmam-Bennani, A., *Thirty years of experimental electron-electron (e,2e) coincidence studies: achievements and perspectives*. Journal of Electron Spectroscopy and Related Phenomena, 2002. **123**(2-3): p. 365-376.
4. Schulz, M., et al., *Three-dimensional imaging of atomic four-body processes*. Nature, 2003. **422**(6927): p. 48-50.
5. Rescigno, T.N., et al., *Collisional Breakup in a Quantum System of Three Charged Particles*. Science, 1999. **286**(5449): p. 2474-2479.
6. Berakdar, J. and Briggs, J.S. *Three-body Coulomb continuum problem*. Physcial Review Letters, 1994. **72**(24): p. 3799-3802.
7. Berakdar, J., Lahmam-Bennani, A. and Dal Cappello, C. *The electron-impact double ionization of atoms: an insight into the four-body Coulomb scattering dynamics*. Physics Reports, 2003. **374**(2): p. 91-164.
8. Taouil, I., et al., *Fully Determined (e,3e) Experiments for the Double Ionization of Helium*. Physical Review Letters, 1998. **81**(21): p. 4600-4603.
9. Lahman-Bennani, A., et al., *(e, 3e) absolute five-fold differential cross sections for double ionization of krypton*. Journal of Physics B: Atomic, Molecular and Optical Physics, 1992. **25**(12): p. 2873.
10. Lahmam-Bennani, A., et al., *Origin of dips and peaks in the absolute fully resolved cross sections for the electron-impact double ionization of He*. Physical Review A, 1999. **59**(5): p. 3548-3555.
11. Wehlitz, R., et al., *Triple Photoionization of Lithium*. Physical Review Letters, 1998. **81**(9): p. 1813-1816.
12. Maydanyuk, N.V., et al., *Projectile–Residual-Target-Ion Scattering after Single Ionization of Helium by Slow Proton Impact*. Physical Review Letters, 2005. **94**(24): p. 243201.
13. Fischer, D., et al., *Systematic analysis of double-ionization dynamics based on four-body Dalitz plots*. Physical Review A, 2009. **80**(6): p. 062703.
14. Ciappina, M.F., Kirchner, T. and Schulz, M. *Double ionization of helium by highly-charged-ion impact analyzed within the frozen-correlation approximation*. Physical Review A, 2011. **84**(3): p. 034701.
15. McCarthy, I.E. and Weigold, E. *Electron momentum spectroscopy of atoms and molecules*. Reports on Progress in Physics, 1991. **54**(6): p. 789.
16. Lahmam-Bennani, A., *Recent developments and new trends in (e,2e) and (e,3e) studies*. Journal of Physics B: Atomic, Molecular and Optical Physics, 1991. **24**(10): p. 2401.
17. Lahmam-Bennani, A., et al., *Signature of the target two-electron momentum space wavefunction in the (e, 3e) angular distributions from the double ionization of helium and argon*. Journal of Physics B: Atomic, Molecular and Optical Physics, 2002. **35**(10): p. L215.
18. Weigold, E. and McCarthy, I.E. *(e, 2e) Collisions*, in *Advances in Atomic and Molecular Physics*, D.R. Bates and B. Benjamin, Editors. 1979, Academic Press. p. 127-179.
19. Camilloni, R., et al., *Mechanism of the (e, 2e) reaction with atoms*. Physical Review A, 1978. **17**(5): p. 1634-1641.
20. Fournier-Lagarde, P., Mazeau, J. and Huetz, A. *Electron impact ionisation of helium: a measurement of (e, 2e) differential cross sections close to threshold*. Journal of Physics B: Atomic and Molecular Physics, 1984. **17**(17): p. L591.
21. Ehrhardt, H., et al., *Differential cross sections of direct single electron impact ionization*. Zeitschrift für Physik D: Atoms, Molecules and Clusters, 1986. **1**(1): p. 3-32.
22. Lahmam-Bennani, A., et al., *Coincidence electron impact ionisation of helium: absolute experimental cross sections and comparison with first-order theories*. Journal of Physics B: Atomic and Molecular Physics, 1984. **17**(15): p. 3159.

23. Lahmam-Bennani, A., Dupré, C. and Duguet, A. *Electron-impact double ionization of argon studied by double and triple coincidence techniques: The first (e,3e) experiment.* Physical Review Letters, 1989. **63**(15): p. 1582-1585.
24. Dupré, C., A. Lahmam-Bennani, and A. Duguet, *About some experimental aspects of double and triple coincidence techniques to study electron impact double ionizing processes.* Measurement Science and Technology, 1991. **2**(4): p. 327.
25. Duguet, A. and A. Lahmam-Bennani, *Double ionization mechanisms from (e, 3–1)e and (e, 3e) experiments.* Zeitschrift für Physik D Atoms: Molecules and Clusters, 1992. **23**(4): p. 383-388.
26. El Mkhanter, R., et al., *On the mechanisms for double ionization: a study of (e, 3 - 1e) experiments on argon.* Journal of Physics B: Atomic, Molecular and Optical Physics, 1996. **29**(5): p. 1101.
27. Berakdar, J., *Double-ionization mechanisms and asymmetry parameters for (e,3-1e) reactions.* Physical Review A, 1996. **53**(4): p. 2281-2288.
28. Lahmam-Bennani, A., et al., *Identification of mechanisms of electron impact double ionizing collisions by e,(3-1)e experiments.* Journal of Physics B: Atomic, Molecular and Optical Physics, 1991. **24**(16): p. 3645.
29. El Marji, B., et al., *Evidence for a shake-off mechanism being responsible for electron-impact double-ionization of argon at 5.5 keV.* Journal of Physics B: Atomic, Molecular and Optical Physics, 1996. **29**(5): p. L157.
30. El Marji, B., et al., *Angular correlation of ejected electrons in e,(3-1)e electron impact double ionization of helium.* Journal of Physics B: Atomic, Molecular and Optical Physics, 1995. **28**(23): p. L733.
31. Götz, J.R., Walter, M. and Briggs, J.S. *Appearance of non-first-Born effects in (e, 3e) on helium.* Journal of Physics B: Atomic, Molecular and Optical Physics, 2003. **36**(4): p. L77.
32. Hda, H., Cappello, C. and Langlois, J. *Angular distributions of electrons in the (e, 3e) reaction.* Zeitschrift für Physik D Atoms, Molecules and Clusters, 1994. **29**(1): p. 25-29.
33. Joulakian, B., Dal Cappello, C. and Brauner, M. *Double ionization of helium by fast electrons: use of correlated two electron wavefunctions.* Journal of Physics B: Atomic, Molecular and Optical Physics, 1992. **25**(12): p. 2863.
34. Ancarani, L.U., et al., *Interplay of initial and final states for (e,3e) and (γ,2e) processes on helium.* Physical Review A, 2008. **77**(6): p. 062712.
35. Ciappina, M.F., et al., *Distorted Wave Theories Applied to Double Ionization by Ion Impact: Simulation of Higher-Order Processes.* Journal of Atomic, Molecular, and Optical Physics, 2010. **2010**.
36. Madison, D.H. and Al-Hagan, O. *The Distorted-Wave Born Approach for Calculating Electron-Impact Ionization of Molecules.* Journal of Atomic, Molecular, and Optical Physics, 2010. **2010**.
37. Kheifets, A.S., et al., *DWBA-G calculations of electron impact ionization of noble gas atoms.* Journal of Physics B: Atomic, Molecular and Optical Physics, 2008. **41**(14): p. 145201.
38. Ancarani, L.U. and Dal Cappello, C. *The use of Pluvinage-type wavefunctions in describing the double ionization of helium.* Journal of Electron Spectroscopy and Related Phenomena, 2007. **161**(1–3): p. 22-26.
39. McGuire, J.H., *Double Ionization of Helium by Protons and Electrons at High Velocities.* Physical Review Letters, 1982. **49**(16): p. 1153-1157.
40. Tweed, R.J., *Double ionization by electron impact: I. General theory.* Journal of Physics B: Atomic and Molecular Physics, 1973. **6**(2): p. 259.
41. Tweed, R.J., *Double ionization by electron impact: II. Calculations of cross sections for H^-, He and Li^+.* Journal of Physics B: Atomic and Molecular Physics, 1973. **6**(2): p. 270.
42. Tweed, R.J., *The second Born approximation for ionization.* Journal of Physics B: Atomic and Molecular Physics, 1973. **6**(3): p. 398.
43. Woollings, M.J. and McDowell, M.R.C. *Collisions of fast electrons with helium. I. Various forms of the second Born approximation.* Journal of Physics B: Atomic and Molecular Physics, 1972. **5**(7): p. 1320.

44. Tweed, R.J., *Double processes in e^--He collisions.* Zeitschrift für Physik D Atoms, Molecules and Clusters, 1992. **23**(4): p. 309-320.
45. Carlson, T.A. and Krause, M.O. *Electron Shake-Off Resulting from K-Shell Ionization in Neon Measured as a Function of Photoelectron Velocity*. Physical Review, 1965. **140**(4A): p. A1057-A1064.
46. McGuire, J.H., *High-velocity limits for the ratio of double to single ionisation by charged particles and by photons.* Journal of Physics B: Atomic and Molecular Physics, 1984. **17**(22): p. L779.
47. Deutsch, H., et al., *Application of the Modified Additivity Rule to the Calculation of Electron-Impact Ionization Cross Sections of Complex Molecules.* The Journal of Physical Chemistry A, 1998. **102**(45): p. 8819-8826.
48. Weck, P., et al., *Two-effective center approximation for the single ionization of molecular hydrogen by fast electron impact.* Physical Review A, 2001. **63**(4): p. 042709.
49. Weck, P.F., et al., *Two-center continuum approximation with correct boundary conditions for single-electron emission in e^-+H_2 collisions.* Physical Review A, 2002. **66**(1): p. 012711.
50. Ochbadrakh, C., et al., *Modified two-centre continuum wavefunction: application to the dissociative ionization of H + 2 by fast electrons.* Journal of Physics B: Atomic, Molecular and Optical Physics, 2004. **37**(12): p. 2607.
51. Vladislav, V.S., et al., *Ionization excitation of diatomic systems having two active electrons by fast electron impact: a probe to electron correlation.* Journal of Physics B: Atomic, Molecular and Optical Physics, 2005. **38**(15): p. 2765.
52. Gao, J., D.H. Madison, and Peacher, J.L. *Distorted wave born and three-body distorted wave born approximation calculations for the fully differential cross section for electron impact ionization of nitrogen molecules.* J. Chem. Phys., 2005. **123**: p. 204314.
53. Gao, J., J.L. Peacher, and Madison, D.H. *An elementary method for calculating orientation-averaged fully differential electron-impact ionization cross sections for molecules.* J. Chem. Phys, 2005. **123**: p. 204302.
54. Stia, C.R., et al., *Molecular three-continuum approximation for ionization of H_2 by electron impact.* Physical Review A, 2002. **66**(5): p. 052709.
55. Stia, C.R., et al., *Interference effects in single ionization of molecular hydrogen by electron impact.* Journal of Physics B: Atomic, Molecular and Optical Physics, 2003. **36**(17): p. L257.
56. Brauner, M. and et al., *Triply-differential cross sections for ionisation of hydrogen atoms by electrons and positrons.* Journal of Physics B: Atomic, Molecular and Optical Physics, 1989. **22**(14): p. 2265.
57. Burke, P.G., A. Hibbert, and Robb, W.D. *Electron scattering by complex atoms.* Journal of Physics B: Atomic and Molecular Physics, 1971. **4**(2): p. 153.
58. Burke, P.G. and Robb, W.D. *The R-Matrix Theory of Atomic Processes*, in *Advances in Atomic and Molecular Physics*, D.R. Bates and B. Benjamin, Editors. 1976, Academic Press. p. 143-214.
59. Burke, P.G., Noble, C.J. and Burke, V.M. *R-Matrix Theory of Atomic, Molecular and Optical Processes*, in *Advances In Atomic, Molecular, and Optical Physics*, C.C.L. P.R. Berman and E. Arimondo, Editors. 2006, Academic Press. p. 237-318.
60. Curran, E.P. and Walters, H.R.J. *Triple differential cross sections for electron impact ionisation of atomic hydrogen-a coupled pseudostate calculation.* Journal of Physics B: Atomic and Molecular Physics, 1987. **20**(2): p. 337.
61. Bray, I. and Stelbovics, A.T. *Convergent close-coupling calculations of electron-hydrogen scattering.* Physical Review A, 1992. **46**(11): p. 6995-7011.
62. Bray, I., D.V. Fursa, and Stelbovics, A.T. *Close-coupling approach to ionization processes.* Correlations, Polarization, and Ionization in Atomic Systems, 2002. **604**: p. 90-95.
63. Abdurakhmanov, I.B., et al., *Coupled-channel integral-equation approach to antiproton–hydrogen collisions.* Journal of Physics B: Atomic, Molecular and Optical Physics, 2011. **44**(7): p. 075204.
64. Gasaneo, G. and Ancarani, L.U. *Treatment of the two-body Coulomb problem as a short-range potential.* Physical Review A, 2009. **80**(6): p. 062717.

65. Rescigno, T.N., et al., *Making complex scaling work for long-range potentials*. Physical Review A, 1997. **55**(6): p. 4253-4262.
66. McCurdy, C.W., Rescigno, T.N. and Byrum, D. *Approach to electron-impact ionization that avoids the three-body Coulomb asymptotic form*. Physical Review A, 1997. **56**(3): p. 1958-1969.
67. Pindzola, M.S. and Schultz, D.R. *Time-dependent close-coupling method for electron-impact ionization of hydrogen*. Physical Review A, 1996. **53**(3): p. 1525-1536.
68. Pindzola, M.S., et al., *The time-dependent close-coupling method for atomic and molecular collision processes*. Journal of Physics B: Atomic, Molecular and Optical Physics, 2007. **40**(7): p. R39.
69. Pindzola, M.S. and Robicheaux, F. *Time-dependent close-coupling calculations of correlated photoionization processes in helium*. Physical Review A, 1998. **57**(1): p. 318-324.
70. Colgan, J. and M.S. Pindzola, *Application of the time-dependent close-coupling approach to few-body atomic and molecular ionizing collisions*. The European Physical Journal D, 2012. **66**(11): p. 1-24.
71. Joulakian, B. and Dal Cappello, C. *Theoretical study of the optimal conditions for the measurement of the differential cross section of the double ionization of helium by fast electrons*. Physical Review A, 1993. **47**(5): p. 3788-3795.
72. Dal Cappello, C., El Mkhanter, R. and P.A. Hervieux, *Mechanisms of double ionization of atoms by electron impact*. Physical Review A, 1998. **57**(2): p. R693-R696.
73. Duguet, A., et al., *A multidetection, multicoincidence spectrometer for (e,2e) and (e,3e) electron impact ionization measurements*. Review of Scientific Instruments, 1998. **69**(10): p. 3524-3536.
74. Catoire, F., et al., *New developments for an electron impact (e,2e)/(e,3e) spectrometer with multiangle collection and multicoincidence detection*. Review of Scientific Instruments, 2007. **78**(1): p. 013108-8.
75. Ford, M.J., et al., *Multiple detector triple coincidence spectrometer for (e,3e) electron impact double-ionization measurements*. Review of Scientific Instruments, 1995. **66**(5): p. 3137-3143.
76. Lahmam-Bennani, A., et al., *Predominance of the second-order, two-step mechanism in the electron impact double ionization of helium at intermediate impact energy*. Journal of Physics B: Atomic, Molecular and Optical Physics, 2010. **43**(10): p. 105201.

Chapter 2 *Experimental Apparatus*

2.1 General presentation of the setup

In this chapter, the setup used for the so-called (e, 2e) or (e, 3e) experiments in Orsay's group [1,3] will be described in details.

The setup mainly consists of four parts: the chamber and related components, the electron beam production system, the analyzers and the data acquisition and analysis system. A schematic diagram of the vacuum chamber is shown in figure 1. All elements are housed in this chamber, which is a cylinder of 120 cm diameter and 85 cm height. The earth magnetic field is compensated for by using three pairs of squared (2.5 m per side) mutually perpendicular Helmholtz coils, together with **μ**-metal shields surrounding the vacuum chamber. This ensures the residual magnetic field along the electron trajectories is less than 10 mG. The vacuum satisfying the experimental requirement is accomplished by the diffusion pumps system (see Fig 2.1). There are two oil diffusion pumps named 'main diffusion pump' and 'auxiliary diffusion pump', respectively. They are operated in conjunction with two mechanical pumps named 'main mechanical pump' and 'auxiliary mechanical pump'. The third mechanical pump named 'small mechanical pump' in the figure is needed for the vacuum procedure. Inside the chamber, there are three toroidal analyzers named analyzer A, B and C for analyzing and detecting by double (or triple) coincidence technique the two (or three) electrons resulting from the SI (or DI) process, depending on which kind of experiment we are interested in. The target gas is introduced into the center of the chamber through a mono-capillary of 0.2 mm internal diameter and 8 mm in length, while the electron beam is produced by a homemade electrostatic electron gun.

The collision center is defined by the intersect volume between the electron beam and gas jet, whereas the collision plane is defined by the incident (before collision, $\vec{k}_0$) and scattered (after collision, $\vec{k}_a$) beam directions (see Fig. 2.2). In this coplanar case, the scattering plane which contains the vectors $\vec{k}_0$ and $\vec{k}_a$ is characterized by the azimuthal angle $\varphi_a = 0$. The other azimuthal angles φ_b and φ_c can have values either 0 or π. The polar θ_b and θ_c will vary between 0° and 360°. A Faraday cup called 'Beam Stop' (BS) is installed along the incident direction at a distance of ~130 mm from the collision center with the function of collecting those electrons which did not have any interaction with the target. All ejected electrons emitted into the collision plane are energy analyzed and collected over almost full planar angular range (θ_c: 20°-160° and θ_b: 200°-340°) and detected in coincidence with the scattered one.

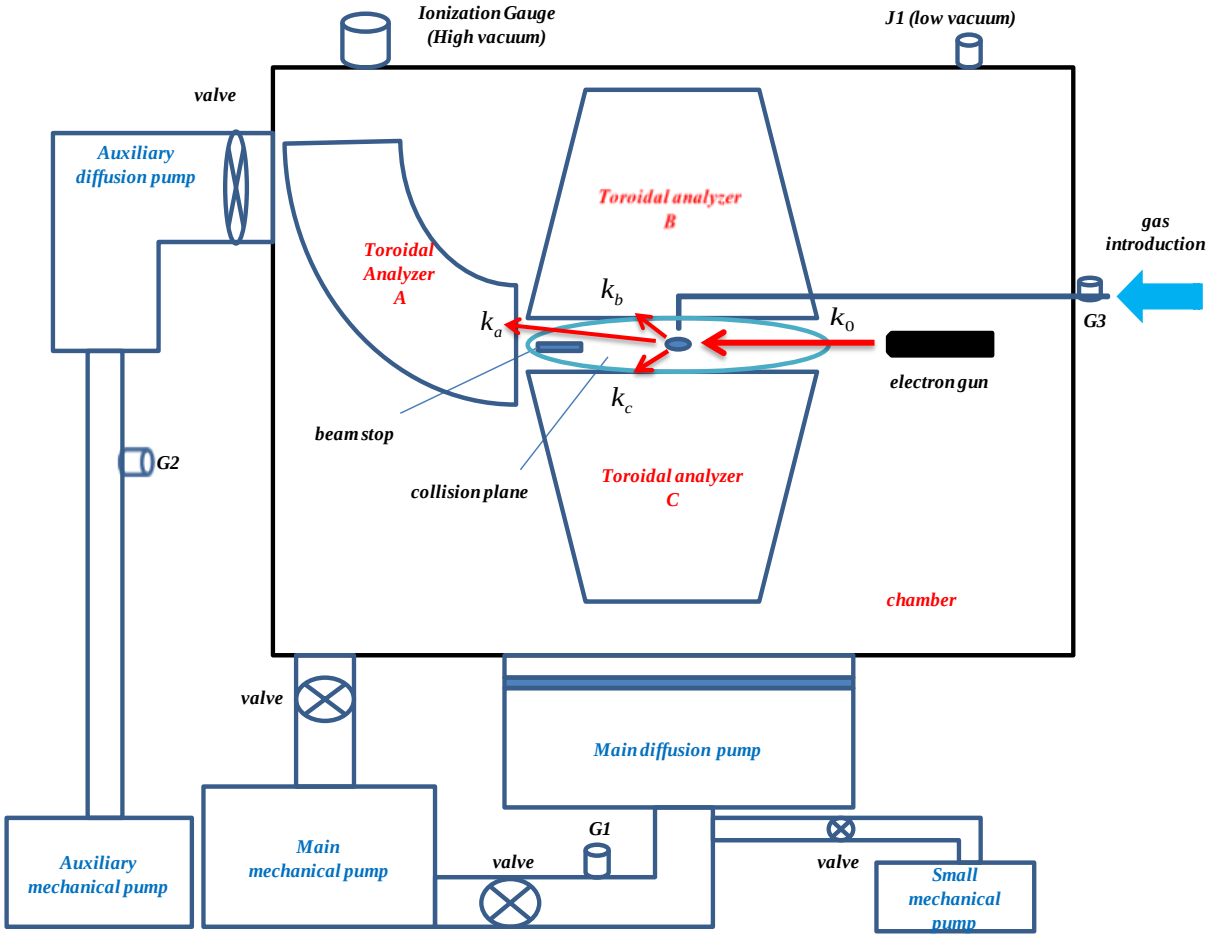

Figure 2.1 *A schematic drawing of the (e, 2e)/(e, 3e) multi-coincidence spectrometer*

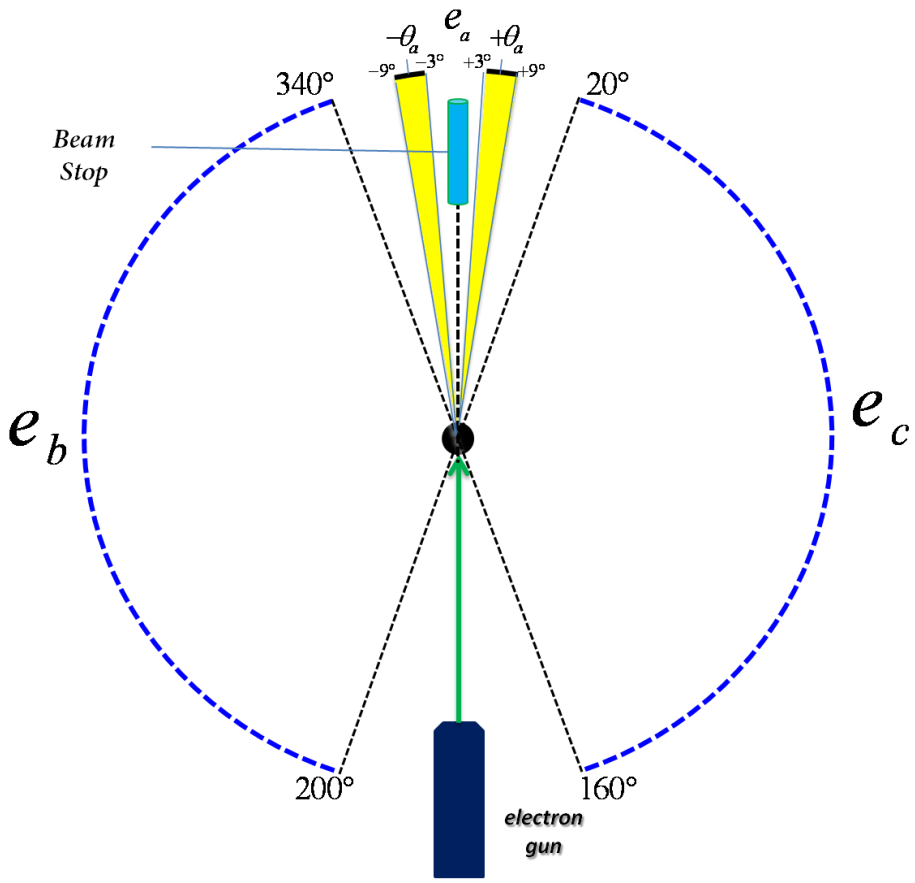

Figure 2.2 *Schematic diagram showing the angular ranges accessible for the three outgoing electrons (in the collision plane)*

2.2 Vacuum system

It is well known that high-vacuum diffusion pumps are always operated in conjunction with fore-vacuum pumps. A PAD 6250 type oil diffusion pump is installed for our setup as main diffusion pump (see Fig. 2.1). It has a pumping speed of 2350 $l{\cdot}s^{-1}$(new pump: DIP 3000 $l{\cdot}s^{-1}$) and an ultimate limit pressure of less than $4x10^{-7}$ Torr. A mechanical pump with ability of pumping speed of about 65 $m^3{\cdot}h^{-1}$ and ultimate pressure less than 1×10^{-4} mbar is combined with the main diffusion pump. Besides, a water cooling system and a freon cold trap are utilized routinely for the main oil diffusion pump to prevent fluid from flowing back into the vacuum vessel. The auxiliary mechanical and diffusion pumps are operated in a similar way, except there is no freon cold trap. The small mechanical pump serves for evacuating the main diffusion pump when the main mechanical pump is used for pumping the chamber (by switching on or off the valves to achieve, see Fig. 2.1). Typically, with these combined pumps, a high vacuum of $\sim1x10^{-6}$ Torr is achieved inside the chamber without target gas injection, and $\sim2\times10^{-5}$ Torr with gas injected through the nozzle. Such a pressure ensures a good background-to-signal scattering ratio for the planned (e, 2e) or (e, 3e) experiments.

There are five vacuum gauges in total allocated at different positions for vacuum control and measurement. The gauge named J1 is used for low vacuum measurement (> 10^{-3} Torr) whereas the ionization gauge located on the top of the chamber is for high vacuum measurement (< 10^{-3} Torr). The two gauges located between mechanical and diffusion pumps named G1 and G2 are used for monitoring the vacuum before diffusion pump to make sure they are working under permitted pressure (typically < 10^{-3} Torr).

2.3 Electron beam system

The aim here is to produce a monochromatic and well focused beam of electrons at a predetermined energy, where the direction and energy spread of the electrons is reduced until it is almost monochromatic. In general, the beam production consists of an electron gun with an extraction electrode and a focusing electrostatic lens system, associated with deflector plates and a collimation aperture. A Beam Stop (BS) and a pin-hole assembly serve to monitor the beam intensity and shape. Because of the double or triple coincidence technique itself, one significant characteristic of the so-called (e, 2e) or (e, 3e) experiment is the long data acquisition time to approach satisfactory statistics. Therefore, a long time stable, well focused electron beam with a constant current intensity becomes crucial. The three parts of the electron beam production will be introduced individually.

2.3.1 Electron gun and electrostatic lens system

The scheme of the electron gun is presented in Fig. 2.3. With this electron gun, a well focused electron beam with a wide energy range of ~400 eV to 2000 eV can be produced.

A tungsten filament emits electrons by thermo electronic effect. It is identical to those used in electronic microscopy, folded in the shape of a hairpin on top of which is deposited a very fine tip point of diameter 0.3 mm. This point ensures a better local electron emission and thus allows obtaining a point source. A negative high voltage is applied to the filament in order to accelerate the emitted electrons.

The Wehnelt electrode is equipped with a diaphragm of 2 mm in diameter and is biased with a voltage slightly more negative than that of the filament. The adjustment of this voltage changes the flow rate and concentration of electrons emitted by the filament. Thus, the role of this electrode is to optimize the trajectory of the electrons emitted by the filament and therefore to minimize the angular dispersion of the beam. The conical shape and size of the diaphragm of the Wehnelt electrode are chosen to minimize the angular dispersion of the electron beam. Optimal operation is achieved when the tip of the filament is positioned close to the diaphragm, within ± few tenths of mm.

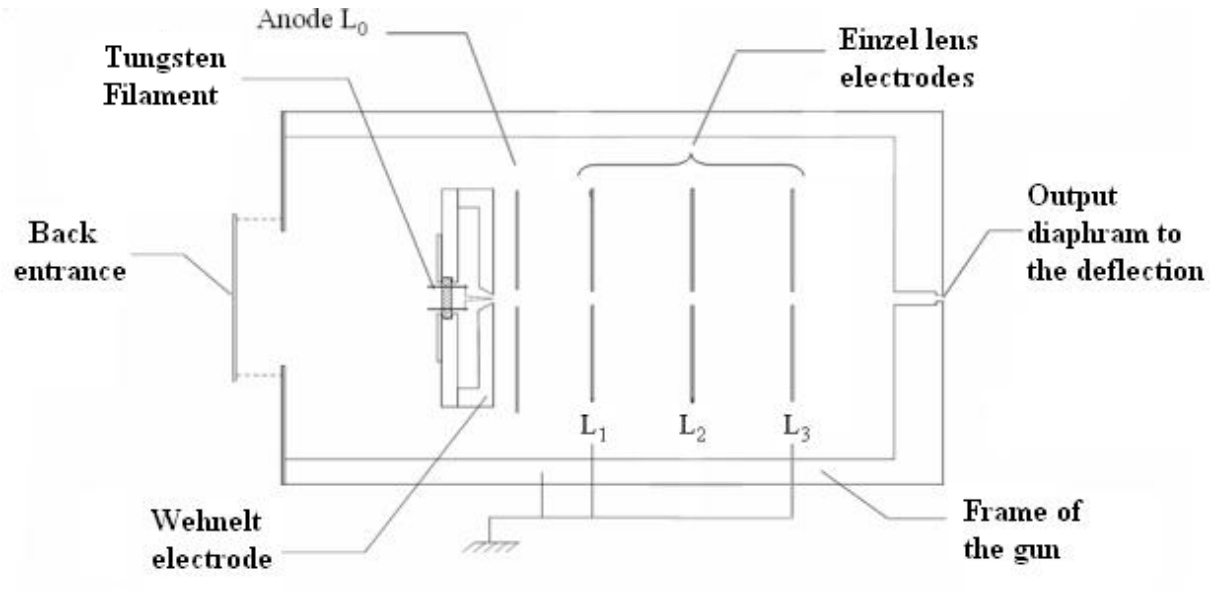

Figure 2.3 *Schematic diagram of the electron gun*

The electrode denoted L_0 plays the role of an anode: it is connected to ground and is used to accelerate the electrons.

The electrostatic Einzel lens [10][12][13] is used for adjusting the focusing of the electron beam. It consists of three electrodes with a central opening of 3 mm in diameter. Two of these electrodes (L_1 and L_3) are at zero potential and they are arranged symmetrically on either side of the central electrode (L_2), on which an adjustable negative voltage is applied.

Two pairs of deflector plates are positioned at the exit of the electron gun. They consist of four planar electrodes arranged as orthogonal pairs. Each set is used to move the beam horizontally or vertically to maximize its focus on the axis of the gas jet.

2.3.2 Beam Stop and pin-hole

As mentioned at the beginning of Section 2.3., a Faraday cup called 'Beam Stop' (BS) is positioned immediately at the exit of the dual toroidal analyzers along the incident direction at a distance of ~130 mm from the collision center. The BS plays two roles: 1) to collect the projectile electrons which have not undergone collision and trap them, hence minimizing their extraneous scattering in the chamber; 2) to monitor the intensity of the incident electron current.

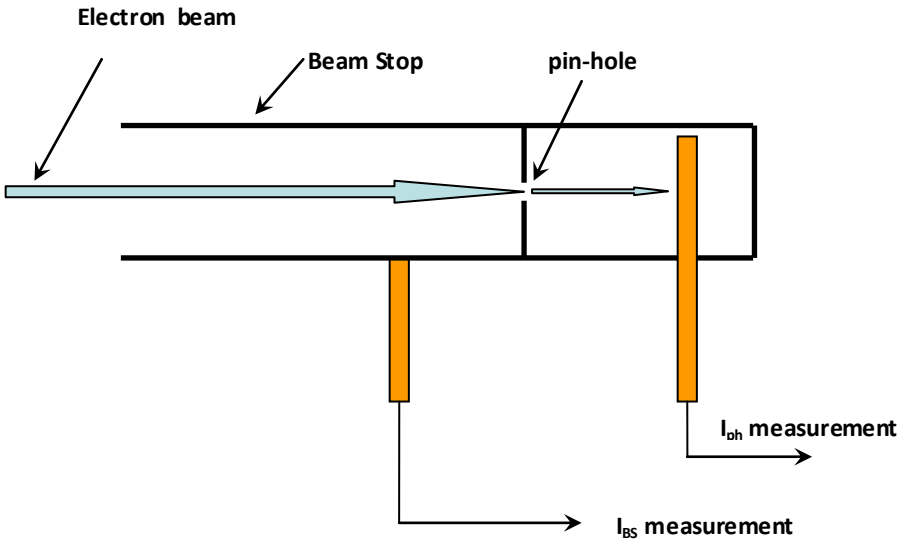

Figure 2.4 *Schematic diagram of the beam stop and pin-hole*

Inside the BS, there is an opening hole of 0.1 mm in diameter. This 'pin hole' is followed by a metal conductive rod which is used for measuring the current passing though the hole. This so-called 'pin hole current' (I_{ph}), is typically about 0.5 to 1% of the 'BS main current' (I_{BS}) (see Fig. 2.4).

The electron gun deflectors (see Fig. 2.5, §2.5) can also be used to measure the shape and size of the beam at BS and pin-hole assembly. The spatial distribution of the intensity of the electron beam is of Gaussian type whose full width at half maximum (FWHM) defines the 'diameter' of the beam, typically in the order of ~1mm. We can image that I_{ph} is the intensity in given coordinates, each I_{ph} corresponds to a unique coordinate (Y, Z). If we move the beam in horizontal and vertical direction, then it gives an intensity distribution of I_{ph} in Y- Z plan. A good beam is then a beam which is thin (~1 mm in diameter) and symmetric both in Y and Z directions [12].

Under normal operating conditions, the full width at half maximum (FWHM) of the beam is estimated to be about 1 to 1.5 mm in both Y and Z directions, at the incident energies considered in this work, E_0 ~500-700 *eV*.

2.4 Gas source and collision volume

The gas jet (see Fig. 2.1) is of the effusive type. It is formed by expansion though a monocapillary (so-called 'nozzle') of 0.2 mm in internal diameter and 8 mm in length. The nozzle is carefully and precisely adjusted along the Z axis of the system, which is perpendicular to the collision plan. Also, the nozzle is electrically isolated so as to allow measuring the current collected. When the beam is touching in the middle of the nozzle, the measured 'nozzle' current, I_{noz}, gets a maximum value. This indicates that the beam is exactly passing through the center of the gas jet in horizontal direction. Hence, next we need to adjust the beam carefully in vertical direction to form a small collision

volume with gas jet. These alignments, together with the small dimensions of the electron and gas beams, are needed to ensure a very good definition of the collision volume, which is a crucial point for the angular resolution of the toroidal analyzers. Usually, the beam is positioned ~1 mm below the nozzle, a good compromise between removing it away from the nozzle to minimize secondary electrons produced by metal scattering from the nozzle tip and bringing it closer to increase the target density in the collision volume. As mentioned before, the pressure inside the chamber is $\sim 2.0 \times 10^{-5}$~2.0×10^{-5} Torr with target gas. However, typically the gas density of collision volume is of the order ~$\sim 10^{12}$ - 10^{13} atoms/cm^3, about two orders of magnitude larger than the background pressure. This collision volume gas density guarantees the experimental condition that the average distance between two atoms or molecules (5×10^{-7}m) is much larger than the distance where van der Waals force works (10^{-9} – 10^{-11} m). Meanwhile the mean free velocity is much less than incident electrons with energy about ~500-700 eV ($\sim 1.0 \times 10^{-7} m/s$~$1.0\times 10^{7}$ m/s, assuming the electron has static mass). So we can treat each target as to be free and static with respect to the incident electron (without van der Waals force acting between each other).

2.5 Three toroidal analyzers

A general schematic view of the present spectrometer is shown in Fig. 2.5. The electron beam produced by the electron gun comes to collide with the gas jet issuing from a small capillary at the center of the apparatus, and the cross-section of the two beams defines the collision volume. After interaction with the target, the electrons emitted into the collision plane (defined by incident and scattered directions) are analyzed in our (e, 3e) spectrometer in energy and angle. The main components of the (e, 3e) spectrometer are the twin toroidal analyzers named ‘toroid B’ and ‘toroid C’ for energy selection and angular analysis of the ejected electrons plus the third one named ‘toroid A’ for energy selection and angular analysis of the scattered electrons. Each toroid is equipped at its end with a position sensitive detector (PSD) comprising 3 micro channel plates (MCP) and a resistive anode. All of the two (or three) outgoing electrons are detected by MCP in coincidence. From the arrival position on MCP, the in-plane angular and energy distributions of the scattered and ejected electrons can be reconstructed.

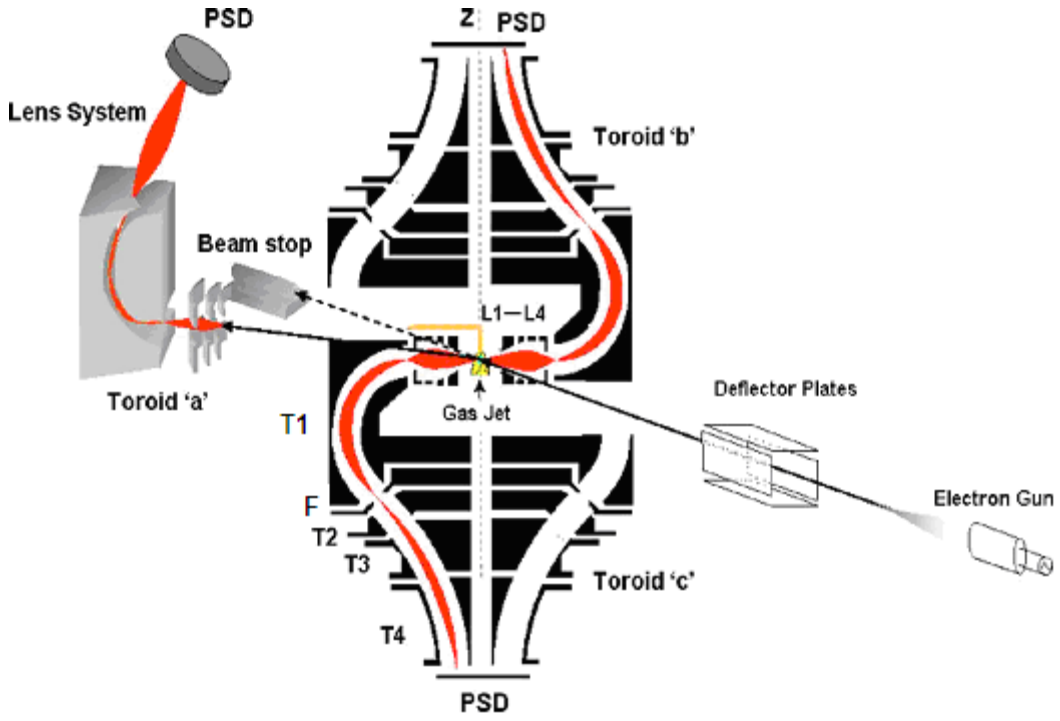

Figure 2.5 *Schematic view of the (e, 2e)-(e, 3e) electron-impact ionization spectrometer. The beam of unscattered electrons is collected in the beam stop. The dual toroidal analyzers 'b' and 'c' are of cylindrical symmetry about the Z axis. They are preceded by the entrance annular lenses, L_1–L_4, and followed by two four-element toroidal lenses, T_1–T_4. Electrons ejected in the x-y horizontal plane of collision are imaged as two half-rings on the position sensitive detectors (PSDs) at the top and the bottom, respectively. The fast, scattered electrons are analyzed in the toroid 'a' over the "useful" angular range ±10° and are detected on a third PSD.*

2.5.1 Twin toroidal anayzers

The main function of the twin toroidal analyzers is for energy selection and angular analysis of the ejected electrons. They are exactly identical to each other. Each toroid consists of a cylindrical radius a = 60 mm and a spherical radius b = 75 mm, with a deflection sector angle of 145°. Four-element semi-annular entrance lenses, named L_1 to L_4 in Fig. 2.5, are positioned between the collision center and the entrance to the toroids. Their function is to accelerate or decelerate the electrons before entering the toroids. The prior acceleration decreases the energy resolution of the analyzer whereas the deceleration increases it. The last element (L_4) is designed as a slit-like shape whose opening (ε_1) can be adjusted mechanically. The voltage (V_4) applied on L_4 (with respect to ground) combined with T_{1int} and T_{1ext} determine the pass energy of the analyzer, which is

$$E_p = E_{b/c} - eV_4 \tag{2.1}$$

where $E_{b/c}$ stands for the ejected electron energy of electron 'b' or 'c'.

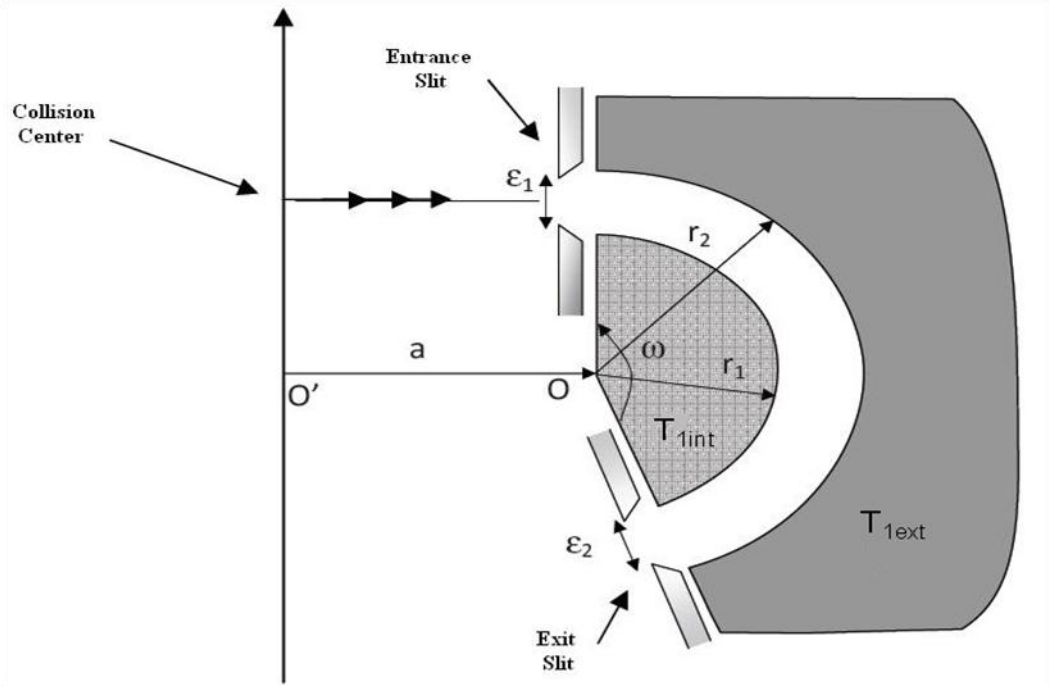

Figure 2.6 *Vertical cross-section of the toroidal analyzer, which defines the main parameters*

Because the field is constrained between two toroidal metal surfaces in the actual analyzer, the electric field is nearly normal to these surfaces. Fig. 2.6 represents a vertical cross-section of simplified scheme of the toroidal analyzer. From this scheme we can define the main parameters of the toroid [7], which are described as follows.

If Q(ω) is the function of charge quantity with specific angle ω [7], then according to Gaussian law the electric field with arbitrary radius r can be written as

$$E_r = \frac{Q(\omega)}{r(a+r\sin\omega)}. \tag{2.2}$$

If we apply a potential difference $\Delta V = V_2 - V_1$ between internal electrode (T_{1int}) of radius r_1 and external electrode (T_{1ext}) of radius r_2, the electric field between T_{1int} and T_{1ext} with radius of r ($r_1 < r < r_2$) can be expressed by:

$$E_r(r,\omega) = -\Delta V \cdot a\left\{ln\left[\frac{r_2(a+r_1\sin\omega)}{r_1(a+r_2\sin\omega)}\right]\cdot r(a+r\sin\omega)\right\}^{-1} \tag{2.3}$$

If we define $b = \frac{r_1+r_2}{2}$ for non relativistic electrons, the kinetic energy of the electron $U = eV_p$ when passing into the analyzer, we have the following relation:

$$\frac{1}{2}mv^2 = U = eV_p \tag{2.4}$$

For the case where electron path corresponds to the central circle of radius b, we have

$$eE(b) = \frac{mv^2}{b} = \frac{2U}{b} = \frac{2eV_p}{b} \tag{2.5}$$

Then we obtain the equation:

$$V(r) = \frac{2V_p}{\pi a}(\pi a + 2b) \ln\left[\frac{b(2r+\pi a)}{r(2b+\pi a)}\right] \tag{2.6}$$

which gives the polarization of the two tores, the interior one for r=r_1 (called T_{1int}) and the exterior one for r = r_2 (called T_{1ext}), which are applied to determine the passing energy.

We recall that the geometrical parameters of our double toroids are: a = 60 mm, b = 75 mm, r_1 = 60 mm and r_2 = 90 mm. In practice, the values of the calculated potential T_{1int} and T_{1ext} are adjusted slightly for fixed pass energy to ensure the electrons analyzed being properly focused on the surface of the detectors.

An exit slit so-called 'F' (see Fig. 2.5) is equipped just after the toroid, on which the same potential as L_4 (playing a role of entrance slit) is applied and also the opening (ε_2, see Fig. 2.6) can be adjusted mechanically combining with L_4 depending the energy resolution requirement of the experiment.

There are other three pairs of electrodes named T_2, T_3 and T_4. These three pairs of electrodes are used as electrostatic lenses to focus the energy selected electrons and ensure them impacting normally onto the surface of the detectors. There are two reasons that the trajectory of the detected electrons is required to impact normally onto the surface of the detector. First, as to be discussed in §2.6, for energetic electrons the detection efficiency of MCPs is largely improved. Otherwise the efficiency is enormously reduced and the distortions caused by differences in incidence angle onto the detector are brought in [8]. Second, the electrons with E_p are further focused by T_2-T_4 before impacting the detector. The final geometrical configuration of the three elements (T_2-T_4, see Fig.2.5) corresponds to a cylindrical an a spherical radius of 222 and 206 mm, respectively, and deflection sector angles of 10 °, 15 ° and 30 °, respectively [5].

2.5.2 'A-toroidal' analyzer

The 'toroid A' corresponds to a cylindrical radius a = 260 mm and a spherical radius b = 111mm, with a deflection angle of 135 °. The designed angular acceptance of θ_a is 30 °. However, due to the edge effects which produce fringing electric field distortions and due to the limited size of the MCP (40 mm in diameter), the useful angular range was limited to 20 °.

Before the scattered electron entering into the toroid A to be analyzed, they have to pass two symmetric slits (with respect to incident direction) in front of the entrance lens of the toroid to determine the scattering angle within collision plane. The width of these two slits can be adjusted to satisfy different angular resolution requirement for the experiment. In this work, because we aim to study the double ionization (DI) process at intermediate incident energy, for accumulation time consideration, the two slits were set for the scattering angle at -6 ° ±3 ° and +6 ° ±3 ° (see Fig. 2.7, right panel at bottom). That means the slits open from -3 ° to -9 ° and +3 ° to +9 °, where the 0 ° is defined by incident beam direction (see Fig. 2.2).

Similar to the twin toroidal analyzers, a four-element toroidal lens is positioned between the collision center and the entrance of the toroid for focusing the out-of-plane electron trajectories onto the entrance slit to the toroidal sector on the one hand and for accelerating or decelerating the electrons prior to analysis, depending on the requirements of the experiment, on the other hand. A three-element toroidal lens is also positioned between the exit of the toroid and the detector and is used to further focus the azimuthal angle of electron trajectory onto the detector [1][12] (see Fig. 2.7).

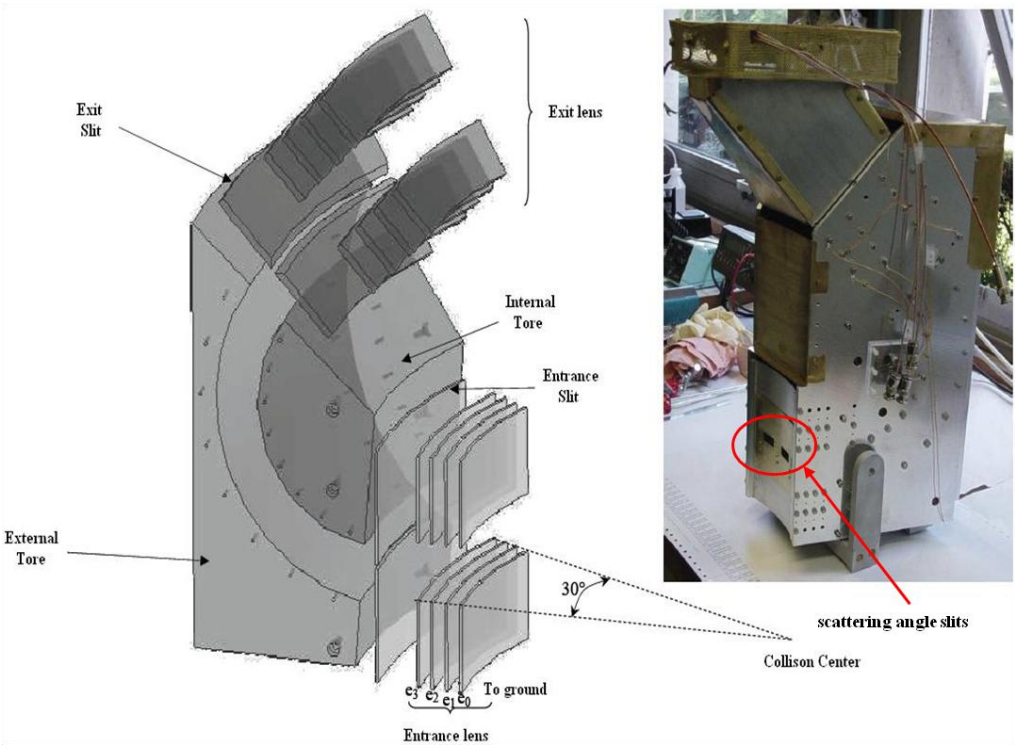

Figure 2.7 *Full view of toroidal analyzer A and its physical picture*

The energy of scattered electron (E_a) is given by

$$E_a = E_{pass} - eV_{dec} \tag{2.7}$$

where E_{pass} E_{pass} is the pass energy at which the electrons are actually analyzed between the toroidal electrodes, V_{dec} is the decelerating (or accelerating) potential. The energy resolution of toroid A is largely determined by the combined opening of the entrance and exit slits, and can be obtained from the measurement of the elastic peak width by setting $E_0 = E_a$. The elastic spectrum and energy determination as well as the energy resolution will be discussed in details in §2.8.

2.6 Position sensitive detectors and coincidence technique

As mentioned in §2.5., a position sensitive detector (PSD) is installed at the end of each analyzer. From PSDs, the angular and energy as well as the time information of detected electron can be provided from the arrival position on the surface of micro channel plate (MCP). The time signal can be analyzed by coincidence technique. With the time and position information, the electron impact single ionization (SI) or double ionization (DI) physical picture can be fully reconstructed. In the following part we will describe the PSD and the coincidence technique applied in our apparatus.

2.6.1 Position Sensitive Detector

The detection system mounted with each of the three analyzers consists of three commercial Micro Channel Plates (MCPs) with a 40 mm diameter active area and a two-dimensional resistive anode. Each arriving electron is amplified by the MCPs and induces a charge distribution on the resistive anode. The first MCP gives a time signal when one electron impacts on its surface, and the resistive anode gives four corner charge signals, from which the arrival position can be determined.

A. Micro Channel Plate (MCP)

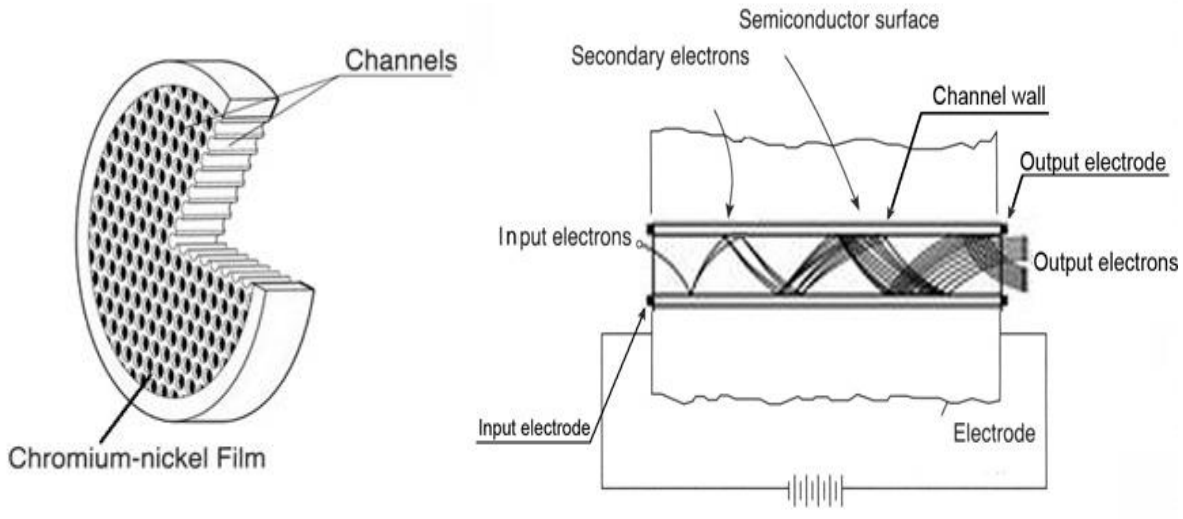

Figure 2.8 *Appearance and cross -section view of a MCP*

A MCP is an assembly of tubes or channels (each of 12.5 μm in diameter and 0.48 mm in length) (see Fig. 2.8). The total number of channels is about 10^6 to 10^7. The distance between channels is 15 μm. The inner channel wall is made of a material with a high power of secondary electron emission. An incident electron produces several electrons after collision on the wall. The tubes which form the MCP are inclined by about 8° to normal, first to increase the collision chance on the wall and second to minimize electron backscattering from the tubes, while the incident electron impacts on in perpendicular direction with respect to MCP surface. It has been shown that for energetic electrons the detection efficiency of MCPs is largely reduced when the angle of incidence with respect to the normal exceeds 30° or 40° [8].

Each of our detectors consists of three MCPs. The gain of each plate is about 10^3 to 10^4, so that a total gain of about 10^7 to 10^8 can be obtained by each detector. The three MCPs are in zigzag alignment to maximize secondary electron gain. (see Fig. 2.11)

B. Resistive anode and position signal

The resistive anode utilized for our three detectors is of 'Quantar Technology' [14].

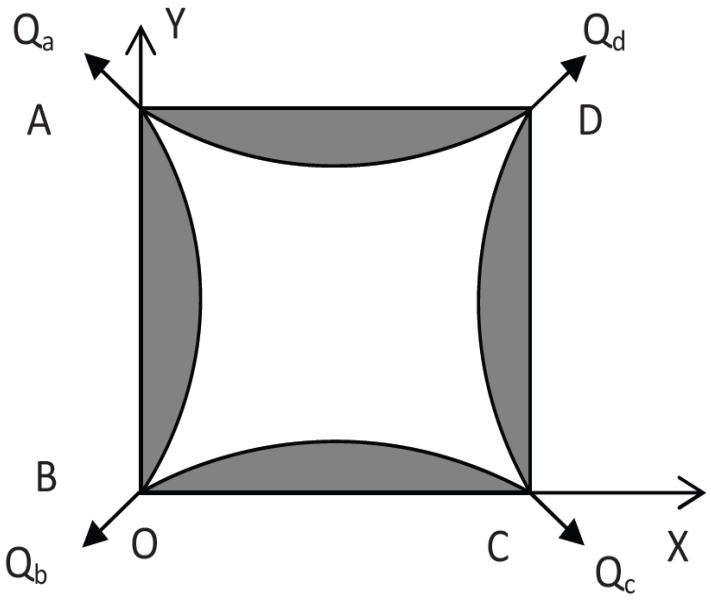

Figure 2.9 *Scheme of the resistive anode*

As shown in Figs. 2.9 and 2.11, when the electron cloud impacts on the surface of the anode, it induces a charge distribution at four corners of the anode. By measuring the amount of charge Q_A, Q_B, Q_C and Q_D from four corners of the anode, the impact position coordinates (X, Y) can be determined by the following formula:

$$X = \frac{Q_c+Q_d}{Q_a+Q_b+Q_c+Q_d} = \frac{Q_c+Q_d}{Q} \quad X = \frac{Q_C+Q_D}{Q_A+Q_B+Q_C+Q_D} = \frac{Q_C+Q_D}{Q}$$

$$Y = \frac{Q_A+Q_D}{Q_A+Q_B+Q_C+Q_D} = \frac{Q_A+Q_D}{Q} \tag{2.8}$$

where $Q = Q_A + Q_B + Q_C + Q_D$ is the total collected charge and Q_A, Q_B, Q_C and Q_D are the charges corresponding to each corner named A, B, C and D (see Fig. 2.9). These corner signals are firstly amplified by preamplifiers and then connected via shaping amplifiers to the data acquisition system.

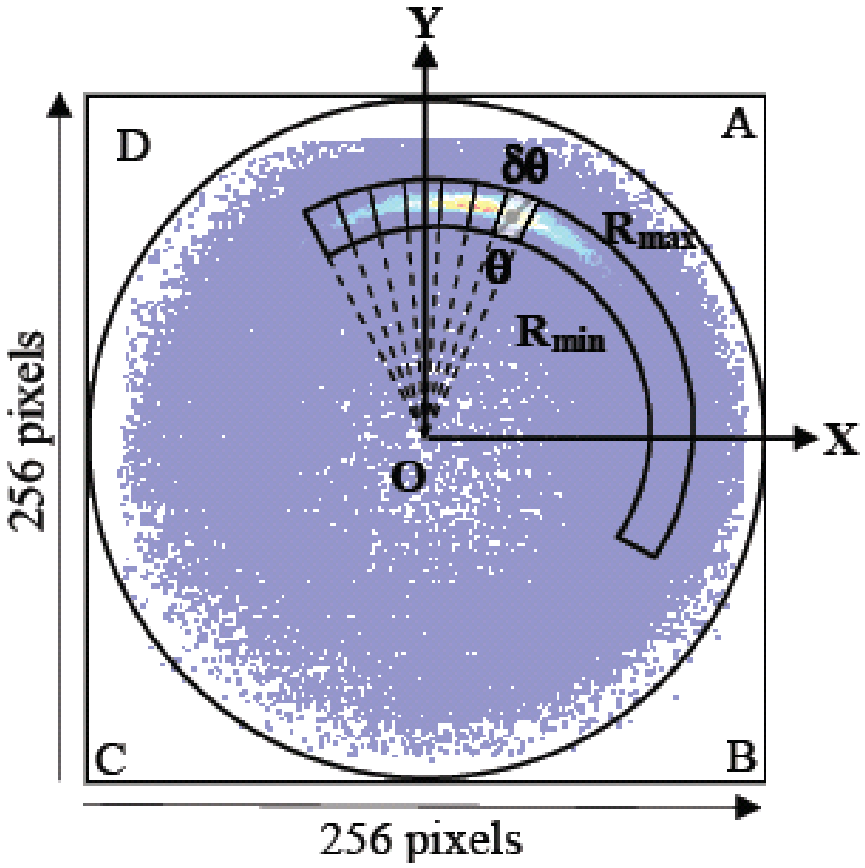

Figure 2.10 *Diagram of angular reconstruction by electron distribution at the surface of MCP*

As shown in Fig. 2.10 [1], if we create a coordinate system with collision center as the origin, the incident direction $\overrightarrow{BD}$ as zero degree, from the arrival position of the detected electron onto the surface of the detector, the position information then can be converted into angular distribution. Here the surface of the detector represents the collision plane. We define the origin O and zero direction as the collision center and incident direction $\overrightarrow{BD}$ in Fig. 2.10, respectively. The ejected angle is defined clockwise starting from incident direction $\overrightarrow{BD}$. The intensity of ejected electrons is represented by false color pixels. In the offline analysis, the angular range is divided into sectors of 5°width. Thus the angular distribution at fixed θ_a can be reconstructed eventually.

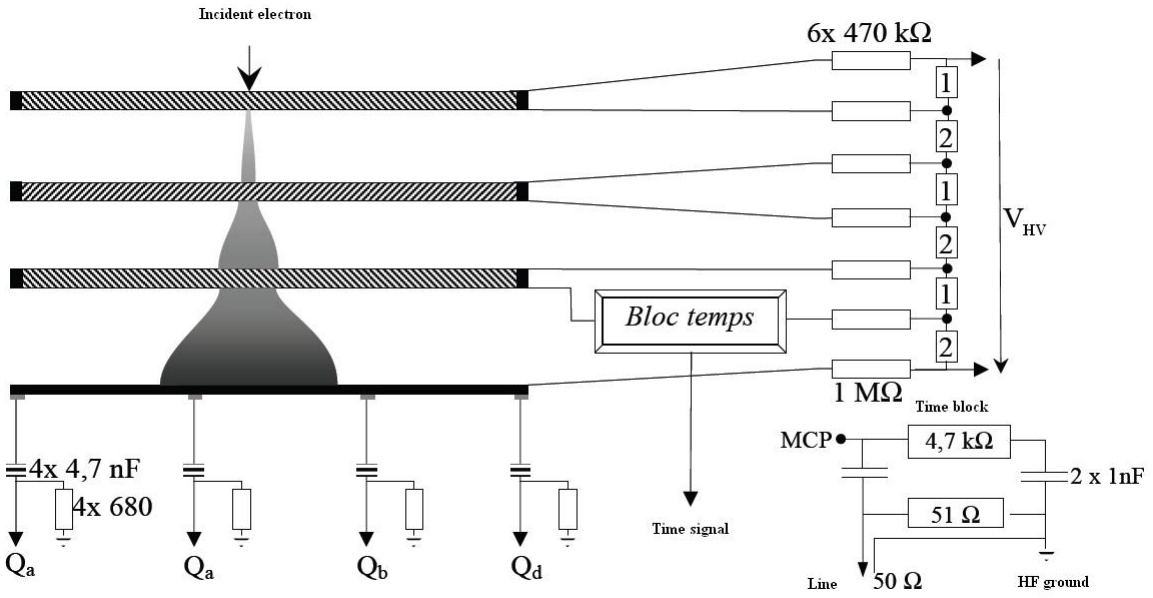

Figure 2.11. *Simplified assembly diagram of PSD*

C. Time signal

The arrival time signals associated to the relevant collision event are directly picked up on the rear face of the third MCP of each detector (Fig. 2.11). These signals are used for the coincidence technique, see next section.

2.6.2 Double and triple coincidence technique in (e, 2e)/(e, 3-1e)/(e, 3e) experiments

The data acquisition system is based on two identical time-to-amplitude converters (TACs) and a homemade system called correlation cube (CC), whose role is to adequately correlate the signals depending on the type of experiment which is performed, to make the corresponding analog-to-digital (AD) conversions and to establish the dialog with a computer specially dedicated to the control of the experiment and to the data storage [5][12].

The two TACs are started by the same time signal from one detector, say detector A and stopped by the time pulse from detector B or C. Thus this process generates two single channel analyzer (SCA) logical signals and two analog signals whose amplitudes are proportional to the arrival time T_{ab} and T_{ac} for the two ejected electrons b- and c-electrons, respectively, relative to the fast one: a-electron. In a complete (e, 3e) experiment, ten signals carrying time and position information are fed into the CC: two time signals (T_{ab} and T_{ac}) issued from the two TACs and eight charge signals issued from the four corners of the two resistive anodes of detectors B and C. In (e, 2e) or (e, 3-1e) cases, of course, some of them are not present. For instance, in (e, 3-1e) ab-mode experiment (where the scattered a-electron and one ejected b-electron are detected in coincidence), only T_{ab} is needed. Alternatively, in an

complete (e, 3e) experiment, both two time signals T_{ab} and T_{ac} from TACs are needed for triple coincidence acquisition. That is, two time signals T_{ab} and T_{ac} from TACs and eight charge position signals are processed by analog to digital converters. The correlation cube (CC) is a modular system, designed for measuring time correlation between two or three particles. If the three outgoing electrons are correlated to the same event, then two time signals and eight position signals will be registered by the computer. Otherwise, the event is rejected and the system will be re-initialized and wait for next start signal. Therefore, a triple coincidence is recorded only if the two time signals from TACs are within a time window of 200 ns. If such an event occurs, the acquisition sequencer 'tells' the computer that a true event has happened and send all the information of the event to computer. Then the computer computes 'b' and/or 'c' position information in each event and stores them with time information T_{ab} and T_{ac} (see Fig. 2.12).

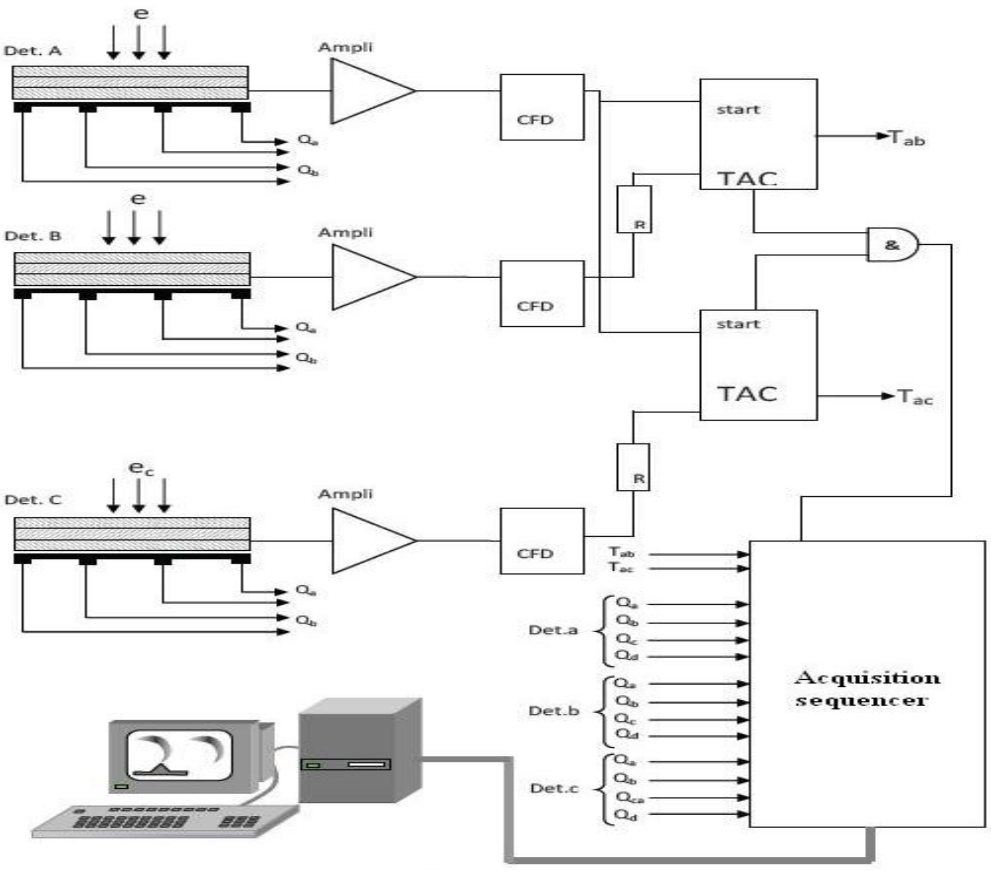

Figure 2.12. *Electronic data acquisition system*

2.7 Procedure of data analysis

Because of long time of data acquisition needed to obtain satisfactory statistics, and also because of the stability consideration of (e, 2e) / (e, 3-1e) / (e, 3e) experiments, the data are accumulated into several separated files. Before and after each separate file, for all kind of coincident experiments the non-coincident, named double differential cross sections (DDCSs) of analyzer A, B or/and C are recorded and compared both with previous measurements obtained with our spectrometer under same experimental conditions and with the well accepted Opal's results [4] (see Fig. 2.27, §2.8.2). In addition, measurements of the (e, 2e) triple differential cross section (TDCS) for the well-known target He are performed before and after (e, 3e) data acquisition and compared with our previous measurements as well as with theoretical calculation results to confirm the stability of the apparatus in data acquisition duration. This comparison of DDCS and (e, 2e) TDCS with known results allows making sure that these test runs yield practically identical angular distributions, thus excluding any long term drifts in the data. The same comparison is made among the 'individual' (e, 3e) (or (e, 3-1e) and (e, 2e)) files, with their inherent bad statistics, to also exclude the doubtful ones, if any. The raw data from the "good" files are then concatenated into a sum file.

We first introduce the (e, 2e)/(e, 3-1e) (they are identical in technique point of view) data exploitation procedure then alternate to explain how to explore the more complicated case of (e, 3e). Here we take an (e, 2e) ac coincident experiment of He for instance. The others use the same procedure.

2.7.1 Experimental data exploitation

As shown in Fig. 2.13, when the (e, 2e) data of ac coincident experiment on He is imported into the exploitation program, the false color image of two detectors is displayed. The false color represents the intensity of correlated electrons in coincidence. To avoid any distortion due to edge effect, the mechanical angular acceptance range (157°) of the toroidal analyzers B and C is usually limited to the 140° range extending from 20° to 160° (in (e, 2e)-ac experiment, analyzer B is absent here). The two inner circles allow us defining the width of effective energy window, which is used for data analysis procedure. This energy window in fact is the energy resolution, which might be changed by adjusting the mutual distance ΔR between the two inner and outer circles. The electrons out of ΔR range are filtered and excluded from further data process.

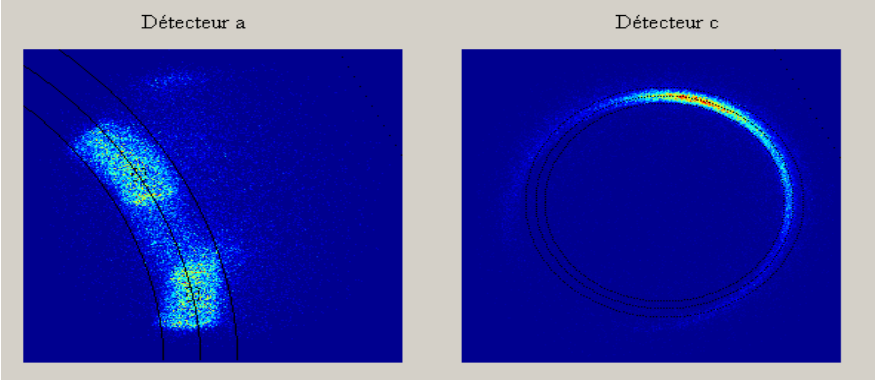

Figure 2.13 *False color images of detector A and C in the double coincident exploitation*

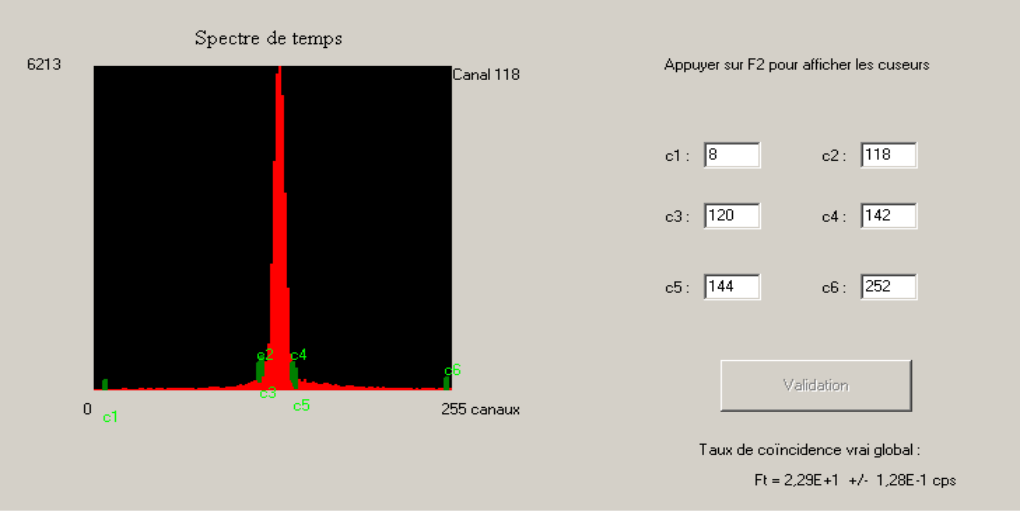

Figure 2.14 *Time spectra of a typical double coincident experiment*

In double coincidence experiment, there is one start signal triggered by fast scattered electron named 'a' and one stop signal triggered by ejected electron named 'c'. If the system receives a start signal, it will open a time window of 200 ns waiting for the ejected one. Hence the ejected electron arrives as a stop signal within 200 ns, this event will be recorded and the system will be re-initialized for next event. If the arrival time of the ejected electron is longer than 200 ns, the event will be rejected and the system will be reinitialized either. The background signal which is normally averagely distributed in time spectra should be considered in analysis stage. The parameters c1 and c6 in the time spectra is to determine the analysis range of the data, while c_2-c_5 determines the true events time range and background signal's level. Then the background coincidence signal will be subtracted from the total true coincidence signal. Hence, the data after subtraction of the background signals are pure true coincident events (see Fig. 2.14 and §2.7.2 for more details). We have two scattered angles

at -6 °and +6 °, so ac coincidence experiment utilizing analyzers A and C (angular acceptance is 20 °-160 °) can be extended to almost full angular range according to the symmetry property of the apparatus. As shown in Fig. 2.2, the scattered electron are detected at θ_a = - 6 ° ± 3 °and + 6 ° ± 3 °by analyzer 'A'. In double coincidence experiment (such as (e, 2e) and (e, 3-1e) experiments), the ejected electron are detected in coincidence with a-electron at both positive and negative directions. Because of symmetric property of the scattered direction, if we reverse the coincidence data by b-electron and a-electron at θ_a = + 6 ° ± 3 ° to θ_a = - 6 ° ± 3 °, the corresponding b-electron coincident angular distribution (θ_b) ranging between 20 °and 160 °with θ_a = + 6 ° ± 3 °becomes θ_b ranging between 200 ° and 340 ° with θ_a = - 6 ° ± 3 °. Combining the coincident data set of θ_b ranging between 20 ° and 160 ° with θ_a = - 6 ° ± 3 °and in spite of the angular acceptance limitation of the spectrometer, θ_b runs almost from 0 °to 360 °.

In the following part, I will focus on explaining the principle and procedure of (e, 3e) data exploitation.

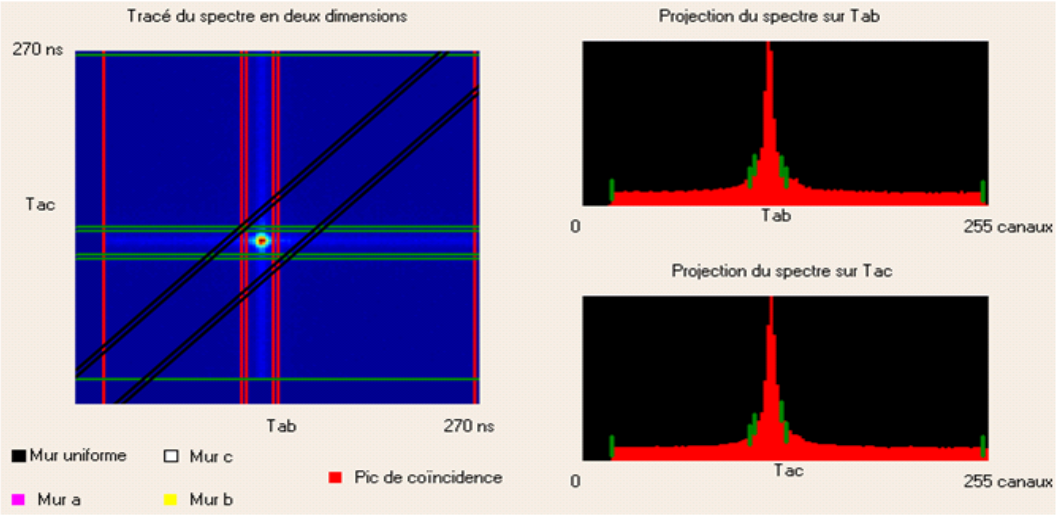

Figure 2.15 *Typical time spectra in an (e, 3e) experiment. Left panel: two dimensional time spectrum (T_{ac} versus T_{ab}, see definition in §2.6.2) of the triple coincidence. The cross sector of the 'walls' T_{ac}, T_{ab} and diagonal T_{bc} (represents b- and c- electron coincidence event) is the (e, 3e) triple coincident signal. Right panel: separate time spectrum of T_{ab} and T_{ac}, each of them corresponding to an (e, 2e) double coincident event of ab or ac coincidence.*

The two dimensional coincidence time spectra, e_a-e_b and e_a-e_c, (see Fig. 2.15) and then a false color image of the triple coincidence time spectrum (from which the true and accidental coincidence windows used in the data analysis are determined) are displayed in Figs. 2.15. A false color image of the triply coincident events accumulated on each PSD is displayed [see Fig. 2.16]. The center of the image represents the collision center. The angular shape reflects the intensity distribution over the full angular range subtended by the toroidal analyzer including edge effects and "spiraling" trajectories, while the radial distance from the center corresponds to varying transmitted energy. Though the

collision volume and the detector assemblies are carefully mechanically aligned on the Z axis of the toroids, some slight misalignment (especially of the detectors) may subsist.

Fig. 2.16 displays the false color images of three detectors in the triply coincident events. The circles and rings stand for the same meaning as in (e2e) ac coincident cases described above in addition of a third analyzer B. Because of low count rate in (e3e) experiment, usually the integration is performed over all transmitted energy range. However, it is possible to limit ΔR to increase the energy resolution.

Figure 2.16 *False color images of three detectors in the triply coincident events*

Finally, the Cartesian coordinates (X, Y) are converted into polar coordinates (r, θ), and the total useful angular range is divided into sectors $\Delta\theta_b$ or $\Delta\theta_c$, whose width is integrated to represent the middle angle as one data point of an angular distribution. $\Delta\theta_b$ and $\Delta\theta_c$ can be different, depending on the type of the measurements. The sectors widths are usually ±1°, ±5° and ±8° for double differential cross section (DDCS), triple differential cross section (TDCS) and five-fold differential cross section (5DCS), respectively.

A typical three-dimensional triple coincidence time spectrum is shown in Figs. 2.17 and 2.18.

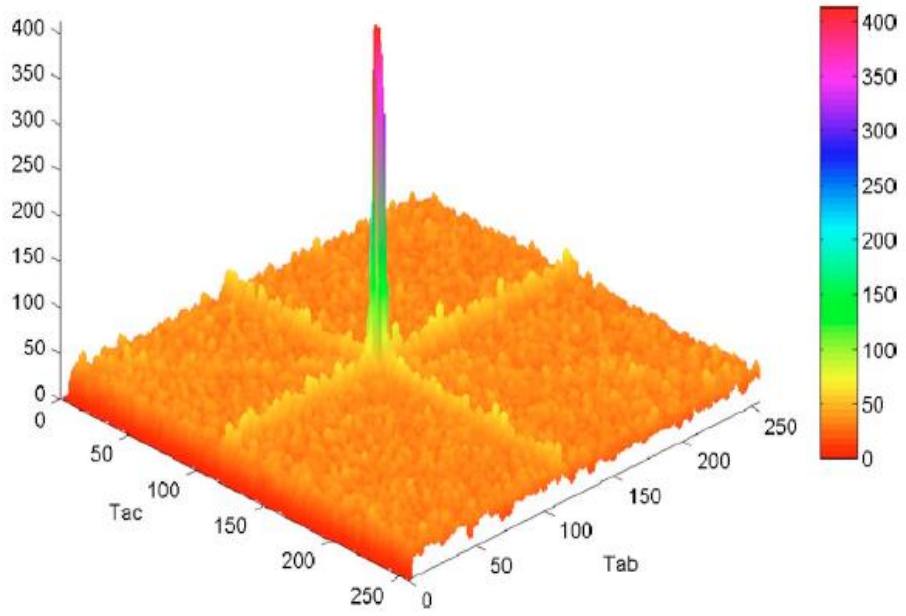

Figure 2.17 *3-D histogram diagram of a measured triple coincidence time spectra*

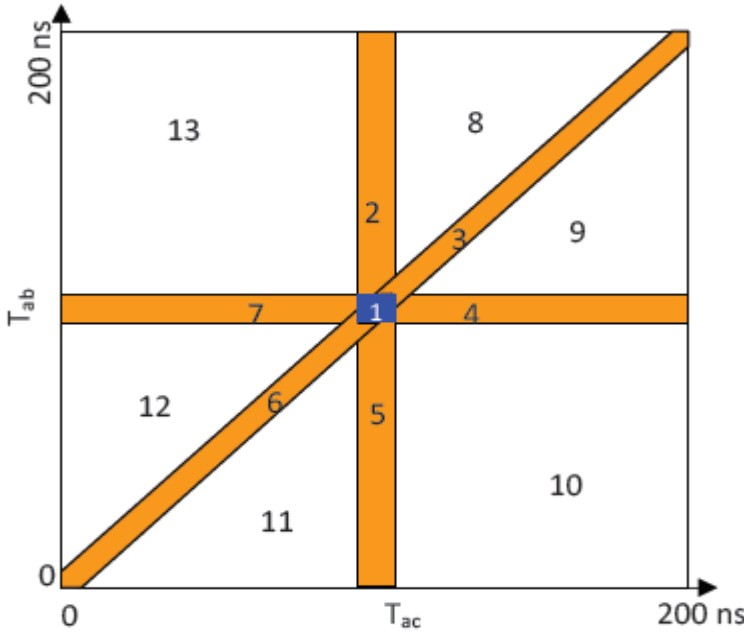

Figure 2.18 *2-D projection of triple coincident time spectra*

In these figures, the data from all θ_b and θ_c angles have been combined, that is integrating over the whole useful areas of the detectors. The T_{ab} and T_{ac} axes of the spectrum are the arrival times of the slow b and c electrons with respect to the fast one. The peak at the center corresponds to the triple coincidence double ionization signal, superimposed on a background due to four different contributions as detailed below:

I) Fully accidental signal, where the three electrons e_a, e_b and e_c are uncorrelated, hence a uniform time distribution, corresponding to the areas marked 8-13 in Fig. 2.18.

II) e_a-e_b coincident contribution (named e_a-e_b wall or 'ab wall') with correlated pair e_a-e_b and random arrival time of e_c. This corresponds to the areas marked 7 and 4.

III) e_a-e_c coincident contribution (named e_a-e_c wall or 'ac wall') with correlated pair e_a-e_c and random arrival time of e_b, corresponding to the areas marked 2 and 5

IV) e_b-e_c coincident contribution (named e_b-e_c wall or 'bc wall') with correlated pair e_b-e_c and random arrival time of e_a, corresponding to the areas marked 6 and 3

V) e_a-e_b-e_c triple coincident contribution, corresponding to the area marked 1

Note that each of these walls is also a double ionization signal, which measures the respective (e, 3-1e) cross sections within collision plane, but with a very low efficiency given by the probability of simultaneously finding a third electron within the 200 ns time interval corresponding to the TAC ramps.

2.7.2 Quantitative analysis

Fig. 2.19 shows a typical (e2e) coincidence time spectrum. The time window's length is 200 ns, which is divided into 256 channels (0.78 ns per channel). The time spectrum in fact consists of three parts. The first part is the central peak that contains n channels. Besides the central peak, there are two other blocks which correspond to false coincidences for which the scattered and ejected electrons are not correlated between each other. These two blocks contain N_1 and N_2 channels respectively.

The central peak is constituted of the false and true coincident contributions [3,9]. We can define the following relations [6]:

$$N_f = N_{f1} + N_{f2}$$

$$r_f = \frac{N_f}{N_1 + N_2} \tag{2.9}$$

N_f represent the total false coincidence out of the peak, and r_f the false coincidence number per channel out of the peak. To obtain the pure true coincidence number (N_t) in the peak, one has to subtract the false coincidence contribution, hence the following relation:

$$N_t = N_{tf} - r_f n = N_{tf} - rN_f \quad N_t = N_{tf} - r_f n = N_{tf} - rN_f \text{ where } r = \frac{n}{N} \; r = \frac{n}{N} \text{ and } N = N_1 + N_2$$

$$N = N_1 + N_2 \tag{2.10}$$

where N_{tf} is the total coincidence number in the peak and n is the number of channels of the peak.

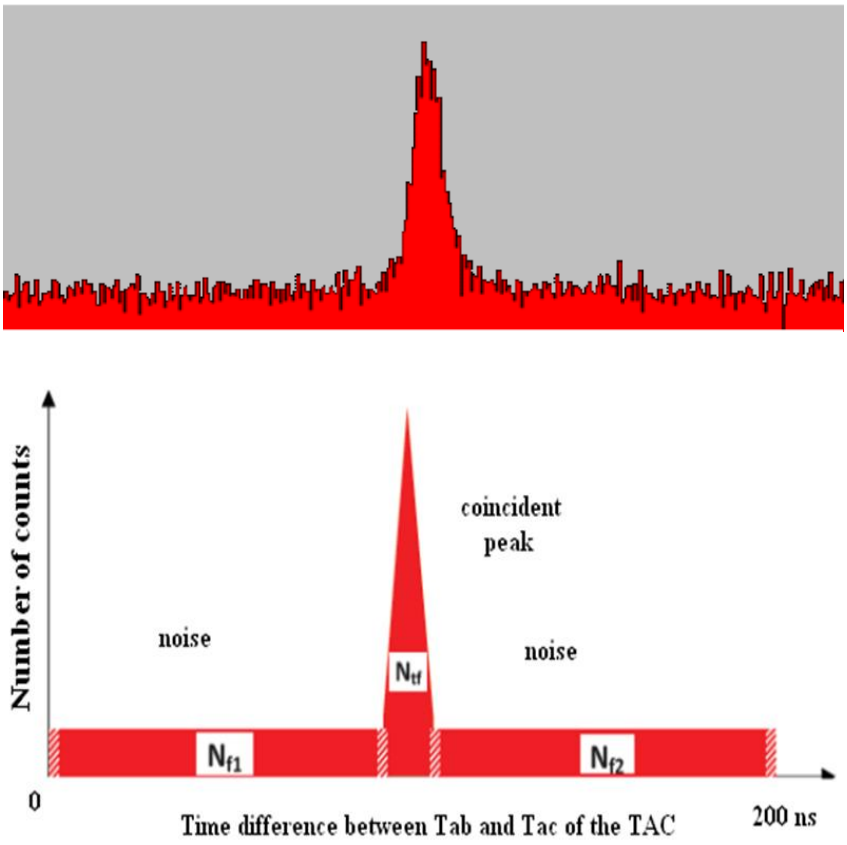

Figure 2.19 *Double coincidence spectrum: above, experimental spectrum; below, simplified schematic illustration. The indications 't' and 'f' correspond to 'true' and 'false' signals (see definition of all notations in §2.7.2)*

To estimate the statistical uncertainty on N_t, we can write:

$$(\Delta N_t)^2 = \left(\Delta N_{tf}\right)^2 + r^2\left(\Delta N_f\right)^2 \quad \text{or alternatively} \quad \sigma_t^2 = \sigma_{tf}^2 + r^2\sigma_f^2 \; \sigma_t^2 = \sigma_{tf}^2 + r^2\sigma_f^2 \quad . \tag{2.11}$$

The convolution of N_{tf} and N_f whose standard deviation is the square root of the sum of squared deviations of each of the two contributions. So the above relation could also be written as:

$$\sigma_t^2 = N_{tf} + r^2 N_f \;\; \sigma_t^2 = N_{tf} + r^2 N_f \tag{2.12}$$

The relative statistical uncertainty σ can then be defined as [6]:

$$\sigma^2 = \frac{N_{tf} + r^2 N_f}{N_t^2} \sigma^2 = \frac{N_{tf} + r^2 N_f}{N_t^2} \tag{2.13}$$

The signal to noise ratio (SNR) is also a critical parameter in coincidence experiments. The influence of the experimental parameters might be quite different on SNR and σ due to their definition.

There are two parameters in an experiment, the accumulation time T and the beam current I, which influence the SNR and σ. In practice, N_t and N_f can be written as:

$$N_t = Tf_t \;\; N_t = Tf_t \quad \text{and} \quad N_f = Tf_a f_b N\tau = Tf_a f_b\, 200 \cdot 10^{-9} \tag{2.14}$$

Here $N=N_1+N_2$, τ is the time duration of each channel of the spectrum, f_t is the count rate per second or frequency of true coincidences and f_a and f_b are the non coincidence frequencies on detectors A and B, respectively. Each of these frequencies is proportional to current I and we can write such relation as following

$$f_t = K_t I = k_t \sigma_{ab} I \quad f_a = K_a I = k_a \sigma_a I \quad f_b = K_b I = k_b \sigma_b I \tag{2.15}$$

where σ_{ab}, σ_a and σ_b are the cross sections for production of correlated pair (e_a,e_b), scattered electron e_a and ejected electron e_b, respectively.

If we substitute all of these relations into definition of σ^2, then we get:

$$\sigma^2 = \frac{N_t + rN_f + r^2 N_f}{K_t^2 I^2 T^2} = \frac{K_t IT + r(r+1)TN\tau K_a K_b I^2}{K_t^2 I^2 T^2} = \frac{1}{K_t IT} + r(1+r)\frac{N\tau K_a K_b}{T}$$

$$\text{or } \sigma^2 T = \frac{N_t + rN_f + r^2 N_f}{K_t^2 I^2 T} = \frac{K_t IT + r(r+1)TN\tau K_a K_b I^2}{K_t^2 I^2 T} = \frac{1}{K_t I} + r(1+r)N\tau K_a K_b$$

$$\sigma^2 T = \frac{N_t + rN_f + r^2 N_f}{K_t^2 I^2 T} = \frac{K_t IT + r(r+1)TN\tau K_a K_b I^2}{K_t^2 I^2 T} = \frac{1}{K_t I} + r(1+r)N\tau K_a K_b \tag{2.16}$$

Thus the SNR have the new form:

$$SNR = \frac{N_t}{N_f} = \frac{K_t IT}{TN\tau K_a K_b I^2} = \frac{K_t}{N\tau K_a K_b I} \tag{2.17}$$

The above formula indicates an inverse relation between σ^2 and current I for a fixed duration time T of the experiment. For large I case, σ tends to a limited value with fixed T. The SNR is also inversely proportional to I. It is necessary to choose an adequate I value to balance its influence on σ^2 and SNR. For (e, 2e), a current I is set to have a visually satisfactory SNR and the duration of the experiment is then adapted.

Basically, an acquisition of (e, 3e) type experiment is not much different from (e, 2e) case. There are three electrons which are detected in coincidence rather than two and the time spectrum is a two-dimensional one. Here we use n_j with j=a, b or c, to indicate the number of channels contained in the wall j and N_j is the number of events. Similarly, n_u and N_u, are the number of channels and events of uniform noise. Therefore, each wall contains N_j' events of two correlated electrons, just like (e, 2e) case. Hence N_j' and N_j have the following relation:

$$N_j^{'} = N_j - \frac{n_j}{n_u} N_u \tag{2.18}$$

N_{tf} denotes the number of events in the coincident peak. To obtain the true events number N_t in the peak, the contributions of each wall and the continuum noise should be subtracted from N_{tf}. So that

$$N_t = N_{tf} - \sum_{j=a,b,c} \frac{n}{n_j} N_j^{'} - \frac{n}{n_u} N_u = N_{tf} - \sum_{j=a,b,c} \frac{n}{n_j} \left(N_j - \frac{n_j}{n_u} N_u \right) - \frac{n}{n_u} N_u =$$
$$N_{tf} - \sum_{j=a,b,c} \frac{n}{n_j} N_j + 2 \frac{n}{n_u} N_u \tag{2.19}$$

Do note that the contribution of noise to the walls has already been counted in for each N_j, hence the factor 2 appears in Eq. 2.19.

Or, using the notation $r_j = \frac{n}{n_j}$ for j=a, b, c or u:

$$N_t = N_{tf} - \sum_{j=a,b,c} r_j N_j + 2 r_u N_u \tag{2.20}$$

Similarly as (e, 2e), we can write the relative statistical uncertainty as:

$$\sigma^2 = \frac{N_{tf} + \sum_{j=a,b,c} r_j^2 N_j + 2 r_u^2 N_u}{N_t^2} \tag{2.21}$$

Instituting N_{tf} by the above equation, we get a new expression of $\sigma^2 \sigma^2$.

$$\sigma^2 = \frac{N_t + \sum_{j=a,b,c} r_j^2 N_j - 2 r_u N_u + \sum_{j=a,b,c} r_j^2 N_j + 2 r_u^2 N_u}{N_t^2} = \frac{N_t + \sum_{j=a,b,c} r_j (1 + r_j) N_j + 2 r_u (r_u - 1) N_u}{N_t^2} \tag{2.22}$$

Again similarly as (e, 2e), the different contributions are of the function of I to the fixed accumulation time T, and can be written as following formulae:

$$N_t = T k_t \sigma_{abc} I = T K_t I \tag{2.23}$$

$$N_u = T k_u \sigma_a I \sigma_b I \sigma_c I = T K_u I^3 = T f_a \tau f_b \tau f_c \tau \tag{2.24}$$

$$N_j = T k_j \sigma_j I \bar{\sigma_j} I + T k_j^u \sigma_a I \sigma_b I \sigma_c I = T K_j I^2 + T K_j^u I^3 \tag{2.25}$$

The different terms k_t, k_u, k_j and k_j^u depend on the experimental condition, mainly contributed by the gas intensity and beam current I. σ_j is the cross section of one electron with the energy E_j in an accepted solid angle of analyzer. This term is proportional to f_j. $\bar{\sigma_j}$ is the cross section of two correlated electrons. Finally, σ_{abc} is the six fold differential cross section of (e, 3e) process.

Instituting above equations into Eq. 2.16, the expression can be rewritten as:

$$\sigma^2 T = \frac{1}{K_t I} + \sum_{j=a,b,c} r_j(1+r_j)\frac{K_j}{K_t^2} + \left[\sum_{j=a,b,c} r_j(1+r_j)\frac{K_j^u}{K_t^2} + \frac{2r_u(r_u-1)K_u}{K_t^2}\right] I \qquad (2.26)$$

The first two terms are comparable to (e, 2e) case, while the third term is proportional to *I*. It is clear that if the beam current *I* is great, the third term will increase the value of σ^2 and if the current *I* is small, the first term will increase the value of σ^2. It is obvious that there is an optimized current *I*, with which we can obtain the lowest value of σ^2.

We recall that r_u is the ratio between the channel number in the peak region (n) and the channel number of uniform noise (N_u). It is clear that $n \ll N_u$ (in other word, $r_u \ll 1$, for $r_u = N/N_u$ $r_u = n/N_u$). Because the uniform noise has an identical contribution per channel in all regions of the time spectrum, its contribution in the wall j is simply proportional to the number of channels contained in the wall. That means

$$TK_j^u = n_j \frac{N_u}{n_u} \text{ or } TK_j^u I^3 = n_j \frac{TK_u i^3}{n_u} \text{ where } K_j^u = \frac{n_j}{n_u} K_u \qquad (2.27)$$

Utilizing the relation: $\frac{n_j}{n_u} = \frac{r_u}{r_j}$ we obtain:

$$\sigma^2 T = \frac{1}{K_t I} + \sum_j r_j(1+r_j)\frac{K_j}{K_t^2} + \frac{K_u}{K_t^2}\left[r_u(2r_u + 1 + \sum_j r_j)\right] I \qquad (2.28)$$

A straightforward calculation also leads to the signal-to-background ratio as

$$SNR = \left[\sum_{j=a}^{c} \frac{r_j}{4}\left(\frac{K_j^j}{K_t} I + \frac{K_j^u}{K_t} I^2\right) - \frac{r_u}{2}\frac{K_u}{K_t} I^2\right]^{-1} \qquad (2.29)$$

The final σ^2 is determined by the total contribution of three terms (see Fig. 2.20).

From Eq. 2.28, it is shown that $\sigma^2 T$ is determined by the sum of three terms with the function of electron beam current I: inverse term $\frac{1}{K_t I}$, constant term $\sum_j r_j(1+r_j)\frac{K_j}{K_t^2}$ and proportional term $\frac{K_u}{K_t^2}\left[r_u(2r_u + 1 + \sum_j r_j)\right] I$, which are labeled '$T_1$', '$T_2$' and '$T_3$', respectively, with the same labels as in Fig. 2.20. The dependence of $\sigma^2 T$ upon *I*, shown schematically in Fig. 2.20, implies the existence of a minimum which determines the optimum choice of *I*, named I_{opt}. Similarly, an additional term also appears in the expression of the *SNR* of Eq. 2.29, which makes this quantity decrease very rapidly as *I* increases, roughly as a function of I^2. This criterion might make it preferable to choose *I* value smaller that I_{opt}, depending on the experimental *K* factors of the particular experiment. In our real experimental data exploitation program, the optimized incident electron beam current can be calculated to be a reference for the current experiment itself and for the next experiment both in (e, 2e) and (e, 3e) cases.

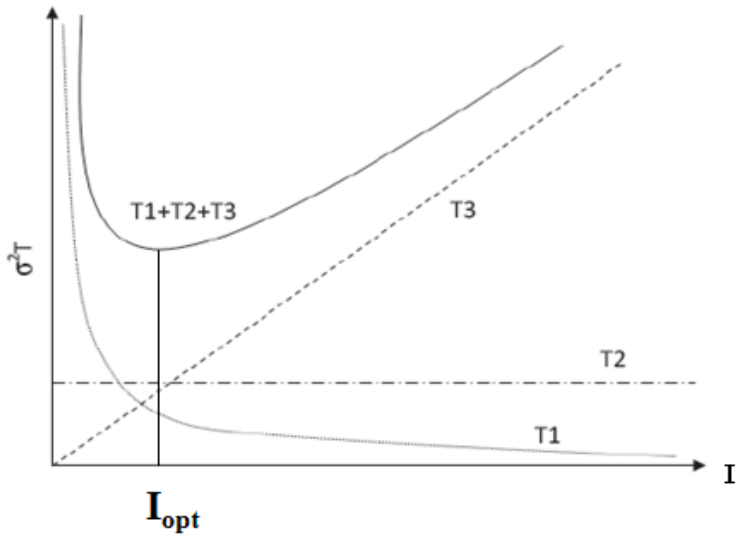

Figure 2.20 *Variation of statistical precision as a function of incident electron beam intensity. Arbitrary units are used on both axes. The successive terms in the right-hand side of Eq. 2.28 are represented by the dot, dash dot and dash curves labeled T_1, T_2 and T_3. Note that T_1 has same form as Eq. 2.16 except a constant term. The optimum choice for I, I_{opt}, is obvious in the (e, 3e) case as being represented by the solid curve labeled $T_1+T_2+T_3$.*

2.8 Calibration and experimental procedure

In this section, we will introduce the method used for the determination of the analyzed energy and of the energy resolution for each toroidal analyzer. The angular calibration and resolution will also be introduced in this section.

2.8.1 Energy calibration and energy resolution

As mentioned in the end of §2.5, the energy resolution of toroid A can be determined by an elastic scattering experiment. As well known, electron-target interaction results in different scattering channels strongly depending on incident energy. Generally speaking, all electron-target interaction channels are divided into two types: elastic and inelastic scattering. The differences are that in elastic scattering 1) the total kinetic energy of the colliding bodies is conserved, meaning that no energy is lost to other processes; 2) the colliding particles remain intact. On the other hand, in inelastic scattering the total kinetic energy of the colliding bodies is not conserved, meaning that energy is taken up by other processes. For example, electron impact excitation and ionization belong to inelastic processes. In elastic case, the incident electron only changes direction but there is no energy exchange with target, so that we have the relation of elastic collision: $E_0=E_a$. Here we consider E_{pass} is constant for fixed E_a and the scattering angle is fixed at -6°. Because $E_a = E_{pass} + eV_{dec}$, if we vary V_{dec}, the detected E_a also changes accordingly. This detected 'E_a' will have intensity distribution in elastic scattering spectrum as function of V_{dec} and thus approach the maximum intensity when satisfy the

following condition: $E_a=E_0=E_{pass}+ eV_{dec}$, where E_{pass} and E_0 are fixed. So by varing V_{dec}, we can obtain an energy loss spectrum for electron-a at $\theta_a= -6°$ in a non-coincidence mode, including the elastic scattering channel and the inelastic ones. A typical example is given in Figs. 2.21 and 2.22. With known V_{dec} and E_0 at maximum position in the energy loss spectrum, E_{pass} can be calculated. By varying V_{dec}, according to the formula: $E_a= E_{pass}- eV_{dec}$, we can set any scattering energy value we want.

From elastic scattering peak results, we find a maximum position at around -331.1± 0.3 V. If we substitute this value into the equation: $E_a=E_0=E_{pass}- eV_{dec}$ (here $E_a = E_0 = 536.6$ eV), the practical E_{pass} is thus 205.5 ± 0.3 eV. Also we can obtain the energy resolution of the analyzer A (ΔE_a) from the FWHM of elastic peak, which is 4.3 ± 0.3 eV in this case.

So far, the detected scattering energy 'E_a' can be changed by varying V_{dec} (in all our "real" experiments presented in this thesis, E_a is fixed at 500 eV. This means V_{dec}=500 -205.5 = 294.5 ± 0.3 eV).

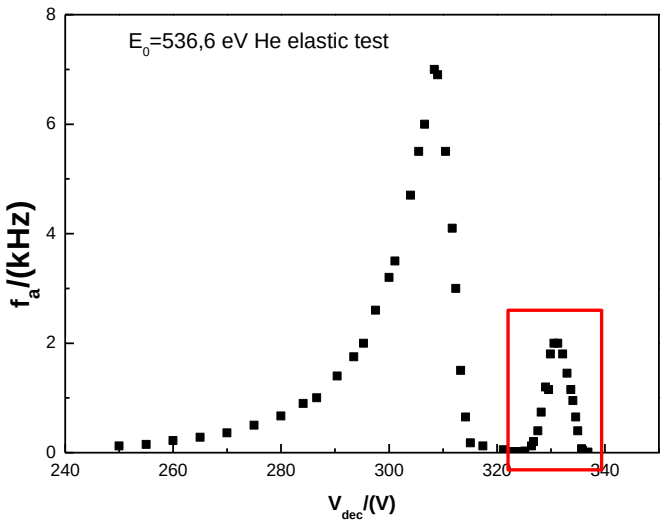

Figure 2.21 *Energy loss spectrum obtained for He target using the toroid A with E_0=536.6 eV. The black solid square represents the experimental data. The elastic peak is seen on right red rectangle (see the zoom in Fig. 2.22).*

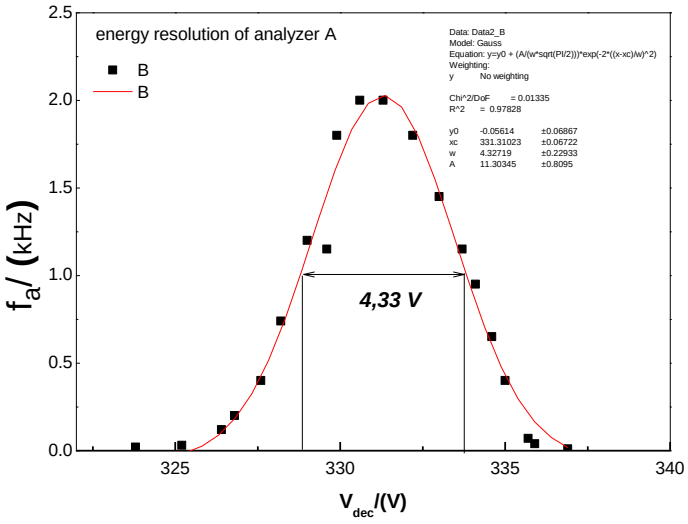

Figure 2.22 *Same data as in Fig. 7, but local zoomed of V_{dec} from 322 to 340 V (embraced by a red hollow box in Fig. 21) with a Gaussian fit (red solid line), which gives a prediction at maximum at -331.1 ±0.3 V.*

As mentioned above, E_{pass} is constant for fixed E_a. However, we try to study the variation of E_{pass} as E_a changes. As stated above, E_0 equals E_a in an elastic spectrum. Each time with fixed E_0=E_a, the V_{dec} is kept changing until approaching the maximum of DDCS for the scattered electron. Then E_{pass} can be determined from the equation: $E_a=E_0=E_{pass}- eV_{dec}$, consisting one data point: (E_a:E_{pass}). We selected 7 different E_0=E_a, ranging from ~430 to ~780 eV, and represent the final results in Fig. 23. The result indicates that E_{pass} enhances slightly when E_0=E_a increases.

The data is fitted by polynomial, represented by red solid curve in Fig. 2.23. For validation of above conclusion, we choose a point at E_a=536.6 eV, which is same as the real elastic energy of E_a. The polynomial fit gives an E_{pass} prediction at ~205.6 V. The elastic spectrum also indicate the passing energy at E_a = E_0 =500 eV is about 204.7 ± 0.3 eV, which has about 1 eV difference to E_a = E_0 = 536.6 eV. This conclusion is useful to predict the value of E_{pass} with different energy E_a. However, this difference is within the energy resolution of each analyzer, which is ~ 4.0 eV.

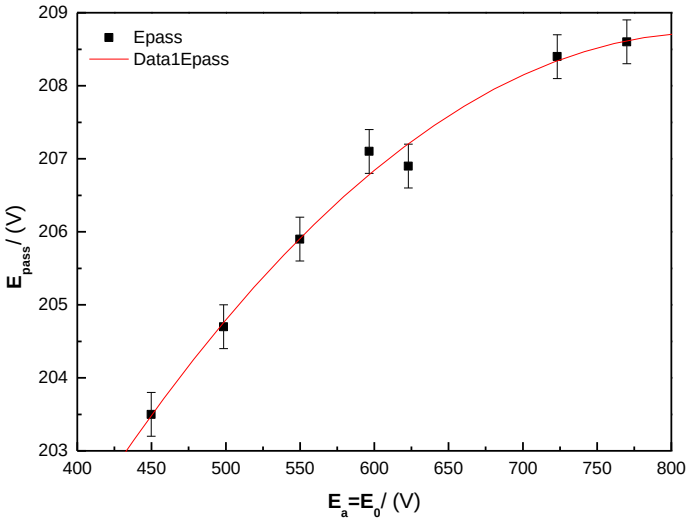

Figure 2.23 *Variation of E_{pass} with the function of E_{inc} for toroid A*

Then we can perform the so-called 'binding energy spectra' measurements by varying V_{dec} (or E_0 as they are essentially equivalent) to determine the other two detected energies of ejected electrons, namely E_b and E_c. the results are shown in Fig. 2.24 and Fig. 2.25 for analyzer B and C, respectively. The 'binding energy spectra' measurements is a coincidence a-b (or a-c) experiment in which E_0 corresponds to total energy needed for single ionization ($E_0 = E_a + E_{b/c} + IP^+$), E_a and $E_{b/c}$ correspond to scattered and ejected electron energies and the electrons 'a' and 'b/c' are energy analyzed and detected in coincidence at fixed scattering direction. Usually, we choose He as a target for these binding energy spectra measurements because He is well studied and it has a distinguishable energy gap ($\Delta E = IP^{2+} - IP^+ = 79$ eV - 24.6 eV=54.4 eV) between single (IP^+=24.6 eV) and double ionization (IP^{2+}=79 eV) potentials, so that there will be no mixture channel occurring which would affect the observed coincidence energy resolution. From the maximum position of such binding energy test, we can obtain the detected energy in practice and drive out the energy resolution ΔE_b and ΔE_c of analyzer B or C from energy resolution of toroid A (ΔE_a) and coincidence energy resolution ΔE^{coin} by following formulae [6]:

$$(\Delta E_{ab/ac}^{BE})^2 = \Delta E_a^2 + \Delta E_{b/c}^2$$

$$\Delta E_{coin}^{-2} = \Delta E_a^{-2} + \Delta E_{b/c}^{-2} \quad (\Delta E_{ab/ac}^{coin})^{-2} = \Delta E_a^{-2} + \Delta E_{b/c}^{-2} \tag{2.30}$$

$\Delta E_{coin}^{-2} = \Delta E_a^{-2} + \Delta E_b^{-2} + \Delta E_c^{-2}$ where $\Delta E_{ab/ac}^{BE}$ ΔE is what we can obtain from binding energy spectrum. In Fig. 2.24 and Fig. 2.25, ΔE_{ab}^{BE} and ΔE_{ac}^{BE} are 5.5 ± 0.3 eV and 5.4 ± 0.3

eV for ab and ac cases respectively. The maximum positions are V_{dec}= –295.0 ± 0.3 V and V_{dec}= –295.3 ± 0.3 V for ab and ac binding energy measurements, so the detected energy of analyzer B and C can be derived from energy conservation $E_0 = E_a + E_b + IP^+$ and are E_b ~ E_c ~11.2 ± 0.3 eV within error bars. Hence the energy resolution is $\Delta E_b \sim \Delta E_c \sim 3.4 \pm 0.3$ eV. The double coincident energy resolution can also be derived from the last two equations, that is $\Delta E_{ab}^{coin} \sim \Delta E_{ac}^{coin} \sim 2.7 \pm 0.3$ eV.

The energy uncertainty of triple coincidence is defined as [3,6,9]

$$\Delta E_{abc} = \frac{\Delta E_a \Delta E_b \Delta E_c}{\sqrt{\Delta E_a^2 + \Delta E_b^2 + \Delta E_c^2}}. \tag{2.31}$$

If we institute ΔE_a= 4.3 ± 0.3 eV, $\Delta E_b \sim \Delta E_c \sim 3.4 \pm 0.3$ eV into above equation, then we obtain the energy uncertainty of triple coincidence is about 7.7 ± 0.3 $(eV)^2$.

To summarize the above discussion, the energy resolution of the three analyzers A, B and C are $\Delta E_a \sim 4.3 \pm 0.3$ eV directly obtained from elastic spectrum, $\Delta E_b \sim \Delta E_c \sim 3.4 \pm 0.3$ eV derived from binding energy spectrum, respectively. The energy resolutions of ab and ac double coincidence experiment are $\Delta E_{ab}^{coin} \sim \Delta E_{ac}^{coin} \sim 2.7 \pm 0.3$ eV. and for triple coincidence experiment, the energy resolution is ~7.7 ± 0.3 $(eV)^2$ according to their definition. Such energy resolution is satisfactory for both electron impact single and double ionization investigation.

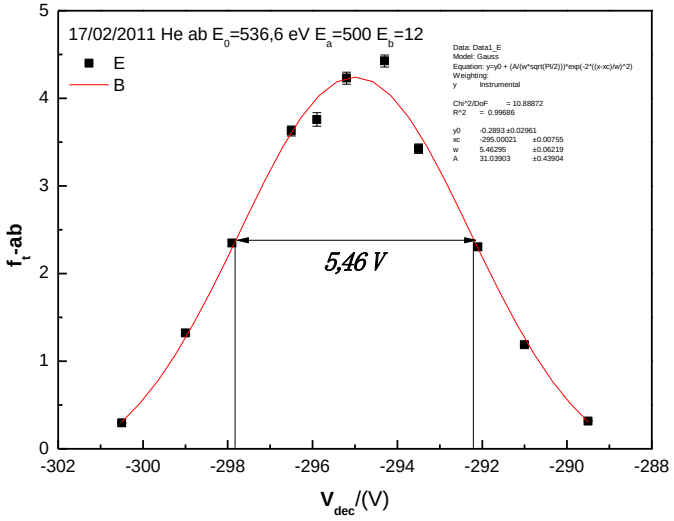

Figure 2.24 *Binding energy test of ab coincidence experiment with E_0=536.6 eV which corresponds to (e, 2e) experiment on He with E_a=500 eV and E_b=12 eV. Here f_t-ab represents integration including contribution from all accessible detection angles of triple differential cross section. The solid square with one standard deviation*

error bar and red solid curve represent the experimental data and a Gaussian fit, respectively. The Gaussian fit indicates a maximum position at about -295.0 V and full width at half maximum (FWHM) ΔE of 5.5 ± 0.3 eV.

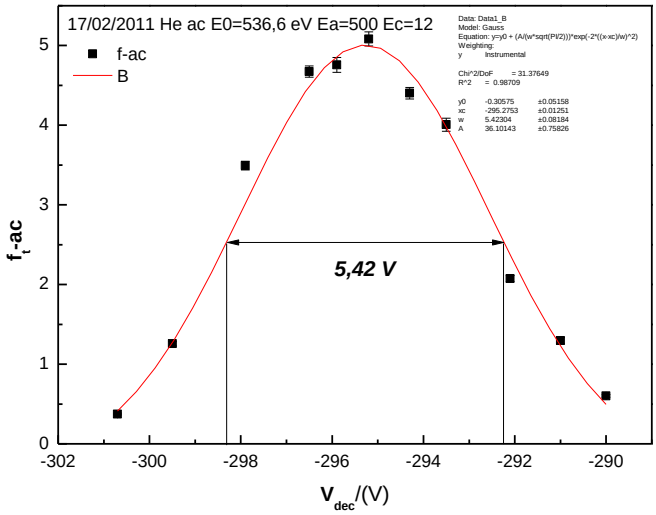

Figure 2.25 *Same as Fig. 2.24 but for ac coincidence case. The Gaussian fit indicates a maximum at about -295.3 V and FWHM ΔE of 5.4 ± 0.3 eV.*

2.8.2 Angular Calibration

If the collision volume is an ideal point source, the detected electrons will travel along ideal trajectories issued from a point source located on the axis of the toroidal analyzer and follow the radial electric field lines all the way up to the detector where they appear at exactly the same angle as their emission.

In practice, the electron trajectory inside analyzer are effected by many factors, such as edge effects, mechanical misalignments of the electron optics elements, the impinge on the detector at a different angle from the emission angle (so-called spiraling effect), etc.

To determine the linearity of the angular scale and the angular resolution of each analyzer, an annular 'stop' where five small, circular holes with an equal spacing of certain angle can be put in front of the analyzer before the entrance of the electron to the analyzer instead of L_4 [5]. Each opening hole corresponds to the scale of 1°. Instead of gas jet, scattering from the tip of a thin wire (0.1 mm diameter) placed at the nozzle position is used to simulate an 'ideal point' source. Consequently, on the detector, there are five equally spaced narrow peaks with FWHM of ±1°. Then using the real gas source, five peaks are still observed equally spaced but with a FWHM of ±7°. The above is operated in no-coincidence mode. It is difficult to estimate the angular resolution in coincidence mode, however since the overlap of the peaks is smaller than the no-coincident collision volume seen by

each toroidal analyzer, the angular resolution in coincidence mode is thus better than ± 7 ° (see Fig. 2.26).

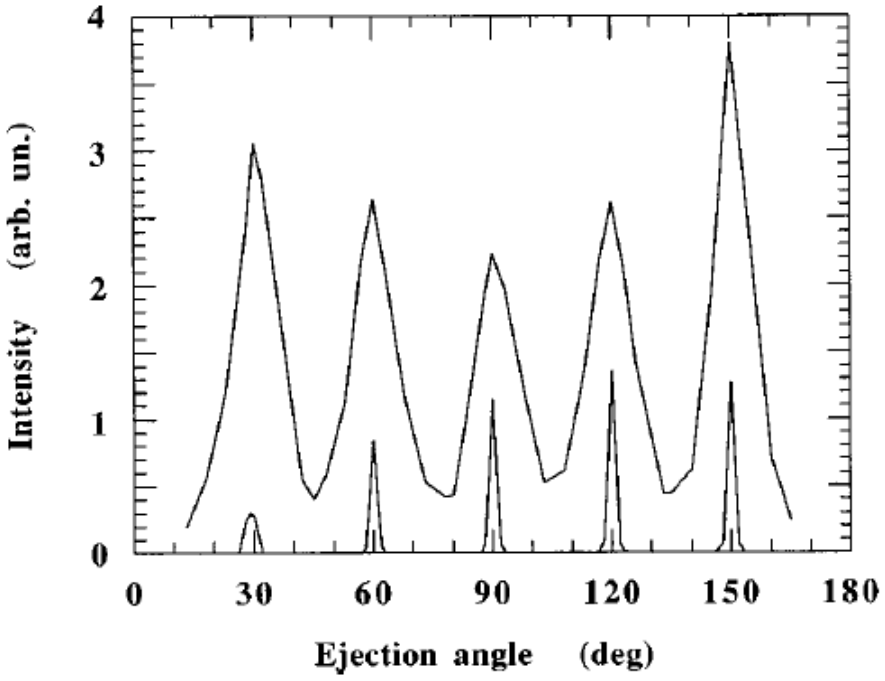

Figure 2.26 *Angular intensity distribution on the detector when the entrance to toroidal is blocked by five small, equally spaced holes. Narrow peaks (below): 'point source', wide peaks (above): gas jet. This results are take from Ref.[5].*

However, once the above calibration is finished, it is not convenient to be operated routinely without interrupt the experiment. Hence it is necessary to find reliable well-accepted standards to validate and calibrate the angular measurement. Generally, we choose He as a calibration target. We compare our DDCS measurement with Opal's results [4] and (e, 2e) TDCS measurement with theoretical calculation as well as reference results under exactly the same experimental condition.

Here is the example of DDCS-C and DDCS-A. Note that for DDCS-A, the symmetric structure and identical intensity distribution with respect to 0 ° (incident beam direction) between positive and negative angle are essential.

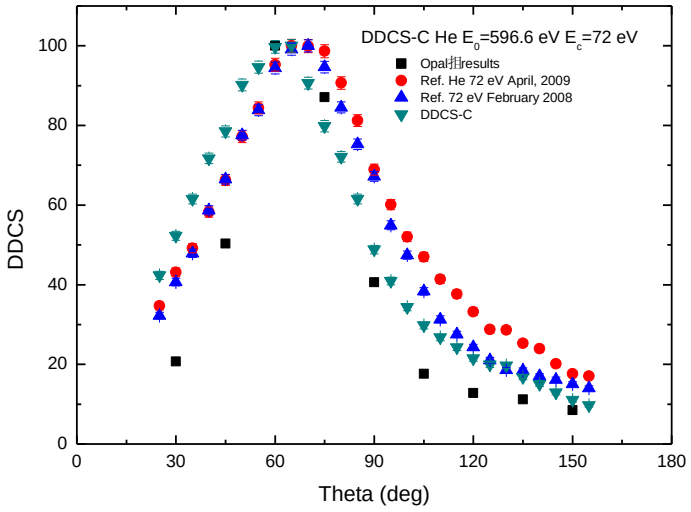

Figure 2.27 *DDCS-C distribution of He with E_0=596.6 eV and E_c=72 eV. The solid black squares, solid red circle, solid blue regular triangle and solid inverted triangle symbols represent Opal's results, reference measurement in April, 2009, reference measurement in February 2008 and present measurement with one standard deviation statistical error bar, respectively. All results are arbitrarily scaled to 100 for the best visual fit at maximum.*

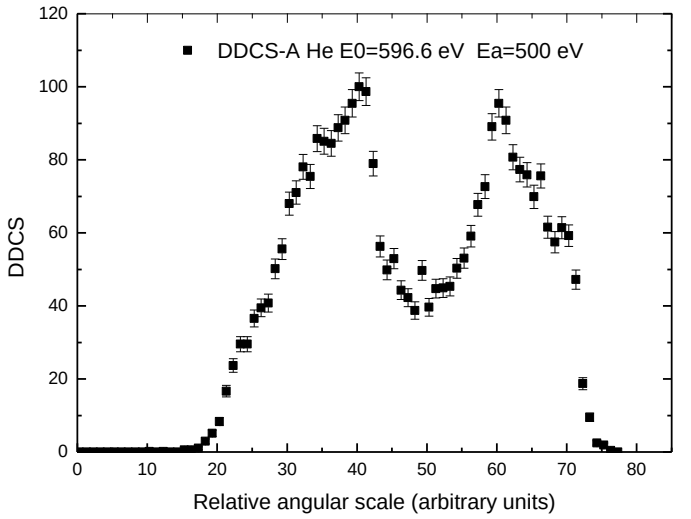

Figure 2.28 *DDCS-A distribution of He with E_0=596.6 eV and E_a=500 eV. The minimum at middle indicates the zero degree direction or incident direction. The solid square symbols represent the experimental measured DDCS of A with one standard deviation statistical error bar. The experimental results are arbitrarily scaled to 100 for the best visual fit at maximum.*

2.8.3 Validation of the experimental procedure

To validate the calibration of the apparatus, an (e, 2e) experiment is performed on He with E_0=596.6 eV, E_a=500 eV and E_c=72 eV. The measurement is also compared with results from the

convergent close-coupling [15] (CCC) method which describes the single ionization process on He very well and the calculation is well accepted. We find the experimental result in Fig. 2.29 is in good agreement with CCC calculation. This ensures the validation of the following experimental measurement.

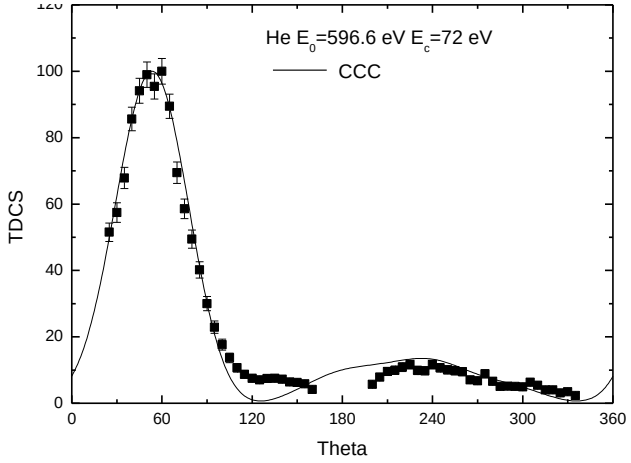

Figure 2.29 *Triple differential cross section distribution of He with E_0 = 596.6 eV E_a = 500 eV and E_c = 72 eV. The solid square with standard deviation error bar and solid curve represent the experimental measurement and CCC theoretical calculation, respectively. The experimental and theoretical results are arbitrarily scaled to 100 for the best visual fit at maximum.*

2.9 Bibliography

1. Catoire, F., et al., *New developments for an electron impact (e,2e)/(e,3e) spectrometer with multiangle collection and multicoincidence detection.* Review of Scientific Instruments, 2007. **78**(1): p. 013108-8.
2. Leckey, R.C.G. and Riley, J.D. *A toroidal angle-resolving electron spectrometer for surface studies.* Applications of Surface Science, 1985. **22–23, Part 1**(0): p. 196-205.
3. Dupré, C., Lahmam-Bennani, A. and Duguet, A. *About some experimental aspects of double and triple coincidence techniques to study electron impact double ionizing processes.* Measurement Science and Technology, 1991. **2**(4): p. 327.
4. Opal, C.B., Beaty, E.C. and Peterson, W.K. *Tables of secondary-electron-production cross sections.* Atomic Data and Nuclear Data Tables, 1972. **4**(0): p. 209-253.
5. Duguet, A., et al., *A multidetection, multicoincidence spectrometer for (e,2e) and (e,3e) electron impact ionization measurements.* Review of Scientific Instruments, 1998. **69**(10): p. 3524-3536.
6. Lahmam-Bennani, A., et al., *High-energy electron impact spectrometer for absolute triple differential cross sections.* Review of Scientific Instruments, 1985. **56**(1): p. 43-51.
7. Toffoletto, F., Leckey, R.C.G. and Riley, J.D. *Design criteria for an angle resolved electron spectrometer of novel toroidal geometry.* Nuclear Instruments and Methods in Physics Research Section B: Beam Interactions with Materials and Atoms, 1985. **12**(2): p. 282-297.
8. Fraser, G.W., *The Electron Detection Efficiency of Microchannel Plates.* Nuclear Instruments & Methods in Physics Research, 1983. **206**(3): p. 445-449.
9. Duguet, A., et al., *High-accuracy (e, 2e) cross sections for helium: reference data in the first Born approximation.* Journal of Physics B: Atomic and Molecular Physics, 1987. **20**(22): p. 6145.
10. Boerboom, A.J.H., *Ion Trajectories and Imaging Aberrations in an Imperfectly Shaped Toroidal Energy Analyzer.* International Journal of Mass Spectrometry and Ion Processes, 1989. **93**(3): p. 267-282.
11. Naja, A., *étude expérimentale par impact électronique de l'ionisation simple et double d'atomes et de petites molécules*, in *Université Paris Sud XI*. 2008, Université Paris Sud XI. p. 114.
12. Catoire, F., *étude théorique et expérimentale de la double ionisation par impact électronique incluant l'effet Auger: Interférences d'échanges et de processus*, in *Université Paris Sud XI*. 2006, Université Paris Sud XI. p. 215.
13. Taouil, I., Thèse de doctorat, in *Université Paris Sud*. 2000, Université Paris Sud.
14. Lampton, M. and Carlson, C.W. *Low-distortion resistive anodes for two-dimensional position-sensitive MCP systems.* Review of Scientific Instruments, 1979. **50**(9): p. 1093-1097.
15. Bray, I., Fursa, D.V. and McCarthy, I.E. *Convergent close-coupling method for electron scattering on helium.* Journal of Physics B: Atomic, Molecular and Optical Physics, 1994. **27**(14): p. L421.

Chapter 3 *Coplanar asymmetric (e, 3-1e) measurements on He, Ne and Ar atoms: predominance of the second-order, two-step mechanism*

3.1 Introduction

The first (e, 3e) measurements of 5DCS and (e, 3-1e) measurements of 4DCS were performed on Ar by Lahmam-Bennani, et al [1] [2] in 1989 and 1991, respectively. Their results indicated good consistence with a Shake-off mechanism for the DI process, at the high incident energy (several keV) considered in these works. Soon later, in 1992, (e,3e) angular distributions from the DI of krypton have been measured at ~5.5 keV incident energy and at a variety of ejected energies. In those measurements, the angular distributions were detected both in θ_a-mode (where θ_a is varied while θ_{bc} is kept in constant) and in θ_b-mode (where θ_b is varied while θ_a and θ_c are fixed at θ_a = -1 °and θ_c = 104 ° (or 254 °), respectively) in [3] by Orsay group. It was found that the momentum transfer direction is no longer a symmetric axis, indicating the presence of non-first order features. Then El Marji, et al [4, 5] studied Ar and He by (e,3-1e) experiments in which only two of three outgoing electrons are detected in coincidence while the third one is undetected. In their work the observations provide clear indication for a Shake-Off mechanism being responsible of the double-ionization process at ~5.5 keV incident energy. Afterwards, similar (e, 3e) experiments were performed on Ar [6] (El Marji, et al.) and Ne [7] (Schröter, et al.), respectively. All of above (e, 3e) experiments are operated with two electrons in fixed direction, while the third one is variable. The real breakthrough came with the experiments published by Taouil, et al.[8] and Lahmam-Bennani, et al.[9] , where fully determined (e, 3e) experiments for DI of He were reported on an absolute scale. In that work, both the angles of two ejected electrons are variable in collision plane while only the scattered electron is detected at fixed angle (e.g., θ_a = 0.45 °±0.10 °, 20 °<θ_b<160 ° and 200 °<θ_c<340 °). Dorn et al also performed a series of (e, 2e+ion) experiments using so-called reaction microscope setup to investigate the mechanisms in DI of helium by fast electron impact [10-13].

Basically, all of these measurements have been carried out at a relatively high impact energy (~5.5 keV to ~1.1 keV) and a small momentum transfer to the target. Therefore the corresponding theoretical models by Lahmam-Bennani, et al. and other groups [14-17] have been designed in the spirit of the first Born approximation (FBA) for the projectile-target interaction. Most of these theoretical results have been obtained using He as a target since the residual ion is a pure positively charged particle without internal structure. This property of He leads to a simplified theoretical treatment. The calculations compared to experimental measurements have in common the following aspects. First, the absolute magnitude of the calculated cross sections was largely different from one calculation to another and from the experimental absolute data of Lahmam-Bennani et al [9, 14, 18]. Second, however, the qualitative features of the measured angular correlation patterns at various fixed ejection angles were reproduced by the theories. Third, the significant deviation of calculations from experimental data was partly attributed to the non-first Born effects which were not included in these first Born approximation models.

Such non-first Born effects are expected to be more important or even predominant in the experiments reported at intermediate incident energy (~600 eV) in electron impact DI process by Lahmam-Bennani, et al. [19, 20]. In [21] (Lahmam-Bennani, A., et al.), the great importance of second- or higher-order effects were observed in the projectile-target interaction on He and molecular hydrogen at intermediate incident energy of ~600 eV with a symmetric energy sharing among the two ejected electrons. At the same time, several (e,3e) experiments on Ar by Jia, et al.[22, 23] and He by Lahmam-Bennani, et al.[18] were reported, providing more evidence of second- or higher-order contribution in DI process. Simultaneously, new theoretical models including correlated wave function Bolognesi et al. [24], second Born approximation Elazzouzi, et al.[25] and post collision interaction (PCI) as well as all exchange effects Elazzouzi, et al.[26] were developed, which can better describe DI than the ones which only include first order term.

In the work performed by Götz et al [27] the 4-particle continuum (consisting of 3 electrons and the ion) was described by six coulomb wavefunctions (6C) which takes all 2-body interactions into account, and hence goes beyond the 2nd-Born approximation. Even then, this 6C treatment could not reproduce the previously published experimental results Lahmam-Bennani, et al.[21]. For this reason, Götz et al [27] questioned these results by saying 'we suggest that it is very important to establish the validity or otherwise of the asymmetry in the experimental data'. To definitely answer this questioning, Lahmam-Bennani et al measured the (e,3-1e) 4DCS for DI of helium in coplanar asymmetric geometry for a wide range of ejected electron energies and at an incident energy of about 600 eV (Lahmam-Bennani, et al.) [28]. The main features of the experimental data are large angular shifts of the forward and backward intensity distributions with respect to momentum transfer direction or its opposite. This validated the previous results Lahmam-Bennani, et al. [21] and proved a predominance of the second-order, two-step mechanism in the electron impact DI of He at intermediate impact energy. Meanwhile, Lahmam-Bennani et al developed a simple two-step-2 (TS2) kinematical analysis (a detailed description will be given later in this chapter) which can well explain the disagreement between experimental results and first order calculations. In this chapter, we aim to extend such (e,3-1e) study at intermediate incident energy to a wider range of ejected electron energies and very asymmetric energy sharing (Staicu Casagrande, et al.) [29]. Furthermore, we also extend it to more complex atomic targets (Li, et al.) [30] such as Ne, Ar rather than only He to get a general conclusion on the role of second order effects. The experimental results are compared with both first order and second order theoretical calculations.

3.2 Details of theory used for comparison

Before going further to show experimental results and discussion, the details of theory used for comparison in Chap. 3 will be introduced. Generally, DI theoretical models can be classified into two different groups, depending on the number of interactions between the incident electron and the target. In the following, we introduce first and second order theoretical models used for comparison.

3.2.1 First Born Approximation with Three Coulomb waves and First Born Approximation with Two Coulomb waves plus Gamow factor

The First Born Approximation Three Coulomb waves (FBA-3C or B1-3C in short) calculation uses the BBK (Brauner, Briggs, and Klar) [31] or 3C model where the final state, orthogonalized to the initial state, is described by the product of three Coulomb waves. Two of the three Coulomb functions describe each electron in the field of the residual ion and the third Coulomb function describes the interaction between the two emitted (slowest) electrons, i.e. takes into account the electron-electron correlation in the continuum. In this model, the initial and final states of the collision system are described by correlated wave functions. The target initial state is described by a wave function which only includes a part of the radial correlation (Dal Cappello, et al.) [32]. The incident and fast scattered electrons are described by plane wave functions. These calculations only include first order DI mechanisms, namely the SO [33] (in which Tweed showed that SO dominated in DI at about 5keV incident energy [33]) and TS1 [34] (developed by Carlson and Krause) (which plays a important role at about 1 keV incident energy [35, 36] (described by McGuire)). In this work He is taken as an example to describe the procedure of theoretical calculation. For other more complex targets, the initial and final state as well as interaction potential are different, but have same frame of calculation process as He. Furthermore, the multi-electron target problem can be reduced to a two-electron target by using the well-known frozen-core approximation. In this case, the two target outermost (or valence shell) electrons will be ejected during the double ionization process and the other electrons in the doubly charged ion core are assumed to remain unaffected by the ionization process Hda, et al. and Cooper, et al. [37, 38]. In all first order DI models for multi-electron targets rather than He, the interaction between residual doubly charged ion and two ejected electrons is not included in these models since a frozen-core approximation is used.

The following formulae description is developed by Joulakian et al [65] and Ancarani et al [66].

In DI process of He, the 5DCS is given by

$$\frac{d^5\sigma}{d\Omega_a d\Omega_b d\Omega_c d(k_b^2/2) d(k_c^2/2)} = \frac{(2\pi)^4 k_a k_b k_c}{k_0} \left|T_{fi}\right|^2 \tag{3.1}$$

where the Ω_i and the k_i (i=a,b and c) represent, respectively, the detection solid angles and the moduli of the different wave vectors. The conservation of energy imposes

$$\frac{k_0^2}{2} = I^{2+} + \frac{k_a^2}{2} + \frac{k_b^2}{2} + \frac{k_c^2}{2} \tag{3.2}$$

where I^{2+} represents the double ionization energy. T_{fi} represents the T-matrix element given by

$$T_{fi} = \langle \Psi_f^- | V | \Psi_i \rangle \tag{3.3}$$

where the integration runs over all space and spin coordinates. Ψ_f^- and Ψ_i represent the wave functions describing the whole system in its final and initial state respectively. V represents the interaction between the incident electron and the target:

$$V = -\frac{Z}{\vec{r_0}} + \frac{1}{\vec{r}_{0b}} + \frac{1}{\vec{r}_{0c}} \tag{3.4}$$

where $\vec{r}_{0b}$ and $\vec{r}_{0c}$ stands for the relative distance between incident and two ejected electrons. Z is the nuclear charge.

The initial state consists of the incident electron and two bound electrons. The incident electron will be described by a plan wave:

$$\frac{e^{i\vec{k}_0\cdot\vec{r}_0}}{(2\pi)^{3/2}} \tag{3.5}$$

where $\boldsymbol{r}_0$ stands for the position of the incident electron; The ground state of the two bound electrons will be given by a Hylleraas-type [39] solution of the form

$$\varphi_i(\vec{r}_b, \vec{r}_c) = N(e^{-ar_b}\, e^{-br_c} + e^{-br_b}\, e^{-ar_c})\left(1 + \sum_n C_n\, r_{bc}^n\, e^{-\lambda_n r_{bc}}\right) \tag{3.6}$$

where N is the normalization factor, and r_{bc} the electron-electron distance. The initial state can also be described by a Hartree-Fock wave function of Clementi and Roetti [40] for more complex targets than He, for instance Ne and Ar. Therefore the initial state of the system is taken to be

$$|\Psi_i >= |\frac{e^{i\vec{k}_b\cdot\vec{r}_0}}{(2\pi)^{3/2}}\varphi_i(\vec{r}_b\cdot\vec{r}_c)\rangle \tag{3.7}$$

In the final state, the scattered electron will be described by the same plane wave solution as in the initial state and the two ejected electrons by the BBK [31, 41] wave function in its general form:

$$\langle\Psi_f^-| = \langle\frac{e^{i\vec{k}_a\cdot\vec{r}_0}}{(2\pi)^{3/2}}\frac{1}{\sqrt{2}}\left(\varphi_f(\vec{r}_b, \vec{r}_c) + \varphi_f(\vec{r}_c, \vec{r}_b)\right)| \tag{3.8}$$

At the exception of the 6C model (Götz, et al.) [27] which rapidly reveals to be very tedious or even untraceable, the BBK or 3C model is actually the best treatment to describe the double continuum of the two ejected electrons in the field of an ion. But it is not easy to apply to complex targets rather than He because of the complexity of target. Therefore one may consider the approximate method where the third Coulomb wave function which describes the electron-electron correlation of the two ejected electrons is replaced by a simplified so-called Gamow factor, hence the name B1-2CG [37] for this approximation. With this Gamow factor, we lose the precise determination of the magnitude of the cross sections but we keep the repulsive factor which is sufficient to explain

the strong angular correlation in the final state. This approximation was checked by comparison with pure 3C model in (e, 3e) on He and the same angular distribution was found, the only noticeable differences being on the amplitude of the cross section [42].

3.2.2 Second Born approximation model and Second Born approximation with two Coulomb functions plus Gamow factor

Second Born approximation is similar to first Born but differs by taking into account second-order mechanisms, such as TS2. The initial state is described by a wave function which only includes a part of the radial correlation [32] and the final state is orthogonalized to the initial one. The well-known closure approximation [43] is used with a parameter corresponding to the average excitation energy fixed here to 79 eV for He case. This value corresponds to the energy of the initial state. The final state is described either by three Coulomb wave functions or by two Coulomb functions plus Gamow factor, hence the designations B2 model and B2-2CG model, respectively. For numerical reasons, these models can only be applied to light atoms such as atomic H [43] (Byron Jr, et al.) and He [32, 44] (Dal Cappello, et al. and Byron Jr , et al.) and to the simplest molecule H_2. The following formulae description is developed by Dal Cappello et al [32].

In the second Born approximation the 5DCS is given by

$$\sigma^{(5)} = \frac{d^5\sigma}{d\Omega_b d\Omega_c d\Omega_a dE_b dE_c} = \frac{k_a k_b k_c}{k_0} |f_{B1} + f_{B2}|^2 \tag{3.9}$$

where $d\Omega_a$, $d\Omega_b$ and $d\Omega_c$ represent the elements of solid angles for the scattered 'a' and the ejected electrons 'b' and 'c', respectively, whereas the energy intervals for the ejected electrons are represented by dE_a and dE_b.

The first Born term f_{B1} is given by

$$f_{B1} = -\frac{1}{2\pi} \langle \left(\exp(i\vec{k}_a \cdot \vec{r}_0)\right) \Psi_f^{\perp}(\vec{k}_b, \vec{r}_b, \vec{k}_c, \vec{r}_c) | V | \left(\exp(\vec{k}_0, \vec{r}_0) \Phi_i(\vec{r}_b, \vec{r}_c)\right) \rangle \tag{3.10}$$

where $\Phi_i(\vec{r}_b, \vec{r}_c)$ is the initial wave function of the target and $\Psi_f^{\perp}\left(\vec{k}_b, \vec{r}_b, \vec{k}_c, \vec{r}_c\right)$ is the final wave function of the system of two continuum electrons and ion which is orthogonalized to the initial state and $\vec{r}_0$, $\vec{r}_b$ and $\vec{r}_c$ represent the position of incident (or scattered), fast ejected and slow ejected electrons, respectively. The potential V stands for the Coulomb interaction between the incoming electron and the target electrons which is given by

$$V = \frac{1}{\vec{r}_{0b}} + \frac{1}{\vec{r}_{0c}} - \frac{2}{\vec{r}_0} \tag{3.11}$$

The initial state is represented by an accurate Hylleraas-type wave function given by Bonham and Kohl [45]. The final state wave function is the so-called approximate BBK wave function with the Gamow factor being used instead of the third Coulomb wave function [42] (Dal Cappello, C. and B. Joulakian), hence the more appropriate name 2CG.

This model includes the second Born term f_{B2} which describes a process where the incident electron interacts twice with target as is the case in the TS2 mechanism [35] (McGuire).

This term is given by

$$f_{B2} = \frac{2}{8\pi^4}\sum_n \int \frac{d\vec{q}}{q^2 - k_n^2 - i\varepsilon} \langle exp(\vec{k}_a \cdot \vec{r}_0)\, \Psi_f^{\perp}(\vec{k}_b, \vec{r}_b, \vec{k}_c, \vec{r}_c) | V | exp(i\vec{q} \cdot \vec{r}_0) \Phi_n(\vec{r}_b, \vec{r}_c) > \\ \langle exp(i\vec{q}_0 \cdot \vec{r}_0) \Phi_n(\vec{r}_b, \vec{r}_c) | V | exp(i\vec{k}_0 \cdot \vec{r}_0) \Phi_i(\vec{r}_b, \vec{r}_c) \rangle \quad (3.12)$$

where the summation over n means that all the contributions of the n discrete and continuum states of the target are taken into account.

The electron impact DI can be analyzed in terms of different mechanisms. Thus the theoretical calculation may describe the DI process by contributions from various reaction mechanisms to the 5DCS. However, from a theoretical perspective it is the inclusion of electron-electron correlations that makes the calculations difficult. Up to now there has been no calculation that includes these three mechanisms. In first order mechanisms (SO), the second electron is ejected through a rearrangement process in the target ion induced the change of the target Hamiltonian due to the ejection of the first electron. In second order mechanism (TS2), though the two target electrons probably being ejected independently from two successive incident-target interaction (here the electron-electron correlation does not play an essential role), the intermediate state in TS2 mechanism process obviously will increase the order of integration for calculation of 5DCS. This is really a challenge for theorist.

3.2.3 Two Step 2-Monte Carlo Event Generator

The two step 2-Monte Carlo Event Generator (TS2-MCEG) calculation is based on the first Born approximation (FBA), but second order contributions are included using the MCEG technique to simulate the TS2 mechanism by convoluting two successive SI events which are both calculated in the FBA. These are first a SI of the target by the incident electron followed by another SI of the resulting singly charged ion by the intermediate scattered electron. The final-state repulsion between the ejected electrons was accounted for by the Gamov factor.

The MCEG technique, well-known from elementary particle physics by Gieseke [46], is very powerful because it allows performing the convolution repeatedly and event-by-event. This method was firstly applied to ion impact DI by Fischer, et al. [47] in a context where it was claimed that the

observed discrepancies between experiments and model calculations are merely a result of the experimental resolution. Thereafter, the method was later extended to electron impact DI by Ciappina, et al. and Dürr, et al. [48, 49].

The TS2-MCEG simulation results were convoluted with the experimental resolution as described by Dürr et al [50] for ion impact ionization firstly. Then Ciappina et al [47] extended this technique to electron impact DI of He. The idea is to convolute twice of the single ionization (SI) events, which are both calculated by FBA model. The first SI step corresponds to the single ionization of the neutral helium atom by the incoming electron, while the second step is the ionization of the He^+ ion. For each ionization event the file contains momentum components which are required to fully determine the kinematics. This file thus represents a theoretical simulation of the events recorded during a measurement. From the simulated data, cross sections are extracted using the same analyzing procedure applied for the extraction of the real experimental spectra from the data. The experimental resolution can be modeled by adding random numbers to the individual momentum components of each generated event, which simulate the various experimental uncertainties. The random numbers follow a certain distribution, which is chosen according to the expected instrumental influence. This way the experimental error sources included in the simulation can be easily varied in order to systematically study their effect on the extracted cross sections.

The FDCS of each SI step is given by

$$\sigma_{SI,SI^+} = \frac{d^5\sigma}{dk d\, q_\perp} \propto \left|T_{if}^{FBA}\right|^2 \delta\left(E_f - E_i\right) \tag{3.13}$$

where we have ignored the constants because they cancel out during the normalization procedure required by the MCEG. Within the FBA, the transition amplitude $\left|T_{if}^{FBA}\right|$ can be written as

$$\left|T_{if}^{FBA}\right| = \left\langle \chi_f^- \middle| V_i \middle| \chi_i^+ \right\rangle \tag{3.14}$$

where the initial (final) wave χ_i^+ (χ_f^-) is an approximation to the initial (final) state which satisfies outgoing-wave (+) (incoming-wave (-)) boundary conditions. The perturbation potential V_i is the Coulomb interaction between the projectile electron and the active target electron.

Note that in all models described above we neglect the exchange effects between the incident electron and the ejected electrons because both the incident and the scattered electrons are faster than any ejected one.

3.3 Experimental conditions and calibration

The experiments described here were performed on the (e, 2e)/(e, 3e) spectrometer currently in use in Orsay. Its main characteristic is the unique combination of three high-efficiency, multi-angle toroidal electrostatic energy analyzers. A detailed description of the apparatus and energy and angular calibrations has been given in Chap. 2.

Due to the low coincidence rate, all three toroidal analyzers were operated at reduced energy resolution, $\Delta E_a \sim \pm 4.3$ eV and $\Delta E_c \pm 3.2$ eV. Hence the coincident energy resolution ΔE_{coin} is $\sim \pm 6.8$ eV. This value did not allow resolving the final ionic states of the targets. For argon, the ground state of the Ar^{2+} $3p^4$-ion final states is the ^3P ground state and the excited metastable states are $^1D_2$ and $^1S_0$, with excitation energies of 1.9 and 4.2 eV [22] (Jia, C.C., et al.); in Ne-$2s^2 2p^4$ case, the ground state is ^3P and the excited metastable states are ^1D and ^1S with excitation energy of 3.1 eV and 6.8 eV Kilin, V.A., et al. [51]. According to former works and theoretical calculation, the ground state of the final double ionic target in the present study gives the dominant contribution to the measured cross section [6, 22, 52-55] (El Marji, B., et al., Wiesemann, K.,et al. and Naja, A., et al.).

The experiments were performed in the coplanar asymmetric geometry. The collision plane is defined by the incident and scattered momentum vectors, $\boldsymbol{k_0}$ and $\boldsymbol{k_a}$. The zero degree is defined by incident direction. Throughout this work, positive angles are counted clockwise starting from incident beam direction. The fast scattered electron (indexed 'a') was detected at fixed energy E_a=500 eV and at two symmetric scattering angles, $\theta_a = +(6° \pm 3°)$ and $-(6° \pm 3°)$ as set by input slits at the entrance of the 'a'-toroidal analyzer. In the unequal energy sharing (UES) case, the two ejected electron shares differently the excess energy. The faster one (labeled 'b') among the two ejected electrons resulting from DI of the target is detected with energy E_b in coincidence with 'a'-electron, whereas the slower one, (labeled 'c') remains undetected, hence an (e, 3-1e) experiment. Of course in equal energy sharing case, where 'b' and 'c' have identical energies, such distinction does not hold, but the same labeling 'b' is kept for the detected electron. These 'b'-electrons are multi-angle analyzed in the double toroidal analyzer over the angular ranges θ_b=20°-160° and 200°-340°. In the off-line analysis, the total θ_b angular range is divided into sectors of width $\Delta\theta_b$=5°. Although the emission direction of the third 'c' electron is unknown, its kinetic energy E_c can be derived from energy conservation: $E_c = E_0 - E_a - E_b - IP^{2+}$, where IP^{2+} is the double ionization potential of the target, leaving the ion in its ground state (the DI process leading to the ground state largely dominates over excited ion states Van der Wiel, et al. [56], when removing two outermost orbital electrons). The translational energy of the target atom and the recoil energy transferred to the ion are here neglected, due to the small electron to ion mass ratio.

The experiments were performed at a variety of ejected electron energies ranging from 12 to 144 eV and corresponding either to an equal (E_b=E_c) or unequal (E_b>E_c) energy sharing among ejected 'b' and 'c' electrons. The energy of detected 'b'-electron is varied while the undetected 'c'-electron has a constant energy at E_c=12 eV. The energy loss (E_0-E_a) suffered by the projectile varies from 67 to 235 eV. The incident energy is consequently adjusted to fulfill the energy conservation requirement for the different targets, with IP^{2+}=79.0, 62.6 and 43.0 eV for He, Ne and Ar, respectively. The investigated kinematical conditions are summarized in Tab. 3.1.

The momentum transfer from the projectile to the target, defined by $\vec{K}=\vec{k}_0-\vec{k}_a$, varies in magnitude from K=0.88 au at E_b+E_c=24 eV to K=1.46 au at E_b+E_c=156 eV, while its direction θ_K varies from ~46 ° to ~26 ° for these two extreme cases. Simultaneously, due to the quite large acceptance in θ_a angle, $\Delta\theta_a$=±3°, the momentum transfer resolution amounts to ΔK~±0.2 au and the uncertainty in the momentum transfer direction is $\Delta\theta_K$ ~ ±10 °.

To validate the calibration of the apparatus, (e, 2e) experiments for SI of the He 1s orbital are performed with the same E_a and E_b values as those used in the (e,3-1e) experiments. The method of calibration is described in chapter 2, see §2.8.3.

3.4 (e, 3-1e) results and discussion

The angular distributions of the (e,3-1e) 4DCS $d^4\sigma/dE_a dE_b d\Omega_a d\Omega_b$, for DI of He, Ne and Ar are shown in Figs 3.1 to 3.6. The kinematical parameters considered in this study are listed in Tab. 3.1. To summarize, the (e, 3-1e) 4DCS measurement for He with energy sharing (E_b:E_c) = (72:12) eV and (144:12) eV, for Ne and Ar with energy sharing (E_b:E_c) = (12:12) eV, (72:12) eV and (144:12) eV are performed, respectively. The experimental results in Figs. 3.1(a)-(b), Fig. 3.2(c) and Fig. 3.3(f) have been previously published by Lahmam-Bennani, A., et al [28]. The other cases are the new results. For completeness of the discussion, we represent these former results, in which the two ejected electrons have unequal energy sharing. The 4DCS scale shown is arbitrary, where all experimental and theoretical results are inter-normalised for best visual fit at the maximum of the forward lobe.

$E_a = 500\ eV \qquad \theta_a = -6\ deg$

Target	*Case*	E_0 *(eV)*	E_b *(eV) detected*	E_b *(eV) (undetected)*	K *(au)*	θ_K / θ_{-K} *(deg)*	$\theta_{F\text{-}TS2} / \theta_{B\text{-}TS2}$ *(deg)*	$\theta_{-K(F\text{-}TS2)} / \theta_{-K(B\text{-}TS2)}$
He	a*	601	17	5	0.88	46 / 226	82 / 290	262/110
	b*	621	37	5	0.96	41/221	79/297	259/117
	c*	658	74	5	1.12	34/214	74/297	254/117
	d	663	72	12	1.14	34/214	76/300	256/120
	e	735	144	12	1.46	26/206	67/315	247/135
	f*	613	17	17	0.93	43/223	84/282	264/102
Ne	a	586.6	12	12	0.77	50 / 230	86 / 280	266/100
	b	646.6	72	12	1.07	36 / 216	77 / 299	257/119
	c	718.6	144	12	1.39	27 / 207	67 / 315	247/135
Ar	a	567.2	12	12	0.76	56 / 236	86 / 278	266/98
	b	627.2	72	12	0.99	40 / 220	77 / 301	257/121
	c	699.2	144	12	1.30	29 / 209	67 / 318	247/138

Table 3.1 *Kinematical parameters studied in this work. Experimental data for the cases indicated with the superscript * have been published in [101]. The eighth column indicates the forward and backward directions of ejection of the 'b'-electron ($\theta_{F\text{-}TS2}$ and $\theta_{B\text{-}TS2}$, respectively) as predicted by our kinematical model, the ninth column indicates the recoil contribution prediction ($\theta_{-K(F\text{-}TS2)}$ and $\theta_{-K(B\text{-}TS)}$, respectively) in second SI step of TS2 kinematical analysis, see text.*

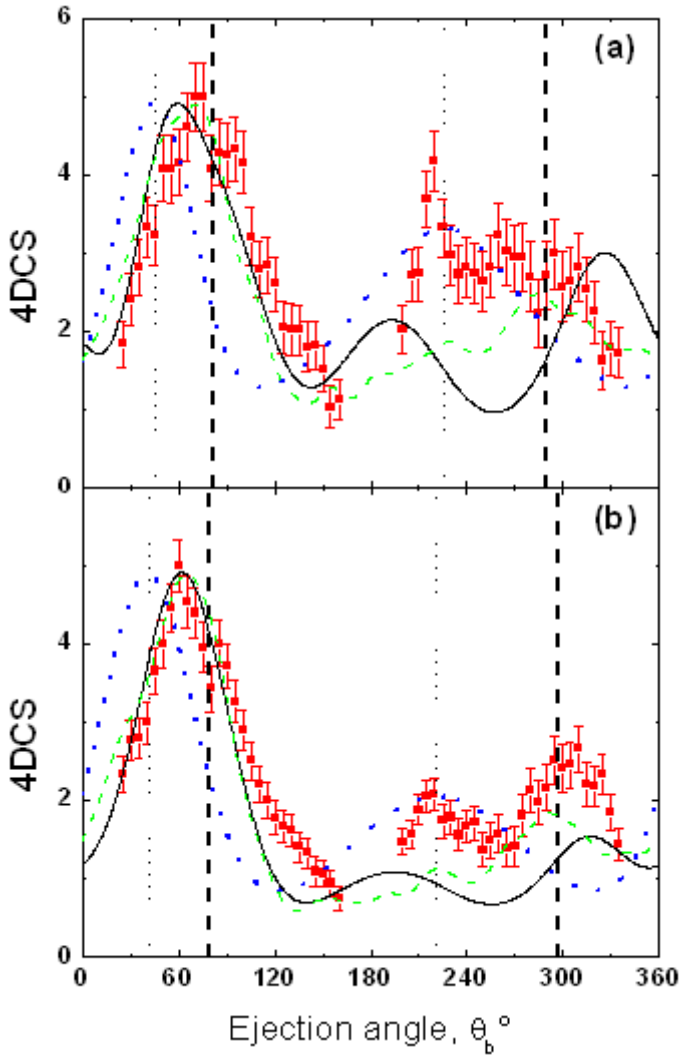

Figure 3.1 *Relative four-fold differential cross sections (4DCS) for double ionisation of He. The scattered electron with energy E_a = 500 eV is detected at an angle θ_a = – 6 °in coincidence with the fast-emitted electron with energy E_b, whereas the slow-emitted electron with energy E_c remains undetected. Panel (a): (E_b:E_c)= (17:5) eV, (b): (E_b:E_c)= (37:5) eV. Full squares are the experimental data, with one standard deviation statistical error bar. Theoretical models' predictions are from: first-order FBA-3C (dotted blue curves), TS2-MCEG (dashed green curves) and second-order B2 (full black curves). The 4DCS scale shown is arbitrary, where all experimental and theoretical results are arbitrarily inter-normalised for best visual fit at the maximum of the forward lobe. The thin dotted vertical lines indicate the direction of the momentum transfer (θ_K) and its opposite (θ_{-K}). The heavy dashed vertical lines indicate the directions of ejection of the 'b'-electron, ($\theta_{F\text{-}TS2}$ and $\theta_{B\text{-}TS2}$) as predicted by the given TS2 kinematical analysis, see text.*

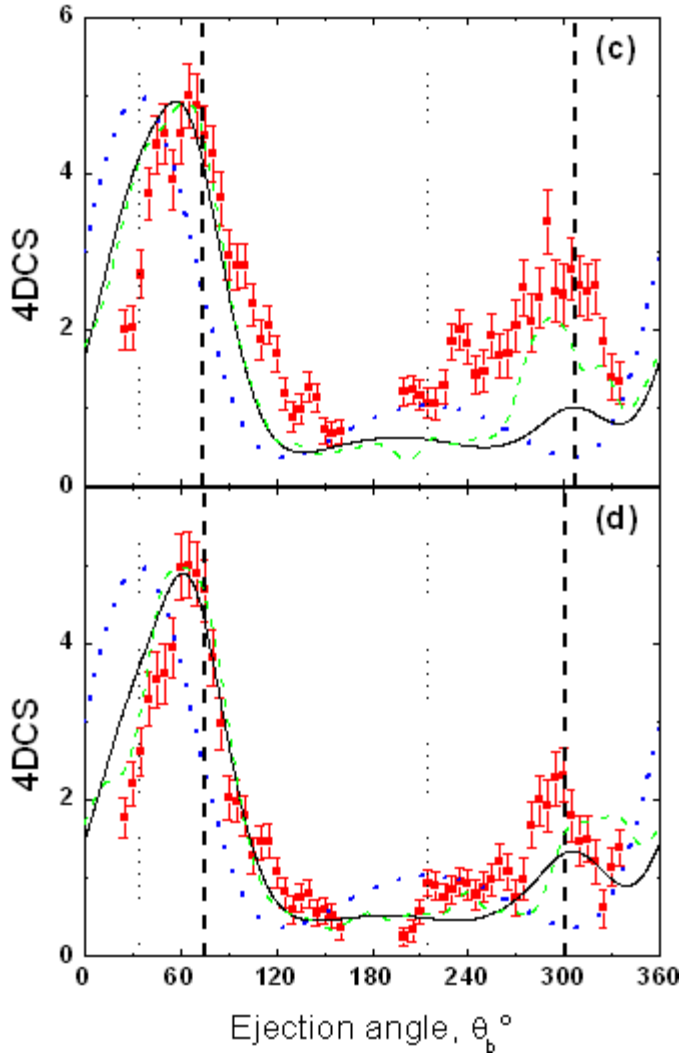

Figure 3.2 *The same as Fig. 3.1 but for panel (c): (E_b:E_c)= (74:5) eV, (d): (E_b:E_c)= (72:12) eV.*

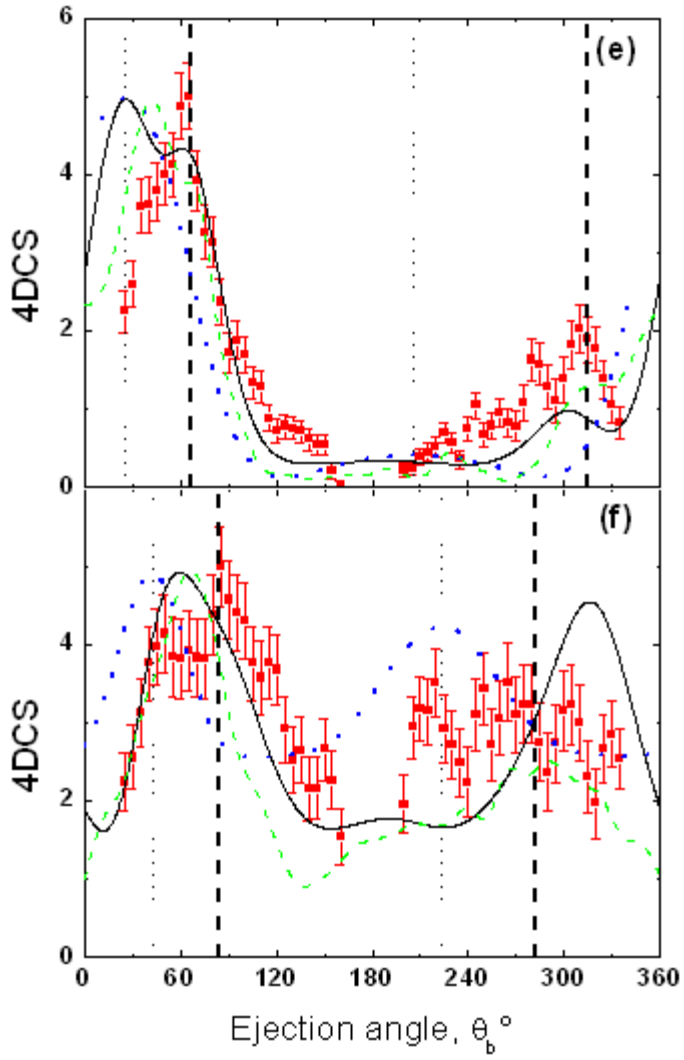

Figure 3.3 *The same as Fig. 3.1 but for panel (e): (E_b:E_c)= (144:12) eV and (f): (E_b:E_c)= (17:17) eV.*

3.4.1 General observation and comparison with theoretical calculation

First of all, we emphasize here that the agreement between our experimental data and theoretical models refers mainly to the position of the peaks, the shape of the 4DCS and the backward-to-forward peak ratio at the maximum of the two peaks, since the experimental data are given on a relative scale.

A. (e, 3-1e) results discussion of He

The experimental (e,3-1e) measurements show the 4DCS $d^4\sigma/dE_a dE_b d\Omega_a d\Omega_b$ for electron impact DI of He at (E_b:E_c) = (a): (17:5) eV, (b): (37:5) eV, (c) (74:5) eV, (d): (72:12) eV, (e): (144:12) eV and (f): (17:17) eV in Figs. 3.1 to 3.3, respectively. Our data are compared with the calculated results using FBA-3C or BBK model (which is based on first order mechanisms such as SO and TS1), TS2-MCEG and B2 models (which include second order mechanism such as TS2). Details of these models have been given in §3.2. The full squares are experimental data while FBA-3C, TS2-MCEG and B2 calculations are represented by dotted blue, dashed green and full black curves, respectively in Figs. 3.1-3.3. Since the experimental cross sections are obtained on a relative scale, both experimental data and theoretical calculations are normalized to an arbitrary value of 5 at the maximum intensity of the angular distribution.

All the experimental as well as theoretical distributions of the 4DCS show a two-lobe structure: a forward lobe pointing roughly in the momentum transfer direction ($+\vec{K}$) and a backward lobe roughly pointing in the opposite direction ($-\vec{K}$). These two directions are indicated by the vertical thin dotted lines in Figs 3.1 to 3.3.

However, a significant disagreement is observed between this first-order theory and experiments for all energy sharing considered in Figs. 3.1 to 3.3. The most distinct differences are:

(i) The breaking of symmetry about $\pm\vec{K}$ directions in the measured distributions whereas the FBA-3C calculations do show such symmetry

(ii) The large shift in the angular position of the experimental lobes, ~30 ° to 70 ° with respect to $\theta_{\pm K}$. The uncertainty in the momentum transfer direction due to angular resolution in θ_a is ~10 °, that is significantly smaller than the observed shift, and hence it only marginally affects this shift.

(iii) The existence of structures in the forward and backward lobes, for instance, in Figs. 3.1(a) and 3.1(b) at ~ 300 °, in Figs. 3.2(c) and 3.2(d) at ~ 300 °, in Figs. 3.3(e) at ~315 ° and 3.3(f) at ~270 °, new structures far away from $\pm\vec{K}$ directions lobes are observed.

These differences clearly indicate the presence of significant non-first Born effects in (e, 3-1e) 4DCS distributions for He under the present kinematical conditions. As predicted by McGuire [35] the TS2 mechanism contribution to DI process is significantly important with respect to SO

mechanisms at intermediate impact energy (see Fig. 3.6). In [35], the DI of helium impacted by proton at high projectile velocities, v, is considered in terms of two mechanisms: SO and TS. The observed energy dependence of the cross section for the double ionization of helium near $v \sim 10v_B$ (where v_B is the Bohr velocity, $10v_B$ corresponds to ~1keV for proton) and observed differences in this cross section for ionization by proton and electron impact have been explained in terms of a combination of amplitudes for SO mechanism and TS mechanism. At low incident energy, TS mechanisms are more important than SO since TS contribution increases very fast as the incident

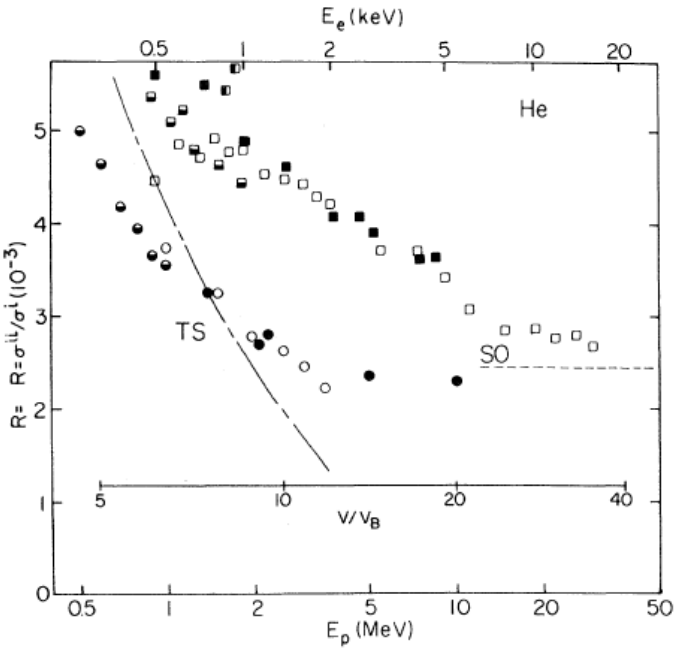

Figuer 3.6 *Taken from Ref. [11]. Ratio, R, of double- to single-ionization cross sections in helium vs projectile (proton) velocity (in units of $v_B=2.2\times10^9$ cm/sec).The closed circles, open circles and half-open circles represent the experimental data by proton impact,respectively, corresponding to the below two energy scales. The open squares, closed squares, squares devided into horizontal halves and squares devided into vertical havles represent the experimental data by electron impact, respectively, corresponding to above energy scale. The curve TS denotes the $(v^2 \ln v)^{-1}$ velocity dependence of the two-step mechanism, and curve SO represents the constant velocity dependence of the shake off (SO) mechanism. Amplitudes for these mechanisms interfere [48].*

energy decreases, whereas SO contribution is independent of the incident energy. These observations are also consistent with former studies by Lahmam-Bennani, et al. in [21] and [28]. In [21], Lahmam-Bennani et al performed coplanar (e, 3-1e) experiments on DI of helium and molecular hydrogen at about 600 eV incident energy with asymmetric energy sharing among the two ejected electrons. The results showed two important observations: first, the symmetry about $\pm\vec{K}$ is broken; and second, a large shift in the angular position of the lobes, ~40 °-60 ° are observed. In [28], the (e, 3-1e) 4DCS are measured for the DI of helium under same experimental condition, in addition of more different energy sharing among the two ejected electrons. Similar results are observed in [28]. In addition, some new structures appear in 4DCS angular distribution rather than classical 'two lobes' structure

predicted by first order theory. These are clearly the evidences of non-first-order effects in DI by electron impact. Hence, Lahmam-Bennani et al developed a TS2 kinematical analysis based on TS2 DI mechanism and was successfully used for explaining the DI experimental results recently in the group of Lahmam-Bennani, et al.[19, 20, 28-30].

Having noted the failure of FBA-3C calculation, we proceed further by comparing our measured 4DCS distributions with the calculated results obtained using two newly developed theoretical models. Details of these models have been given in §3.1. Briefly, the first model is based on the first Born approximation, but higher order effects are incorporated using the Monte Carlo event generator (MCEG) technique [48] (Ciappina, M.F., et al.) to simulate the TS2 mechanism by convoluting two SI events which are both calculated in the FBA. This means that in the first SI of He, the incident electron impact results in one intermediate scattered electron, one slower ejected electron and the He^+ ion, whereas in the second SI of He^+ ion, the intermediate scattered electron impact results in one scattered, one faster ejected electron and the He^{2+} ion. Note that the basic idea of these two steps 'decomposition' is the same here as that of the kinematical model considered in the following paragraphs.

The second theoretical model is more elaborate as it makes use of the second Born approximation and the closure approximation in the way described by Dal Cappello, et al. [32]. In this model, the final state is described by the approximate BBK or 3C wave functions where two of the three coulomb wave functions describe the two ejected electrons and the third one describes the interaction between these two ejected electrons.

The calculated results of these two models (TS2-MCEG and B2) are displayed in Figs. 3.1 to 3.3 by dashed green and solid black curves, respectively. The main general observation is the overall improved agreement with experiments, as compared with FBA-3C results discussed above. Although both theories yield some differences in their results, they both predict correctly the large angular shift of both forward and backward lobes to larger angular direction with respect to $\pm\vec{K}$ and also have additional structures, especially in the backward region, similar to the behaviour found in the experimental data.

B. Discussion of Ne and Ar (e, 3-1e) results

Figs. 3.4 to 3.5 show the experimental (e,3-1e) measurements of the 4DCS $d^4\sigma/dE_a dE_b d\Omega_a d\Omega_b$ for electron impact DI of *Ne* and *Ar* at (a): (E_b:E_c) = (12:12) eV, (b): (72:12) eV, (c): (144:12) eV, respectively. There is no theoretical TS2-MCEG calculation up to date for Ne and Ar under considered kinematical conditions due to the complexity of the target with respect to He. Therefore, we only have B1-3C calculation of Ne. Instead of B1-3C and B2 models, we compared our experimental results for Ar target to B1-2CG and B2-2CG models, which have two coulomb wave

functions representing two ejected electrons and in which the correlation between them is described by a simplified Gamow factor rather than a third coulomb wave function (see details in §3.1.2).

The discussion and conclusions of He hold for Ne and Ar cases. Compared to He, the ejected electron angular distributions exhibit similar features, that is, large shifts from the momentum transfer axis as well as marked structures in the forward and backward lobes. To better understand the origin of these features, the experimental data are compared with the calculated results obtained for Ne using the first Born-three Coulomb waves (B1-3C) model and B1-2CG model (see details in §3.1.2.1). However, due to the very long computational time needed for the full B1-3C model, it was decided to perform only B1-2CG calculation for the Ar case. For both Ne and Ar targets, the theoretical models B1-2CG and B2-2CG have included the contributions of the three residual states, namely ^{3}P, ^{1}D and ^{1}S. Both these B1 calculations are shown as dashed curves (B1-3C) and dotted curves (B1-2CG) in Figs. 3.4 to 3.5. I recall here that they only include first-order DI mechanisms, namely the SO and TS1. To account for the second-order TS2 mechanism, calculations were also performed for Ne and Ar within the framework of the second Born approximation where the final state is described by the approximate 2CG wavefunction. Here again, the use of the full 3C wave function with the second Born approximation needs much computer time especially for (e, 3-1e). The B2-2CG results are shown as full curves in Figs. 3.4 to 3.5. Note that the experimental data are relative differential cross section. Hence in all result presentations, both experimental and theoretical results are normalized to the maximum of the forward lobe with an arbitrary scale.

Strong disagreement is found between first Born calculations and experiments for Ne and Ar, the disagreement being appreciably more pronounced than was observed for He [28, 29] (Lahmam-Bennani, et al. and Staicu Casagrande, et al.). Indeed, for both atomic targets the B1-3C and B1-2CG models yield forward and backward angular distributions which are symmetrically distributed about the $\pm\boldsymbol{K}$ directions which are not observed in the experiments. Moreover, the predicted backward intensity by B1-3C and B1-2CG is much smaller than the experimental results (relative to the forward one). This feature is a clear evidence that strong non-first Born effects are present in the (e, 3-1e) 4DCS distributions. In other words, the contribution of the TS2 or higher order mechanisms to the DI process is sufficiently important with respect to that of SO and/or TS1 to impose its fingerprint on the angular distributions. We thus confirm the observations made for He in [28,29] (Lahmam-Bennani, et al. and Staicu Casagrande, et al.). However, the qualitative success of the second Born B2-2CG model reported for He is far from being found here again in the Ne and Ar cases. Indeed, when compared to B1-2CG predictions, the B2-2CG model does yield a breaking of symmetry with respect to $\pm\boldsymbol{K}$ directions (at least in Figs 3.4(a) and 3.5(b)) as seen in the experiments. But, if we despite the magnitude difference of the differential cross section (absolute quantity given by the models), the small difference in the shape of the angular distributions is not sufficient to bring the B2-2CG results

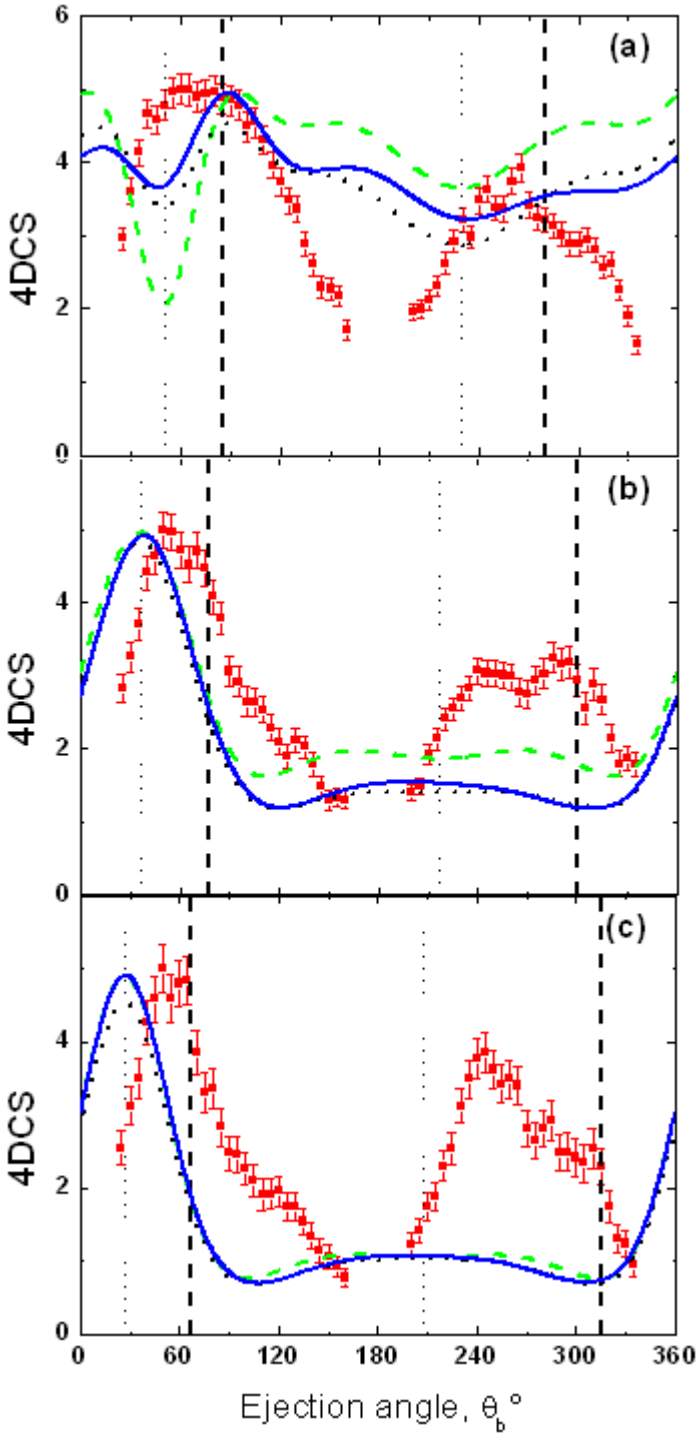

Figure 3.4 *Relative four-fold differential cross sections (4DCS) for double ionisation of Ne ($2p^{-2}$). The scattered electron with energy E_a = 500 eV is detected at an angle θ_a = – 6 °in coincidence with the fast-emitted electron with energy E_b, whereas the slow-emitted electron with energy E_c remains undetected. Panel (a): (E_b:E_c)= (12:12) eV, (b): (E_b:E_c)= (72:12) eV, (c): (E_b:E_c)= (144:12) eV . Full squares are the experimental data, with one standard deviation statistical error bar. Theoretical models' predictions are from: first-order FBA-3C or B1-3C (dashed green curve), B1-2CG (dotted black curve) and second Born B2-2CG models (full blue curve). The 4DCS scale shown is arbitrary, where all experimental and theoretical results are inter-normalised for best visual fit at the maximum of the forward lobe. The thin dotted vertical lines indicate the direction of the momentum transfer (θ_K) and its opposite (θ_{-K}). The heavy dashed vertical lines indicate the directions of ejection of the 'b'-electron, ($\theta_{F\text{-}TS2}$ and $\theta_{B\text{-}TS2}$) as predicted by the given TS2 kinematical analysis, see text.*

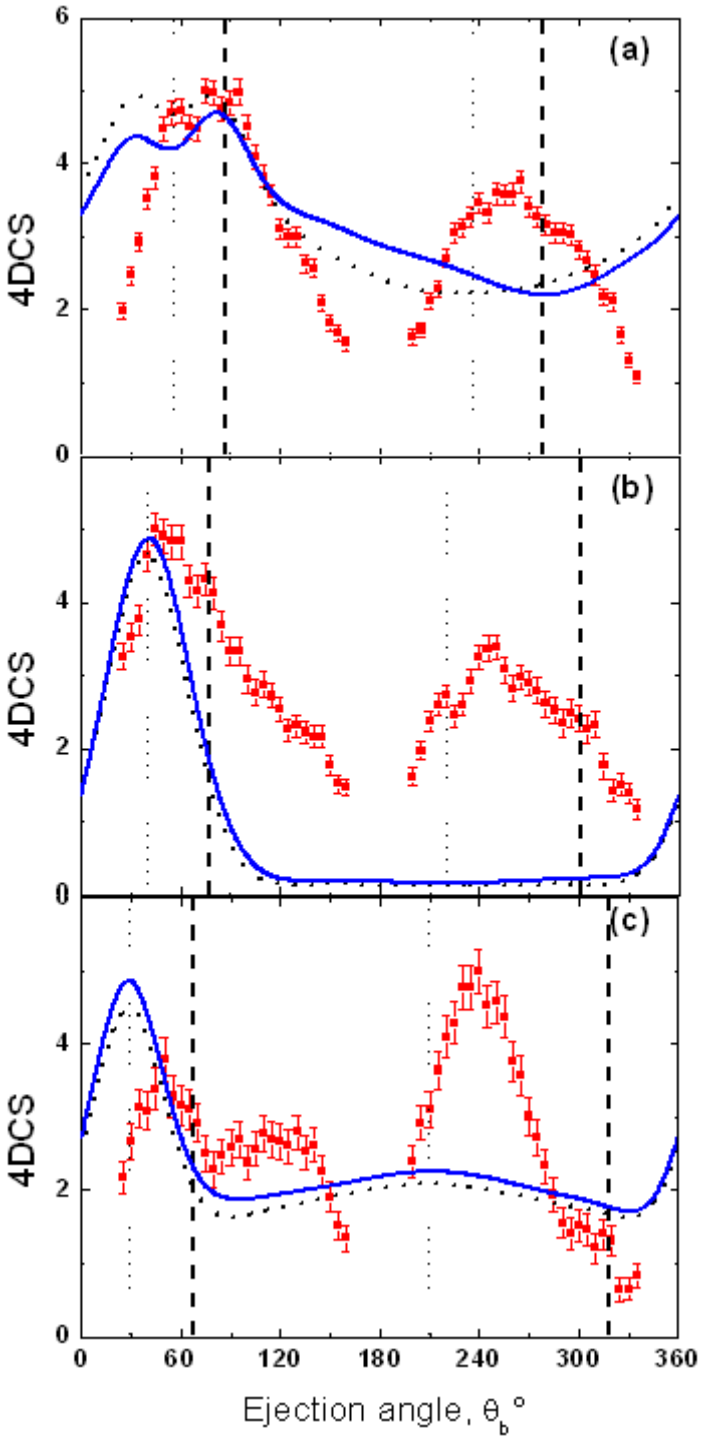

Figure 3.5 *The same as in Fig. 3.4 but for DI of Ar ($3p^{-2}$). For Ar, the B1-3C calculation is absent.*

significantly in better agreement with experiments than B1-2CG. The disagreement between our B2-2CG and experiments here is certainly due to the approximations made for treating the DI of a noble gas. In this case, we reduce the problem of a 6-electron target $(np)^6$ to that of two active electrons (the two ejected electrons) [57]. Moreover, Dal Cappello *et al* [57] have shown that the closure approximation used in the B2 model yields results which strongly depend on the value of the parameter $\bar{\omega}$ used, where $\bar{\omega}$ is the average excitation energy. We note that here we used the same kinematical parameters for the cases of the DI of noble gases as for helium.

3.4.2 Two-Step 2 kinematical analysis

Lahmam-Bennani et al [28] developed a kinematical analysis based on TS2 mechanism, which treats TS2 DI process as two successive (e, 2e)-like events. This simple kinematical analysis reveals the features of second Born effects and gives reasonable prediction of the lobes' position which are (as noticed above) noticeably distinct from $\pm\boldsymbol{K}$ direction. Since we use this method for analysis all (e, 3-1e) experimental results, in the following section, a detailed description about this kinematical analysis method is given by taking Fig. 3.3 (e) as example.

For the simplicity of the presentation, we first ignore the recoil contribution in first SI step. However, we will see that it is needed to include the recoil contribution in order to explain most of the observed structures.

A. Including only the binary contribution

The experimental parameters in this case (Fig. 2.3(e), He) are as follows: E_0=735 eV, E_a=500 eV, E_b=144 eV E_c=12 eV, θ_a = -6 °, IP^+=24.6 eV, IP^{2+}=79 eV.

In the first step (sketched in the top panel of figure 7) the slowest c-electron (E_c=12 eV) is ejected in an (e, 2e)-like process where the relevant scattered electron a* has the energy $E_{a^*}=E_0-E_c-IP^+$=735-12-24.6=698.4 (eV) with highest probability to appear at the Compton scattering angle, $\pm\theta_{a^*}$, corresponding to Bethe ridge condition: $E_0-E_{a^*}=E_0\sin^2(\theta_{a^*})$. For the given kinematics, θ_{a^*} is ~ ±13 °. The ± sign stands for the fact that the scattered a*-electron has two possibilities to appear both at positive or negative direction. The associated c-electron is most likely to be ejected at the corresponding momentum transfer direction, that is θ_{K^*} ~ ±77 °with respect to incident direction.

In the second step of TS2, a*-electron plays the role of an incident electron in a second (e, 2e) ionization of the target, where the scattered a-electron with E_a=500 eV and θ_a= -6 °and fast ejected b-electron with energy E_b = 144 eV are detected effectively. The b-electron is also most likely to be ejected at the momentum transfer direction but with respect to a*-electron's direction. Hence, depending upon whether the intermediate a*-electron is scattered at θ_{a^*} ~ –13 °or +13 °, two scenarios

may occur, which are sketched in Fig. 3.7 on top and bottom panels, respectively. In both scenarios, the scattered a-electron is detected at -6 °.

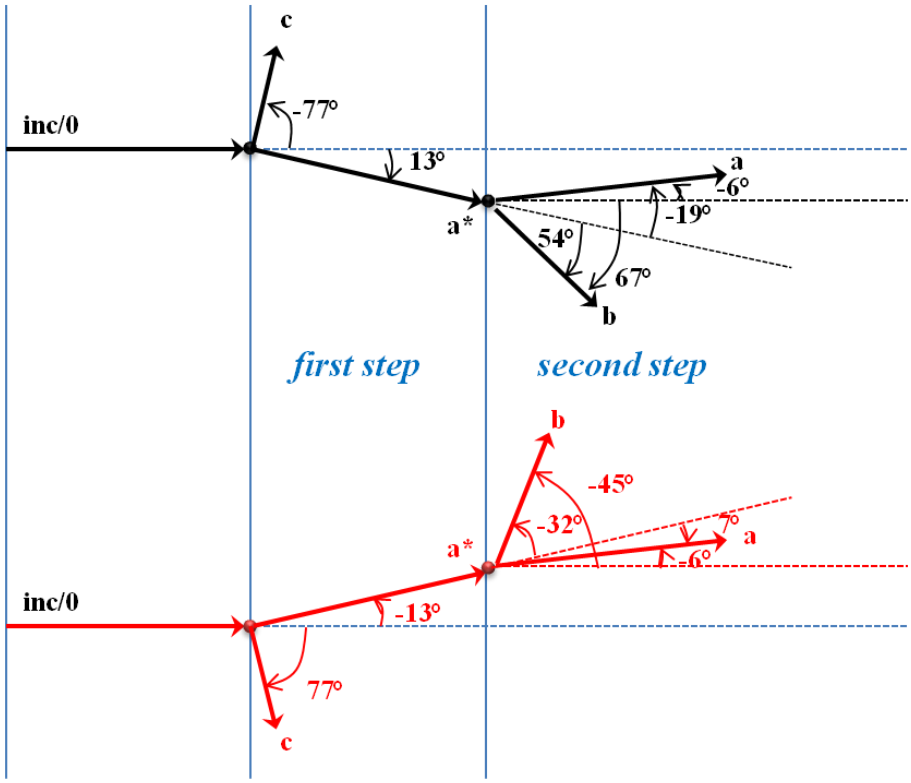

Figure 3.7 *Sketch of the kinematics of a two step 2 (TS2) process, in the case of (E_b:E_c) = (144:12) eV of He. Top panel displays the procedure for the case where the intermediate a* electron is scattered at a positive θ_{a^*} angle while the bottom panel for the case of intermediate a* electron being scattered at a negative θ_{a^*} angle. The positive angles are counted clockwise from the incident direction. See details in the text.*

(1) In scenario 1 (top panel in Fig. 3.7), θ_{a^*} is ~ +13 ° with respect to incident direction, hence it will be scattered at ~ -19 ° in second SI step to satisfy the experimental requirement that a-electron is detected at -6 °. While the b-electron in second step is essentially ejected from the target via a binary collision and appears in the momentum transfer direction, which is $\theta_{K'}$ ~ +54 ° but with respect to a*-incident direction. So the b-ejected electron is expected to appear at θ_b ~ +(54+13) ° = +67 °, which is labelled $\theta_{F\text{-}TS2}$ in Tab. 3.1(eighth column) and displayed by vertical thick dashed lines in Fig. 3.3(e). This value is far away from momentum transfer direction θ_K ~27 ° where the maximum position of forward lobe is predicted by first order mechanisms SO and TS1. However, the experimental results indicate a lobe position at ~65 ° which is in good agreement with this TS2 kinematical prediction. Thus we conclude that the shift of the forward lobe is largely due to TS2 contribution according to this scenario 1. However, the contributions

of SO and TS1 of course exist but they are of marginal importance with respect to TS2 contribution.

(2) The scenario 2 (bottom panel in Fig.3.7 is similar to scenario 1 except that the intermediate a* electron is scattered at $\theta_{a*} \sim -13°$ with respect to incident direction thus the a-scattered electron will appear at $\sim -7°$ from the intermediate a*-electron direction for the same reason described in scenario 1. While the associated b-electron in second step is most likely ejected in the momentum transfer direction from a*-electron direction, which is $\theta_{K'} \sim -32°$. So the b-ejected electron is expected to appear at $\theta_b \sim -(32+13)° = -45°$, or alternatively at $\theta_b \sim 360° - 45° = 315°$ from the primary incident direction. This θ_b - angle is labelled $\theta_{B\text{-}TS2}$ in Tab. 3.1 and is displayed by vertical thick dashed line in Fig. 3.3(e). The experimental results show a lobe located almost at the same position of 315°, which is in very good agreement with TS2 prediction while it is far away from opposite momentum transfer direction $-\boldsymbol{K}$, $\theta_K \sim 207°$, where the first-order SO and TS1 contributions should be at their maximum. This confirms the conclusion in scenario 1 once again that SO and TS1 contributions are much smaller than TS2 at present kinematical conditions.

The conclusions drawn above from the combination of scenarios 1 and 2 hold for all energy sharing considered in this work (see Tab. 3.1and Figs 3.1 to 3.5), from equal (Fig.s 3.3(f), 3.4(a) and 3.5(a)) to highly unequal (Figs. 3.3(e), 3.4(c) and 3.5(c)) sharing. The comparison is reasonable not only for He but also for the other targets considered here. However, there are some differences for different targets. For instance, the intensity of the backward lobes of Ne and Ar is much higher than He.

To summarize, the forward and backward structures' positions in Figs. 3.1 to 3.5 are strongly influenced or even dominated by the TS2 contribution, according to the above kinematical TS2 analysis while the first order SO and TS1 contributions are less important than that of TS2 in present study.

Note that in all above discussion about TS-2 kinematical analysis, we only consider the binary collision effect in two successive (e, 2e)-like processes in which the electrons are ejected at momentum transfer direction (relative to incident and intermediate incident direction) in each step. The recoil contribution in these (e, 2e)-like processes, where the ejected electron goes at opposite direction of momentum transfer (see Fig. 3.8), is completely ignored.

B. Including both binary and recoil contributions

To move a step forward, we decided to incorporate the recoil contributions in this TS2 kinematical model by considering that in the two successive (e, 2e)-like processes, rather than being ejected with highest possibility in the two momentum transfer directions, θ_{K*} and $\theta_{K'}$ in first step and second step

for both cases of $\pm\theta_{a^*}$, alternatively, the ejected electron also has the possibility of being emitted in the directions opposite to momentum transfers in each step, θ_{K^*} and $\theta_{K'}$.

The recoil contribution is incorporated into TS2 kinematical analysis for the following reasons:

First, the recoil lobe in (e, 2e) studies is generally interpreted as due to a three-body interaction electron-electron-ion where the ejected electron is elastically reflected backwards in the target potential well before being emitted [55, 58-62], hence named recoil lobe. The enhanced magnitude of the recoil peak is generally assigned to a strong interaction of the ejected electron with the residual ion [59, 63]. It is well known from previous (e, 2e) studies [55, 60, 62] that the intensity ratio of recoil to binary lobe is generally small for helium (typically less than 10%) in the impact energy regime relevant for this work, E_0 ~ 500 – 700 eV, except in the limit of small ejected electron energies, say below ~ 10 eV, where the magnitude of the recoil lobe progressively becomes comparable to that of the binary one (or even higher in the case of more complex targets).

Second, some of the measured 4DCSs for the three atomic targets considered here (He, Ne and Ar) exhibit puzzling multi-lobe structure which cannot be explained neither by first order and second order theoretical calculations, nor by the TS2 kinematical analysis proposed above. These are, for instance, the forward lobe in Figs. 3.4(b) and 3.5(c) or else the backward lobes in Figs. 3.2(c)-(d), 3.3(e), 3.4(b)-(c), 3.5(a)-(b)-(c), etc. Hence, it strongly encourages us to take into account the recoil contributions in the TS2 kinematical analysis model as first step to attempt to figure out the origin of those structures from the given predictions including recoil contribution rather than just considering binary part.

Third, in the cases depicted in Figs. 3.3(f), 3.4(a) and 3.5(a), the two ionized electrons share equally the energy and hence are fully undistinguishable: one neither knows which one is emitted first and which is emitted in the second step, nor which one is detected and which one is undetected. This results are in two additional emission angles for the detected electron, which are located along the intermediate momentum transfer direction $\vec{K}^*$ and its opposite direction $-\vec{K}^*$ of the first SI (e,2e) collision.

Based on the above considerations, we extend here the TS2 kinematical analysis by including the recoil contribution in the second step of (e, 2e)-like process for unequal energy sharing cases and in both first and second steps of (e, 2e)-like process for equal energy sharing cases between the two ejected electrons. Note that as stated above, for equal energy sharing cases, the TS2 kinematical analysis will give four more angular positions than unequal energy sharing cases.

Here we take Ne (Fig. 3.4(b)) with (E_b:E_c)=(72:12) eV as an example to explain the recoil contribution in TS2 kinematical model. The conclusion is generally holds for all other cases.

This is an unequal energy sharing case, so we only take into account the recoil contribution in the second SI (e,2e)-like step because whether the first ejected electron is emitted in the momentum transfer direction $+\boldsymbol{K}^*$ (binary contribution) or in the opposite direction $-\boldsymbol{K}^*$ (recoil contribution), it is undetected in practical (e,3-1e) measurement. The equal energy sharing cases are similar to this procedure except that recoil contribution in first SI (e, 2e)-like step predicts four more lobes' positions (see Fig. 3.15, indicated by blue dash dot lines) because the two ejected is undistinguishable in real (e, 3-1e) detection. The predictions incorporating recoil contribution are summarized in last column in Tab. 3.2 and indicated in Figs. 3.9 to 3.15 by vertical dash-dotted lines.

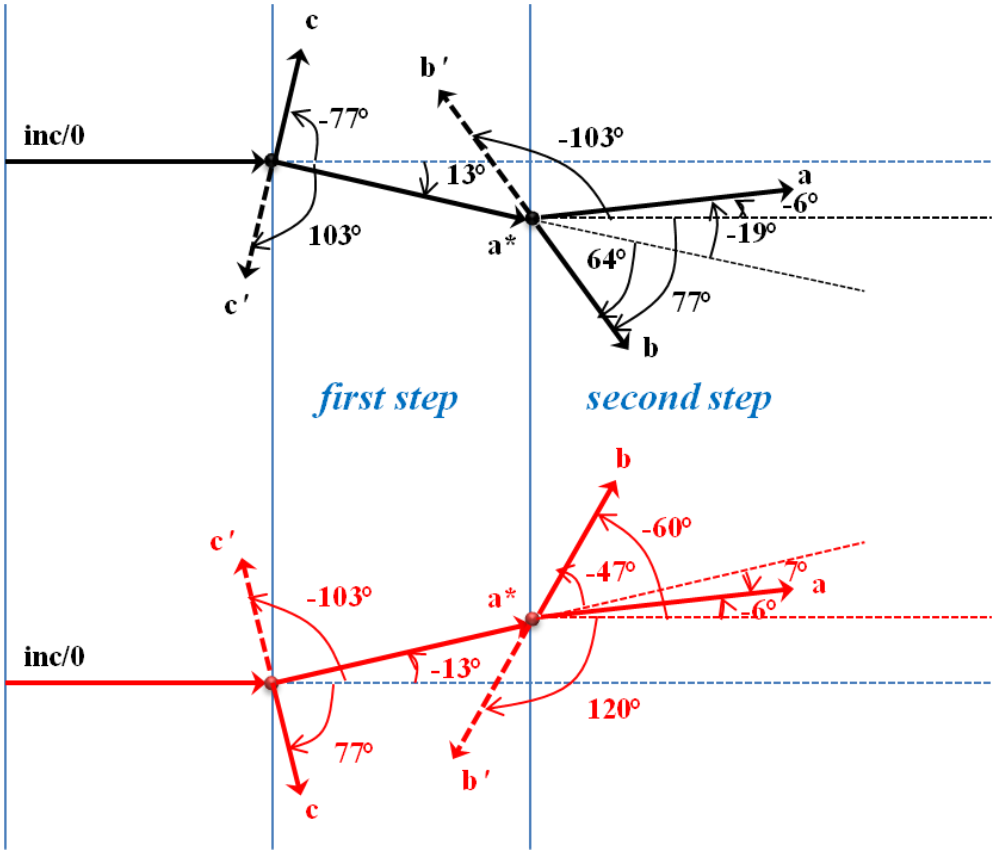

Figure 3.8 *The same as Fig.3.7, but for Ne at (E_b:E_c) = (72:12) eV. In addition, the recoil contribution (indicated by dotted arrow lines in each step) is taken into account.*

In Fig.3.8, the recoil contribution in TS2 kinematical analysis is incorporated, which are indicated by dotted arrow lines both in first and second step. In first step, the c-electron is ejected into opposite directions of momentum transfer $-\theta_{-K^*}$. These are predicted at ~103 ° and ~257 ° for E_c=12 eV, depending on whether the intermediate scattered electron is emitted above or below incident direction, respectively. In the second step, the TS2 kinematical analysis yields two new predictions of lobe's position due to recoil contribution, which are at ~ -103 ° (or ~257 °) and ~120 ° for scenarios 1 and 2

cases, respectively. We note that these recoil contribution predictions in first (e, 2e)-like SI step will not appear in (e,3-1e) 4DCS angular distribution for unequal energy sharing case since the two ejected electrons are distinguished by their different energy and the ejected slowest electron in first step is undetected. In contrast, these predictions appear in equal energy sharing case of (e, 3-1e) measurement since the two ejected electrons are indistinguishable in real experimental detection. All binary and recoil contribution will be shown in (e, 3e) measurement where all three outgoing electrons are detected simultaneously by triple coincidence technique (see details in Chapter 4), whatever the two ejected electrons sharing equal or unequal energies. In this example, it is unequal energy sharing (e, 3-1e) 4DCS measurement, so the recoil contribution prediction in first step will not appear in the results. These new predictions by TS2 kinematical analysis model including recoil contribution are summarized in the last column of Tab. 3.1 and indicated in Figs. 3.8 to 3.15 by dash dot lines.

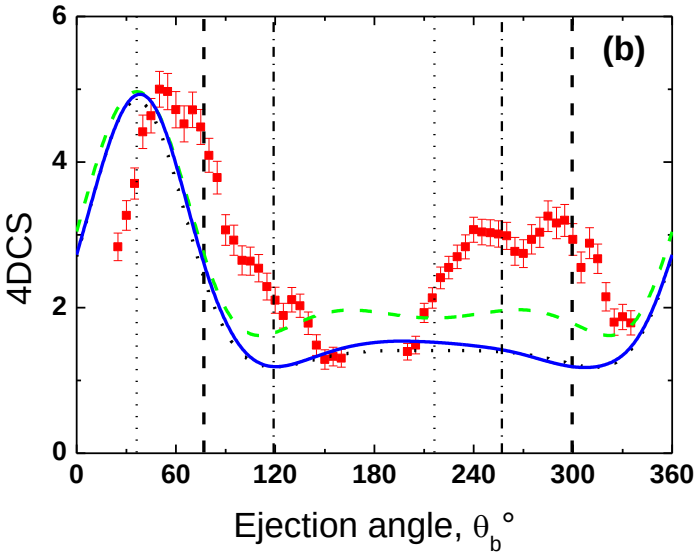

Figure 3.9 *The same as Fig. 3.4(b) for Ne at (E_b:E_c) = (72:12) eV, but in addition the recoil contribution (indicated by dash dot lines) is taken into account.*

It is remarkable that the experimental 4DCS distribution displayed in Fig. 3.9 for Ne shows a small peak at ~ 130 ° and a saddle structure at ~ 245 °, which are very close to the TS2 recoil contribution angle predictions located ~ 119 ° and ~ 257 °. Considering the angular uncertainty of our spectrometer, maybe we can propose that this reveals the contribution of recoil contribution in second step of DI TS2 mechanism. Similar features can be found in almost all cases such as in Fig. 3.11(d) of He at ~256 °, Fig. 3.12(a) of Ne at ~280 °, 3.12(b) at ~257 °, 3.12(c) at ~247 °, Fig. 3.13(a) of Ar at ~247 °, 3.13(c) at ~138 ° etc (see Figs 3.9-3.13). In spite of the modest angular resolution of <7 ° [64], which

is necessary to reach reasonable statistics in a reasonable data accumulation time, these angular lobe's position predictions of TS2 kinematical model are in good agreement with the observed experimental structures. All of these proofs strongly drive us to make a general conclusion that the recoil contribution plays also an important role in TS2 mechanisms. Though they have smaller contribution than binary contribution, they are at least not negligible.

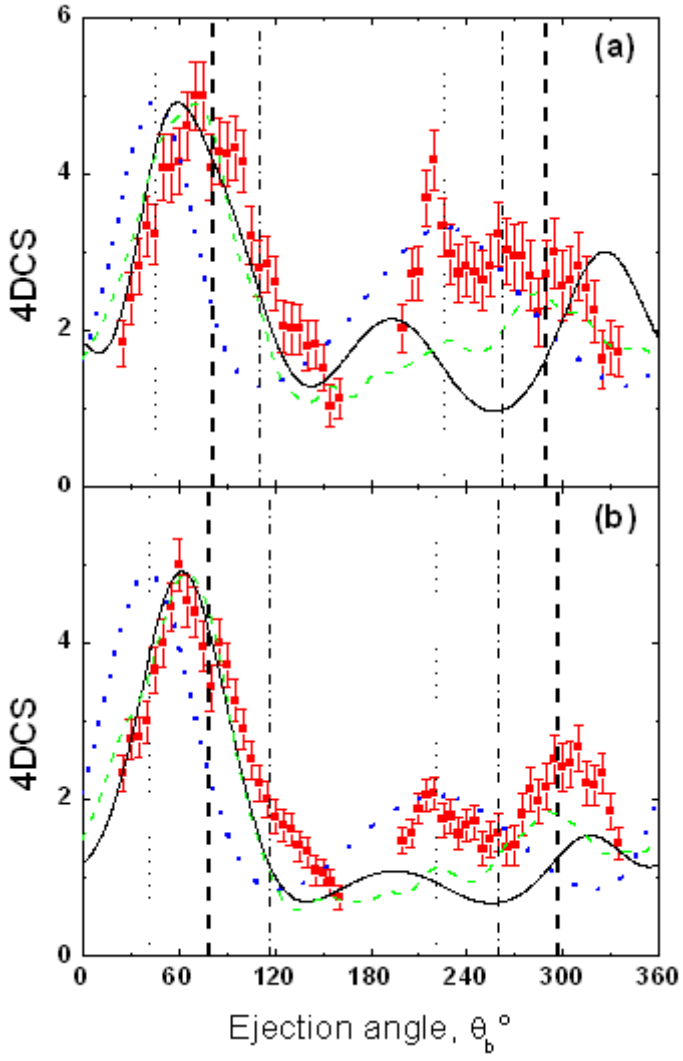

Figure 3.10 *The same as Fig. 3.1 for He at: panel (a): (E_b:E_c)= (17:5) eV, (b): (E_b:E_c)= (37:5) eV, respectively. In addition the recoil contribution (indicated by dash dot lines) is taken into account.*

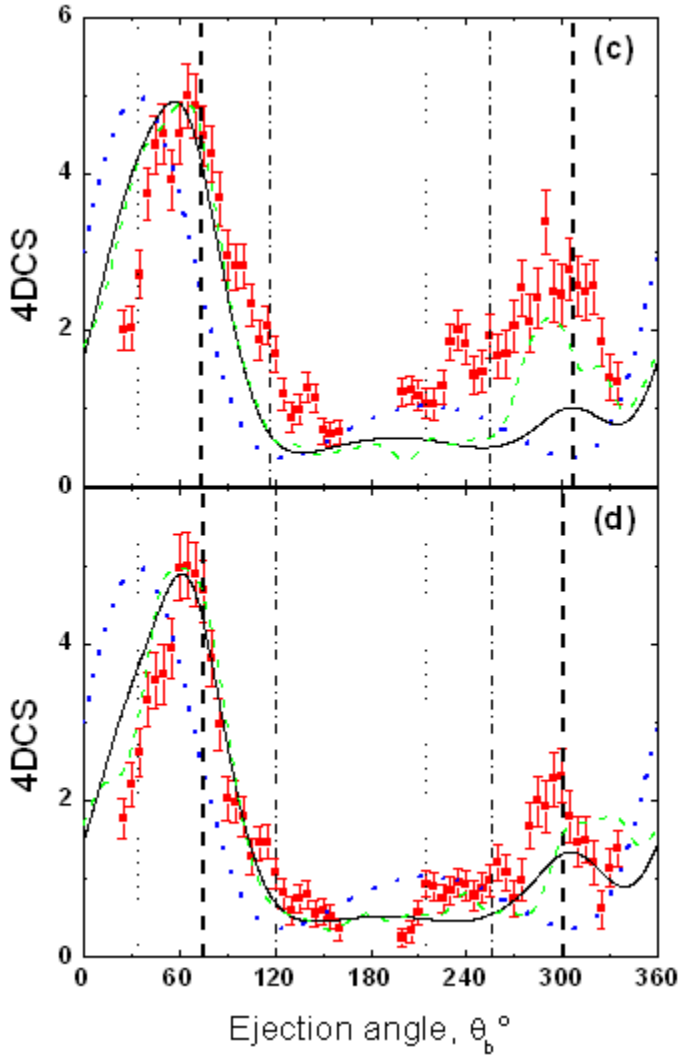

Figure 3.11 *The same as Fig. 3.2 for He at: panel (c): (E_b:E_c)= (74:5) eV, (d): (E_b:E_c)= (72:12) eV, respectively. In addition the recoil contribution (indicated by dash dot lines) is taken into account.*

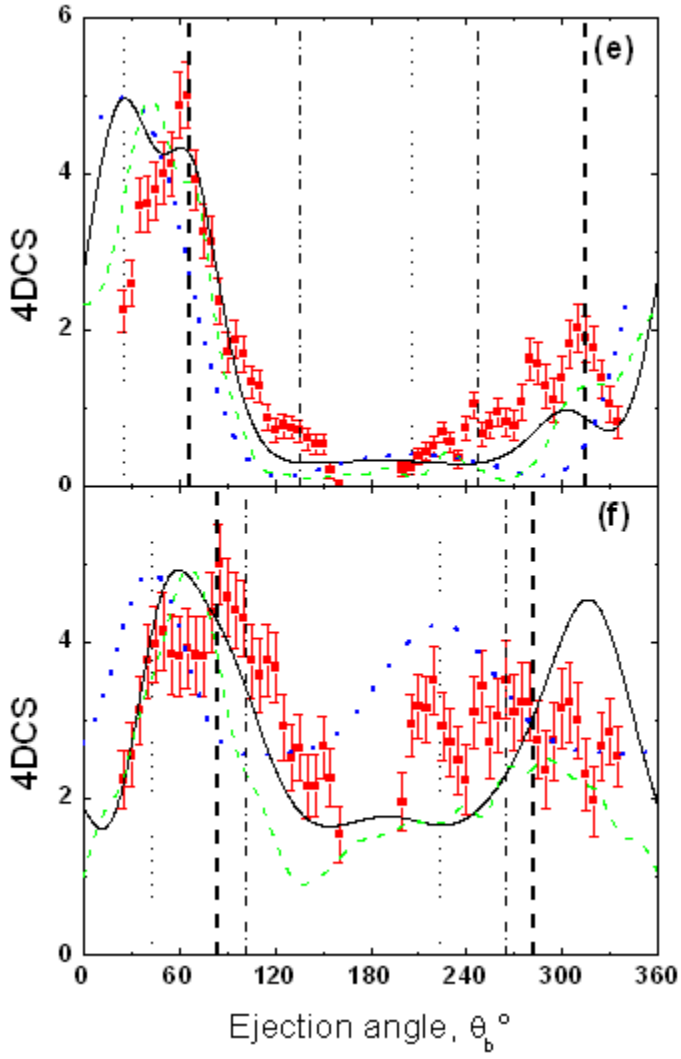

Figure 3.12 *The same as Fig. 3.3 for He at for panel (e): (E_b:E_c)= (144:12) eV, (f): (E_b:E_c)= (12:12) eV, respectively. In addition the recoil contribution (indicated by dash dot lines) is taken into account.*

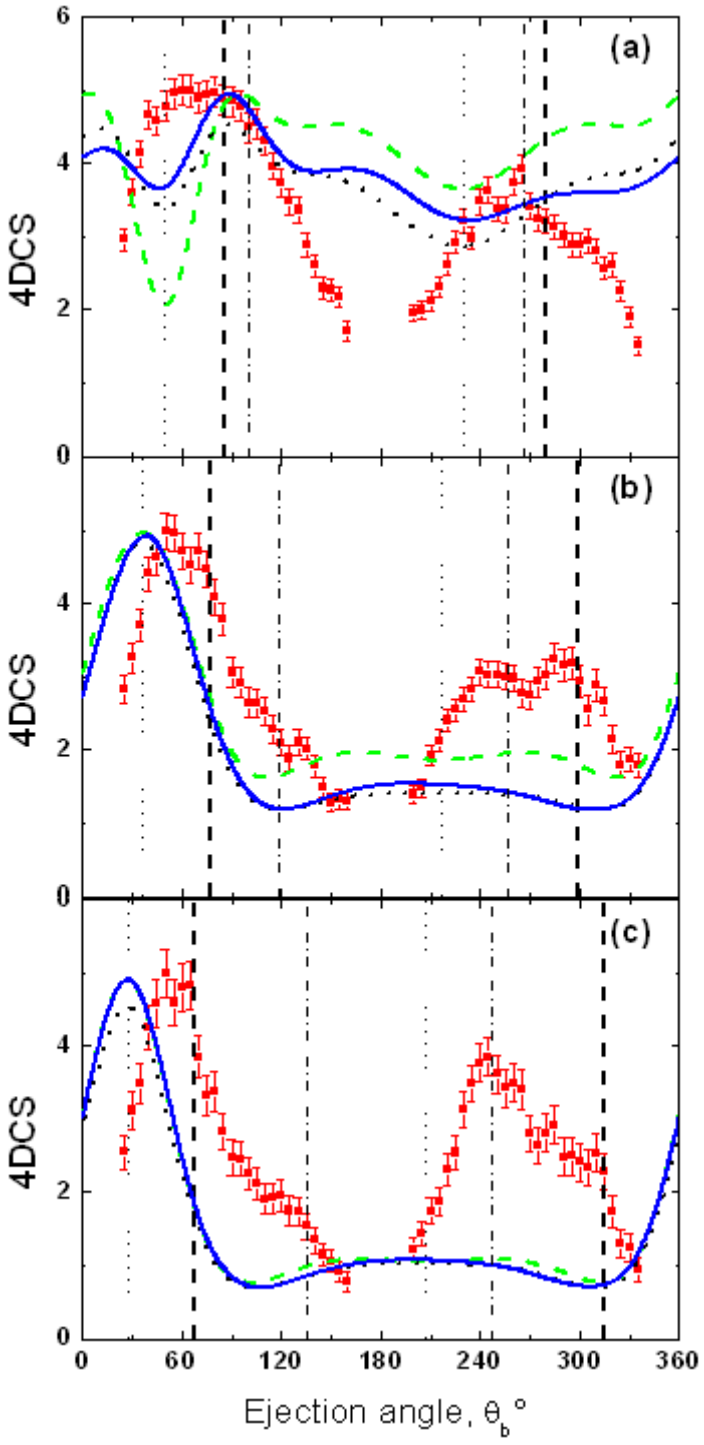

Figure 3.13 *The same as Fig. 3.4, 4DCS measurements for Ne at (E_b:E_c) = (12:12) eV (panel (a)), (72:12) eV (panel (b)) and (144:12) eV (panel (c)), respectively. In addition the recoil contribution (indicated by dash dot lines) is taken into account.*

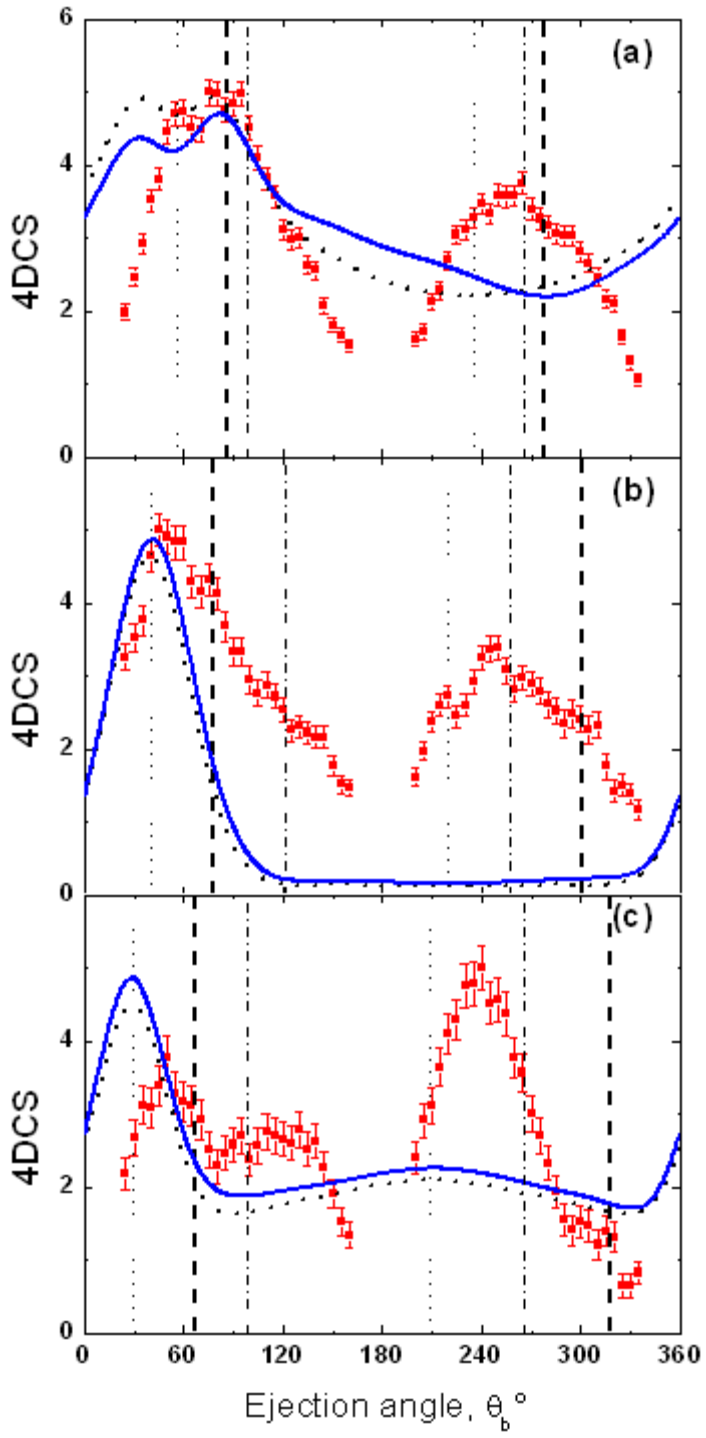

Figure 3.14 *The same as Fig. 3.5, 4DCS measurements for Ar at (E_b:E_c) = (12:12) eV (panel (a)), (72:12) eV (panel (b)) and (144:12) eV (panel (c)), respectively. In addition the recoil contribution (indicated by dash dot lines) is taken into account.*

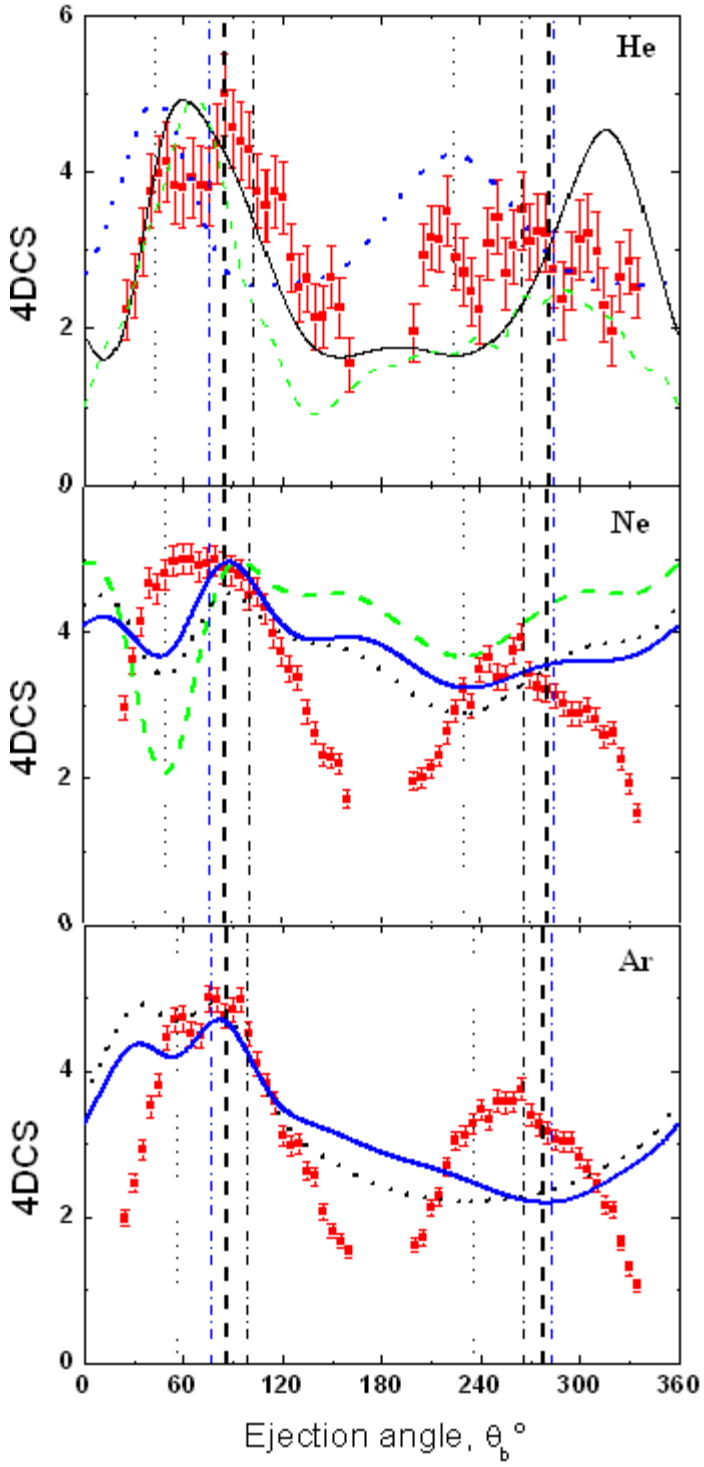

Figure 3.15 *TS2 kinematical prediction with recoil panel (c): (E_b:E_c)= (74:5) eV, (d): (E_b:E_c)= (72:12) eV, respectively. In addition the recoil contribution (indicated both in first step and second step of (e,2e)-like processes for equal energy sharing cases: upper panel, He (E_b:E_c)= (17:17) eV; middle panel, Ne (E_b:E_c)= (12:12) eV; bottom panel, Ar (E_b:E_c)= (12:12) eV, respectively. The recoil contribution in first step of (e, 2e) are indicated by blue-dash-dotted lines.*

C. Two-Step 2 kinematical analysis including both binary and recoil contribution in equal energy sharing case

In Fig. 3.15, the equal energy sharing cases are collected together for three different atomic targets: He, Ne and Ar. Because of the undistinguishibility of the two ejected electrons, the recoil contribution in first SI step is also included in TS2 kinematical analysis and these predictions are indicated by blue dash dot lines in Fig. 3.15. We can find that recoil prediction in first and second SI steps are on either side of TS2 binary prediction. All of TS2 kinematical predictions in equal energy sharing cases form a set of relatively narrow angular band. These bands extend from 75 ° to 102 ° and 264 ° to 285 ° in the case of He (E_b:E_c) = (17:17) eV, from 76 ° to 100 ° and 266 ° to 284 ° in the case of Ne (E_b:E_c) = (12:12) eV and from 77 ° to 98 ° and 266 ° to 283 ° in the case of Ar (E_b:E_c) = (12:12) eV. It is remarkable that most of additional structures rather than first order prediction position ($\pm\vec{K}$) fall within these angular bands for both forward and backward lobes. The presence of these structures is obviously at the origin of the non-symmetry about $\pm\vec{K}$. We thus conclude that the angular distributions are strongly influenced by TS2 mechanism. Of course, the contributions from TS1 and SO mechanism are not excluded but their effects should be more important in the momentum transfer directions ($\pm\vec{K}$) than at larger angles. Hence these observations comfort the conclusion that a first order theory would not be sufficient to explain the experimental data.

Note that this kinematic model does not include any quantum effects or post collision interaction (PCI). The electron-electron correlation within target is also not considered. So the remaining disagreement between the experimental results and the model prediction are probably mainly due to its simplicity, being based on pure kinematical considerations [30].

The conclusions obtained from TS2 kinematical model are consistent with non-first order theoretical models (TS2-MCEG, B2 and B2-2CG) that second or higher order mechanisms are predominant over first order mechanism under present kinematics.

3.5 Conclusion

The (e, 3-1e) experiments for the DI at few hundred eV impact energy are extended from simplest atomic target helium to more complex targets, namely neon and argon. The ejected energy of two emitted electrons in this work is extended from small and equal energy sharing to large ejected and more asymmetric energy sharing. For all targets, the ejected electron angular distributions exhibit similar features, that is, large shifts from the momentum transfer axis as well as marked structures in the forward and backward lobes. For He, the first Born-3C prediction does not reproduce the observed shifts and structures of the 4DCS distribution, whereas the two new developed theoretical models, namely the TS2-MCEG and B2 treatments, very clearly constitute a considerable improvement, both

for the position of the forward lobe which is correctly reproduced and for the structure of the backward lobe which is qualitatively well predicted. For Ne and Ar, these features are not reproduced by a first Born B1-3C model, nor by a second Born (B2-2CG) model which does only slightly better. For all targets, the qualitative TS2 kinematical model shows that under present kinematics the TS2 mechanism dominates over the SO and TS1 and is mostly responsible for the structures and angular positions of the measured lobes. This TS2 kinematical model is extended by considering the recoil contribution in each step of TS2 mechanism and the new prediction of lobes' position are generally in good agreement with 4DCS measurements for all targets. However, it needs more elaborate theoretical calculations to confirm the origin of the role of recoil contribution in DI process.

3.6 bibliography

1. Lahmam-Bennani, A., et al., *Identification of mechanisms of electron impact double ionizing collisions by e,(3-1)e experiments*. Journal of Physics B: Atomic, Molecular and Optical Physics, 1991. **24**: p. 9.
2. Lahmam-Bennani, A., Dupré, C. and A. Duguet, *Electron-impact double ionization of argon studied by double and triple coincidence techniques: The first (e,3e) experiment*. Physical Review Letters, 1989. **63**(15): p. 1582-1585.
3. Lahmam-Bennani A, et al, (e, 3e) absolute five-fold differential cross sections fro double ionization of krypton, Journal of Physics B: Atomic, Molecular and Optical Physics, 1992. **25**: p.2873.
4. El Marji, B., et al., *Evidence for a shake-off mechanism being responsible for electron-impact double-ionization of argon at 5.5 keV*. Journal of Physics B: Atomic, Molecular and Optical Physics, 1996. **29**(5): p. L157.
5. El Marji, B., et al., *Angular correlation of ejected electrons in (e, 3-1)e electron impact double ionization of helium*. Journal of Physics B: Atomic, Molecular and Optical Physics, 1995. **28**(23): p. L733.
6. El Marji, B., et al., *Dynamics of the double ionization process from (e,3e) experiments: I. Absolute cross sections for argon*. Journal of Physics B: Atomic, Molecular and Optical Physics, 1997. **30**(16): p. 3677.
7. Schröter, C., et al., *Dynamics of the double-ionization process from (e, 3e) experiments: II. Fivefold differential cross sections for neon*. Journal of Physics B: Atomic, Molecular and Optical Physics, 1998. **31**(1): p. 131.
8. Taouil, I., et al., *Fully Determined (e,3e) Experiments for the Double Ionization of Helium*. Physical Review Letters, 1998. **81**(21): p. 4600-4603.
9. Lahmam-Bennani, A., et al., *Complete experiments for the double ionization of He: (e, 3e) cross sections at 1 keV impact energy and small momentum transfer*. Journal of Physics B-Atomic Molecular and Optical Physics, 2001. **34**(15): p. 3073-3087.
10. Dorn, A., et al., *Appearance and disappearance of the second Born effects in the (e,3e) reaction on He*. Physical Review A, 2003. **68**(1): p. 012715.
11. Dorn, A., et al., *Double ionization of helium by electron impact in the impulsive regime*. Physical Review A, 2002. **65**(3): p. 032709.
12. Dorn, A., et al., *Double Ionization of Helium by Electron-Impact: Complete Pictures of the Four-Body Breakup Dynamics*. Physical Review Letters, 2001. **86**(17): p. 3755-3758.
13. Dorn, A., et al., *Double Ionization of Helium by Fast Electron Impact*. Physical Review Letters, 1999. **82**(12): p. 2496-2499.
14. Lahmam-Bennani, A., et al., *Origin of dips and peaks in the absolute fully resolved cross sections for the electron-impact double ionization of He*. Physical Review A, 1999. **59**(5): p. 3548-3555.
15. Anatoli, K., et al., *A comparative experimental and theoretical investigation of the electron-impact double ionization of He in the keV regime*. Journal of Physics B: Atomic, Molecular and Optical Physics, 1999. **32**(21): p. 5047.
16. Mkhanter, R.E. and Dal Cappello, C. *A study of the two-step mechanism in the double ionization of helium by fast electrons*. Journal of Physics B: Atomic, Molecular and Optical Physics, 1998. **31**(2): p. 301.
17. Grin, M., et al., *Angular distribution in (e, 3e) collisions on helium*. Journal of Physics B-Atomic Molecular and Optical Physics, 2000. **33**(2): p. 131-141.
18. Lahmam-Bennani, A., et al., *Importance of non-first-order effects in the (e,3e) double ionization of helium*. Physical Review A, 2003. **67**(1): p. 010701.
19. Lahmam-Bennani, A., et al., *Predominance of the second-order, two-step mechanism in the electron impact double ionization of helium at intermediate impact energy*. Journal of Physics B: Atomic, Molecular and Optical Physics, 2010. **43**(10): p. 105201.

20. Li, C., et al., *Identification of first order and non-first order contributions in the (e,3–1e) and (e,3e) double ionization of molecular nitrogen.* Journal of Physics B: Atomic, Molecular and Optical Physics, 2012. **45**(13): p. 135201.
21. Lahmam-Bennani, A., Duguet, A. and Roussin, S. *Observation of non-first-order effects in an (e, 3-1e) investigation of the double ionization of helium and molecular hydrogen*. Journal of Physics B: Atomic, Molecular and Optical Physics, 2002. **35**(2): p. L59.
22. Jia, C.C., et al., *Dynamics of the double ionization process by electron impact: Ar (e, 3e) experiments at low collision energy*. Journal of Physics B: Atomic, Molecular and Optical Physics, 2002. **35**(4): p. 1103.
23. Jia, C.C., et al., *Deviations between experimental and theoretical results in Ar (e, 3e) double ionization.* Journal of Physics B-Atomic Molecular and Optical Physics, 2003. **36**(1): p. L17-L24.
24. P. Bolognesi , et al, *Double ionization of He by electron impact at large momentum transfer*. Physical Review A, 2003. **67**(3).
25. Elazzouzi, S., et al., *Double ionization of helium by electron impact: angular distributions at low incident energy.* Journal of Physics B: Atomic, Molecular and Optical Physics, 2005. **38**(10): p. 1391.
26. Elazzouzi, S., et al., *Double ionization of argon by electron impact: use of the approximate 6C model*. Journal of Physics B-Atomic Molecular and Optical Physics, 2006. **39**(23): p. 4961-4976.
27. Götz, J.R., Walter, M. and Briggs, J.S. *Appearance of non-first-Born effects in (e, 3e) on helium.* Journal of Physics B: Atomic, Molecular and Optical Physics, 2003. **36**(4): p. L77.
28. Lahmam-Bennani, A., et al., *Predominance of the second-order, two-step mechanism in the electron impact double ionization of helium at intermediate impact energy*. Journal of Physics B-Atomic Molecular and Optical Physics, 2010. **43**(10).
29. Staicu Casagrande, E. M., et al., *Experimental and theoretical confirmation of the role of higher order mechanisms in the electron impact double ionization of helium.* Journal of Physics B: Atomic, Molecular and Optical Physics, 2011. **44**(5): p. 055201.
30. Li, C., et al., *Electron impact double ionization of neon, argon and molecular nitrogen: role of the two-step mechanism.* Journal of Physics B: Atomic, Molecular and Optical Physics, 2011. **44**(11): p. 115201.
31. Brauner, M. and et al., *Triply-differential cross sections for ionisation of hydrogen atoms by electrons and positrons*. Journal of Physics B: Atomic, Molecular and Optical Physics, 1989. **22**(14): p. 2265.
32. Dal Cappello, C., et al., *The second Born approximation for the single and double ionization of atoms by electrons and positrons*. Journal of Physics B: Atomic, Molecular and Optical Physics, 2011. **44**(1): p. 015204.
33. Tweed, R.J., *Double processes in e^--He collisions.* Zeitschrift für Physik D Atoms, Molecules and Clusters, 1992. **23**(4): p. 309-320.
34. Carlson, T.A. and Krause, M.O. *Electron Shake-Off Resulting from K-Shell Ionization in Neon Measured as a Function of Photoelectron Velocity*. Physical Review, 1965. **140**(4A): p. A1057-A1064.
35. McGuire, J.H., *Double Ionization of Helium by Protons and Electrons at High Velocities*. Physical Review Letters, 1982. **49**(16): p. 1153-1157.
36. Mcguire, J.H., *High-Velocity Limits for the Ratio of Double to Single Ionization by Charged-Particles and by Photons*. Journal of Physics B-Atomic Molecular and Optical Physics, 1984. **17**(22): p. L779-L784.
37. Hda, H., Dal Cappello, C. and Langlois, J. *Angular distributions of electrons in the (e, 3e) reaction*. Zeitschrift für Physik D Atoms, Molecules and Clusters, 1994. **29**(1): p. 25-29.
38. Cooper, J.W. and van Boeyen, R.W. *Double ionization of argon by electron impact: new theoretical results.* Journal of Physics B: Atomic, Molecular and Optical Physics, 2004. **37**(4): p. L77.
39. Hylleraas, E.A., *Neue Berechnung der Energie des Heliums im Grundzustande, sowie des tiefsten Terms von Ortho-Helium.* Zeitschrift für Physik A Hadrons and Nuclei, 1929. **54**(5): p. 347-366.

40. Clementi, E. and Roetti, C., *Roothaan-Hartree-Fock atomic wavefunctions: Basis functions and their coefficients for ground and certain excited states of neutral and ionized atoms, Z≤54.* Atomic Data and Nuclear Data Tables, 1974. **14**(3-4): p. 177.
41. Garibotti, C.R. and Miraglia, J.E. *Ionization and electron capture to the continuum in the H^+-hydrogen-atom collision*. Physical Review A, 1980. **21**(2): p. 572-580.
42. Dal Cappello, C. and Joulakian, B. *Double Ionization of Noble Gases by Electron Impact (e,2e) and Related Processes*, C.T. Whelan, et al., Editors. 1993, Springer Netherlands. p. 341-355.
43. F. W. Byron, J., Joachain, C.J. and Piraux, B. *Triple differential cross sections for the ionisation of atomic hydrogen by fast electrons: a second Born treatment*. Journal of Physics B: Atomic and Molecular Physics, 1980. **13**(22): p. L673.
44. F. W. Byron, J., Joachain, C.J. and Piraux, B. *On the second Born approximation for the ionisation of atomic hydrogen and helium by fast electrons*. Journal of Physics B: Atomic and Molecular Physics, 1982. **15**(8): p. L293.
45. Bonham, R.A. and Kohl, D.A. *Simple Correlated Wavefunctions for the Ground State of Heliumlike Atoms*. The Journal of Chemical Physics, 1966. **45**(7): p. 2471.
46. Gieseke, S., *Monte Carlo Event Generators*. Nuclear Physics B - Proceedings Supplements, 2012. **222–224**(0): p. 174-186.
47. Fischer, D., et al., *Systematic analysis of double-ionization dynamics based on four-body Dalitz plots*. Physical Review A, 2009. **80**(6): p. 062703.
48. Ciappina, M.F., M. Schulz, and Kirchner, T. *Reaction dynamics in double ionization of helium by electron impact*. Physical Review A, 2010. **82**(6): p. 062701.
49. Dürr, M., et al., *(e,3e) on Helium at Low Impact Energy: The Strongly Correlated Three-Electron Continuum*. Physical Review letters, 2007. **98**(19): p. 193201.
50. Dürr, M., et al., *Analysis of experimental data for ion-impact single ionization of helium with Monte Carlo event generators based on quantum theory*. Physical Review A, 2007. **75**(6): p. 062708.
51. Kilin, V.A., et al., *State-selective single-photon double ionization of Ne indicating singlet-triplet mixing of doubly excited LS -states*. Journal of Physics B: Atomic, Molecular and Optical Physics, 2000. **33**(22): p. 4989.
52. Wiesemann, K., J. Puerta, and Huber, B.A. *Double ionization of Ar atoms by single electron impact*. Journal of Physics B: Atomic and Molecular Physics, 1987. **20**(3): p. 587.
53. Huetz, A., et al., *Wannier theory for double photoionization of noble gases*. Journal of Physics B: Atomic, Molecular and Optical Physics, 1991. **24**(8): p. 1917.
54. Naja, A., et al., *An (e, 2e)-(e, 3e) investigation of argon: competition between inner-shell single ionization and direct double ionization processes*. Journal of Physics B-Atomic Molecular and Optical Physics, 2007. **40**(14): p. 2871-2884.
55. Naja, A., et al., *(e, 2e) triple differential cross-sections for ionization beyond helium: the neon case at large energy transfer*. Journal of Physics B-Atomic Molecular and Optical Physics, 2008. **41**(8).
56. Van der Wiel, M.J. and Wiebes, G. *Multiple ionization of Ar by 10 keV electrons as a function of the energy loss*. Physica, 1971. **53**(2): p. 225-255.
57. Dal Cappello, C., Hda, H. and Roy, A.C. *Angular distributions in the double ionization of the noble gases by electron impact*. Physical Review A, 1995. **51**(5): p. 3735-3744.
58. Whelan, C.T., et al., *Coulomb 3-Body Effects in (e,2e) Collisions - the Ionization of H in Coplanar Symmetrical Geometry*. Physical Review A, 1994. **50**(5): p. 4394-4396.
59. Ehrhardt, H., et al., *Ionization of Helium: Angular Correlation of the Scattered and Ejected Electrons*. Physical Review Letters, 1969. **22**(3): p. 89-92.
60. Kheifets, A.S., et al., *An energetic (e, 2e) reaction away from the Bethe ridge: recoil versus binary*. Journal of Physics B: Atomic, Molecular and Optical Physics, 2009. **42**(16): p. 165204.
61. Naja, A., et al., *Triply differential (e,2e) cross sections for ionization of the nitrogen molecule at large energy transfer*. Journal of Physics B-Atomic Molecular and Optical Physics, 2007. **40**(18): p. 3775-3783.

62. Kheifets, A.S., et al., *DWBA-G calculations of electron impact ionization of noble gas atoms*. Journal of Physics B-Atomic Molecular and Optical Physics, 2008. **41**(20): p. 145201
63. McConkey, J.W., A. Crowe, and M.A. Hender, *Differential Cross Sections in the Electron Impact Ionization of Atoms and Molecules*. Physical Review Letters, 1972. **29**(1): p. 1-4.
64. Duguet, A., et al., *A multidetection, multicoincidence spectrometer for (e,2e) and (e,3e) electron impact ionization measurements*. Review of Scientific Instruments, 1998. **69**(10): p. 3524-3536.
65. Joulakian, B., et al., *Double ionization of He by fast electron: use of correlated two electron wave function*. Journal of Physics B-Atomic Molecular and Optical Physics,, 1992. **25**: p. 2863.
66. Ancarani, L. U., et al., *Interplay of initial and final states for (e,3e) and (γ,2e) processes on helium,* Physical Review A, 2008. **77**(6): p. 062712

Chapter 4 *(e,3-1e) and (e,3e) measurements for N_2 at intermediate impact energy: identification of first order and non-first order contributions*

4.1 Introduction

4.1.1 Overview of previous works on ionization of molecular targets by electron impact

Over last few decades, the single and double ionization dynamical studies have been extensively performed both theoretically and experimentally for atomic targets but remain very rare until today for molecular targets. For theory, it is mainly due to the difficulty in describing the multi-electron process and also in finding tractable target wave functions. There are several reasons for this scarcity. First, because of the close spacing and contributions from vibrational and rotational states of molecular electronic states, it is difficult to resolve them in an experimental measurement. Second, theoretical calculations are obtained for a fixed molecular orientation whereas the experiments are in general performed for randomly oriented molecular targets. Therefore an average over all orientations must be made in the theoretical calculations to compare with experimental results. Third, but not least most important reason is the difficulty of correctly describing electron impact SI and DI process from theoretical point of view, especially due to the molecular characteristic of multicentre nature of the target wave function (or non-spherical nature which has less symmetric properties) [1]. Although many measurements are concerned with atomic targets [2], a growing interest in the investigation of molecular targets has appeared in the last few years due to the development of powerful experimental techniques [3-5]. The SI or DI dynamical studies span a wide range of molecular targets, from simple diatomic molecules (H_2 [6-8], O_2 [9], N_2 [1, 10-13]) to more complex molecular targets such as CO_2 [10, 14], CH_4 [15], H_2O [16-20], etc. On the theoretical side, the most difficult problems of molecular target are multi-centre nature of the target and the random orientation of the molecules which is to be handled by averaging the cross sections for all molecular orientations. This orientation average can be achieved by an orientation averaged molecular orbital (OAMO) [21] method.

There are only few theoretical researches relevant to the investigation of dynamics of DI for molecular target. Mansouri et al [8] and Serov et al [22] used second Born approximation for describing the DI of H_2. Dal Cappello et al [20] investigated the DI of isolated water molecules fixed in space within a theoretical approach based on the second-order Born approximation. Besides, Chuluunbaatar et al [123] applied the modified two-centre continuum wave function to the dissociative double ionization of H_2 by electron impact. Later they used a correlated product of two two-centre continuum Coulomb waves to describe the state of two ejected electrons in the (e, 3e) double ionization of the two diatomic molecules, H_2 and N_2 [24].

On the experimental side, to our best knowledge, there are very few DI dynamical investigations on molecular targets [25]. Therefore, such DI experiments on molecular targets are highly expected.

In (e, 3e) measurement, the scattered and the two ejected electrons are detected in triple coincidence, while only two of three outgoing electrons are detected in double coincidence in (e, 3-1e) measurement. These (e, 3e) experiments are limited to noble gases and more particularly to the helium atom, which is an ideal target for the theoretical studies (see details in §3.1.1). Besides, due to the difficulty of describing the molecular target wave function on theory side, there are up to now no such (e, 3e) experiment existing to our best knowledge. This is another reason for us to perform (e, 3e) experiments on N_2.

In chapter 3, we applied the TS2 kinematical analysis model to predict electron impact DI process of atomic targets. Here we extend this TS2 kinematical model to molecular target under alike kinematics to validate or invalidate its prediction both in (e, 3-1e) and (e, 3e) measurements.

4.1.2 Description of the theoretical model for molecular double ionization

In this work, our (e, 3e) experimental results of N_2 are compared with the theoretical calculations performed in Metz by Joulakian and coworkers [24] using the correlated two centre continuum (TCC) wave for the description of the ejected electrons, in a procedure which takes into account only the first term of the Born series. Hereafter, we give a brief description of this model.

Because of randomly oriented targets, the integration over all possible and equally probable directions of the molecule in space must be done at the beginning, reducing the six-fold differential cross section to five-fold differential cross section (5DCS).

$$\sigma^{(5)} = \frac{1}{4\pi} \int d\Omega_\rho \, \sigma^{(6)}(\vec{\rho}) \tag{4.1}$$

where ρ is the internuclear distance.

The conservation of energy for the fixed internuclear distance ρ gives

$$E_0 = E_a + E_b + E_c + IP^{2+} \tag{4.2}$$

where E_0, E_a, E_b and E_c represent the energies of the incident, scattered, faster ejected and slower ejected electrons respectively, with IP^{2+} being the energy necessary to eject two electrons from the target at the equilibrium internuclear distance (or so-called 'double ionization potential').

The transition matrix is given by the first term of the Born series:

$$T_{fi} = \frac{1}{2\pi} \int d\overrightarrow{r_a} \int d\overrightarrow{r_b} \times \int d\overrightarrow{r_c} \exp\left(i\vec{K} \cdot \overrightarrow{r_a}\right) \overline{\chi_f}(\overrightarrow{r_b}, \overrightarrow{r_c}) V \varphi_i(\overrightarrow{r_b}, \overrightarrow{r_c}). \tag{4.3}$$

Here, the over line indicates that the complex conjugate $\varphi_i(\overrightarrow{r_b}, \overrightarrow{r_c})$ represents the space part of the initial state wavefunction. $\overrightarrow{r_a}$ is the position of the fast incident-scattered electron, which are described

in [24] as a plane wave. $\vec{r_j}$ (j=b, c) refer to the positions of the bound (ejected) electrons. $\boldsymbol{K}= \boldsymbol{k_0} - \boldsymbol{k_a}$ is the momentum transferred to the target and V represents the Coulomb interaction between the incident electron and the target given by

$$V = -\frac{1}{|\vec{r_a}-\vec{\rho}/2|} - \frac{1}{|\vec{r_a}+\vec{\rho}/2|} + \frac{1}{|\vec{r_a}-\vec{r_b}|} + \frac{1}{|\vec{r_a}-\vec{r_c}|}. \tag{4.4}$$

The final state wavefunction

$$\chi_f(\vec{r_b},\vec{r_c}) = \frac{\phi_f(\vec{k_b},\vec{r_b},\vec{k_c},\vec{r_c})+\phi_f(\vec{k_b},\vec{r_c},\vec{k_c},\vec{r_b})}{\sqrt{2}} \tag{4.5}$$

describes the state of the two equivalent ejected electrons, where

$$\phi_f(\vec{k_b},\vec{r_b},\vec{k_c},\vec{r_c}) = v(k_{bc})_1F_1\left(i\alpha_{bc},1,-i\left(k_{bc}r_{bc}+\vec{k_{bc}}\vec{r_{bc}}\right)\right)T(\vec{k_b},\vec{r_b})T(\vec{k_c},\vec{r_c}) \tag{4.6}$$

in which the electron-electron correlation is introduced. Here, $\vec{r_{bc}} = \vec{r_b} - \vec{r_c}$ and

$$v(k_{bc}) = \exp\left(-\frac{\pi\alpha_{bc}}{2}\right)\Gamma(1-i\alpha_{bc}) \tag{4.7}$$

represents the Gamow factor with

$$\alpha_{bc} = \frac{1}{2k_{bc}}, \vec{k_{bc}} = \frac{1}{2}(\vec{k_b} - \vec{k_c}). \tag{4.8}$$

The TCC wavefunction is borrowed from [23] for describing the ejected electron in the field of two Coulomb centres.

4.1.3 Two-Step 2 kinematical model for double ionization of N_2

The TS2 kinematical model is described in §3.4. The full details of this analysis have been first reported in [26] and so are only briefly summarized here. TS2 is a two-step process, which is assumed to proceed via two successive (e, 2e)-like ionizations of the target: in the first step, the 'c'-electron is ejected while the projectile is scattered with the highest probability at the $\pm\theta_{a^*}$ angle corresponding to the Bethe ridge [27, 28]. This intermediate 'a*'-scattered electron acts as a new projectile in a second (e, 2e) ionization of the intermediate, singly charged ion, resulting in the pair of electrons ('a': 'b').

However, only the binary scattering, associated to each of the two (e, 2e) SI events which constitute the TS2 mechanism, were taken into account in our previous work [26]. In the (e, 3-1e) and (e, 3e) measurements of N_2, we also consider the complex situation where the recoil scattering from the nucleus, is included [13]. The details will be discussed in §4.3.1.

4.2 Results and discussion

4.2.1 Experimental conditions

The experimental set-up and procedure used in this work are identical to those used in [5, 12, 13, 26]. The incident electron with energy E_0 is scattered with fixed energy E_a=500 eV under two symmetrical angles θ_a = + (6° ± 3°) and θ_a = - (6° ± 3°). Coplanar equal and unequal energy sharing configurations are used for 4DCS (e, 3-1e) measurements while only coplanar equal energy sharing configuration is used for 5DCS (e, 3e) measurements. In (e, 3-1e) experiments, the slower ejected electron (labeled c-electron) is undetected, while the faster ejected electron (labeled 'b'-electron) is detected with the 'a'-electron in double coincidence, whereas the 'c'-electron is emitted in random direction. Alternatively, in the (e, 3e) case, the 'b' and 'c' ejected electrons are energy and multi-angle analyzed and detected in triple coincidence with the scattered 'a'-electron in coplanar symmetric energy condition.

The present (e, 3e) as well as the (e, 3-1e) experiments for N_2 are performed with ejected electron energies (E_b:E_c) = (12:12) eV and (E_b:E_c) = (37:37) eV (so-called equal energy sharing case). In addition, the (e, 3-1e) experiments with ejected energies (E_b:E_c) = (72:12) and (E_b:E_c) = (144:12) are also performed (so-called unequal energy sharing case). Same as stated in §3.2, due to the low DI coincidence rate, all three toroidal analyzers were operated at reduced energy resolution. In order to ensure reasonable coincidence rates, the energy resolution for each analyzer is set to $\Delta E_a \sim \Delta E_b \sim \Delta E_c \sim$ 3eV, resulting in an 'effective (e, 3e) energy resolution' as defined in [29] (see §2.8.1) of $\Delta E_5 \sim \Delta E_a \Delta E_b \Delta E_c / (\Delta E_a^2 + \Delta E_b^2 + \Delta E_c^2)^{1/2} \sim$5.2 $(eV)^2$ and an 'effective (e, 3-1e) energy resolution' of $\Delta E_4 \sim \Delta E_a \Delta E_b \sim$ 9.0 $(eV)^2$. We suppose that the measured 4DCS and 5DCS are dominated by DI process removing two electrons from the outermost orbital $3\sigma_g$ of N_2. However， the measurements are influenced due to this limited energy resolution [1, 10, 15]. To estimate the amount of influence of the target outermost orbital from the neighboring orbitals, we assume the coincidence energy distribution to be a Gaussian function. It was shown in previous (e, 2e) studies of He [30] that the satellite structure located a few electron volts from the main line is fairly weak. Moreover, van der Wiel and Wiebes [31] have shown that contribution from the ionizing processes where the ion is left in its ground state are dominating over processes including ion excited states. Though the above arguments are valid for SI study, we may transpose an (e, 2e) conclusion to DI (e, 3-1e) and (e, 3e) measurements and hence we consider the outermost orbital $3\sigma_g$ of N_2 to be the main contributor to DI detected signals [31].

The incident energy E_0 is adjusted to fulfill the energy conservation, $E_0 = E_a + E_b + E_c + IP^{2+}$, with IP^{2+} = 43 eV being the DI potential of the N_2 molecule removing two electrons from its ($3\sigma_g$) outermost orbital.

As it is well known that (e, 3e) experiments are very time consuming due to their multi-differential character, the measurements need a very long accumulation time to achieve reasonable statistics. The final cross section distribution is obtained by adequately adding up the data from both θ_a and $-\theta_a$ angles [5, 32]. It is to be noted that the raw (e, 3e) data were analyzed using overlapping sectors with a width $\Delta\theta_b = 8°$.

Given the above experimental parameters, the momentum transfer to the target, defined by $\boldsymbol{K} = \boldsymbol{k_0} - \boldsymbol{k_a}$, varies in the magnitude from $K = 0.76$ au at $E_0 = 567$ eV to $K = 1.30$ au at $E_0 = 699$ eV, while its direction θ_K varies from ~56 ° to ~29 ° for these two extreme cases (shown in the fifth and sixth rows of Table 4.1). Simultaneously, due to the ±3 ° acceptance in θ_a angle, the momentum transfer resolution amounts to $\Delta K \sim \pm 0.2$ au and the spread in the momentum transfer direction is $\Delta\theta_K \sim \pm 10°$.

The experimental kinematical parameters are summarized in Table 4.1.

Target: N_2	***E_a = 500 eV***	***θ_a = - 6 deg***	***IP^{2+} =43 eV***
***E_0* (eV)**	567	617	627	699
***E_b* (eV)**	12	37	72	144
***E_c* (eV)**	12	37	12	12
K(au)	0.76	0.95	0.99	1.30
θ_K/θ_{-K}(deg)	56/236	42/222	40/220	29/209

Table 4.1 *Kinematical conditions of (e, 3-1e) and (e, 3e) experiments on N_2. The first two columns ($(E_b:E_c)$=(12:12) eV and $(E_b:E_c)$=(37:37) eV) are measured both by (e, 3-1e) and (e, 3e) experiments. The third and fourth columns are only measured by (e, 3-1e) experiments.*

4.2.2 (e, 3-1e) measurements of equal and unequal energy sharing

The angular distributions of the (e, 3-1e) 4DCS, $d^4\sigma/dE_a\,dE_b\,d\Omega_a\,d\Omega_b$ for the DI of the outermost orbitals of N_2 $(3\sigma_g)^{-2}$ are shown in Figs. 4.1(a), 4.1(b), 4.2(a) and 4.2(b) at the four different energy sharings for the ejected electrons: $(E_b:E_c)$ = (12:12), (37:37), (72:12), (144:12) eV, respectively (listed in Table 4.1). Note that the experimental data are obtained on a relative scale and have been arbitrarily normalized to the same value at the maximum of the forward lobe.

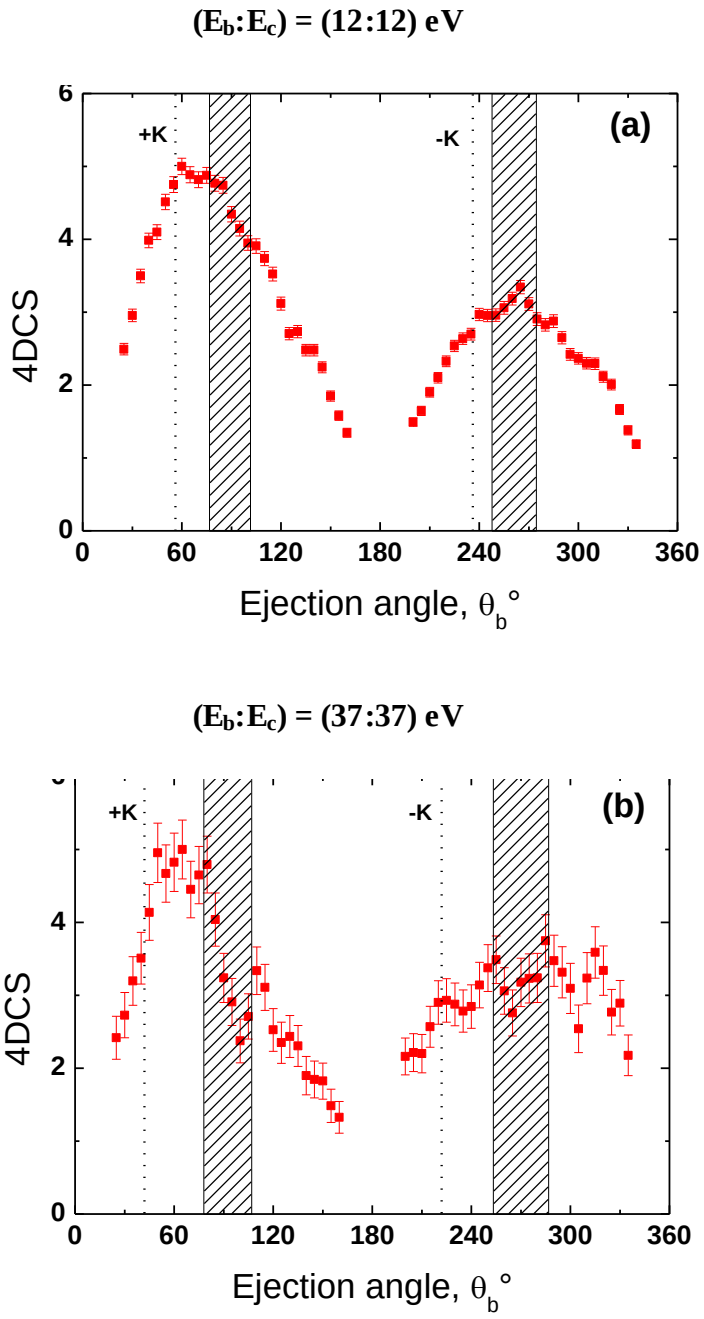

Figure 4.1 *Four-fold differential cross sections (4DCS) for double ionization of N_2. The scattered electron with energy E_a = 500 eV is detected at an angle θ_a = -6 ° in coincidence with one of the emitted electrons, while the second electron remains undetected (these are designated as 'b' and 'c' electrons, respectively). Panel (a): (E_b:E_c) = (12:12) eV; Panel (b): (E_b:E_c) = (37:37) eV. The experimental data (full squares) are represented with one standard deviation statistical error bar. The dotted vertical lines indicate the direction of momentum transfer (θ_K) and its opposite (θ_K). The dashed areas indicate the angular ranges predicted by the kinematical TS2 model for ejection of the 'b'-electron, see §4.3.1.*

$(E_b:E_c)$ = (72:12) eV

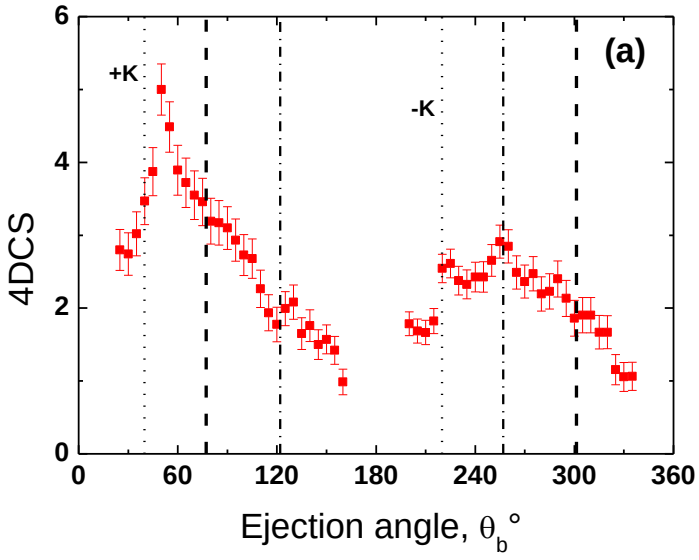

$(E_b:E_c)$ = (144:12) eV

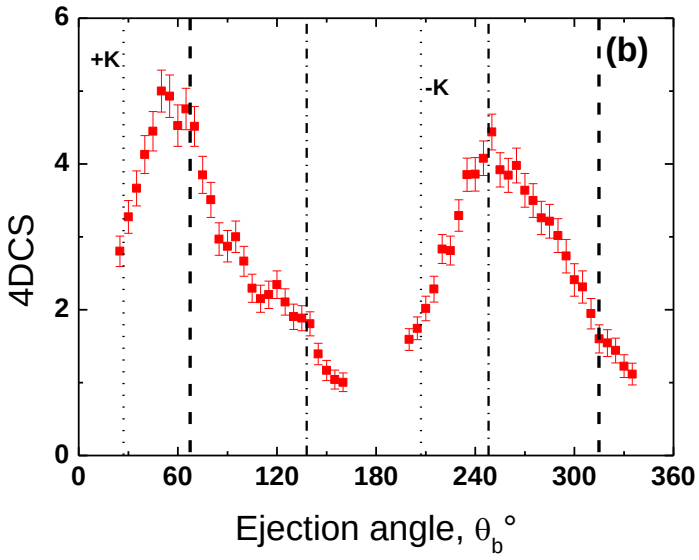

Figure 4.2 *Four-fold differential cross sections (4DCS) for double ionization of N_2. The scattered electron with energy E_a = 500 eV is detected at an angle θ_a = -6 ° in coincidence with one of the emitted electrons, while the second electron remains undetected (these are designated as 'b' and 'c' electrons, respectively). Panel (a): (E_b:E_c) = (72:12) eV; Panel (b): (E_b:E_c) = (144:12) eV. The experimental data (full squares) are represented with one standard deviation statistical error bar. The dotted vertical lines indicate the direction of momentum transfer (θ_K) and its opposite (θ_{-K}). The thick dash lines and dash dotted lines indicate the binary and recoil contribution predictions of TS2 kinematical model, respectively, see §4.3.1.*

As a general observation, some important common features are noticed.

I. We find for all energies cases (symmetric and asymmetric) the same general behavior. That is all angular distributions display a forward and a backward lobe. Here, the labels forward lobe and backward lobe designate the lobe pointing roughly in the momentum transfer direction (+***K***) and in the opposite direction (-***K***), respectively. These two directions are indicated by vertical dotted lines in the Figs. 4.1 and 4.2.

II. We also observe that both lobes are not symmetrically distributed about the ±***K*** axis and that their maxima are shifted from this axis direction by large amounts, ~30 ° (see Fig. 4.1(b)) to ~60 ° (see Fig. 4.2(b)). The uncertainty of ~10 ° in momentum transfer direction is significantly smaller than the observed shift, and hence it only marginally affects this shift.

III. As a consequence of second point, the intensity distribution in each lobe is not symmetrically distributed about the ±***K*** direction, as it would be expected [33, 34] if the electron impact DI process was solely due to a first order mechanism (SO and/or TS1). Moreover, we observe an important backward intensity relative to the forward one, which shows that strong non-first order effects are present in the (e, 3-1e) distributions.

IV. The distributions exhibit additional structures for both the forward and backward lobes. These additional structures are located at larger angles with respect to the momentum transfer direction.

Thus, in order to explain the above features (third and fourth items), it is necessary to take into account not only first order mechanisms (SO and TS1) but also higher order mechanisms (such as TS2).

In the absence of theoretical calculations for 4DCS of N_2, and considering the fact that the kinematical analysis proposed in [26] has proved to be greatly successful to predict the observations made in the (e, 3-1e) measurements for atomic targets, He, Ne and Ar [12, 26], we aim to apply this TS2 kinematical model to our new (e, 3-1e) results for molecular target N_2. This model is expected to give a qualitative interpretation of the observed structures as well as an estimation of the angular positions of the lobes in terms of physical effects included in the TS2 mechanism. The full details of this analysis has been reported in [26]. Furthermore, we extended this analysis by considering the recoil contribution in each SI (e, 2e) step of TS2 mechanism, which gives two more angular predictions of the lobes position. This 'extended' TS2 kinematical model is described in detail in §3.3. All angular predictions by this TS2 kinematical model including recoil contribution are summarized in Tables 4.2 to 4.5.

At this point, a concise elucidation is necessary for clarifying the different notations used in §3 and §4. Briefly, the essence of this analysis was to consider that the double ejection results from two successive binary (e, 2e) processes where each of the ejected electrons is mostly emitted along the

direction of the intermediate momentum transfer direction K* for the first SI (e, 2e) collision and along the momentum transfer direction K' for the second SI (e, 2e) collision, respectively. This gave rise in the (e, 3-1e) case to two possible scenarios depending on the sign of the angle θ_{a^*} of the intermediate 'a*'-scattered electron. In our earlier work [26], these scenarios yielded two expectation values for the emission angles of the detected ejected electron, which are essentially located along the momentum transfer K' of the second SI-collision. Therefore, we label these directions as $\theta_K^{<\pi}$ and $\theta_K^{>\pi}$ (see tables 4.2 to 4.5)†, where the superscript $<\pi$ (respectively $>\pi$) stands for the emission in the half-plane corresponding to ejection angles smaller (larger) than 180 °.

In the previous (e, 3-1e) work [12], the 'b' and 'c' electron shared very unequally the excess energy left to the target. Hence the undetected 'c' electron could be distinguished by its energy from the detected 'b' electron as being the slowest. In contrast, not only the unequally shared excess energy cases but also equally shared excess energy cases between two ejected electrons are studied. The major difference comes from the fact that the two ionized electrons can share the excess energy equally and hence are fully undistinguishable in the final state: one neither knows which one is emitted in the first step and which is emitted in the second step, nor which one is detected and which one is ignored. This results in two additional expected emission angles for the detected electron, which are essentially located along the intermediate momentum transfer direction **K*** of the first SI (e,2e) collision. Therefore, we label these directions as $\theta_{K^*}^{<\pi}$ and $\theta_{K^*}^{>\pi}$ (see Tables 4.2 to 4.5).

$(E_b:E_c)$ = (12:12) eV

first order mechanisms θ_K / θ_{-K}	second order TS2 mechanism				
	intermediate θ_{a^*}	first step θ_{K^*}	second step $\theta_{K'}$	expected $(\theta_b:\theta_c)$ for (e,3e)	expected θ_b for (e,3-1e) case
56 ° / 236 °	positive	bin $\theta_{K^*}^{>\pi}$ = 283 °	bin $\theta_{K'}^{<\pi}$ = 87 °	(283 °:87 °)	283 ° or 87 °
			rec $\theta_{-K'}^{>\pi}$ = 267 °		
		rec $\theta_{-K^*}^{<\pi}$ = 103 °	bin $\theta_{K'}^{<\pi}$ = 87 °		
			rec $\theta_{-K'}^{>\pi}$ = 267 °	(103 °:267 °)	103 ° or 267 °
	negative	bin $\theta_{K^*}^{<\pi}$ = 77 °	bin $\theta_{K'}^{>\pi}$ = 278 °	(77 °:278 °)	77 ° or 278 °
			rec $\theta_{-K'}^{<\pi}$ = 98 °		
		rec $\theta_{-K^*}^{>\pi}$ = 257 °	bin $\theta_{K'}^{>\pi}$ = 278 °		
			rec $\theta_{-K'}^{<\pi}$ = 98 °	(257 °:98 °)	257 ° or 98 °

Table 4.2 *Expected emission directions for the 'b' and 'c' electrons in the case $(E_b:E_c)$ = (12:12) eV associated to: first order mechanisms SO and/or TS1 (first column); second order mechanism TS2 predicted by our kinematical model in the (e,3-1e) case (columns 3 and 4); in the (e,3e) case, taking into account the fact that both ejected electrons are detected in opposite half-planes (column 5); in the (e, 3-1e) case, same as in (e,3e) case (column 6).*

†*In previous published articles and in §3, these directions were labeled as $\theta_{F\text{-}TS2}$ and $\theta_{B\text{-}TS2}$.*

$(E_b:E_c)$ = (37:37) eV

first order mechanisms θ_K / θ_{-K}	second order TS2 mechanism				
	intermediate θ_{a*}	first step θ_{K*}	second step $\theta_{K'}$	expected $(\theta_b:\theta_c)$ for (e,3e)	expected θ_b for (e,3-1e) case
42 ° / 222 °	positive	bin $\theta_{K*}^{>\pi}$ = 287 °	bin $\theta_{K'}^{<\pi}$ = 87 °	(283 °:87 °)	283 ° or 87 °
			rec $\theta_{-K'}^{>\pi}$ = 267 °		
		rec $\theta_{-K*}^{<\pi}$ = 107 °	bin $\theta_{K'}^{<\pi}$ = 87 °		
			rec $\theta_{-K'}^{>\pi}$ = 267 °	(107 °:267 °)	107 ° or 267 °
	negative	bin $\theta_{K*}^{<\pi}$ = 73 °	bin $\theta_{K'}^{>\pi}$ = 276 °	(73 °:276 °)	73 ° or 276 °
			rec $\theta_{-K'}^{<\pi}$ = 96 °		
		rec $\theta_{-K*}^{>\pi}$ = 253 °	bin $\theta_{K'}^{>\pi}$ = 276 °		
			rec $\theta_{-K'}^{<\pi}$ = 96 °	(253 °:96 °)	253 ° or 96 °

Table 4.3 *The same as in Table 4.2 but for $(E_b:E_c)$ = (37:37) eV.*

$(E_b:E_c)$ = (72:12) eV

first order mechanisms θ_K / θ_{-K}	second order TS2 mechanism			
	intermediate θ_{a*}	first step θ_{K*}	second step $\theta_{K'}$	expected θ_b for (e,3-1e) case
40 ° / 220 °	positive	bin $\theta_{K*}^{>\pi}$ = 282 °	bin $\theta_{K'}^{<\pi}$ = 77 °	77 °
			rec $\theta_{-K'}^{>\pi}$ = 257 °	257 °
		rec $\theta_{-K*}^{<\pi}$ = 102 °	bin $\theta_{K'}^{<\pi}$ = 77 °	
			rec $\theta_{-K'}^{>\pi}$ = 257 °	
	negative	bin $\theta_{K*}^{<\pi}$ = 78 °	bin $\theta_{K'}^{>\pi}$ =302 °	302 °
			rec $\theta_{-K'}^{<\pi}$ = 122 °	122 °
		rec $\theta_{-K*}^{>\pi}$ = 258 °	bin $\theta_{K'}^{>\pi}$ =302 °	
			rec $\theta_{-K'}^{<\pi}$ = 122 °	

Table 4.4 *Expected emission directions for the 'b' and 'c' electrons in the case $(E_b:E_c)$ = (72:12) eV associated to: first order mechanisms SO and/or TS1 (first column); second order mechanism TS2 predicted by our kinematical model in the (e,3-1e) case (columns 3 and 4); in the (e,3-1e) case, taking into account the fact that both ejected electrons are detected in opposite half-planes (column 5).*

(E_b:E_c) = (144:12) eV

first order mechanisms θ_K / θ_{-K}	second order TS2 mechanism			
	intermediate θ_{a*}	first step θ_{K*}	second step $\theta_{K'}$	expected θ_b for (e,3-1e) case
27 ° / 207 °	positive	bin $\theta_{K*}^{>\pi}$ = 281 °	bin $\theta_{K'}^{<\pi}$ = 68 °	68 °
			rec $\theta_{-K'}^{>\pi}$ = 248 °	248 °
		rec $\theta_{-K*}^{<\pi}$ = 101 °	bin $\theta_{K'}^{<\pi}$ = 68 °	
			rec $\theta_{-K'}^{>\pi}$ = 248 °	
	negative	bin $\theta_{K*}^{<\pi}$ = 79 °	bin $\theta_{K'}^{>\pi}$ =318 °	318 °
			rec $\theta_{-K'}^{<\pi}$ = 138 °	138 °
		rec $\theta_{-K*}^{>\pi}$ = 259 °	bin $\theta_{K'}^{>\pi}$ =318 °	
			rec $\theta_{-K'}^{<\pi}$ = 138 °	

Table 4.5 *The same as in Table 4.2 but for (E_b:E_c) = (144:12) eV.*

Moreover, the recoil scattering from the nucleus, associated to each of the (e, 2e) SI events which constitute the TS2 mechanism, was not taken into account in previous published papers [12, 26, 35]. In contrast, in present case, one must take into account the possibility for one electron to be ejected in the $-\mathbf{K}^*$ direction in the first SI step, and for the other electron to be ejected in the $-\mathbf{K}'$ direction in the second step. The necessity for including recoil contribution is motivated by two reasons: first, the two ionized electrons have the same kinetic energy and second, the molecular nitrogen target considered here was shown in former (e, 2e) studies [10, 36] to produce large recoil intensity as opposed to helium [37]. Making the same analysis as above yields four other possible ejection directions. These additional recoil contribution angular predictions of TS2 kinematical model are: (a) in the opposite directions of $\theta_{K^*}^{<\pi}$ and $\theta_{K^*}^{>\pi}$ in the first (e, 2e) collision; (b) in the opposite directions of $\theta_{K'}^{<\pi}$ and $\theta_{K'}^{>\pi}$ in the second (e, 2e) collision. Hence, we label these directions as $\theta_{-K^*}^{<\pi}$ and $\theta_{-K^*}^{>\pi}$ for the first SI step, and $\theta_{-K'}^{<\pi}$ and $\theta_{-K'}^{>\pi}$ for the second SI step, respectively, where the implication of the notation is obvious.

For the (e, 3-1e) unequal energy sharing case, because the two ejected electrons are distinguishable in energy and the slower one ejected from first SI step is undetected, the recoil contribution only keeps its signature in the second SI step. The corresponding angles are denoted similar to the equal energy sharing case, i.e., $\theta_{-K'}^{<\pi}$ and $\theta_{-K'}^{>\pi}$ (see Tabs. 4.4 and 4.5).

Alternatively, in the equal energy sharing case, the recoil contribution in both first and second steps is included as stated above. As a consequence, this TS2 kinematical model including recoil

contribution gives two more angular predictions in equal energy sharing case than in the unequal energy sharing case in (e, 3-1e) measurement (see Tabs. 4.2 and 4.3).

At the end, using this TS2 kinematical model we obtain eight possible values in equal energy sharing cases ((E_b:E_c) = (12:12) and (37:37) eV) and four possible values for unequal energy sharing cases ((E_b:E_c) = (72:12) and (144:12) eV) for the emission angles of the detected 'b'-electron. The so predicted values are listed in Tables 4.2 to 4.5 (last columns), for the energies considered in this work.

For equal energy sharing case, since one electron is undetected in an (e, 3-1e) experiment and both electrons are here fully undistinguishable, each one of these eight values of emission angles can occur in our (e, 3-1e) experiments, which makes the analysis of the data displayed in Fig. 4.1 quite complicated. However, the situation is not desperate, as these eight angle values can be grouped into two sets which are well separated from each other as well as from the $\pm \boldsymbol{K}$ direction (corresponding to first order mechanisms), each set forming a relatively narrow angular band. These bands extend from 77 ° to 103 ° and 257 ° to 283 ° in the case of (E_b:E_c) = (12:12) eV and from 73 ° to 107 ° and 253 ° to 287 ° in the case of (E_b:E_c) = (37:37) eV. They are represented in Figs. 4.1(a) and 4.1(b) as the dashed areas. It is remarkable that most of the additional structures mentioned in forth item above fall within these angular bands for both the forward and backward lobes and are located at larger angles with respect to the momentum transfer direction (the most noticeable exception is the structure at ~315 ° whose origin cannot be associated with any of the emission angles predicted by our kinematical two-step model.) The presence of these structures is obviously at the origin of the non-symmetry about $\pm \boldsymbol{K}$ of the distributions discussed in third item above. We thus conclude that the angular distributions are strongly influenced by the TS2 mechanism. Of course, we do not exclude contributions from TS1 and SO mechanisms but their effects should be more important in the momentum transfer direction ($\pm \boldsymbol{K}$) than at larger angles. The present results on N_2 agree with those obtained for DI of rare gases in the same kinematical regime, hence comforting the conclusion that a first order theory is not sufficient to explain the experimental data.

For unequal energy sharing case, since one electron is not detected in an (e, 3-1e) experiment, but the two emitted electrons are distinguishable because of unequally shared energies, the TS2 kinematical model gives only four angular predictions with consideration of recoil contribution. In first SI (e, 2e) step, the ejected electron (corresponding to slower ejected electron, e_c) either from binary or recoil contribution as well as intermediate scattered electron e_{a^*} are not detected in the final (e, 3-1e) 4DCS measurement. The 4DCS of unequal energy sharing coplanar measurements at (E_b:E_c) = (72:12) eV and (144:12) eV are displayed in Figs. 4.2(a) and 4.2(b), respectively. The momentum transfer direction and its opposite $\pm \boldsymbol{K}$ are presented by dotted vertical lines, where the TS2 kinematical model angular predictions attributed to 'binary contribution' and 'recoil contribution' are denoted by dashed and dash-dotted vertical lines, respectively. We find the fact that all the

experimental results shown in Fig. 4.2 do display prominent structures for both forward and backward distributions. Remarkably, the predicted 'binary contribution' angular position values very nicely agree with the angular positions of the structures located at largest angles. This holds for all energy sharings considered in this work, from equal to highly unequal sharing. We thus conclude that the forward and backward structures' positions in Figs. 4.1 and 4.2 are strongly influenced by the TS2 contribution, according to the above qualitative kinematical analysis where the TS2 process is considered as two successive, independent (e, 2e) SI of the target. However, the contributions of first-order mechanisms (SO and TS1) might also be present in the (e, 3-1e) measurements. Their contributions should have their maximum close to momentum transfer direction or its opposite, θ_K or θ_{-K} , but their intensity appears to be appreciably smaller than that of the TS2 contribution for the forward lobe, more so for the backward lobe. The 'recoil contribution' predictions are agreeably in nice agreement with the lobes position of experimental measurements, for instance, in Fig. 4.2(a) at ~122 °, in Fig. 4.2(b) at ~138 ° and 248 ° (see Fig. 4.2 and Tables 4.4 to 4.5). This might indicate that even in the asymmetric case, the recoil contribution plays a very important role in DI under present kinematic conditions. However, all above analysis are generated from purely kinematical considerations. More elaborate theoretical calculations are needed to quantitatively confirm this argument.

To summarize, the (e, 3-1e) measurements demonstrate large deviations from first order prediction, such as large angular shift of the lobes from $\pm K$ direction, symmetry breaking of the lobes with respect to $\pm K$ direction, new structures, etc. We apply the TS2 kinematical model to give an explanation for the experimental results. This model yields good agreement with the observed lobes positions, especially for the new structures which are not in the vicinity of $\pm K$. The success of this TS2 kinematical model testifies that the second order dominates in DI process at present kinematics.

4.2.2 (e,3e) symmetric coplanar measurements

A. General analysis with TS2 kinematical model

Figs. 4.3(a) and 4.4(a) show in 2D representation the measured (e, 3e) five-fold differential cross section (5DCS) angular distribution of N_2 for (E_b:E_c) = (12:12) eV and (37:37) eV, respectively. To our best knowledge such (e, 3e) angular correlation diagrams are experimentally obtained here for the first time for a molecular target. We also display in Figs. 4.3(b) and 4.4(b) the calculated results obtained by Chuluunbaatar *et al* [24] using a correlated two center continuum (TCC) wave function for the description of the ejected electrons in a procedure which takes into account only the first term of the Born series (see §4.1.3). The presentation of these results is limited to the angular ranges (θ_b, θ_c) accessible in our experimental set up, where the angular detection ranges are limited to one half plane for each emitted electron, that is, 20 °<θ_c<160 ° and 200 °<θ_b<340 °. Note that we do not show here the

less sophisticated theoretical results obtained in [24] by neglecting the correlation in the final state and which drastically differ from the correlated results. However, in the 'cuts' presented later in Figs. 4.8 to 4.11, both theoretical calculations either with a correlation or without correlation in the final state are compared with the experimental data.

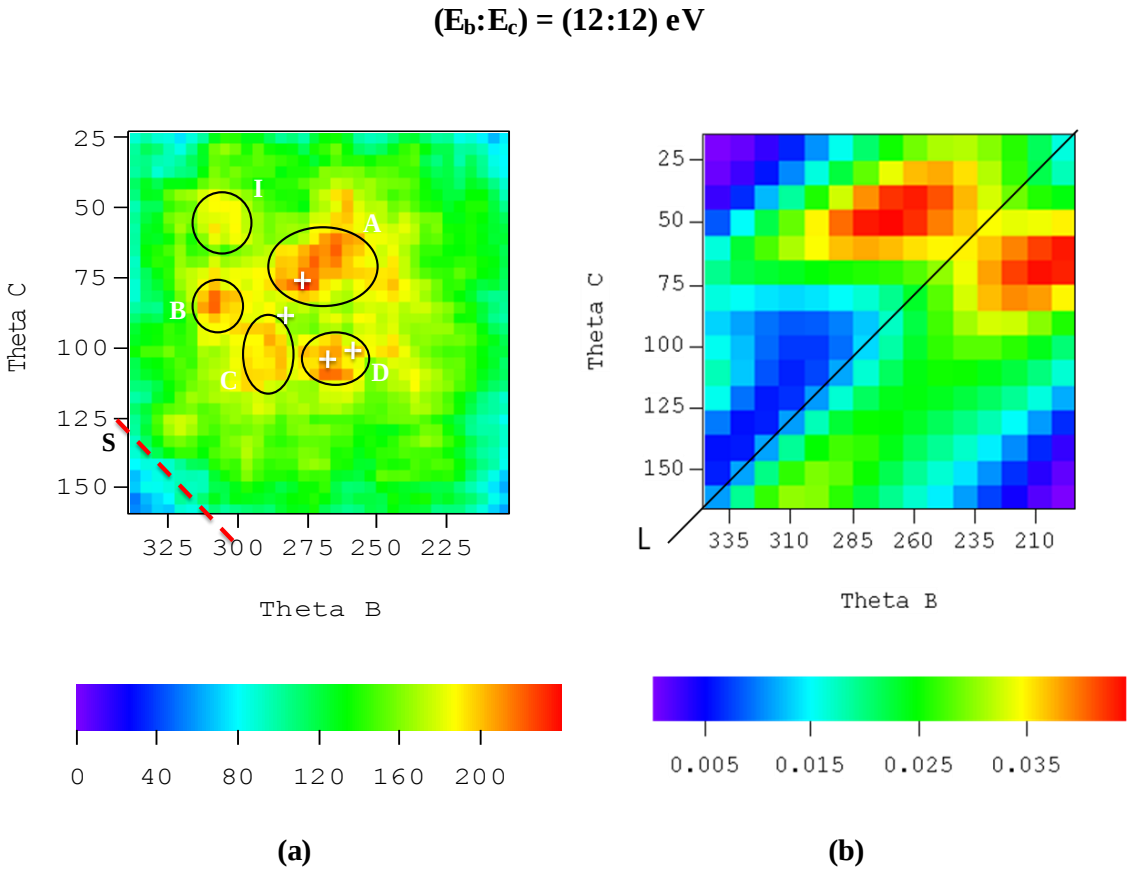

Figure 4.3 *Five-fold differential cross sections (5DCS) for double ionization of N_2. Panel (a): experiment; panel (b):FBA theory using a correlated TCC wave function (Ref. [149]). The scattered electron with energy E_a = 500 eV is detected at an angle θ_a = -6 ° in coincidence with both emitted electrons with an energy sharing of (E_b:E_c) = (12:12) eV. The bar gives the relative scale of the cross section. The most preeminent and the secondary structures in the experimental results are encircled and labeled A, B, C, D and I, respectively. The crosses indicate the most probable emission directions predicted by our kinematical two step model. See text. The dashed red line indicates the symmetry line for two emitted electrons with respect to momentum transfer direction +**K**. The diagonal line (L) indicates the back-to-back emission direction.*

(E_b:E_c) = (37:37) eV

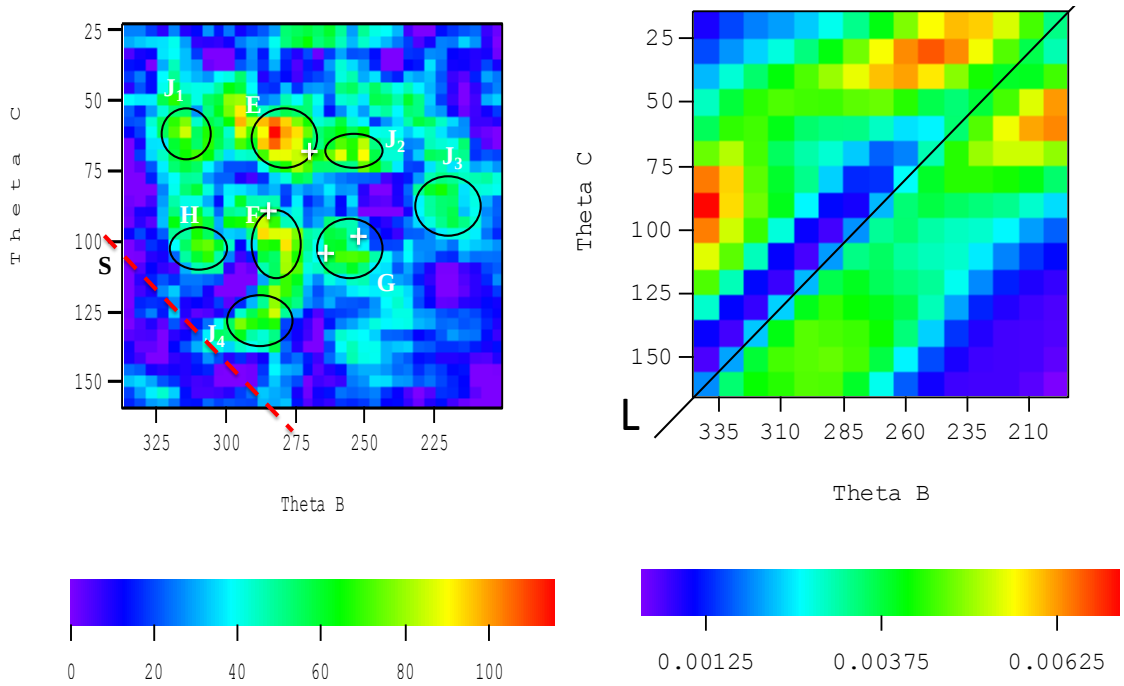

Figure 4.4 *The same as in Fig. 4.3, but for an energy sharing (E_b:E_c) = (37:37) eV. The encircled most preeminent and secondary structures are now labeled E, F, G, H and J_1, J_2, J_3, J_4, respectively (See sections A and B). The diagonal line (L) indicates the back-to-back emission direction. The 'S' line indicates the symmetry line for two emitted electrons with respect to momentum transfer direction* ***+K.***

The experimental 2D-diagrams display rich structure with several maxima, indicating the complex interaction with the target at low ejected energies. We want to emphasize that, despite the modest energy and angular resolution, we believe these structures do have physical meaning for two reasons. First, each peak structure is not made of one single bin but of several neighboring bins. It is the integral of the structure which defines whether a peak is present or not. Second, the intensity that is present out of the peaks is not a background but pure true (e, 3e) triple coincidence signal forming a more or less uniform contribution. The noise signal contribution has been subtracted from the raw data.

For convenience, the structures present in Figs. 4.3(a) and 4.4(a) are encircled in the figures and are labeled as A, B, C, D, I for (12:12) eV case and E, F, G, H, J_1, J_2, J_3, J_4 for (37:37) eV case, respectively. Though there are plentiful structures shown in Figs 4.3(a) and 4.4(a), only preeminent structures for instance A, B, C, D and E, F, G, H will be discussed in details and for other secondary structures such as I, J_1, J_2, J_3, J_4, we only make a tentative interpretation.

Firstly we compare our experimental results with the theoretical ones [24]. We may have a general observation that there is almost general disagreement between experiments and theory as to the intensity distribution for both considered energy sharings. None of the maximum intensity structures predicted by theory is found in the experiments. In Fig. 4.4(b) of (37:37) eV case, the theory predicts a 'valley' along the direction $\theta_b \sim \theta_c + 180°$ shown by the diagonal line named 'L'. This minimum stands for the well-known forbidden node in the back to back emission geometry predicted by theory in the case of photo double ionization of He, see e.g. [38, 39]. The experimental results in Fig. 4.4(a) display some similarity with the theory as to this feature, though same as in Fig. 4.3(a) the valley is only partially present and is interrupted in different angular domains. This partial filling of the node in the back-to-back emission might be due to the complexity of the molecular target and also due to the experimental overall energy resolution which does not allow discriminating among the first states of the residual N_2^{2+} ion. In Fig. 4.3(a) (for (12:12) eV case), the structure 'A' is roughly in agreement with the theoretical prediction that the maximum position located at around $(\theta_b,\theta_c) = (260°, 50°)$ if we take into account the fact that 'A' extends over a wide angular range, that is, $\sim 235° < \theta_b < \sim 300°$, $\sim 40° < \theta_c < \sim 80°$. This could be the signature of the presence of first order contribution in the measured 5DCS distribution. Since the first order (first Born) fails to predict the experimental results, we could conclude that under the present kinematics, the DI process is largely dominated by second (or higher) order mechanism, such as TS2. Thus due to the absence of elaborate theory of DI for molecular, we compare the experimental results with TS2 kinematical model we discussed in Chap. 3.

The angular distributions show that under different equal energy sharing cases, the profile of the maxima's appearance is different. In (37:37) eV case, the maxima are more pronounced and more localized while in (12:12) eV case the maxima are more diffuse. Previous (e, 2e) studies, e.g. [40, 41], showed that the (e, 2e) lobes become narrower as the ejected energy and/or the momentum transfer is

increased. Thus we conclude that our experimental observation is consistent with the (e, 2e) feature. This indirectly supports our TS2 kinematical model where DI is understood as two successive (e, 2e) SI events.

Because the two ejected electrons are detected in opposite halves of the collision plane ($\mathbf{k_0}$, $\mathbf{k_a}$) by the (e, 3e) spectrometer, this limits the eight pairs of possible emission angles discussed in Tables 4.2 to 4.3 (columns 3 and 4) to only four pairs of angles (θ_b:θ_c) as given in column 5 of these Tables. These TS2 kinematical model predictions of the most probable emission directions of the two ejected electrons 'b' and 'c' are indicated with thick crosses in Figs. 4.3(a) and 4.4(a). As discussed before, there is few or no relationship between experimental results and first Born model. The first Born model shows maxima positions at (50 °, 260 °), (70 °, 210 °) for (12:12) eV case and at (90 °, 340 °), (35 °, 250 °) and (60 °, 200 °) for (37:37) eV case. In fact, most of the above positions do not appear in experimental results. In contrast, we find some qualitative similarities (or even quantitative in some cases) between the positions of the experimental structures and TS2 kinematical model predictions.

For instance, we observe for the (12:12) eV case that:

- structure A partly corresponds to the pair (θ_b:θ_c) = (77 °, 278 °);
- structure C partly corresponds to the pair (θ_b:θ_c) = (283 °, 87 °). Note that both of these two structures result from two successive binary – binary (e, 2e) SI collisions by TS2 kinematical model prediction.
- structure A shows two wings elongated symmetrically with respect to upper right corner, these two wings may correspond to the two peaks predicted by theory which are located at (θ_b:θ_c) = (50 °, 260 °) and (70 °, 210 °). Hence the wings could be at least partly the contribution from first order mechanisms.
- structure D corresponds to an admixture of the pairs (θ_b:θ_c) = (103 °, 267 °) and (257 °, 98 °). Similar as structure C, this structure D may result from two successive but recoil – recoil (e, 2e) SI collisions.

Similarly, we observe for the (37:37) eV case that:

- structures F and E are very close to the pair (θ_b:θ_c) = (73 °, 276 °) and (287 °, 87 °), respectively. From Table 4.3, we can find that these two structures F and E may result from two successive binary – binary (e, 2e) SI collisions.
- Structure G corresponds to an admixture of the pairs (θ_b:θ_c) = (96 °, 253 °) and (107 °, 267 °). Again, from Table 4.3, we find that both of these two pairs result from two successive *recoil–recoil* (e, 2e) SI collisions. Hence, structure G also may have a corresponding relationship that it may originate from TS2 recoil – recoil (e, 2e) SI collisions.

B. Discussion of Schematic emission diagrams

In [32], Naja, A. et al proposed a new analysis method for the results of their (e, 3e) measurements of Ar under similar experimental conditions (coplanar, equal energy sharing, θ_a=-6°) but with higher energy of 205 eV for the two ejected electrons. According to the peak's location in (e, 3e) 2D angular distribution, they indicated the corresponding emitting directions of two ejected electrons and gave a physical explanation of the origin for those peaks.

We list all the emission directions of two ejected electrons in DI for those 'additional' structures which could not be interpreted so far neither by first Born theoretical model nor by TS2 kinematical model. Those structures are labeled as 'I' and 'B' in (12:12) eV case and 'J_1', 'J_2', 'J_3' and 'J_4' in (37:37) eV case, respectively. For completeness, we also list the emission directions of the outgoing electrons in DI process for other structures which have already been explained, namely, structures 'A', 'C', 'D' in (12:12) eV case and 'E', 'F', 'G', 'H' in (37:37) case (see Figs. 4.5 and 4.7).

i) In (12:12) eV case, the structure 'I' centered around (θ_b:θ_c) = (-55°, +60°) approximately corresponds to the emission direction where the two electrons are found at about equal but symmetrical angles ±60° from the third scattered electron (θ_a=-6° is close to 0°). We can find similar structure 'J_1' (θ_b:θ_c) = (-45°, +60°) in the (37:37) eV case. These positions of the two structures ('I' on the one side and 'J_1' on the other side) are similar with the structure named 'F' in Naja, A., et al [32] (this 'F' is irrelevant with our 'F' in Fig. 4.5(a) of the present work). These specific peak structures located around ±***K*** are also found in previous (e, 3-1e) experiments [42] on Ar and in recent (e, 3-1e) measurements of N_2 [13] (also presented in §4.2.2). The (e, 3-1e) results in [13] display peak structures at ~60° and ~240° (or -60°) in both (12:12) eV case and (37:37) eV case. The common feature of these (e, 3e) and (e, 3-1e) measurements is that the peaks' positions are such that they are very close to momentum transfer direction (see Figs. 4.1(a) and 4.1(b)). Since our (e, 3e) measurements represent the two dimensional angular distribution of 'b' and 'c' electrons which are indistinguishable, these peaks are found along the momentum transfer direction of 'c' electron, e.g., structure 'I' in (12:12) eV case locating at ~ (θ_b:θ_c) = (-55°, +60°) where the momentum transfer direction of electron 'c' is θ_{-K}=+56°. These peaks being adjacent to ±***K*** in (e, 3-1e) measurements are attributed to first order contribution. In this emission geometry, all of three outgoing electrons move to forward direction, thus it is called 'forward' emission.

ii) Naja, A., et al [32] also found the so-called 'backward' emission of both ejected electrons ejected at about equal angles ±120° from the third one with respect to the incident direction. They argued that the 'backward' emission with highly symmetric situation tends to minimize the final state Coulomb repulsion between the three electrons and these 'forward' and 'backward' structures are associated to a SO process.

(E_b:E_c) = (12:12) eV

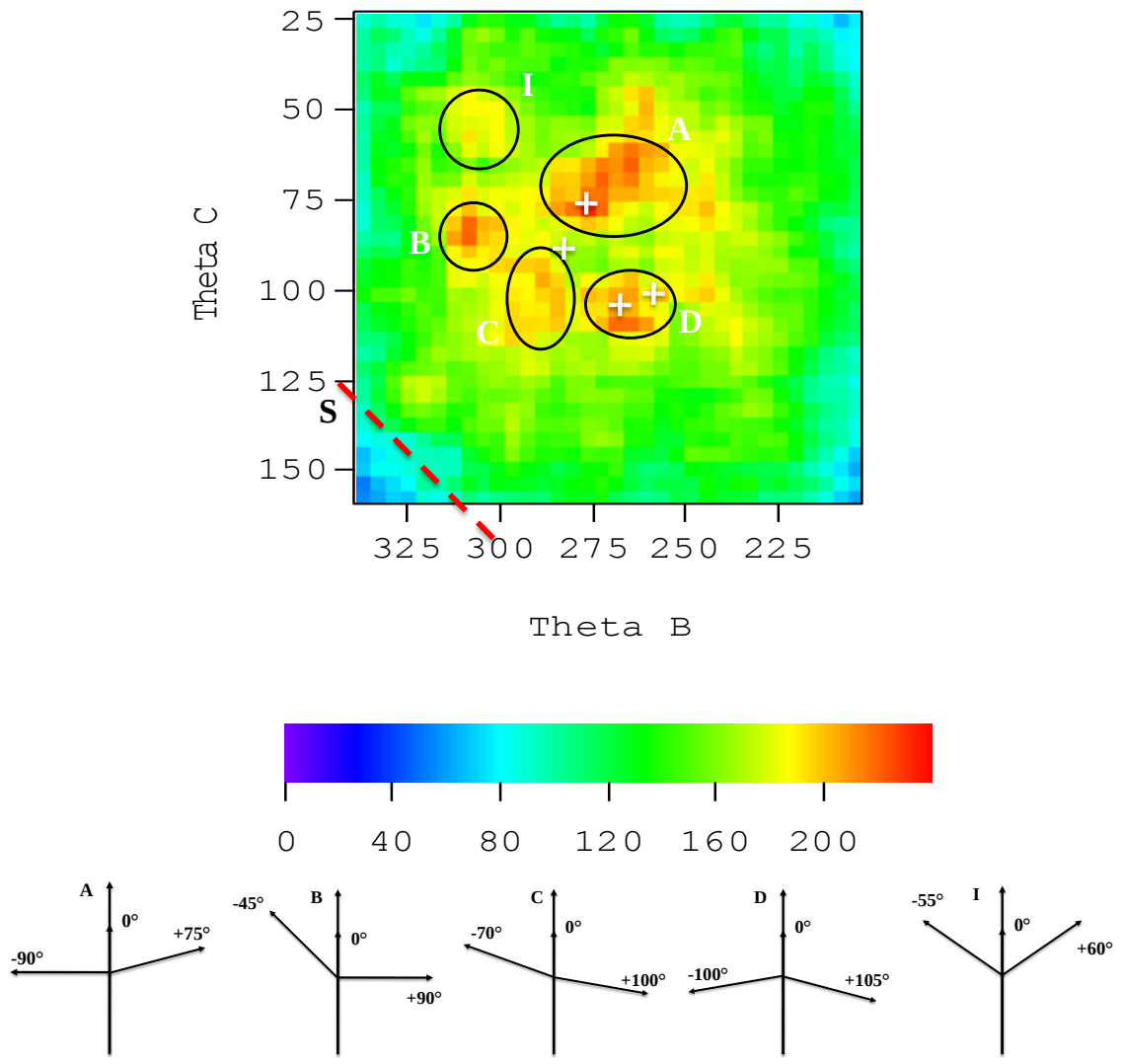

Figure 4.5 *The same as in Fig. 4.3(a). The diagrams at the bottom illustrate the emission directions of the three electrons, for the peaks labeled A, B, C, D and I, respectively, see section B.*

In our experiments, correspondingly, the similar structure can be found in the (e, 3e) results of (12:12) eV and (37:37) eV, respectively, namely the structure 'D' in Fig. 4.3(a) and the structure 'G' in Fig. 4.4(a), which locate at the same position of (θ_b:θ_c) ~ (-100°, +105°). Despite the fact that these two structures had already been attributed to TS2 contribution in previous discussion (see §4.3.2, Sec. A) and more precisely to an admixture of two successive recoil-recoil (e, 2e) SI collision, we can reexamine the origin of these structures 'D' and 'G' by taking into account also the presence of a SO mechanism and its possible interference with the TS2 mechanism. This leads us to consider structures 'D' and 'G' as a complex combination of first and second order mechanisms.

iii) We recall the well-established general feature of (e, 3e) measurement which states that if the DI process is the result of one single projectile-target interaction (or first order mechanisms) then the cross section distribution must exhibit a symmetry axis whose existence corresponds to both electrons being ejected symmetrically with respect to the momentum transfer direction [38]. This symmetry line or so-called 'S' line is defined by $\theta_b - \theta_K = -(\theta_c - \theta_K)$, see Figs. 4.3(a) and 4.4(a), where it is indicated by dash thick line with the notation 'S' at lower left corner). However, in this work, due to a small momentum transfer and due to the practical angular range limitation of present spectrometer for the two ejected electrons, the symmetric 'mirror' structures with respect to S-line cannot be accessed in our experiments. These 'mirror' structures should be found in the angular range of $0° \leqslant \theta_b < 180°$ and $180° \leqslant \theta_c < 360°$ whereas the present angular detection ranges are roughly $200° \leqslant \theta_b < 340°$ and $20° \leqslant \theta_c < 160°$. Therefore, it is highly desirable to perform full angular range (e, 3e) coplanar experiments ($0° \leqslant \theta_b < 360°$, $0° \leqslant \theta_c < 360°$) under same kinematics if possible to testify this symmetric 'mirror' structure assumption on the one hand and confirm the validity of our previous observations on the other hand.

iv) We realize that the relative intensity of the structures reported in Figs. 4.3(a) and 4.4(a), that is the intensity ratio of each structure to maximum intensity reveals the relative importance of the contribution by different mechanisms under various kinematical conditions. As stated in the above two figures, we associated the forward structures 'I' and 'J_1' to first Born contribution. J. H. McGuire [43] predicted that in DI process, second order contribution increases very fast as the incident electron energy decreases below ~ 1keV whereas the first order keeps a constant contribution, independent of incident energy (see Chap. 3, Fig. 3.6). It would be interesting to list all parameters of the (e, 3e) experiments (including Naja et al [32] on Ar), and the intensity ratio of the corresponding forward peaks to the maximum of the scale. From Table 4.1, it is seen that the ratio of the structure 'J_1' (associated to (37:37) eV case) is roughly the same as the structure 'I'

(associated to (12:12) eV case). This is due to the small incident energy difference of 56 eV. However, in Naja, A., et al's results at the much higher incident energy of ~1 keV, the forward peak intensity is comparable to the maximum intensity. Moreover, the incident energy and detected energies are larger than in the present work. This observation is consistent with McGuire J. H.'s prediction [43]. This might be the indirect experimental proof that as the incident energy is decreased, the role of first order mechanism contribution will become less important. In other words, the non-first order mechanisms such as TS2 mechanism play a more and more important role or even predominate over first order mechanisms when incident energy decreases to present kinematics. This conclusion is also consistent with previous studies [12, 13, 44, 45].

(E_b:E_c)	N_2 (12:12) eV	N_2 (37:37) eV	Ar (205:205) eV
E_0/eV	561	617	953
Relative intensity of forward peak	~ 185	~ 88	~ 37
Maximum intensity of the scale	~ 240	~ 120	~ 37
Intensity ratio	~ 0.77	~ 0.73	~1.0

Table 4.1 *Relative intensity ratio of forward emission peak to maximum of the scale. Ar results are deduced from the data of Naja, A. et al [32].*

(E_b:E_c) = (37:37) eV

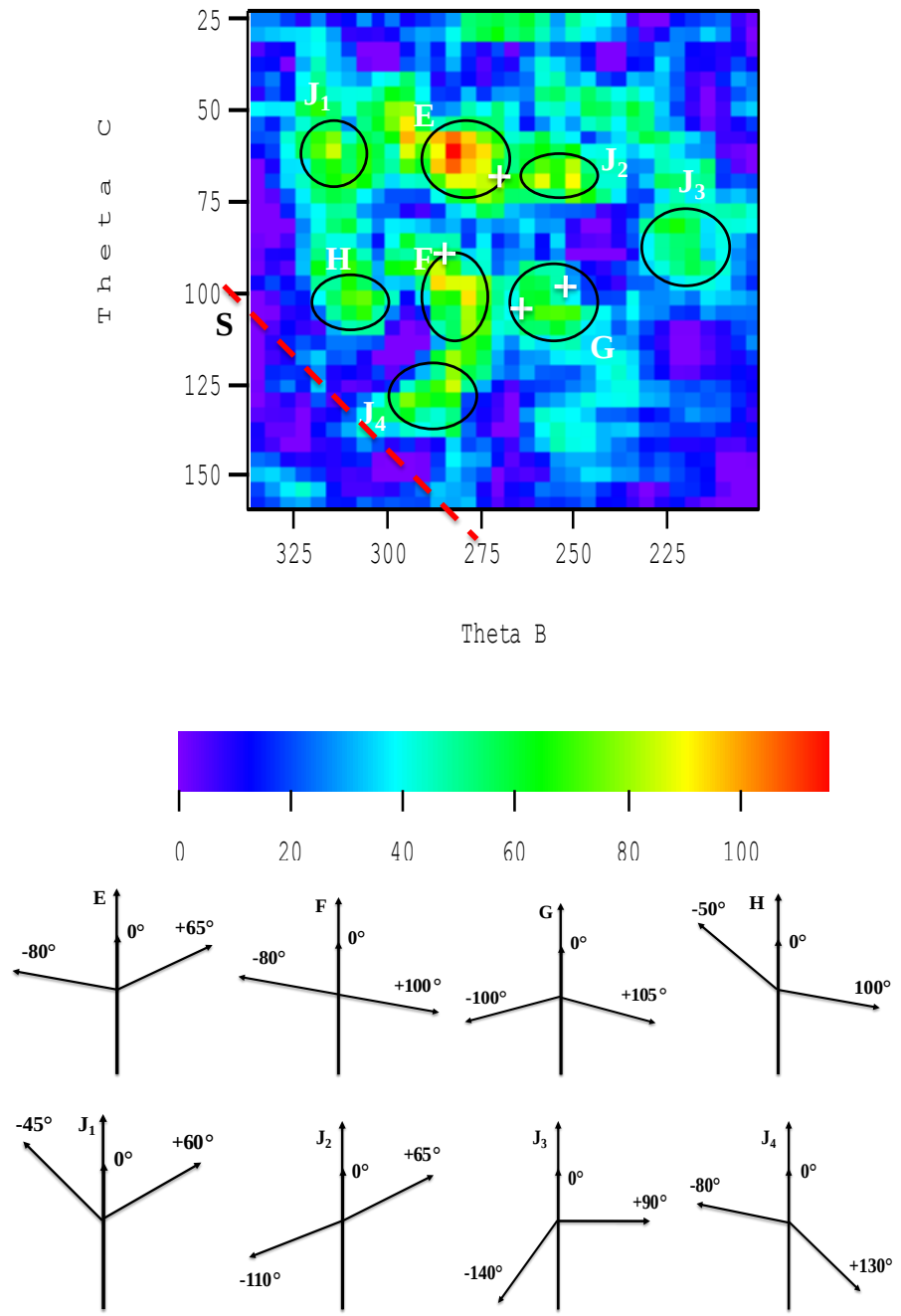

Figure 4.6 *The same as in Fig. 4.4(a). The diagrams at the bottom illustrate the emission directions of the three electrons, for the peaks labeled E, F, G, H, J_1, J_2, J_3 and J_4, respectively, see section B.*

v) We come back now to the emission diagrams shown in Fig. 4.5 and 4.6. The structures 'B' occur at the angles (θ_b:θ_c) = (-45°, +90°) in the (12:12) eV case, and the structures 'H', 'J_2'

and 'J_3' occur at (-50°, +100°), (+65°, -110°) and (-140°, +90°) in the (37:37) eV case. The structures 'B' and 'H' are located roughly at the same position though the kinematics is different, while the structure 'J_3' is at a mirror position with respect to fixed $\theta_c \sim +90°$. Indeed the structures 'B' and 'H', the 'c'-electron is ejected to perpendicular direction from incident direction while the 'b' electron is emitted to $\theta_b \sim -45°$. For structure 'J_3', the 'c'-electron is ejected to perpendicular direction ($\theta_c \sim +90°$) with respect to the incident direction but 'b'-electron is ejected to symmetric direction of $\theta_b \sim -140°$, with respect to 'b'-electron direction of structures 'B' and 'H'. For 'J_3', it seems to be irrelevant to neither first order nor second order mechanisms. The similarity of these four structures ('B', 'H', 'J_2' and 'J_3') is that one of the ejected electrons is emitted approximately at perpendicular direction from incident direction. A more elaborate theoretical model is desirable to explain these structures.

These two structures 'J_4' located at (θ_b:θ_c) ~ (-80°, +130°) and 'J_2' located at (θ_b:θ_c) ~ (-110°, +65°) will be discussed in detail in §4.3.2, Sec. C.

vi) Finally, the deviation of the experimental structures' position from TS2 predictions (e.g., structure 'C' in Fig. 4.3(a) and structures 'E' and 'F' in Fig. 4.4(a)) can be attributed to the simplicity of the TS2 kinematical model, in which neither the post collision interaction between the outgoing electrons nor the initial and final electronic state of the target is taken into account. Moreover, we notice the fact that additional structures ('I', 'J_1' to 'J_4') do exist in Figs. 4.3(a) and 4.4(a) which are not be predicted by the kinematical TS2 model. Their presence certainly testifies of the intrinsic complexity of molecular DI process. In particular, it should be noted that the observed structures B and H (for the (12:12) eV and (37:37) eV cases, respectively), do appear at about the same angular position as the structures at ~315° shown in the (e,3-1e) results (Figs. 4.1(a) and 4.1(b)) whose origin could not be associated with none of the emission angles predicted by this TS2 kinematical model.

C. Different cuts mode discussion

The relative success of our TS2 kinematical model as compared to the almost complete failure of the first Born predictions leads us to conclude that the measured (e, 3e) angular distributions for DI of N_2 molecule under the present kinematics is largely dominated by higher order processes such as TS2. Such conclusion is consistent with and confirms the one reported above for (e, 3-1e) experiments. It is also in good accord with the previous works of our group on atomic targets in a very similar kinematical regime, both in the (e,3-1e) case [12, 25, 26, 45] and in the (e,3e) case [46]. Due to the dual multi-angle data accumulation in this work, and to the continuous nature of both θ_b- and θ_c-variables, the data may be sorted in a variety of modes, which correspond to different cuts through the

2-dimensional intensity angular distribution in Figs. 4.3(a) and 4.4(a). Hence, a large number of angular distributions can be produced.

The information contained in the 2-D diagrams presented in Figs. 4.3(a) and 4.4(a) is a global one. To go into a detailed discussion of the corresponding (e, 3e) results, we here consider different cuts of the 2-D diagrams.

There are different methods to make such cuts. For example, in [47], El Marji, et al proposed three different modes:

i) either at fixed θ_b and varying θ_c, or vice versa, hereafter referred to as 'θ - variable mode';

ii) or at varying θ_b and θ_c, but keeping fixed the mutual angle θ_{bc}, hereafter denoted 'fixed mutual angle mode'. A case of particular interest is the one where the mutual angle is fixed to the value of π: this corresponds to a back-to-back emission of both ejected electrons.

iii) or in the so called 'symmetric geometry' with varying but equal angles $\theta_b = -\theta_c$ (or $\theta_b = 360° - \theta_c$).

In [48], Jia et al considered a new mode, namely S-symmetry or S-mode. As expected from any first-order model [49], the theoretical results exhibit a symmetry axis whose existence corresponds to both electrons being ejected symmetrically with respect to the momentum transfer: $\theta_b - \theta_K = -(\theta_c - \theta_K)$ or its opposite.

In [50], Hda et al proposed that in order to test the first Born approximation, a coplanar situation where an ejected electron leaves the target in the direction of the momentum transfer, the second electron being ejected in the plane defined by the incident electron and momentum transfer. If the angular distribution of the second ejected electron is not symmetric around the momentum transfer $\vec{K}$, it will be a proof that the two-step mechanism is not negligible. We note that this is a particular case of the θ-variable mode, when θ_b or θ_c is fixed to $\pm\vec{K}$ direction, i.e. θ_K or θ_{-K}.

In [51] and [52], the 2-dimensional intensity angular distribution of the (e, 3e) results was analyzed by 'θ_b - variable mode' and 'θ_c - variable mode'. The data were also analyzed in the fixed mutual angle mode as well as in the symmetric geometry mode, that is, with $\theta_b = -\theta_c$, and S - mode.

In this work, the momentum transfer is small so that the S-symmetry line proposed by Jia et al in [48] lies in the left bottom corner of 2D (e, 3e) angular distribution, so this S-symmetry property originated from first order mechanism cannot be exploited in the analysis due to the limitation of the detection angular range of the two ejected electrons (see Figs. 4.4(a) and 4.5(a), 'S' lines). On the other hand, since the TCC theoretical results and experimental ones have barely any similarity, it is not useful to perform all accessible θ_b- or θ_c-fixed mode cuts to get more detailed information. Thus, we choose the following geometry cuts to investigate the (e, 3e) measurements in detail (see Fig. 4.7):

i) fixed θ_b or θ_c corresponding to momentum transfer and its opposite directions ($\pm\boldsymbol{K}$)

ii) back-to-back geometry, $\theta_b = \pi + \theta_c$

iii) symmetric geometry, $\theta_b = -\theta_c$.

We emphasize here that in the following cuts analysis, the theoretical calculations are normalized to the maximum of corresponding experimental data over the detected angular range.

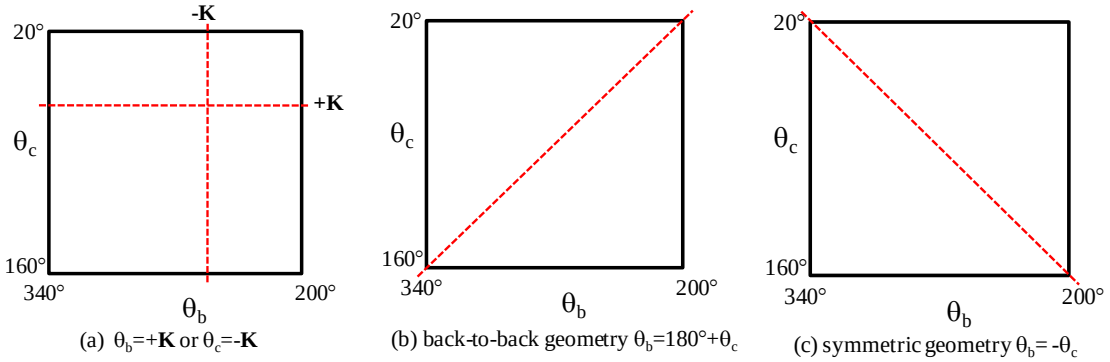

Figure 4.7 *Schematic of three cuts geometry: (a) ±**K**; (b)back-to-back geometry; (c)symmetric geometry. The red lines indicate the cuts from measured (e, 3e) results.*

The cuts are presented in Figs. 4.9 to 4.12. The solid black squares represent the experimental data with one standard deviation error bars. The green vertical arrows represent the directions where the peaks 'A' to 'J' (discussed above in the context of Fig. 4.5 and 4.6) are located along the cuts. The solid red and dash blue curves represent theoretical calculations within first Born approximation TCC-model respectively with and without correlation between the two ejected electrons in final state wave function. The model does not take into account the interaction between incident electron and the core and employs an appropriate correlated two center continuum wave function to describe two slow ejected electrons [24]. For convenience, the models with correlation and without correlation in final state are written for short as TCC-C (Two Center Continuum with Correlation) and TCC-OC (Two Center Continuum without Correlation) in following text, respectively. The theoretical results are normalized to the maxima of the experimental measurements in each energy sharing case, respectively.

From Figs. 4.8 to 4.11 we find large difference between experimental results and theory, either in fixed angle mode or in the symmetric geometry mode and back-to-back geometry mode.

In Fig. 4.8(a) (back-to-back geometry mode), the experimental results show a double peak structure which is symmetric with respect to θ_c = ~90 °, while both theoretical models only display one peak structure which is very roughly in agreement with the left peaks of the experiment. The right peak shown in experiment is completely absent in both theoretical models.

An interesting observation is that the structures 'I' and 'D' are located in the correct positions as compared to the experimental left (below 90°) and right (above 90°) peaks. The structure 'I' is in agreement with the position predicted by these two first order calculations: TCC-C and TCC-OC models while the structure 'D' which had been attributed to TS2 mechanism contribution (see §4.3.2, Sec. A) is absent in these two first order models. Thus we can conclude that (a): the structure 'I' is

relevant to first order contribution and structure 'D' is relevant to second order contribution; (b): under this kinematical condition, non-first order mechanism plays more important role during the interaction process.

Similarly, in Fig. 4.8(b) (symmetric geometry mode), the experimental results display a symmetric structure with respect to θ_c = ~90 °. In contrast, the TCC-OC model shows one single peak distribution with peak position at θ_c = ~90 °, whereas the TCC-C reveals two peaks structures which are more or less symmetric in position relative to θ_c = ~90 °. The intensity of right lobe is some 30% lower than that of the left one, which is roughly in qualitative agreement with the experimental results, although the intensity asymmetry is less pronounced in the experiments. Also, the experimental distribution exhibits more than two peaks. The improvement from TCC-OC to TCC-C model denotes the importance of including correlation in the final state.

In experiment, the two highest peaks close to θ_c = 90 ° are in agreement with the positions of the structures 'A' and 'C' along this cut. We observed that in Fig. 4.3(b) TCC-C indicates a wide 'wing' structure at the upper-right corner which is almost symmetrically distributed with respect to 'L' line (back-to-back emission direction). On the experimental side, a similar 'wing' structure can be found as well (labeled 'A' in Fig. 4.3(a)), though there is an angular shift down and left of ~ 10° and ~15°, respectively, with respect to the position of 'wing' predicted by TCC-C model.

In Fig. 4.8(b), the position of structures 'A' and 'C' along this cut are indicated by green short arrows. We find that the position of 'C' is roughly in agreement with the right peak's position of TCC-C model. We also noticed that the prediction of TS2 kinematical model for structure 'C' is not in the center of the encircled area. Therefore, we may conclude that the structures 'A' and 'C' are combined contribution of first order and second order mechanisms.

For the (E_b:E_c) = (12:12) eV case, Fig. 4.9 displays the fixed angle mode 5DCS distribution in panel (a), $\theta_c = \theta_K$ = 56 ° and panel (b), $\theta_b = -\theta_K$ = 236 °. We notice that the TCC-OC model in both cuts exhibits a single peak distribution centered at $\pm\boldsymbol{K}$ direction while the TCC-C model gets partly success in large angular range (240 °<θ_b<340 °) in panel (a) and in small angular range (20 °<θ_c<90 °) in panel (b). This inadequacy is probably at least partly due to the absence of the second order mechanism in the model.

The arrows denoted 'A' and 'I' in Fig. 4.9(a) are located at the experimental peaks' positions. However, their positions are not in agreement with both first Born theoretical calculations. In combination with the discussion in §4.3.2, Sec. B, we may say that the structure 'A' is partly contributed by first order mechanism (SO or/and TS1) whereas structure 'I' is mainly contributed by first order mechanism (SO and/or TS1).

$(E_b:E_c)$ = (12:12) eV

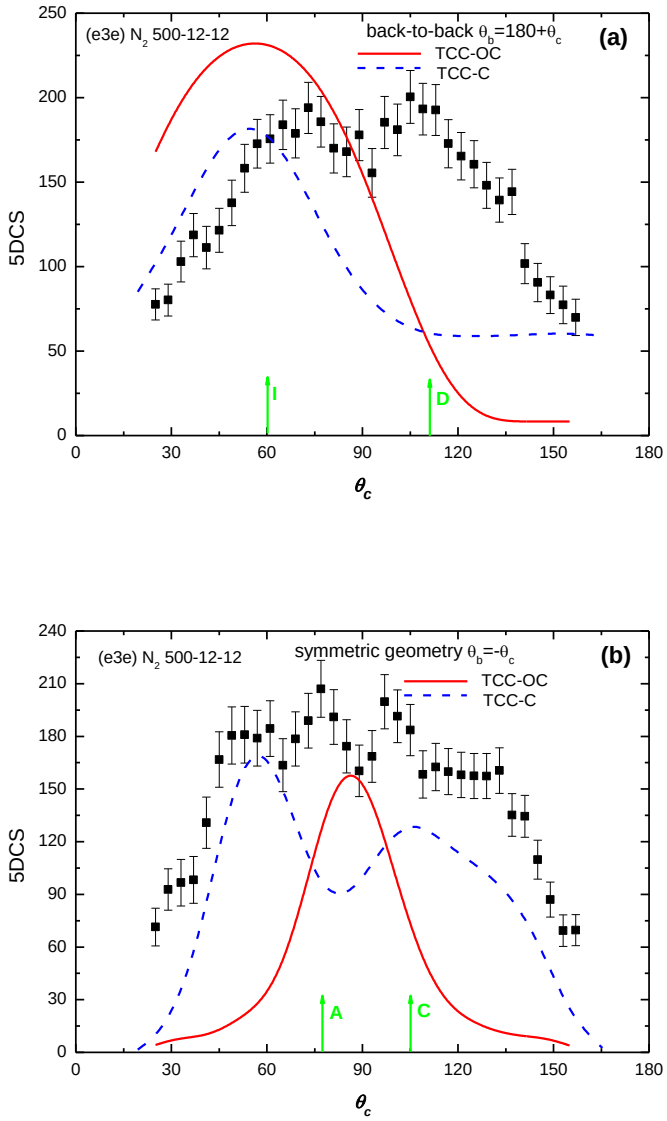

Figure 4.8 *(e, 3e) 5DCS angular distribution for N_2 at (12:12) eV in the 'back-to-back' geometry mode (panel (a)), $\theta_b = \pi + \theta_c$, and 'symmetric' geometry mode (panel (b)), $\theta_b = -\theta_c$, see section C. Full squares, experiments; full red curve, first Born results without correlation in final state; dashed blue curve, first Born results with correlation in final state. The green vertical arrows labeled I, D, C and A represent the positions where the peaks appearing in Fig.4.6 are located along the cuts.*

$(E_b:E_c)$ = (12:12) eV

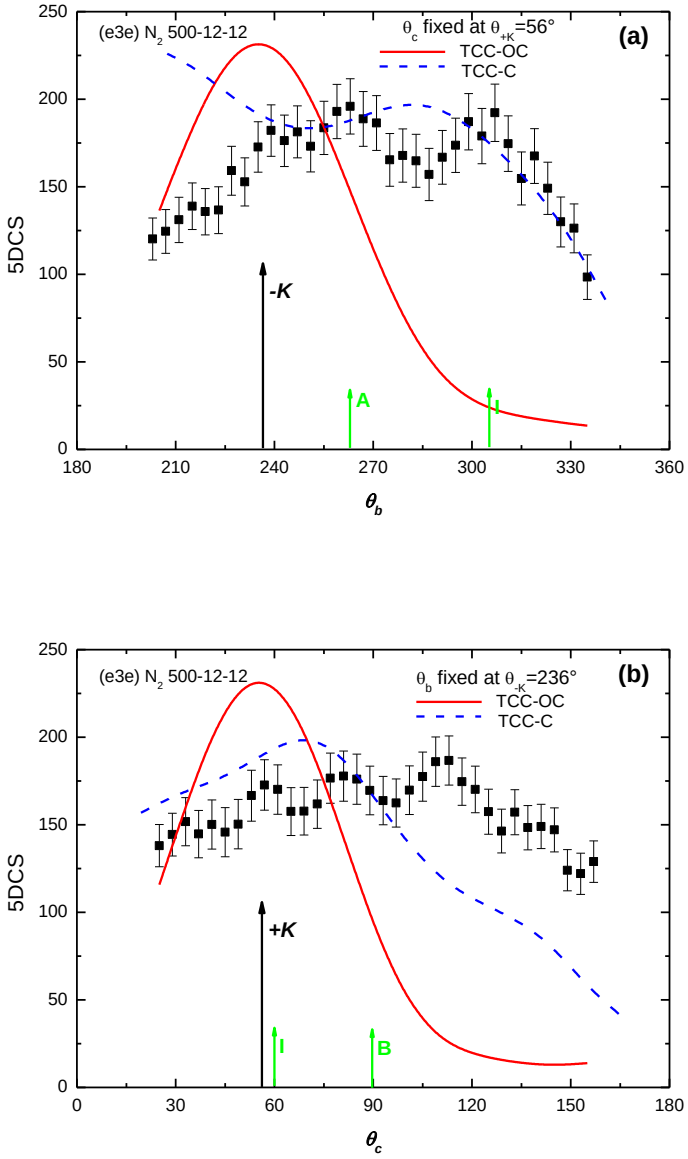

Figure 4.9 *(e, 3e) 5DCS angular distribution at (12:12) eV for N_2 in the fixed angle mode: panel (a), $\theta_c = \theta_K = 56$ °; panel (b), $\theta_b = -\theta_K = 236$ °; see section C. Full squares, experiments; full red curve, first Born results without correlation in final state; dashed blue curve, first Born results with correlation in final state. The green vertical arrows labeled I and A represent the positions where the peaks appearing in Fig.4.6 located along the cuts.*

$(E_b:E_c)$ = (37:37) eV

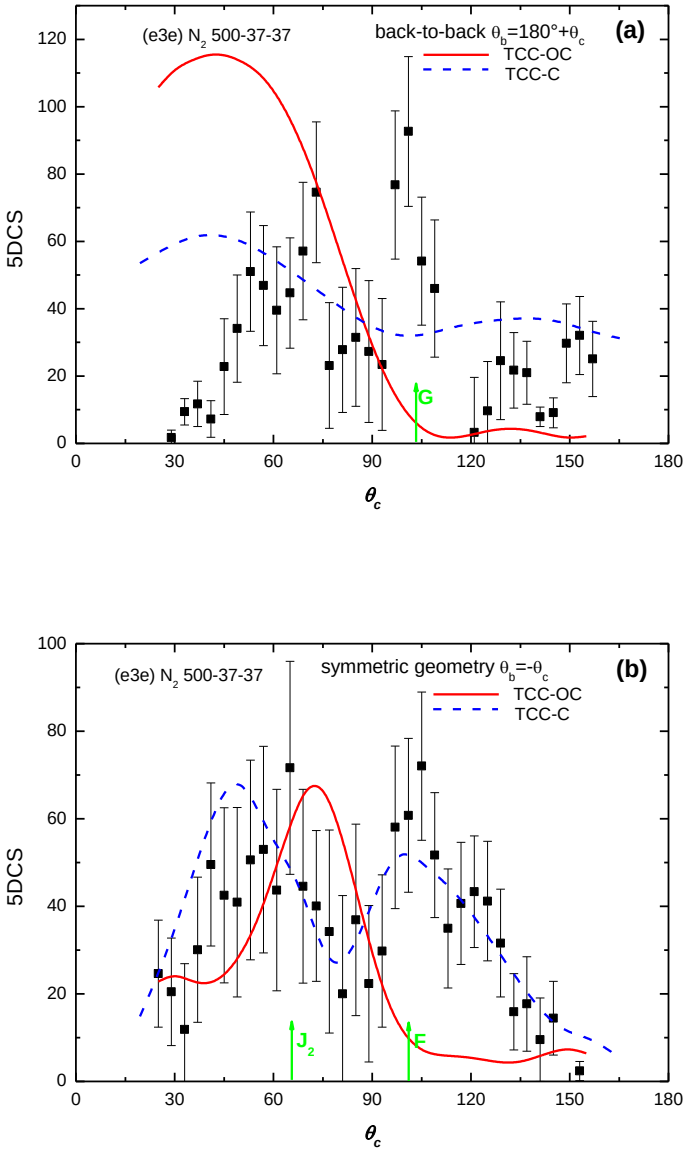

Figure 4.10 *The same as Figure 9 but for the case $(E_b:E_c)$=(37:37) eV. The green short vertical arrows labeled J_2 and F represent the positions where the peaks appearing in Fig.4.7 located along the cuts.*

(E_b:E_c) = (37:37) eV

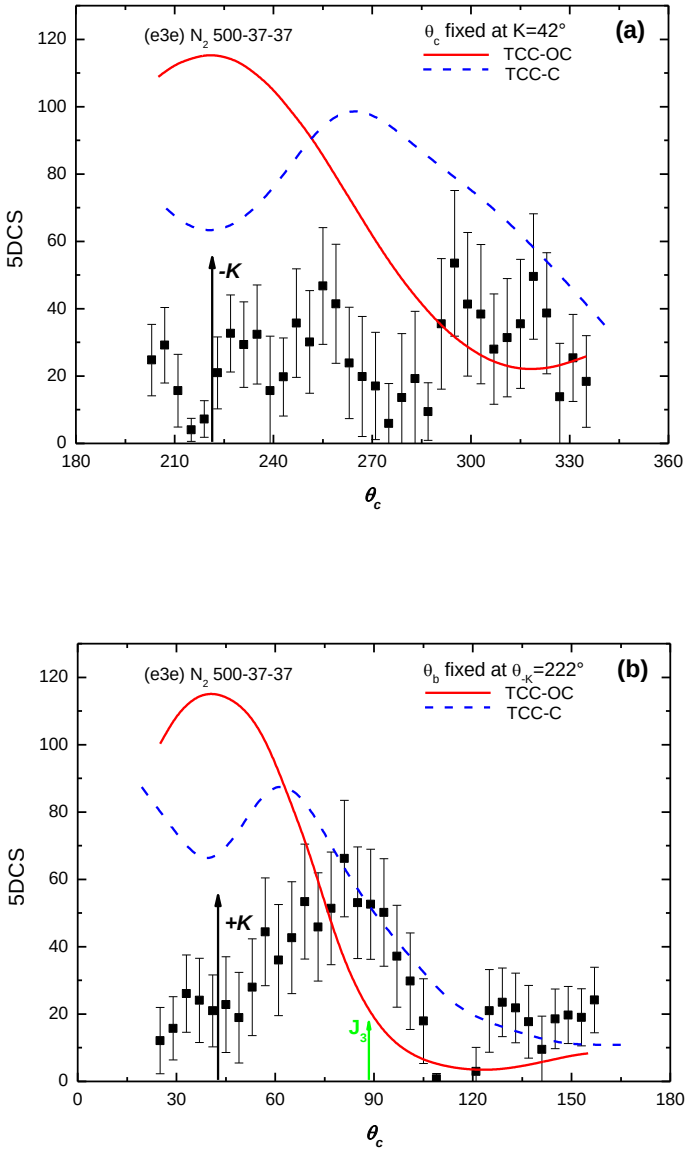

Figure 4.11 *The same as in Fig. 4.9 but for the case (E_b:E_c)=(37:37) eV. Panel (a), $\theta_c = \theta_K = 42$ °; panel (b), $\theta_b = \theta_{-K} = 222$ °, see text. The green vertical arrows labeled J_3 represents the positions where the peaks appearing in Fig.4.7 located along the cuts.*

For the (E_b:E_c) = (37:37) eV case, Fig. 4.10(a) presents results for back-to-back geometry. Here, the TCC-C model is roughly in agreement with the experimental distribution (given the large statistical error bars), except a large angular shift of the peak's position for ~20°-30° to small angular range. Again the TCC-C model is in better agreement with measured result than TCC-OC model.

Fig. 4.10(b) presents results for the symmetric geometry. It is remarkable that TCC-C model is in good agreement with experimental angular distribution. Same as in (12:12) eV case (see Fig. 4.8(b)), TCC-OC model predicts a maximum at ~90° whereas the experimental and TCC-C model show a minimum which corresponds to the case where the two ejected electrons are emitted at (θ_b:θ_c) = (-90°, +90°) geometry. Combined with the observation in (12:12) eV case, we may conclude that: (a) the first order mechanism such as SO and TS1 still play a role and keep its feature present especially in symmetric geometry mode under present kinematics; second, the correlation in the final state is very important: its inclusion definitely improves the results without correlation.

Fig. 4.11 displays the fixed angle mode 5DCS distribution for (E_b:E_c) = (37:37) eV case: in panel (a), $\theta_c = \theta_K$ = 42° and in panel (b), $\theta_b = \theta_{-K}$ = 222°. We notice that the TCC-OC model in both cuts exhibits a single peak distribution at $\pm\boldsymbol{K}$ direction while the TCC-C model indicates a minimum at $\pm\boldsymbol{K}$ direction. In Fig. 4.11(a), due to the low experimental statistics, it is difficult to discuss. In Fig. 4.11(b), compared to experimental measurements, the position of maxima predicted by the TCC-OC model which is at 42° has an angular shift of ~40°, with respect to the experimental maximum position which is at ~80°. Including the correlation in the TCC-C model reduces this angular shift to ~ 25°. Hence we can say that the large angular shift between experiment and theory partly due to the electron-electron correlation in the final state. However, on the other hand, since the first order theoretical model is not sufficient to describe this large angular shift, it might also be associated to the contribution of non-first order mechanisms.

In Fig. 4.11(b), the position of structure 'J_3' is in agreement with the position of the experimental maxima. Unfortunately, the structure 'J_3' is not produced by the first order TCC theoretical model, nor produced by our second order TS2 kinematical model. Thus the new theoretical development for DI of molecular target is awaited for.

To summarize, the first order theories almost fail to predict the (e, 3e) 5DCS measurement. However, the TCC-C model succeeds in predicting parts of the cuts with particular geometry. For example, in the cut of 'symmetric mode', the TCC-C model is in good agreement with experimental data for both energy sharing cases; in 'back-to-back' geometry mode and 'fixed angle' mode at (12:12) eV case, the TCC-C model more or less succeeds in predicting the experimental results over parts of the covered angular range, etc. These features may indicate the signature of first order contribution in

DI of N_2 at present work. Therefore, elaborate theoretical models are highly needed to give a better insight into more details of the DI dynamical process for molecular target.

4.3 Conclusion

We have reported new measurements for DI of molecular nitrogen at about 600 eV electron impact energy and both equal and unequal energy sharing among the two emitted electrons in (e,3-1e) experiments and also at equal energy sharing among the two emitted electrons in full (e,3e) experiments. We note that these are the first (e, 3e) experiments ever performed for a molecular target. The data are compared with the predictions of a simple kinematical model describing the TS2 mechanism as two successive (e, 2e) SI interactions. Due to the complex nature of the target, the model is extended to include binary as well as recoil scattering during the two successive SI events. It is shown to qualitatively predict the correct angular positions for most of the observed structures. Besides, it allows relating the majority of the structures present in the (e, 3e) distributions to particular combinations 'binary - binary' or 'recoil - recoil' scattering during the two successive (e, 2e) SI events.

The (e, 3e) experimental data are also compared with the predictions of a first Born model which is found to yield different angular distributions. Only in some special cut modes, the first order TCC-C model is partly in agreement with experimental results. This observation, together with the relative success of the kinematical two-step model leads us to legitimately conclude that the molecular DI process is largely dominated by TS2 mechanism (without excluding the intervention of higher order mechanisms). This work together with our previous ones on atomic targets thus constitutes a large body of experimental evidence that under the present kinematics the TS2 mechanism dominates over the first order SO and TS1 mechanisms. To further confirm this conclusion, it is highly desirable to develop elaborate first order and/or second order calculations, which are lacking at the time of writing and to which our experimental data could be compared. Two non-first order models have been recently proposed for atomic targets, based on a second Born treatment on the one side [45, 53] and on a Monte Carlo approach of TS2 mechanism, on the other side [45, 54].

4.4 Bibliography

1. Naja, A., et al., *Triply differential (e,2e) cross sections for ionization of the nitrogen molecule at large energy transfer*. Journal of Physics B-Atomic Molecular and Optical Physics, 2007. **40**(18): p. 3775-3783.
2. Lahmam-Bennani, A., et al., *Identification of mechanisms of electron impact double ionizing collisions by e,(3-1)e experiments*. Journal of Physics B-Atomic Molecular and Optical Physics , 1991. **24**: p. 9.
3. Ullrich, J., et al., *Recoil-ion momentum spectroscopy*. Journal of Physics B: Atomic, Molecular and Optical Physics, 1997. **30**(13): p. 2917.
4. Dörner, R., et al., *Cold Target Recoil Ion Momentum Spectroscopy: a 'momentum microscope' to view atomic collision dynamics*. Physics Reports, 2000. **330**(2–3): p. 95-192.
5. Catoire, F., et al., *New developments for an electron impact (e,2e)/(e,3e) spectrometer with multiangle collection and multicoincidence detection*. Review of Scientific Instruments, 2007. **78**(1): p. 013108-8.
6. Casagrande, E.M.S., et al., *(e,2e) ionization of helium and the hydrogen molecule: signature of two-centre interference effects*. Journal of Physics B-Atomic Molecular and Optical Physics, 2008. **41**(2).
7. Al-Hagan, O., et al., *Atomic and molecular signatures for charged-particle ionization*. Nat Phys, 2009. **5**(1): p. 59-63.
8. Mansouri, A., et al., *Double ionization of H_2 by electron impact: a second Born treatment*. Journal of Physics B-Atomic Molecular and Optical Physics, 2004. **37**(6): p. 1203-1214.
9. Yang, J. and J.P. Doering, *Asymmetric (e,2e) study of the 100-eV ionization of the $1\pi_g$, $1\pi_u$, and $3\sigma_g$ molecular orbitals of O_2*. Physical Review A, 2001. **63**(3): p. 032717.
10. Lahmam-Bennani, A., Staicu Casagrande, E.M. and Naja, A. *Experimental investigation of the triple differential cross section for electron impact ionization of N_2 and CO_2 molecules at intermediate impact energy and large ion recoil momentum*. Journal of Physics B-Atomic Molecular and Optical Physics, 2009. **42**(23): p. 235205.
11. Doering, J.P. and Yang, J. *Asymmetric (e,2e) measurement of vibrational intensities in the 100-eV electron-impact ionization of N_2 to the N_2^+ $X^2\Sigma_g^+$ and $A^2\Pi_u$ states*. Physical Review A, 1999. **60**(3): p. 2176-2181.
12. Li, C., et al., *Electron impact double ionization of neon, argon and molecular nitrogen: role of the two-step mechanism*. Journal of Physics B: Atomic, Molecular and Optical Physics, 2011. **44**(11): p. 115201.
13. Li, C., et al., *Identification of first order and non-first order contributions in the (e,3–1e) and (e,3e) double ionization of molecular nitrogen*. Journal of Physics B: Atomic, Molecular and Optical Physics, 2012. **45**(13): p. 135201.
14. Martyn, J.H. and Andrew, J.M. *Low energy (e, 2e) differential cross-section measurements on the $1\pi_g$ and $4\sigma_g$ molecular orbitals of CO_2*. Journal of Physics B: Atomic, Molecular and Optical Physics, 2005. **38**(16): p. 2965.
15. Lahmam-Bennani, A., et al., *Dynamics of electron impact ionization of the outer and inner valence ($1t_2$ and $2a_1$) molecular orbitals of CH_4 at intermediate and large ion recoil momentum*. Journal of Physics B-Atomic Molecular and Optical Physics, 2009. **42**(16).
16. Milne-Brownlie, D.S., et al., *Dynamics in electron-impact ionization of H_2O*. Physical Review A, 2004. **69**(3): p. 032701.
17. Champion, C., et al., *Single ionization of the water molecule by electron impact: Angular distributions at low incident energy*. Physical Review A, 2006. **73**(1).
18. Champion, C., Hanssen, J. and Hervieux, P.A. *Theoretical differential and total cross sections of water-molecule ionization by electron impact*. Physical Review A, 2002. **65**(2): p. 022710.
19. Champion, C., Hanssen, J. and Hervieux, P.A. *Influence of molecular orientation on the multiple differential cross sections for the (e,2e) process on a water molecule*. Physical Review A, 2001. **63**(5): p. 052720.
20. Dal Cappello, C., et al., *Double ionization of single oriented water molecules by electron impact: Second-order Born description*. Physical Review A, 2011. **83**(6): p. 062716.

21. Gao, J., D.H. Madison, and Peacher, J.L. *Distorted wave Born and three-body distorted wave Born approximation calculations for the fully differential cross section for electron impact ionization of nitrogen molecules.* J. Chem. Phys., 2005. **123**: p. 204314.
22. Serov, V.V. and Joulakian, B.B. *Calculation of the multifold differential cross section of the electron-impact ionization of molecular hydrogen by prolate spheroidal external complex scaling method with second Born corrections.* Physical Review A, 2010. **82**(2): p. 022705.
23. Chuluunbaatar, O., et al., *Modified two-centre continuum wavefunction: application to the dissociative double ionization of H_2 by electron impact.* Journal of Physics B: Atomic, Molecular and Optical Physics, 2008. **41**(1): p. 015204.
24. Chuluunbaatar, O., Gusev, A.A. and Joulakian, B.B. *The correlated two-centre double continuum and the double ionization of H_2 and N_2 by fast electron impact.* Journal of Physics B: Atomic, Molecular and Optical Physics, 2012. **45**(1): p. 015205.
25. Lahmam-Bennani, A., Duguet, A. and Roussin, S. *Observation of non-first-order effects in an (e, 3-1e) investigation of the double ionization of helium and molecular hydrogen.* Journal of Physics B: Atomic, Molecular and Optical Physics, 2002. **35**(2): p. L59.
26. Lahmam-Bennani, A., et al., *Predominance of the second-order, two-step mechanism in the electron impact double ionization of helium at intermediate impact energy.* Journal of Physics B: Atomic, Molecular and Optical Physics, 2010. **43**(10): p. 105201.
27. Lahmam-Bennani, A., et al., *Absolute triple differential cross sections for high-energy electron impact ionisation of helium.* Journal of Physics B: Atomic and Molecular Physics, 1983. **16**(12): p. 2219.
28. Avaldi, L., et al., *Absolute triple differential cross sections for electron impact ionisation of He at 1024.6 eV incident energy.* Journal of Physics B: Atomic and Molecular Physics, 1987. **20**(21): p. 5827.
29. Dupré, C., Lahmam-Bennani, A. and Duguet, A. *About some experimental aspects of double and triple coincidence techniques to study electron impact double ionizing processes.* Measurement Science and Technology, 1991. **2**(4): p. 327.
30. Rioual, S., et al., *Absolute (e, 2e) cross sections for the electron-impact ionization of helium in energy sharing kinematics at 44.6 eV.* Journal of Physics B-Atomic Molecular and Optical Physics, 1998. **31**(14): p. 3117-3127.
31. Van der Wiel, M.J. and Wiebes, G. *Multiple ionization of Ar by 10 keV electrons as a function of the energy loss.* Physica, 1971. **53**(2): p. 225-255.
32. Naja, A., et al., *An (e, 2e)-(e, 3e) investigation of argon: competition between inner-shell single ionization and direct double ionization processes.* Journal of Physics B-Atomic Molecular and Optical Physics, 2007. **40**(14): p. 2871-2884.
33. Dal Cappello, C., El Mkhanter, R. and Hervieux, P.A. *Mechanisms of double ionization of atoms by electron impact.* Physical Review A, 1998. **57**(2): p. R693-R696.
34. Dal Cappello, C., et al., *Second-order Born approximation for the ionization of molecules by electron and positron impact.* Physical Review A, 2011. **84**(3): p. 032711.
35. Casagrande, E.M.S., et al., *Experimental and theoretical confirmation of the role of higher order mechanisms in the electron impact double ionization of helium.* Journal of Physics B-Atomic Molecular and Optical Physics, 2011. **44**(5): p. 055201.
36. Avaldi, L., et al., *Ionization of the N_2 $3\sigma_g$ orbital by electron impact studied by asymmetric (e,2e) experiments.* Journal of Physics B: Atomic, Molecular and Optical Physics, 1992. **25**(16): p. 3551.
37. Kheifets, A.S., et al., *An energetic (e, 2e) reaction away from the Bethe ridge: recoil versus binary.* Journal of Physics B: Atomic, Molecular and Optical Physics, 2009. **42**(16): p. 165204.
38. Berakdar, J., Lahmam-Bennani, A. and Dal Cappello, C., *The electron-impact double ionization of atoms: an insight into the four-body Coulomb scattering dynamics.* Physics Reports, 2003. **374**(2): p. 91-163.
39. Kheifets, A.S., *Second-order Born model for two-electron atomic ionization by fast charged-particle impact.* Physical Review A, 2004. **69**(3): p. 032712.
40. Ehrhardt, H., et al., *Differential Cross-Sections of Direct Single Electron-Impact Ionization.* Zeitschrift Fur Physik D-Atoms Molecules and Clusters, 1986. **1**(1): p. 3-32.

41. Duguet, A., et al., *High-Accuracy (e, 2e) Cross-Sections for Helium - Reference Data in the 1st Born Approximation*. Journal of Physics B-Atomic Molecular and Optical Physics, 1987. **20**(22): p. 6145-6156.
42. Catoire, F., Lahmam-Bennani, A. and Duguet, A. *Coincidence angular correlations between scattered, ejected and Auger electrons in electron impact double ionization*. Physica Scripta, 2004. **T110**: p. 228-232.
43. McGuire, J.H., *Double Ionization of Helium by Protons and Electrons at High Velocities*. Physical Review Letters, 1982. **49**(16): p. 1153-1157.
44. Lahmam-Bennani, A., et al., *Predominance of the second-order, two-step mechanism in the electron impact double ionization of helium at intermediate impact energy*. Journal of Physics B: Atomic, Molecular and Optical Physics, 2010. **43**(10): p. 105201.
45. Staicu Casagrande, E.M., et al., *Experimental and theoretical confirmation of the role of higher order mechanisms in the electron impact double ionization of helium*. Journal of Physics B: Atomic, Molecular and Optical Physics, 2011. **44**(5): p. 055201.
46. Lahmam-Bennani, A., et al., *Importance of non-first-order effects in the (e,3e) double ionization of helium*. Physical Review A, 2003. **67**(1): p. 010701.
47. El Marji, B., et al., *Dynamics of the double ionization process from (e,3e) experiments: I. Absolute cross sections for argon*. Journal of Physics B: Atomic, Molecular and Optical Physics, 1997. **30**(16): p. 3677.
48. Jia, C.C., et al., *Deviations between experimental and theoretical results in Ar (e, 3e) double ionization*. Journal of Physics B: Atomic, Molecular and Optical Physics, 2003. **36**(1): p. L17.
49. Dal Cappello, C. and H. Le Rouzo, *Angular distributions in the double ionization of helium by electron impact*. Physical Review A, 1991. **43**(3): p. 1395-1404.
50. Hda, H., Dal Cappello, C. and Langlois, J. *Angular distributions of electrons in the (e, 3e) reaction*. Zeitschrift für Physik D Atoms, Molecules and Clusters, 1994. **29**(1): p. 25-29.
51. Schröter, C., et al., *Dynamics of the double-ionization process from (e, 3e) experiments: II. Fivefold differential cross sections for neon*. Journal of Physics B: Atomic, Molecular and Optical Physics, 1998. **31**(1): p. 131.
52. Lahmam-Bennani, A., et al., *Complete experiments for the double ionization of He: (e,3e) cross sections at 1 keV impact energy and small momentum transfer*. Journal of Physics B: Atomic, Molecular and Optical Physics, 2001. **34**(15): p. 3073.
53. Dal Cappello, C., et al., *The second Born approximation for the single and double ionization of atoms by electrons and positrons*. Journal of Physics B: Atomic, Molecular and Optical Physics, 2011. **44**(1): p. 015204.
54. Ciappina, M.F., Schulz, M. and Kirchner, T. *Reaction dynamics in double ionization of helium by electron impact*. Physical Review A, 2010. **82**(6): p. 062701.

Chapter 5 *Preliminary results for Ne and CH_4 at intermediate incident energy*

In this chapter, new (e, 3-1e) measurements for Ne and CH_4 will be presented and discussed briefly. The experimental (e, 3-1e) results of Ne are compared with both first order and second order theoretical models recently developed by Dal Cappello. Up to date, there is no theoretical calculation existing for the (e, 3-1e) results of CH4 under present kinematics. The TS2 kinematical model which has already been used and successfully validated for previous (e, 3e) and (e, 3-1e) measurements [1-4] is employed for the comparison with the experimental results of Ne and CH_4. For the two isoelectronic targets, it is also very interesting to investigate the target structure influence in DI process under same final kinematical states (see Fig. 5.1).

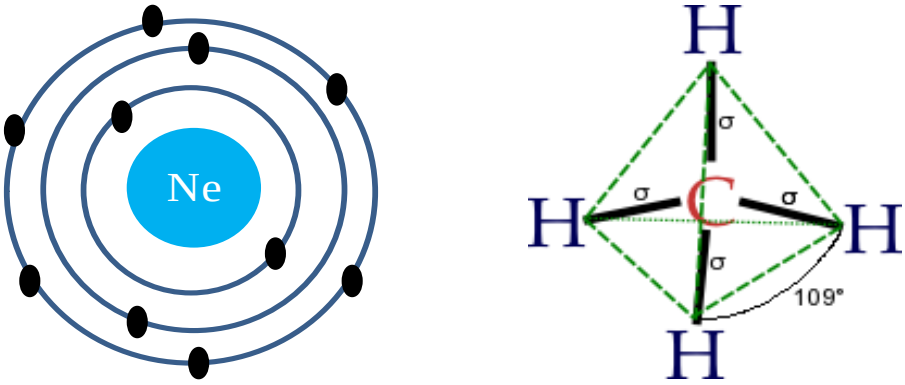

(a) Ne: $1s^2 2s^2 2p^6$ (b) CH_4: $1a_1^2 2a_1^2 1t_2^6$

Figure 5.1 *Schematic diagram of the charge distribution: (a) atomic target Ne and its ground state configuration; (b) molecular target CH_4 and its ground state configuration.*

5.1 Experimental conditions

The experimental setup and configurations are the same as used in Chap. 3 and Chap. 4. Briefly, the scattered 'a'-electron with energy of 500 eV is detected at $\theta_a = +(6° \pm 3°)$ and $\theta_a = -(6° \pm 3°)$ in coincidence with faster ejected 'b'-electron (the slower 'c'-electron is undetected) in coplanar geometry.

The experimental parameters are listed in Tab. 5.1. The present (e, 3-1e) experiments for Ne (2p) and CH_4 ($1t_2$) are performed with ejected electron energies (E_b:E_c) = (37:37) eV and (E_b:E_c) = (37:12) eV, respectively. The incident energy E_0 is adjusted to fulfill the energy conservation, $E_0 = E_a + E_b + E_c + IP^{2+}$, where IP^{2+} = 62.6 eV is the DI potential of Ne for removing two electrons from its (2p) outermost orbital and IP^{2+} = 38.0 eV is the DI potential of CH_4 for removing two electrons from its outermost orbital $1t_2$.

E_a = 500 eV θ_a = - 6 deg				
target	Ne		CH_4	
E_0 (eV)	636.6	611.6	612	587
E_b (eV)	37	37	37	37
E_c (eV)	37	12	37	12
K (a.u.)	1.03	0.93	0.93	0.83
θ_K/θ_{-K}(deg)	38/218	43/223	43/223	50/230

Table 5.1 *(e, 3-1e) experimental parameters for Ne and CH_4*

5.2 Results and discussion

The angular distributions of the (e, 3-1e) 4DCS, $d^4\sigma/dE_a dE_b d\Omega_a d\Omega_b$ for the DI of the outermost orbitals of Ne (2p) and CH_4 ($1t_2$) are shown in Figs. 5.2 and 5.3 at the two different energy sharings for the ejected electrons: (E_b:E_c) = (37:37), (37:12) eV, respectively (listed in Tab. 5.1). Note that the experimental data are obtained on a relative scale and have been arbitrarily normalized to the same value at the maximum of the forward lobe. The 4DCS scale shown is arbitrary, where all experimental and theoretical results are arbitrarily inter-normalised for best visual fit at the maximum of the forward lobe.

5.2.1 General observations

From a general, first view, some important common features are observed from the above experimental results, similar to the observations made for (e, 3-1e) in Chap. 3 and Chap. 4. Briefly, they can be summarized into four items:

a) in all energies cases (including equal and unequal energy sharing) for Ne and CH_4, the angular distributions exhibit a forward and a backward lobe, which roughly point in the momentum transfer direction (+***K***) and in the opposite direction (-***K***), respectively;
b) both lobes are not symmetrically distributed about the ±***K*** axis, and their maxima are shifted from these directions by large amounts;
c) the intensity distribution in each lobe is not symmetrically distributed about the ±***K*** direction;
d) besides, from these forward and backward lobes, there are additional structures exhibited in both Ne and CH4 (e, 3-1e) measurements.

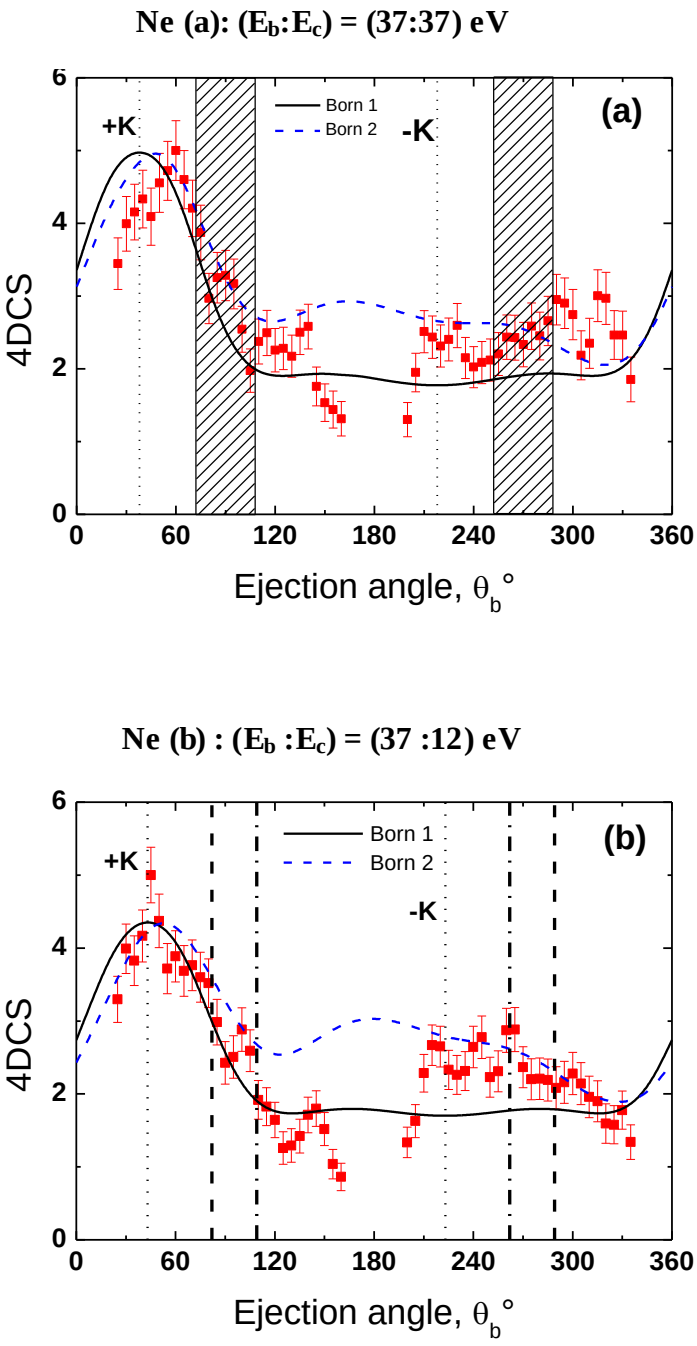

Figure 5.2 *Four-fold differential cross sections (4DCS) for double ionization of Ne. The scattered electron with energy E_a = 500 eV is detected at an angle θ_a = -6 ° in coincidence with one of the emitted electrons, while the second electron remains undetected (these ejected electrons are designated as 'b' and 'c' electrons, respectively). Panel (a): (E_b:E_c) = (37:37) eV; Panel (b): (E_b:E_c) = (37:12) eV. The experimental data (full squares) are represented with one standard deviation statistical error bar. The dotted vertical lines indicate the direction of momentum transfer (θ_K) and its opposite (θ_{-K}). In panel (a), the dashed areas indicate the angular ranges predicted by the kinematical TS2 model for ejection of the 'b'-electron, see Tab. 5.1. In panel (b), the thick dash lines and dash dotted lines indicate the binary and recoil contribution predictions of TS2 kinematical model, respectively, see Tables 5.2 and 5.3. The solid black and dash blue lines represent the first Born and second Born theoretical calculations (unpublished) by Dal Cappello, using same model as in [7]. The 4DCS scale shown is arbitrary, where all experimental and theoretical results are arbitrarily inter-normalised for best visual fit at the maximum of the forward lobe. Note that in panel (b), the theoretical calculations are normalized to the second highest point of experimental data for best guide of view.*

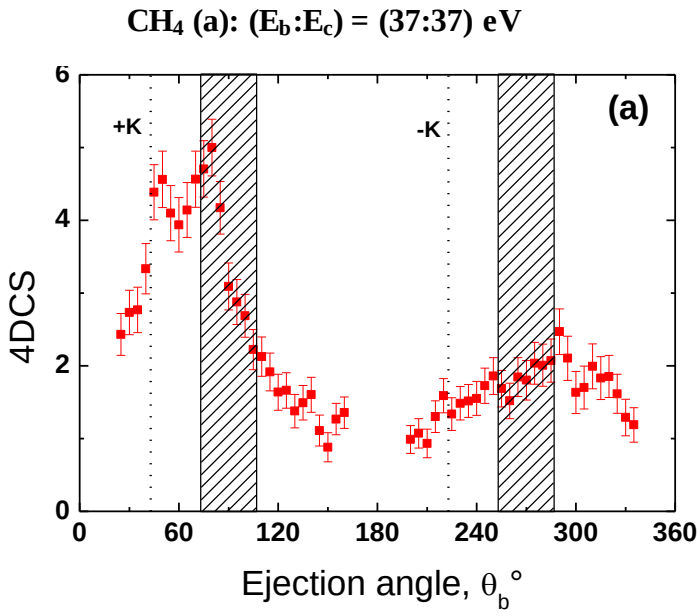

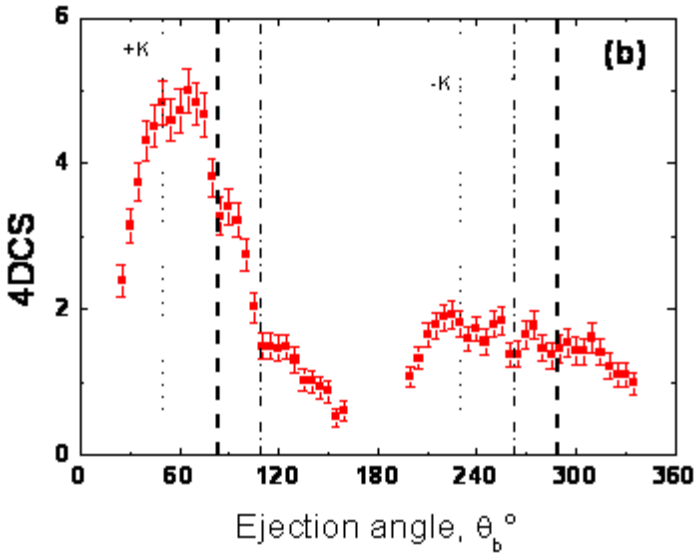

Figure 5.3 *The same as Fig. 5.2 but for CH_4: Panel (a): (E_b:E_c) = (37:37) eV; Panel (b): (E_b:E_c) = (37:12) eV. The TS2 kinematical model predictions are listed in Tables 5.4 and 5.5.*

The first order or first Born mechanisms involve only one single interaction of the projectile with the target and are characterized by its well known features namely the presence of two lobes located at

$\pm\boldsymbol{K}$ axis, and the symmetric intensity distribution about the $\pm\boldsymbol{K}$ axis. In the (e, 3-1e) 4DCS distribution, the symmetry of first order mechanism is obviously broken. Therefore these experimental observations (see above items (a) to (d)) are clear signatures of the presence of non-first-order mechanisms in the DI process [1, 5, 6]. This means that the contribution of TS2 mechanism to the DI process is sufficiently important with respect to that of SO and /TS1 mechanism. These observations are also consistent with previous results [2-4]. Thus, in order to explain the above features (third and fourth items), it is necessary to take into account not only first order mechanisms (SO and TS1) but also higher order mechanisms (such as TS2).

Recently, Dal Cappello et al developed first and second order models obtained within first Born (B1) and second Born (B2) for DI of Ne under the same kinematics as our experimental results. These new, yet unpublished theoretical results are compared with the experimental results (see Figs. 5.2(a) and 5.2(b)). In both B1 and B2 models, the incident and scattered electrons are described by plane wave. The final state wave function is a BBK wave function [13], where the interactions between outgoing electrons are included. In B2 model, the closure approximation is used for taking into account of all excited state of Ne by Dal Cappello et al [7].

The first Born (B1) and second Born (B2) are represented by solid black and dash blue curves for both energy sharing cases in Fig. 5.2, respectively. Both theoretical results are normalized to the maximum of experimental results. Note that as stated in the legend of Fig. 5.2, the two theoretical results in Fig. 5.2(b) are normalized to the second highest point of experimental data for best guide of view.

From Figs. 5.2, we can observe that B1 model shows symmetric distribution with respect to $\pm\boldsymbol{K}$ directions and shows almost flat intensity in backward lobe. On the contrary, B2 model correctly reproduce the angular shift of the forward lobe respect to $+\boldsymbol{K}$ direction and is roughly in good agreement with the experimental 4DCS angular distribution both in forward and backward lobes. Particularly, B2 model predict much higher intensity than B1 model in backward lobe of both energy sharing cases. We notice that in Fig. 5.2(b), the highest point is remarkably higher than its neighbor points. Because in the experiments, the standard deviation statistical error bar is used, we can safely consider this point as a statistics result. Hence it does not bring in any essential influence to our discussion. Though there are still some structures cannot be reproduced by B2 model, e.g. the structure located at ~325 ° in (E_b:E_c)=(37:37) eV (see Fig. 5.2(a)), the agreement between theory and experiment are satisfactory. The large deviation between B2 model and experimental results in the angular range from ~ 150 ° to ~ 210 ° might associate to the edge effect of the analyzers, where B2 shows a lobe and high intensity whereas the experimental results exhibits a minimum. These observations lead us to the conclusion that under present kinematics, second order mechanism plays a

important role to the 4DCS contribution and the (e, 3-1e) experimental results on Ne can be correctly reproduced by B2 model.

5.2.2 Two-Step 2 kinematical model analysis

As discussed in Chaps. 3 and 4, due to the successful achievements in comparison with previous electron impact DI results at intermediate impact energy, the TS2 kinematical model is employed once again for comparison with the experimental results. This TS2 kinematical model was firstly developed by Lahmam-Bennani, A., et al [1] and described in §3.4.2. Moreover, we extend this model by including recoil contribution in second (e, 2e)-like step for unequal energy sharing case and in first and second (e, 2e)-like steps for equal energy sharing case, respectively. The extension of this TS2 kinematical model has also been described in details in §3.4.2 Sec. B and §4.2.2. Because of indistinguishibility of the two ejected electrons for equal energy sharing case, this TS2 model gives four more angular position predictions than unequal energy sharing case. For unequal energy sharing case, only the ejected electron ionized from second (e, 2e)-like step (binary or recoil contribution) is detected in coincidence with the scattered one whereas the ejected electron from first (e, 2e)-like step (binary or recoil contribution) can be distinguished due to their different energies of two ejected electrons. The predictions of TS2 kinematical model are represented in Tables 5.2 to 5.5 and indicated in Figs. 5.2 and 5.3 by different vertical lines (see captions of these figures).

Ne (E_b:E_c) = (37:37) eV

first order mechanisms θ_K / θ_{-K}	second order TS2 mechanism			
	intermediate θ_{a*}	first step θ_{K*}	second step $\theta_{K'}$	expected θ_b for (e,3-1e) case
38 °/ 218 °	positive	bin $\theta_{K*}^{>\pi}$ = 288 °	bin $\theta_{K'}^{<\pi}$ = 98 °	288 ° or 98 °
			rec $\theta_{-K'}^{>\pi}$ = 278 °	
		rec $\theta_{-K*}^{<\pi}$ = 108 °	bin $\theta_{K'}^{<\pi}$ = 98 °	
			rec $\theta_{-K'}^{>\pi}$ = 278 °	108 ° or 278 °
	negative	bin $\theta_{K*}^{<\pi}$ = 72 °	bin $\theta_{K'}^{>\pi}$ =266 °	72 ° or 266 °
			rec $\theta_{-K'}^{<\pi}$ = 86 °	
		rec $\theta_{-K*}^{>\pi}$ = 252 °	bin $\theta_{K'}^{>\pi}$ =266 °	
			rec $\theta_{-K'}^{<\pi}$ = 86 °	252 ° or 86 °

Table 5.2 *Expected emission directions for the 'b' and 'c' electrons in the case (E_b:E_c) = (37:37) eV associated to: first order mechanisms SO and/or TS1 (first column); second order mechanism TS2 predicted by our kinematical model in the (e,3-1e) case by taking into account the fact that both ejected electrons are detected in opposite half-planes (columns 3 and 4). The expected angles by TS2 kinematical model in our experiments are listed in column 5.*

Ne (E_b:E_c) = (37:12) eV

first order mechanisms θ_K / θ_{-K}	second order TS2 mechanism			
	intermediate θ_{a*}	first step θ_{K*}	second step $\theta_{K'}$	expected θ_b for (e,3-1e) case
43 ° / 223 °	positive	bin $\theta_{K*}^{>\pi}$ = 284 °	bin $\theta_{K'}^{<\pi}$ = 109 °	109 °
			rec $\theta_{-K'}^{>\pi}$ = 289 °	
		rec $\theta_{-K*}^{<\pi}$ = 104 °	bin $\theta_{K'}^{<\pi}$ = 109 °	
			rec $\theta_{-K'}^{>\pi}$ = 289 °	289 °
	negative	bin $\theta_{K*}^{<\pi}$ = 76 °	bin $\theta_{K'}^{>\pi}$ =262 °	262 °
			rec $\theta_{-K'}^{<\pi}$ = 82 °	
		rec $\theta_{-K*}^{>\pi}$ = 256 °	bin $\theta_{K'}^{>\pi}$ =262 °	
			rec $\theta_{-K'}^{<\pi}$ = 82 °	82 °

Table 5.3 *The same as Table 5.1 but for Ne (E_b:E_c) = (37:12) eV case.*

CH_4 (E_b:E_c) = (37:37) eV

first order mechanisms θ_K / θ_{-K}	second order TS2 mechanism			
	intermediate θ_{a*}	first step θ_{K*}	second step $\theta_{K'}$	expected θ_b for (e,3-1e) case
43 ° / 223 °	positive	bin $\theta_{K*}^{>\pi}$ = 287 °	bin $\theta_{K'}^{<\pi}$ = 96 °	287 ° or 96 °
			rec $\theta_{-K'}^{>\pi}$ = 276 °	
		rec $\theta_{-K*}^{<\pi}$ = 107 °	bin $\theta_{K'}^{<\pi}$ = 96 °	
			rec $\theta_{-K'}^{>\pi}$ = 276 °	107 ° or 267 °
	negative	bin $\theta_{K*}^{<\pi}$ = 73 °	bin $\theta_{K'}^{>\pi}$ =267 °	73 ° or 267 °
			rec $\theta_{-K'}^{<\pi}$ = 87 °	
		rec $\theta_{-K*}^{>\pi}$ = 253 °	bin $\theta_{K'}^{>\pi}$ =267 °	
			rec $\theta_{-K'}^{<\pi}$ = 87 °	253 ° or 87 °

Table 5.4 *Expected emission directions for the 'b' and 'c' electrons in the CH_4 case (E_b:E_c) = (37:37) eV associated to: (first column): first order mechanisms SO and/or TS1; (columns 3 and 4): second order mechanism TS2 predicted by our kinematical model in the (e,3-1e) case by taking into account the fact that both ejected electrons are detected in opposite half-planes. The expected angles by TS2 kinematical model in our experiments are listed in column 5.*

CH_4 (E_b:E_c) = (37:12) eV

first order mechanisms θ_K / θ_{-K}	second order TS2 mechanism			
	intermediate θ_{a*}	first step θ_{K*}	second step $\theta_{K'}$	expected θ_b for (e,3-1e) case
50 ° / 230 °	positive	bin $\theta_{K*}^{>\pi}$ = 282 °	bin $\theta_{K'}^{<\pi}$ = 137 °	137 °
			rec $\theta_{-K'}^{>\pi}$ = 317 °	
		rec $\theta_{-K*}^{<\pi}$ = 102 °	bin $\theta_{K'}^{<\pi}$ = 137 °	317 °
			rec $\theta_{-K'}^{>\pi}$ = 317 °	
	negative	bin $\theta_{K*}^{<\pi}$ = 78 °	bin $\theta_{K'}^{>\pi}$ =258 °	
			rec $\theta_{-K'}^{<\pi}$ = 78 °	
		rec $\theta_{-K*}^{>\pi}$ = 258 °	bin $\theta_{K'}^{>\pi}$ =258 °	258 °
			rec $\theta_{-K'}^{<\pi}$ = 78 °	78 °

Table 5.5 *The same as Tab.5.4 but for CH_4 (E_b:E_c) = (37:12) eV case.*

The predictions of TS2 kinematical model including recoil contribution are compared with the experimental data. In Figs. 5.2(a) and 5.3(a) of equal energy sharing case for Ne and CH_4, these TS2 predictions listed in Tables 5.2 and 5.4 (fifth column) are indicated by the dash areas, respectively. In Figs. 5.2(b) and 5.3(b) of unequal energy sharing case for Ne and CH_4, these TS2 predictions are indicated by the thick dash lines (binary contribution) and dash dotted lines (recoil contribution), respectively. As shown in these figures, all TS2 predictions generally succeed to predict most structures' positions displayed in (e, 3-1e) experiment. Therefore, we conclude that TS2 mechanism has a important contribution as first order mechanisms (SO and/or TS1) at present kinematical conditions in DI process of Ne and CH_4.

However, there are still some structures that cannot been described by neither first order ($\pm$K) nor TS2 prediction, such as the lobes located at ~140 ° shown in Figs. 5.2(a) and 5.2(b) of Ne; the lobes located at ~310 °, shown in Figs. 5.3(a) and 5.3(b) of CH_4. This limitation of the TS2 kinematical model should be attributed to its simplicity of classical kinematical collision analysis.

5.2.3 Influence of target nature on (e, 2e) and (e, 3-1e) results

Since the targets Ne and CH_4 have the same numbers of electrons and kinematics of three outgoing electrons, it might be interesting to investigate the contribution of the target nature in DI process. Naturally, some of the differences in (e, 3-1e) 4DCS measurements between Ne and CH_4 can be attributed to the difference of target structure (or positive charge distribution) and electronic distribution. For Ne, it is an atomic target and it has a single nucleus structure. For CH_4, because it has

one heavy and four light nuclei, the 10 target electrons are more diffuse with respect to Ne (see Fig. 5.1 (b)). The 'diameters' of Ne and CH_4 are 0.072 nm and 0.414 nm, respectively. This means that the scale of molecular target CH_4 is ~6 times larger than atomic target Ne. Thus we might say that CH_4 might have a more diffused nuclei structure than Ne. Thus, we may assume that the differences in (e, 3-1e) measurements between Ne and CH_4 under same kinematics might essentially be influenced by the target structure and electronic distribution.

The recoil lobe in SI TDCS results represents the contribution of the target nuclei reflection. If we compare the single ionization of Ne and CH_4 in the same kinematics to show the structure influence in SI process, the structure influence can be easily evaluated by comparing the recoil lobe in TDCS angular distribution. However, in DI case, where the target structure influence is much more complex than SI case, only some comments will be done.

Structure influence on (e, 2e) results

As a first step we recall the previously published (e, 2e) measurements of Ne [8] and CH_4 [9] as an evidence for the above argument (see Figs. 5.4 and 5.5).

The triple differential cross section (TDCS) distributions for ionization of the outer 2p orbital of Ne and $1t_2$ orbital of CH_4 at E_b = 37 eV are shown in Figs. 5.4 and 5.5. For CH_4, the data (taken from Ref [9]) are compared with the calculated results obtained using two models : 1 Coulomb Wave [10] (1CW) model, where the scattered electron is described by a plane wave and the ejected electron is described by a Coulomb wave) and Brauner-Briggs-Klar (BBK or 3C) [11] model, where a correct asymptotical Coulomb three-body wave function for the projectile and the ejected electron in the field of the residual ion is used, whereas for Ne, the data (also taken from Ref [8]) are compared with Distorted Wave Born Approximation with Gamow factor (DWBA-G) model [8]. Both two sets of experimental distributions yield the 'familiar' two-lobe structure of the TDCS: first, the so-called binary lobe pointing roughly in the momentum transfer direction (+$\boldsymbol{K}$). This structure is attributed to a classical binary collision between the incident electron and the target electron to be ejected, the rest of the target playing only a small role. The second lobe pointing more or less in the opposite (-$\boldsymbol{K}$) direction is usually smaller and broader than the binary one, and is thought to be due to a first binary collision sending the target electron in the +$\boldsymbol{K}$ direction, followed by a quantum backward reflection in the potential of the residual ion. This lobe is known as the recoil lobe since the nucleus must recoil to conserve the total momentum in the collision.

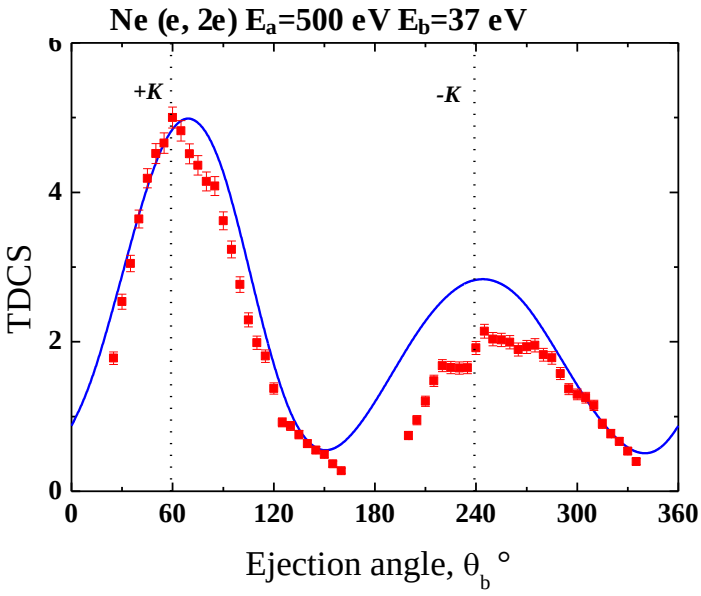

Figure 5.4 *(e, 2e) TDCS for ionization of the outer valence orbital ($2p^6$) of Ne at Ea=500 eV, θ_a=-6 °and E_b = 37 eV. The solid (blue) line denotes the results of Distorted Wave Born Approximation with Gamow factor (DWBA-G) model. The experiment is shown by red squares with standard deviation statistical error bars. All the calculations and the experiment are normalized arbitrarily to the number of 5.0. The vertical dash lines indicate the directions of the momentum transfer ±**K**. The results is taken from Ref. [43]. The TDCS scale shown is arbitrary, where all experimental and theoretical results are arbitrarily inter-normalised for best visual fit at the maximum of the binary lobe.*

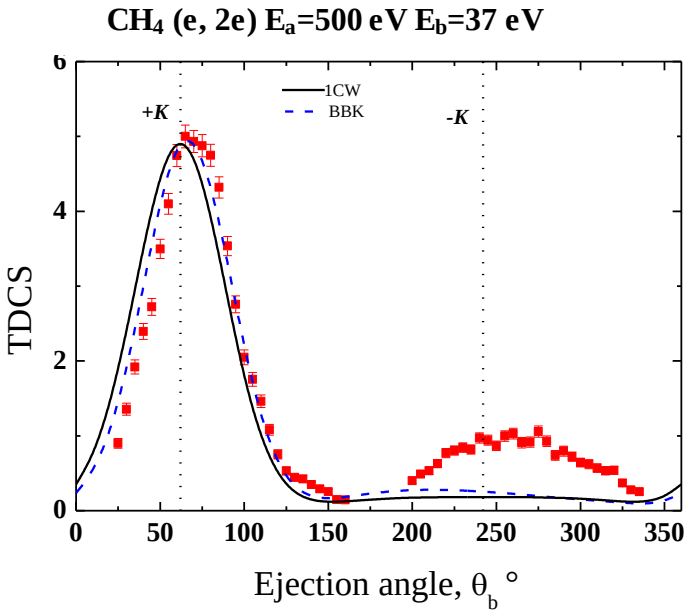

Figure 5.5 *(e, 2e) TDCS for ionization of the outer valence ($1t_2$) orbital of CH_4, plotted versus ejection angle θ_b, at fixed scattering angle, θ_a = -6 °. Kinematical parameters are E_a = 500 eV and E_b = 37 eV. The vertical lines indicate the momentum transfer direction, θ_K and its opposite θ_{-K}. Full black and dash blue lines represent the 1CW and BBK theoretical results, respectively. Solid squares are the experimental data with one standard deviation statistical error bars. Both experimental data and theoretical results are arbitrarily normalized to 5.0 for best guide of view. The results is taken from Ref. [9]. The TDCS scale shown is arbitrary, where all experimental and theoretical results are arbitrarily inter-normalised for best visual fit at the maximum of the binary lobe.*

Because the TDCSs measurements are relative cross sections, it is necessary to use the intensity ratio of recoil to binary lobes to represent the importance of the contribution of the interaction with different targets. Here we take this ratio α as maximum of recoil peak (R) to maximum of binary peak (B), α=R/B. All the parameters are listed in Tab. 5.2. We define α as the relative intensity ratio between maximum of recoil peak to maximum of binary peak for both cases.

Target	Ne	CH_4
Maximum of Recoil peak (R)	2.14	1.05
Maximum of Binary peak (B)	5.0	5.0
Ratio α (R/B)	0.43	0.21

Table 5.2 *The TDCS ratio of recoil to binary for Ne and CH_4 under same kinematical condition in (e, 2e) measurements at fixed scattering angle, θ_a = -6 °. Kinematical parameters are E_a = 500 eV and E_b = 37 eV.*

From Table 5.2, we can find that the most obvious difference between the two sets of TDCSs can be found in their recoil lobes. The ratio of recoil to binary of Ne α_{Ne} is ~ 2 times larger than the ratio of CH_4 α_{CH4}, though the scattered and ejected electron energies are the same for Ne and CH_4 in the (e, 2e) measurements. This can tentatively be attributed to the different target structure influence as discussed before. For Ne, because of its single center property, the target electron might have a localized charge distribution. Hence the quantum backward reflection on nucleus (or interaction between ejected electron and the nucleus) should be stronger than for CH_4, in which it has a multi-center structure (hence a more diffuse charge distribution) thus resulting in a weaker quantum backward reflection (or interaction between ejected electron and nuclei), with respect to Ne.

Structure influence on (e, 3-1e) results

As stated above, the target structure influence on (e, 3-1e) 4DCS is much more complex than in SI case. Indeed, in SI process, the recoil lobe is originated from the reflection of the single ejected electron by the nucleus, whereas in DI there are two ejected electrons. Both these two ejected electrons have the possibilities of being reflected (or not) by the nucleus. Moreover, due to different DI mechanisms, the ejected electron may experience different pathways before being detected.

Despite this difficulty, we can compare Figs. 5.4 and 5.5 for SI to Figs. 5.2 and 5.3 for DI. A striking observation can be made here: as stated above, the SI of the molecular target CH_4 yields smaller recoil intensity (relative to the binary one) than does the atomic target, Ne. Similarly, if we take a global look to the Figs. 5.1 and 5.2, the DI of the CH_4 molecule yields a smaller backward lobe (relative to the forward one) than does the DI of Ne atom. However, this comparison can hardly be

pursued any further since the DI forward and backward lobes are intrinsically different in nature from the SI binary and recoil lobes. Indeed, the DI lobes are formed by complex combinations of binary and recoil scattering events, which are very difficult to disentangle from each other. Similar observation were made in (e, 3-1e) experiments on He and H_2 [12]. Nevertheless, we think that such comparison (atom versus the iso-electronic molecule) might be a promising path which could be exploited in the future with the help of theoretical models to be developed, and which might be able to disentangle first order and second order contributions.

5.3 Conclusion

The (e, 3-1e) 4DCSs at ~600 eV impact energy are represented for DI of the outer valence of Ne (2p) and CH_4 ($1t_2$) in equal and unequal energy sharing cases, respectively. To the best of our knowledge, there are the first experiments performed on methane to study the dynamics of molecular DI by electron impact. All 4DCS results are compared with the prediction of TS2 kinematical model. It is found that these TS2 predictions satisfactorily explain most of the structures shown in (e, 3-1e) experiment of Ne and CH_4, though few structures cannot yet be explained by this model. Due to the absence of theoretical calculations for DI of CH_4, only the theoretical results recently obtained by Dal Cappello for DI of Ne within B1 and B2 models are compared with our data for Ne. The B2 model shows good agreement with experimental results. We conclude that the TS2 mechanism has an important contribution with respect to first order mechanisms (SO and/or TS1) at present kinematics. Also, due to the target property, the influence of the target structure (or nucleus distribution) is explored tentatively. We observed that DI of the CH_4 molecule yields a smaller backward lobe (relative to the forward one) than does the DI of Ne atom. However, it is difficult to disentangle the target recoil contribution in (e, 3-1e) 4DCS results due to the complexity of DI process. New theories for DI of molecules at present kinematics are highly awaited. Further DI experimental data under this kinematics and for different molecular systems are also desirable.

5.4 Bibliography

1. Lahmam-Bennani, A., et al., *Predominance of the second-order, two-step mechanism in the electron impact double ionization of helium at intermediate impact energy*. Journal of Physics B: Atomic, Molecular and Optical Physics, 2010. **43**(10): p. 105201.
2. Li, C., et al., *Electron impact double ionization of neon, argon and molecular nitrogen: role of the two-step mechanism*. Journal of Physics B: Atomic, Molecular and Optical Physics, 2011. **44**(11): p. 115201.
3. Staicu Casagrande, E.M., et al., *Experimental and theoretical confirmation of the role of higher order mechanisms in the electron impact double ionization of helium*. Journal of Physics B: Atomic, Molecular and Optical Physics, 2011. **44**(5): p. 055201.
4. Li, C., et al., *Identification of first order and non-first order contributions in the (e,3–1e) and (e,3e) double ionization of molecular nitrogen*. Journal of Physics B: Atomic, Molecular and Optical Physics, 2012. **45**(13): p. 135201.
5. Carlson, T.A. and M.O. Krause, *Electron Shake-Off Resulting from K-Shell Ionization in Neon Measured as a Function of Photoelectron Velocity*. Physical Review, 1965. **140**(4A): p. A1057-A1064.
6. McGuire, J.H., *Double Ionization of Helium by Protons and Electrons at High Velocities*. Physical Review Letters, 1982. **49**(16): p. 1153-1157.
7. Dal Cappello, C., et al., *The second Born approximation for the single and double ionization of atoms by electrons and positrons*. Journal of Physics B: Atomic, Molecular and Optical Physics, 2011. **44**(1): p. 015204.
8. Kheifets, A.S., et al., *DWBA-G calculations of electron impact ionization of noble gas atoms*. Journal of Physics B: Atomic, Molecular and Optical Physics, 2008. **41**(14): p. 145201.
9. Lahmam-Bennani, A., et al., *Dynamics of electron impact ionization of the outer and inner valence ($1t_2$ and $2a_1$) molecular orbitals of CH_4 at intermediate and large ion recoil momentum*. Journal of Physics B: Atomic, Molecular and Optical Physics, 2009. **42**(16): p. 165201.
10. Champion, C., et al., *Single ionization of the water molecule by electron impact: Angular distributions at low incident energy*. Physical Review A, 2006. **73**(1): p. 012717.
11. Brauner, M., Briggs, J.S. and Klar, H. *Triply-Differential Cross-Sections for Ionization of Hydrogen-Atoms by Electrons and Positrons*. Journal of Physics B-Atomic Molecular and Optical Physics, 1989. **22**(14): p. 2265-2287.
12. Lahmam-Bennani, A., Duguet, A. and Roussin, S. *Observation of non-first-order effects in an (e, 3-1e) investigation of the double ionization of helium and molecular hydrogen*. Journal of Physics B: Atomic, Molecular and Optical Physics, 2002. **35**(2): p. L59.
13. Dal Cappello, C., Joulakian, B., and Langlois, J., *Calculations for (e,3e) and (γ,2e)*. Journal De Physique IV, Colloque C6, supplément au Journal de Physique 11, Volume 3, novembre 1993, p. 125

Conclusion and Perspectives

In this thesis, we have presented a series of experimental results on electron impact double ionization (DI) from atomic targets to molecular targets at intermediate incident energy. These results are obtained from the so-called (e, 3-1e) or from the 'complete' (e, 3e) experiments, under unexplored kinematical conditions, characterized by a large momentum transfer to the residual ion who thus also plays an important role.

We extended the previous (e, 3-1e) measurements for DI of He at ~ 600-700 eV impact energy to larger ejected energies and more asymmetric energy sharing. Our new data display large shifts as well as marked structures in the forward and backward lobes for the ejected electron angular distributions. The TS2 kinematical analysis model recently introduced by our group, and which treats the DI process as two successive (e,2e) single ionizations (SI) was applied to all data sets. This analysis shows that under the present kinematics the two-step 2 (TS2) mechanism dominates over the shake-off (SO) and two-step 1 (TS1) and is mostly responsible for the structures and angular positions of the measured lobes. Besides, the recoil contribution in TS2 kinematical model is considered, which did not appear in previous discussion. By including not only the binary contribution but also the recoil one in each (e, 2e)-like step, we get two or four more angular position predictions for unequal or equal energy sharing between the two ejected electrons, respectively. Most of these new 'recoil' contribution predictions are in good agreement with the structures shown in (e, 3-1e) measurements, which were not predicted by previous TS2 kinematical analysis excluding 'recoil' contribution. Therefore, we emphasize that the recoil contribution in TS2 mechanism plays a comparable role as the binary contribution in each (e, 2e)-like step in TS2.

The prediction of the first Born B1-3C model does not reproduce the observed shifts and structures of the cross-section distribution for He whereas the theoretical results from two second order models, namely the TS2-MCEG and B2 treatments, very clearly constitute a considerable improvement. The forward and backward lobes are correctly or qualitatively well predicted. This confirms again that under the present kinematics the non-first-order mechanism such as TS2 are mostly responsible for the structures observed in the measured distributions.

Further, the (e, 3-1e) experiments for the DI of helium at few hundred eV impact energy are extended to more complex targets, namely neon and argon. Compared to He, the ejected electron angular distributions exhibit similar features, that is, large shifts from the momentum transfer axis as well as marked structures in the forward and backward lobes. For Ne and Ar, these features are not reproduced by a first Born B1-3C model, nor by a second Born (B2-2CG) model which does indeed constitutes an improvements over the first Born. The TS2 kinematical model is applied to these new

data, and it is shown to successfully predict the angular positions of some of the structures of the measured lobes. Similarly as in He case, the extension of TS2 kinematical model by including 'recoil' contribution in each (e, 2e)-like step remarkably predicts more unknown structures which are not predicted neither by the considered theories nor by the previous kinematical model. This work together with the previous one on He thus constitutes a large body of experimental evidence that under the present kinematics the TS2 mechanism dominates over the first-order SO and TS1 mechanisms. We also observe that the measured angular shifts of the forward and backward lobes are quasi-independent of the nature of the target, as also supported by our kinematical model.

The (e, 3-1e) and full (e, 3e) experiments for DI of molecular nitrogen at about 600 eV electron impact energy and equal energy sharing among the two emitted electrons are reported under the same kinematics. The (e, 3e) results are displayed by two dimensional angular distribution of the two ejected electrons and exhibit rich structures. Moreover, we also presented (e, 3-1e) results for nitrogen molecule at unequal energy sharing cases. Up to date neither elaborate first-order nor second-order calculations exist to which the present (e, 3-1e) experimental data for N_2 could be compared. Hence the TS2 kinematical model is applied again for comparison, including both binary and recoil contributions in each step of TS2 mechanism. Again this TS2 kinematical model is found to predict most of the structures shown in (e, 3-1e) angular distributions.

The (e, 3e) experimental data for N_2 are also compared with the predictions of a first Born model which is found to yield different angular distributions. Furthermore, we made three different 'cut'-modes to explore the original contribution of the rich structures shown in the two sets of (e, 3e) 5DCS measurements. These observations, together with the relative success of the TS2 kinematical model lead us to legitimately conclude that the molecular DI process is largely dominated by the TS2 mechanism (without excluding the intervention of higher order mechanisms).

This work together with our previous ones on atomic targets thus constitute a large body of experimental evidence that under the present kinematics the TS2 mechanism dominates over the first order SO and TS1 mechanisms.

In the end, (e, 3-1e) 4DCSs at ~600 eV impact energy are presented for DI of the outer valence of the two isoelectronic targets Ne (2p) and CH_4 ($1t_2$) both in equal and unequal energy sharing cases. All 4DCS results are compared with the prediction of TS2 kinematical model. It is found that these TS2 predictions satisfactorily explain most of the structures shown in (e, 3-1e) results, though few of them still can not be explained by this qualitative analysis model. We conclude that the TS2 mechanism has a comparable contribution with respect to first order mechanisms (SO and/or TS1) at present kinematics. Also, due to the target property, the influence of target structure (or nucleus distribution) is explored tentatively. We conclude that the different target structure has a certain influence on the DI process. New theoretical developments for DI of molecules at present kinematics

are highly expected. Further DI experimental data under this kinematics and for different molecular systems are also desirable.

Perspectives:

- Since there is bare complete (e, 3e) experiments on atomic targets at intermediate incident energy, especially for He which is an ideal target to theorist (e.g., Dürr et al, Phys. Rev. Letter, **98,** 193201 (2007), where (e, 3e) experiment is performed on He at E_0=106 eV and $E_a+E_b+E_c$=27 eV), such experiments are highly awaited for to be performed with as high accuracy as possible, in order to provide a stringent test for theoretical calculations. Only two sets of so-called '(e, 2e)+ion' experiments (which is equivalent to (e, 3e) experiment) were performed by Dürr et al (Phys. Rev. Lett., 98 (2007) 193201) at E_0=106 eV and Dorn et al (Phys. Rev. A, 68 (2003) 012715) at E_0=500 eV. However, due the inherently small DI (e, 3e) cross sections and to the subsequent long accumulation time needed to reach good enough statistics, it remains a challenge for experimentalists.
- The (e, 3-1e) experiments for H_2 at intermediate incident energy are also desirable since it is the simplest molecule and these (e, 3-1e) results can be used for examining the existing models for describing DI process of H_2. The DI experiments for H_2 may open a way for fully understanding the DI process on molecules.
- Also, new theoretical models are expected for comparing with, and tentatively explaining the present experimental results on N_2 and CH_4, etc, which are not well reproduced by the theory.
- Finally, the comparative study between isoelectronic atomic and molecular targets, commenced here for Ne and CH_4, should be pursued both experimentally and theoretically with the aim of evidentiating possible molecular effects in the description of the DI process. The same idea was underlying the work on He and H_2 published by Staicu Casagrande et al (J. Phys. B., 41 (2008) 025204 (7pp)) for SI, and the work published by Lahmam-Bennani et al (J. Phys. B., 35 (2002) L59-L63) for DI.